RECYCLING OF PHOSPHORUS-RECOVERED INCINERATED SEWAGE SLUDGE ASH FOR STABILIZATION/SOLIDIFICATION OF CONTAMINATED MARINE SEDIMENTS

WANG QIMING

PhD

The Hong Kong Polytechnic University

2023

The Hong Kong Polytechnic University

Department of Civil and Environmental Engineering

Recycling of Phosphorus-recovered Incinerated Sewage Sludge Ash for Stabilization/Solidification of Contaminated Marine Sediments

WANG Qiming

A thesis submitted in partial fulfilment of the requirements for the degree of Doctor of Philosophy

December 2022

CERTIFICATE OF ORIGINALITY

I hereby declare that this thesis is my own work and that, to the best of my knowledge and belief, it reproduces no material previously published or written, nor material that has been accepted for the award of any other degree or diploma, except where due to acknowledgement has been made in the text.

_____ (Signed)

_____Qiming Wang_____ (Name of student)

ABSTRACT

To progress our cities towards sustainable waste management, an array of reuse and recycling methods have been developed to manage the growing amounts of incinerated sewage sludge ash (ISSA) from the combustion of dewatered sewage sludge. Phosphorus (P) recovery from ISSA via the cost-effective and highly efficient acid washing method (with H_2SO_4 as the leachant) has been increasingly acknowledged as a critical step to resource efficient recycling of ISSA. However, it generates a residual ash i.e., P-recovered ISSA, accounting for over 80% by mass of the original ISSA. The aim of this study is to explore reuse options for the residual ash so that a complete 'close-loop' recycling of ISSA is achievable without the generation of waste. Given the rich iron content and insignificant amounts of toxic heavy metals in the P-recovered ISSA, the focus of this study has been directed to reuse it as a low-cost supplementary iron source to synthesize iron-containing functional materials for the remediation of heavy metal(loid) contaminated waters and dredged marine sediments.

In this thesis, co-pyrolysis of the P-recovered ISSA with a model biomass material i.e., lignin, for aqueous Cr(VI) removal was firstly explored. The optimized co-pyrolysis process successfully turned most of the iron oxides in the P-recovered ISSA residue into zero-valent iron (ZVI) and improved surface properties of the end composite material that rapidly and effectively removed Cr(VI) from an acidic solution primarily via chemical reductions. In order to extend the scope of feedstock biomass and expand the application horizon, another typical biowaste i.e., peanut shell was then co-pyrolyzed with the P-recovered ISSA for the removal of As(III) and As(V) from aqueous solutions under both acidic and near neutral environments. The effect of silica on the pollutant removal by the resulting composite material was addressed as well considering its dominant presence in the P-recovered ISSA. Silica in the P-recovered ISSA impeded the formation of ZVI and magnetite by forming iron silicon during the co-

pyrolysis process and resulted in notably increased leaching of reactive silica during the sorption process that competed with arsenic for active adsorption sites. The produced sorptive materials derived all from solid waste still exhibited satisfactory removal performance for heavy metals from aqueous under optimized conditions making the co-pyrolysis method attractive for the management of the P-recovered ISSA.

To facilitate finding an end use of the spent material after the removal of pollutants, shaping of the powdery mixture of the P-recovered ISSA, peanut shell and waste bentonite with a mass ratio of 1:1:2 to pelletized granules was achieved via sintering under a nitrogen atmosphere. The end product was produced mechanically strong (4.9 MPa) and lightweight (1.21 g/cm^3) millimeter-sized granules. These granules could remove As(V), Cr(VI), Cu(II) and Pb(II) from aqueous solutions via mechanisms including redox reactions, complexation and (co)precipitation with the corresponding maximum adsorption capacity at 14.11, 5.79, 14.12 and 23.52 mg/g. The spent granules could be environment safely upcycled as a partial river sand replacement in cement mortars based on the Toxicity Characteristics Leaching Procedure. The powdery composite material produced from the co-pyrolysis process could also be used as a green additive in cement-based stabilization and solidification processes that achieved an enhanced immobilization and recycling of As-, Cr- and Cu-contaminated marine sediments into useful construction materials. Thus, the aim of this thesis was realized by providing a technique for ‘close-loop’ recycling of ISSA.

PUBLICATIONS ARISING FROM THE THESIS

The results of this thesis have been published in peer-reviewed journal articles as listed below:

1. **Wang, Q.**, Li, J. S., & Poon, C. S. (2022). Production of sorptive granules from incinerated sewage sludge ash and upcycling in cement mortar. *Separation and Purification Technology*, 309, 123046.

2. **Wang, Q.**, Li, J. S., & Poon, C. S. (2022). An iron-biochar composite from co-pyrolysis of incinerated sewage sludge ash and peanut shell for arsenic removal: Role of silica. *Environmental Pollution*, 120115.

3. **Wang, Q.**, Li, J. S., Xue, Q., & Poon, C. S. (2022). Immobilization and recycling of contaminated marine sediments in cement-based materials incorporating iron-biochar composites. *Journal of Hazardous Materials*, 435, 128971.

4. **Wang, Q.**, Li, J. S., & Poon, C. S. (2021). Novel recycling of phosphorus-recovered incinerated sewage sludge ash residues by co-pyrolysis with lignin for reductive/sorptive removal of hexavalent chromium from aqueous solutions. *Chemosphere*, 285, 131434.

The results of the reuse and recycling of the P-recovered ISSA via a different method have also been published in a journal article, but have not been included in this thesis:

1. **Wang, Q.**, Li, J. S., Xue, Q., & Poon, C. S. (2021). Alkaline modification of the acid residue of incinerated sewage sludge ash after phosphorus recovery for heavy metal removal from aqueous solutions. *Waste Management*, 123, 80-87.

The results presented in the following co-authored peer-reviewed journal articles have not been included in this thesis:

1. Fang, L., Li, L., **Wang, Q.**, Li, J. S., & Poon, C. S. (2022). Agronomic effectiveness of recovered phosphate fertilizer produced from incinerated sewage sludge ash. *Waste Disposal & Sustainable Energy*, 4(2), 157-167.

2. Fang, L., **Wang, Q.**, Li, J. S., Poon, C. S., Cheeseman, C. R., Donatello, S., & Tsang, D. C. (2021). Feasibility of wet-extraction of phosphorus from incinerated sewage sludge ash (ISSA) for phosphate fertilizer production: A critical review. *Critical Reviews in Environmental Science and Technology*, 51(9), 939-971.

3. Li, J. S., **Wang, Q.**, Chen, Z., Xue, Q., Chen, X., Mu, Y., & Poon, C. S. (2021). Immobilization of high-Pb contaminated soil by oxalic acid activated incinerated sewage sludge ash. *Environmental Pollution*, 284, 117120.

4. Nie, J., **Wang, Q.**, Gao, S., Poon, C. S., Zhou, Y., & Li, J. S. (2021). Novel recycling of incinerated sewage sludge ash (ISSA) and waste bentonite as ceramsite for Pb-containing wastewater treatment: Performance and mechanism. *Journal of Environmental Management*, 288, 112382.

5. Gao, S., **Wang, Q**., Nie, J., Poon, C. S., Yin, H., & Li, J. S. (2021). Arsenate (V) removal from aqueous system by using modified incinerated sewage sludge ash (ISSA) as a novel adsorbent. *Chemosphere*, 270, 129423.

Contributions to a conference paper have been presented in this thesis:

1. Poon, C. S., & **Wang, Q.** (2021, October). Beneficial utilization of sewage sludge ash residues for the stabilization/solidification of As-, Cr-, and Cu-contaminated marine sediments. In *IOP Conference Series: Earth and Environmental Science* (Vol. 861, No. 7, p. 072024).

ACKNOWLEDGMENTS

This PhD study has been funded by grants provided by the National Natural Science Foundation of China/Hong Kong Research Grants Council Joint Research Scheme and the Environment and Conservation Fund of the Hong Kong SAR government. Also, the studies would not have been possible without the great support I received from many institutions and individuals.

First and foremost, I am grateful to my chief supervisor, Prof. Chi Sun Poon, for his willingness to give me the opportunity to conduct this research, and for his valuable guidance, professional suggestions, and spiritual support throughout the four-year study. I would also like to express my gratitude to my co-supervisor, Prof. Jiang-shan Li, from the Institute of Rock and Soil Mechanics Chinese Academy of Sciences, for his constructive advice and unfailing support to me.

I am obliged to Ms. Chan Dorothy, Ms. Che Celine, Ms. Ho Pendy, Mr. Lam W.S., Mr. Chan John, Mr. Chan Jonathan, and Dr. Lui Hardy for their help in experiments. Thanks also to many supporting staff at the Hong Kong Polytechnic University for their kind support. I am thankful to group members, old and new, in Prof. Poon's research group, friends, peers, and colleagues at the university for sharing ideas, cakes, jokes, and stories with me, which enriched my life here.

Finally, deep and sincere thanks to my family for their continuous encouragement and unconditional love.

TABLE OF CONTENTS

LIST OF FIGURES

LIST OF TABLES

ABBREVIATIONS

ANC	acid neutralization capacity
BET	Brunauer, Emmet and Teller
C2S	dicalcium silicate
C3A	tricalcium aluminate
C3S	tricalcium silicate
CC	calcium carbonate
CH	calcium hydroxide
C-S-H	calcium-silicate-hydrate
DI	deionized
DOC	dissolved organic carbon
EDX	energy dispersive X-ray
FTIR	Fourier transformation infrared spectroscopy
IC	inorganic carbon
ICP-OES	inductively coupled plasma optical emission spectroscopy
ISSA	incinerated sewage sludge ash
LCEL	lower chemical exceedance level
LOI	loss on ignition
LWA	lightweight aggregate
MIP	mercury intrusion porosity
OPC	ordinary Portland cement
pH_{PZC}	pH of the point of zero charge
ppb	parts per billion
ppm	parts per million

PVC	polyvinylchloride
SAI	strength activity index
SEM	scanning electron microscopy
SEP	sequential extraction procedure
SPLP	synthetic precipitation leaching procedure
S/S	stabilization/solidification
SS	sewage sludge
TC	total carbon
TCLP	toxicity characteristic leaching procedure
TOC	total organic carbon
TGA	thermal gravimetric analysis
UCEL	upper chemical exceedance level
UV-Vis	ultraviolet-visible
XPS	X-ray photoelectron spectroscopy
XRD	X-ray diffraction
XRF	X-ray fluorescence
ZVI	zero valent iron

CHAPTER 1 INTRODUCTION

This chapter commences with a brief introduction of the research background and the motivations, follows by the aim and objectives of this PhD study. The structure of the thesis is provided at the end of this chapter.

1.1 Background of the study

Solid waste disposal as well as water/soil pollution are significant and universal environmental issues and have posed risks to human health and the environment. Tremendous amounts of solid waste have been generated all over the globe and will continue to rise in the following decades (Figure 1-1). In 2016, the carbon dioxide (CO_2) equivalent greenhouse emissions associated with solid waste management and disposal was around 1.6 billion, account for 5% of the total global emission, and the number has been predicted to be 2.6 billion tons by 2050 (Kaza et al., 2018). Meanwhile, some 2.2 billion people suffer from the lack of safely managed drinking water with the COVID-19 exacerbating the situation (DESA UN, n.d.). Various anthropogenic activities (mining, battery, tannery, electroplating industries etc.) produce tremendous heavy metal(loid) containing wastewaters, which can be discharged into natural water bodies without proper treatment, followed by migration in the environment and eventually reaching the ocean and sinking in marine sediments. The remediation of these heavy metal(loid)s contaminated waters and sediments is indispensable due to the potential mutagenicity, carcinogenicity, and teratogenicity (Han, 2020; Prasad et al., 2021; Xia et al., 2019). Attention to and action on reuse and recycling for solid waste, safe management of hazardous waste, and sustainable water and sanitation have been explicitly called for on the 2030 Agenda for Sustainable Development (DESA UN, 2015). Urgent and collective action are needed from all stakeholders to progress our cities towards a sustainable and resilient future.

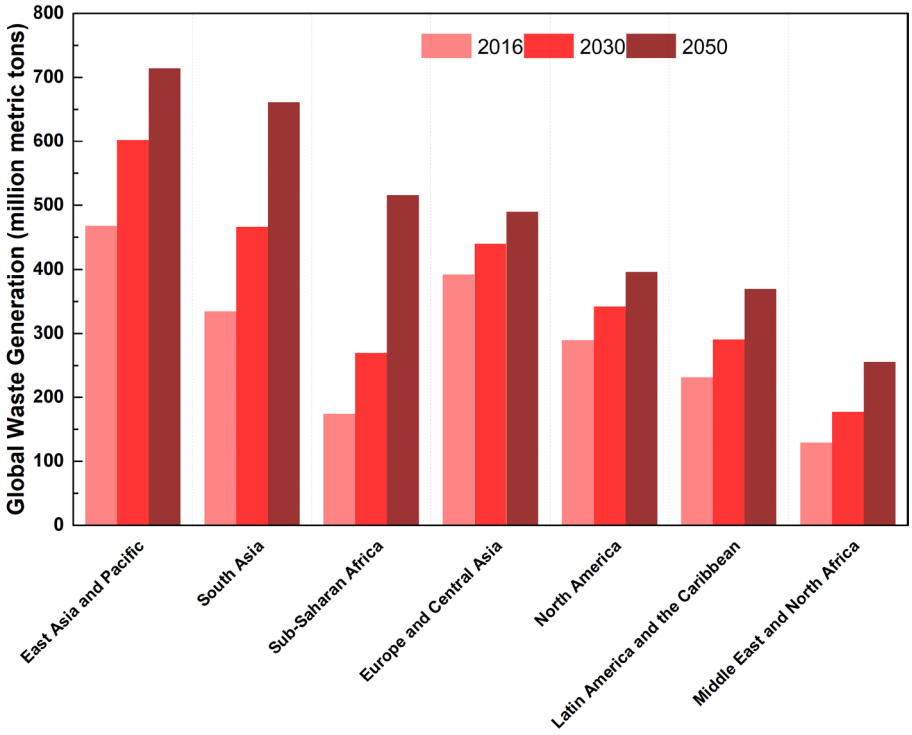

Figure 1-1 Global waste generation (Data from ref. (Kaza et al., 2018)).

Hong Kong as well as many other cities throughout the world are having growing pressure to manage roaring amounts of solid waste due to limited land space and the stringent regulations in response to environmental challenges. Incinerated sewage sludge ash (ISSA) generated from the combustion of increasing amounts of dewatered sewage sludge has been directly sent to landfills without recycling at present (H. K. EPD, 2021; EPD, 2010) that induces enormous pressure to landfills. Tremendous research effort on the reuse and recycling of ISSA has indicated that recovery of phosphorus (P) from it is a critical step to achieving resource efficient recycling of ISSA considering concerns associated with a stable future supply of P rock resources (Fang et al., 2020b). Nevertheless, as the most practical way to extract P from ISSA, the acid washing method produces a residual ash, i.e., P-recovered ISSA which can account for over 80% by mass to the original ISSA (e.g., washed by H_2SO_4). Scanty information is available about the management of this residual ash. This PhD study therefore focuses

primarily on the reuse and recycling of the P-recovered ISSA so that a complete P recovery process from ISSA without the generation of waste can be achievable.

1.2 Research aim and objectives

Given the rich iron content in the P-recovered ISSA, this PhD study focuses on developing means for beneficial recycling of it as a supplementary iron source to fabricate low-cost functional materials in environmental remediation applications. Specifically, the P-recovered ISSA together with waste biomass can be co-pyrolyzed to synthesize iron-biochar composites that can remove multi-toxic heavy metal(loid)s from aqueous solutions. Meanwhile, with the addition of waste bentonite into the mixture of P-recovered ISSA and biomass, lightweight granules with heavy metal(loid) sorptive properties and strong mechanical strength can be synthesized so that the spent granules can further be environmentally safely recycled in cement mortars. The powdery iron-biochar composite finds its application as a green additive in the cement-based stabilization/solidification (S/S) process for enhanced immobilization and recycling of contaminated dredged marine sediments as construction materials.

The specific objectives of this PhD study include:

1) Exploring the feasibility of using the P-recovered ISSA as a low-cost supplementary iron-source for the fabrication of an iron-biochar composite and its applicability for Cr(VI) removal from aqueous solutions;
2) Understanding the role of silica in the P-recovered ISSA residue on properties of the resulting iron-biochar composite relevant to As(III) and As(V) removal from aqueous solutions;
3) Developing millimeter-sized granules with multi heavy metal(loid) sorptive properties to environmentally safe upcycling of the spent granules in cement mortars;

4) Investigating the potential of using the powdery iron-biochar composite as a green additive to immobilize and recycle contaminated marine sediments as construction materials.

1.3 Structure of the thesis

This PhD study comprises eight chapters that are summarized as shown below.

Chapter 1 shows the background, aim and objectives of the study.

Chapter 2 reviews the generation and recycling of ISSA and points out that P-recovery by the cost effective and highly efficient acid washing method is a critical step to achieving resource efficient recycling of ISSA. Then, the characteristics and potential applications of the P-recovered ISSA after the acid washing method have been reviewed. Meanwhile, the heavy metal pollution status of waters and marine sediments is briefly reviewed with opportunities identified in respect to reuse the P-recovered ISSA to tackle these problems.

Chapter 3 describes in detail procedures for samples preparation and characterization, experimental programs, and models required to achieve the objectives of the study.

Chapter 4 investigates the feasibility of reusing the P-recovered ISSA as a low-cost supplementary iron source together with a model biomass material, i.e., lignin to fabricate an iron-biochar composite for aqueous Cr(VI) removal and the associated mechanisms.

Chapter 5 discusses the role of silica present in the P-recovered ISSA on properties of the end iron-biochar composite relevant to As(III) and As(V) removal from aqueous solutions.

Chapter 6 presents kilogram-scale production of millimeter-sized granules solely from waste including the P-recovered ISSA residue, peanut shell and waste bentonite with sorptive properties for multi heavy metal(loid)s, and the environmentally safe upcycling of the spent granules in lightweight mortars.

Chapter 7 assesses the potential of using the produced powdery iron-biochar composite as a green additive in the cement-based S/S process for enhanced immobilization and recycling of contaminated marine sediments as construction materials.

Chapter 8 summarizes major findings and conclusions of this PhD study and gives recommendations for future work.

CHAPTER 2 LITERATURE REVIEW

This chapter discusses pertinent issues that contextualize the study. The chapter first presents a review in respect to the generation of ISSA, its features and recycling status that points out the critical role of P recovery from ISSA and a paucity of information in regard to the management of the generated residual ash after the recovery process. Then, the significance to reuse and recycle the P-recovered ISSA is presented with its characteristics and limited reusing options summarized. Meanwhile, the heavy metal pollution status in waters and marine sediments is briefly introduced with remediation methods reviewed and potential application opportunities of the P-recovered ISSA identified in addressing these issues.

2.1 Reuse and recycling of ISSA

2.1.1 Introduction to ISSA

The rapid growth of world's population, economic development, and urbanization have resulted in a dramatic increase in produced municipal wastewater (as shown in Figure 2-1). With a growing ratio in treatment of municipal wastewater, significant quantities of sewage sludge (SS) are generated all over the globe (Chang et al., 2020). China, America, Japan, Germany and Australia produced around 7.81 (2019), 4.75 (2019), 2.40 (2017), 1.74 (2020) and 0.37 (2020) million dry metric tons of SS in a single year (AWA, 2020; EPA, 2022; FSO, 2022; JEMAI, 2021; Wei et al., 2020).

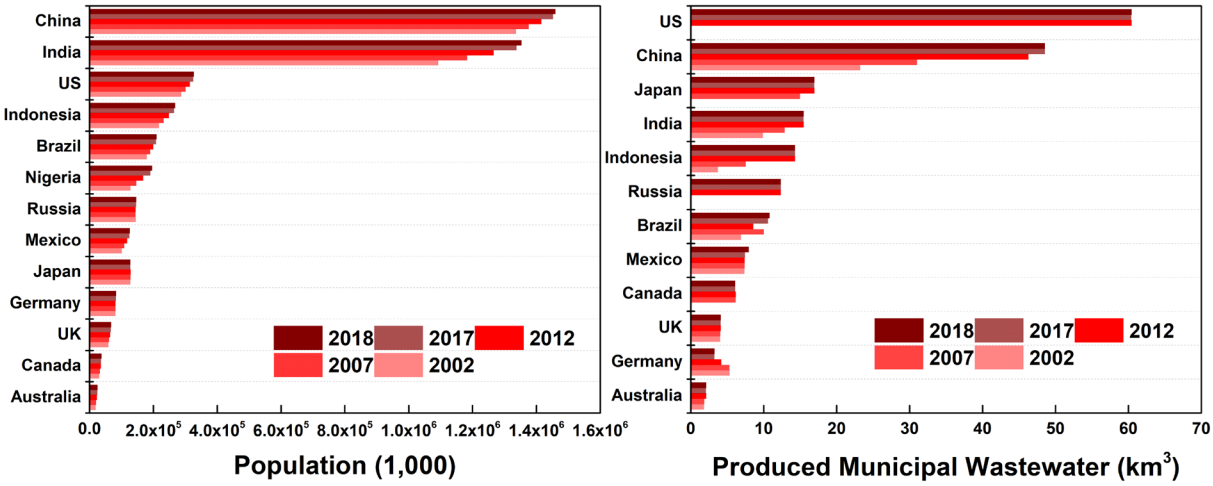

Figure 2-1 World population and produced municipal wastewater by countries (Data from ref. (FAO, n.d.)).

SS is composed of both organic and inorganic substances such as microbial biomass, pathogens, parasites, nutrients (phosphorus and nitrogen), and potentially toxic elements (As, Cr, Pb, Hg, Ni, Cu, Zn, etc.) and compounds (chlorinated paraffin, polycyclic aromatic hydrocarbons, polychlorinated biphenyl, benzotriazoles, etc.) (Chang et al., 2020; Cheeseman and Virdi, 2005). Processing and managing its extremely large amounts present one of the most environmentally challenging issues of municipal wastewater treatment process (Hartman et al., 2005). In Egypt, about 85% of the SS generated are sold without proper treatment (Abdel Wahaab et al., 2020). A company in Xingtai China has illegally received over 88 thousand tons SS from 2017, among which around 13 thousand tons has been directly dumped into arable land without any pollutant control. Similarly, a fertilizer production plant in Tangshan China has illegally received 156 thousand tons SS, and around 32% of which cannot be tracked (h2o-china, 2022).

Traditionally, SS is predominantly applied to agricultural land for nutrients recovery or directly landfilled (Donatello, 2009), which are still important SS management methods in countries

like America and Australia at present (as shown in Figure 2-2). Reuse SS in construction or building materials is another common management method that is mainly practiced in Japan and China. Nevertheless, the harmful substances in SS impede the direct application in farmlands or surrounding areas of cities due to the undesirable effect on human health and the environment particularly under the recent pandemic situation due to COVID-19 (Chang et al., 2020; Ducoli et al., 2021).

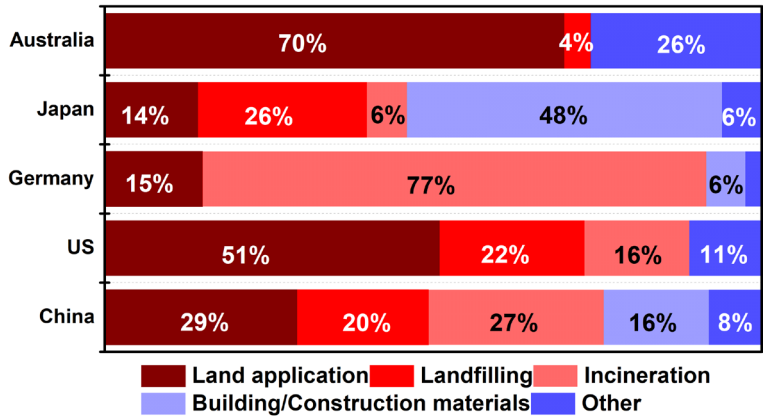

Figure 2-2 Sewage sludge treatment and disposal methods applied by country (Data from refs. (AWA, 2020; EPA, 2022; FSO, 2022; JEMAI, 2021; Wei et al., 2020)).

Given these concerning issues, the well-established incineration technology has been increasingly employed for the management of SS due to the efficient reduction on the SS volume and amount, high degree of process control, destruction of pathogens, and good ability to recover energy (Fang et al., 2020b; Lynn et al., 2016; Schnell et al., 2020). This technology however produces incinerated sewage sludge ash (ISSA), whose mass is around 20~30% of the input SS, leading to an estimated ISSA amount produced in China, America, Japan and Germany respectively at around 0.63 (2019), 0.23 (2019), 0.04 (2017) and 0.40 (2020) million dry tons in a year. Moreover, the daily per capita waste generation in high-income countries is estimated to increase by 19% by 2050, while this increased percentage could be up to 40% in

low/middle-income countries (Kaza et al., 2018) based on economic development, and population and urbanization growth. In China, the SS production amount has been predicted to increase from 7.81 in 2019 to over 12.4 (62 million wet tons) million dry tons in 2025 (h2o-china, 2022). And the country's SS incineration ratio had increased from 26% in 2019 to around 30~40% in 2020. Not only in China, the use of waste-to-energy incineration technology for waste management in upper-middle-income countries has dramatically increased from 0.1% to 10% in recent years (Kaza et al., 2018). For cities with high population densities and limited landfill space such as Hong Kong and Tokyo, nearly all of the generated SS have been incinerated (BOS, n.d.; EPD, 2015). It can be reasonably assumed that the amounts of ISSA will continue to rise, and its management can be a burden at a local level.

At present, T·PARK with a designed maximum SS treatment capacity of 2,000 tons in Hong Kong is the largest SS incineration facility in the world. As shown in Figure 2-3, after storage and deodorization, the dewatered SS is transferred into the incinerator and being combusted at over 850^{o}C for at least 2 seconds. The generated heat is recovered as electricity through a turbine. And the flue gas is cleaned by an effective flue gas cleaning system comprising a multi-cyclone, a dry reactor, and a bag filter. The solid particles collected from the incinerator and multi-cyclone separator are ISSA.

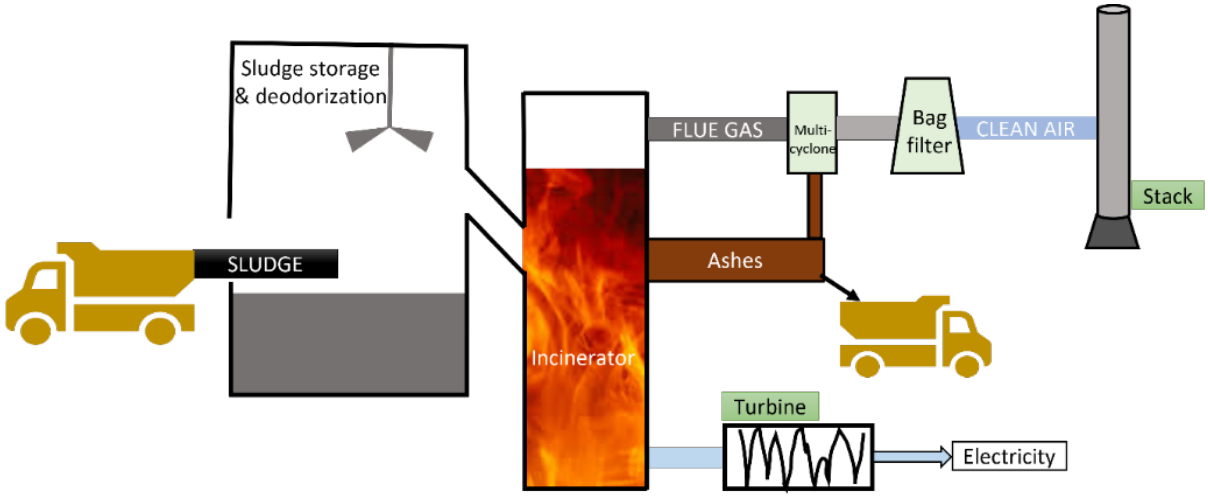

Figure 2-3 Incineration process for SS in T·Park Hong Kong. Adapted from ref. (TPARK, n.d.).

In 2020, around 1,034 tons of dewatered SS per day are collected from major sewage treatment facilities in Hong Kong, and the produced 137 tons ISSA were all disposed at landfills (H. K. EPD, 2021). With more and more large population centers created, disposal of solid waste in landfills will be increasingly difficult (Kaza et al., 2018) which is no longer a way towards sustainable waste management. Finding ways to reuse and recycle ISSA and other incineration residues is essential to help our cities progress towards sustainable waste management.

2.1.2 Characteristics of ISSA

Characterization of ISSA in terms of its compositions, mineralogy, and surface chemistry is essential to design a sustainable waste management process for it. The characteristics of ISSA can be greatly influenced by properties of SS (dependent on the type of sewage and wastewater treatment technology) and the combustion techniques. Variabilities in physical and chemical properties of ISSA are often observed in the literatures. Characteristics of ISSA produced in

the lab-scale combustion equipment can also differ significantly from those collected from real incineration plants.

Generally, most ISSA samples collected from incineration plants do not have a sewage odor (Lynn et al., 2016), and comprise fine-grained particles in a reddish-brown color (as shown in Figure 2-4). The particle sizes of ISSA lie within the range of 1~250 μm (Garcés et al., 2008). The density of ISSA falls in the range of 2.3~3.2 g/cm^3, and a higher SS combustion temperature leads to a higher density of ISSA (Lynn et al., 2016; Vouk et al., 2017). The ash particles are irregular with rough surface textures (Garcés et al., 2008; Lynn et al., 2018), and water washing has little effect on its morphology (Krejcirikova et al., 2019). The loss on ignition (LOI) of ISSA is typically less than 3% due to the oxidation and volatilization of residual organic carbon in the ash (Cheeseman and Virdi, 2005).

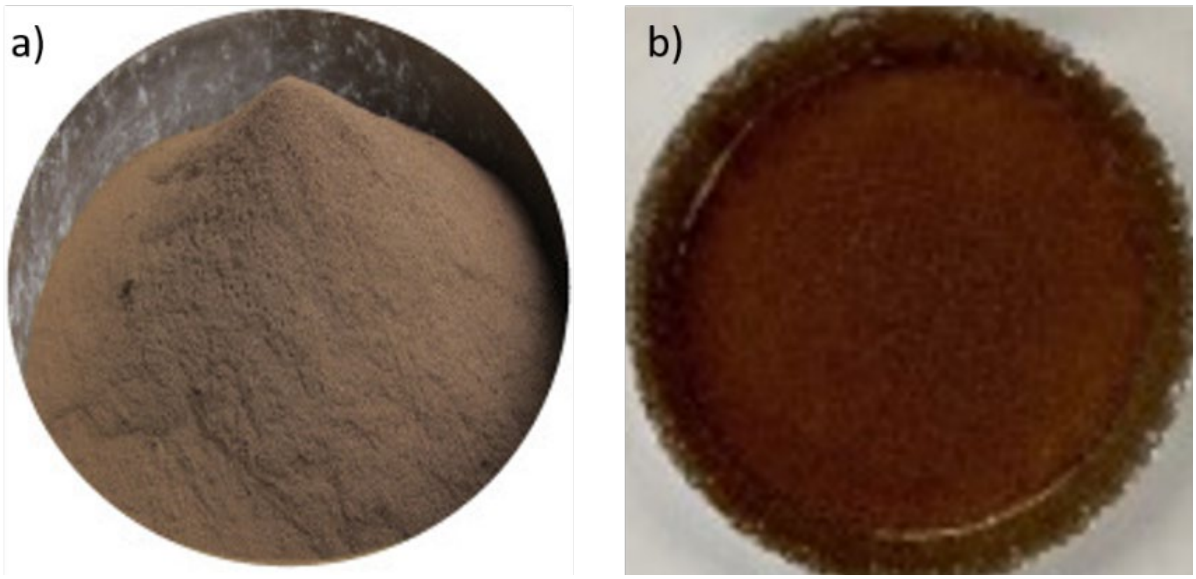

Figure 2-4 Sewage sludge ash collected from T·Park Hong Kong.

The elemental compositions of ISSA mainly include Si, Al, Fe, Ca and P besides O (as shown in Table 2-1) which are significantly influenced by the origin of the wastewater, and the sewage

treatment technology (Benassi et al., 2019; Donatello and Cheeseman, 2013; Smol et al., 2015). The most frequently identified crystalline mineral phases in ISSA include quartz, hematite, anorthite and whitlockite (Zhou et al., 2019). The XRD amorphous glassy phase contents in different ISSA samples can vary greatly. A high amorphous glassy content is of advantage when reusing ISSA as a pozzolanic additive in blended cements (Donatello and Cheeseman, 2013).

Table 2-1 Chemical compositions of ISSA collected from different regions all over the world.

Oxides (wt.%)		SiO_2	Al_2O_3	Fe_2O_3	CaO	MgO	K_2O	Na_2O	TiO_2	SO_3	P_2O_5	Reference
Hong Kong		37	15.2	14	6.91	2.8	2.77	7.11	0.38	3.66	9.12	(Zhou et al., 2019)
France		28.6	17.6	4.4	20.1	2.3	1.9	0.6	1.5	2	19.5	(Mejdi et al., 2020)
Brazil		38.3	20.7	11.3	5.51	1.91	0.73	0.7	3.73	4.18	7.28	(Istuque et al., 2019)
Denmark	Avedøre	15.8	4.4	16.3	23.4	1.82	1.45	0.67	0.83	2	18.3	(Krejcirikova et al., 2019)
	Lynetten	14.3	2.65	7.15	36.4	1.99	1.81	0.81	0.67	4.74	10.3	
Taiwan		63.3	15.4	6.81	1.8	1.03	1.51	0.7		1.02	7.02	(Chiou et al., 2006)
German and Netherland		23.8	24.9	3.2	17.1	0.09	0.95	0.86			19.4	(Adam et al., 2009)
		19.6	15.5	5.7	18.5	3.63	2.05	0.98			25.7	
		23.7	10.3	22.6	14.4	2.14	1.31	0.43			18.9	
Hong Kong		48.6	12.3	12.1	5.85	1.93	1.58	4.48		1.43	7.57	(Tang et al., 2020)
Spain		19.2	8.9	10	30.6	2.7	1.4	0.8		11.1	12.3	(Garcés et al., 2008)

ISSA also contains an array of concerning trace elements (As: 38 mg/kg, Cr: 750 mg/kg, Cu: 2260 mg/kg, Pb: 373 mg/kg and Zn: 3355 mg/kg average values) (Lynn et al., 2015) which significantly affects its reuse options. As the regulations are becoming more and more stringent regarding the potential leaching of chemicals of concern from various solid waste matrices, it is essential to evaluate the leaching potential of these toxic heavy metals from ISSA. Simply associating the environmental leaching risks with the total contents of toxic elements is not reliable that can generally overestimate the associated risk level, thus limiting the applications of ISSA. It is therefore crucial to characterize and predict the heavy metal mobility in ISSA and understand the underlying mechanisms.

The extensively employed leaching protocols for ISSA can be classified into several types including (i) batching leaching tests using deionized (DI) water or similar leachant without a buffering capacity; (ii) the column test/flow-through test; (iii) Toxicity Characteristic Leaching Procedure (TCLP), Synthetic Precipitation Leaching Procedure (SPLP), and so on, mimicking specific scenarios, and (iv) acid extractions, performed under aggressive conditions (pH < 2) that are hardly related to field conditions, but can be used to obtain in-depth knowledge of the ash chemistry (Izquierdo and Querol, 2012). These methods as well as other unstandardized methods but appropriate to assess the leaching of elements from ISSA are quite different in respect to the complexity from variations in test methods such as chemicals involved, reaction temperature and time, agitation method, and liquid-to-solid ratio. The heterogeneity of ISSA and differences in leaching protocols make it hard to compare the data based on the absolute values extracted from the literatures. Among these leaching methods, TCLP is the most widely adopted one, which shows ISSA as a non-hazardous waste in most cases (Li et al., 2018). The sequential extraction procedure (SEP) is also useful to identify the mobility and bioavailability of a heavy metal in the solid waste matrices (Du Laing, 2011). As shown in Figure 2-7, ISSA has barely any exchangeable Zn and Cu, while the corresponding residual fractions are around

77% and 64% contributing to their low leachability as assessed by TCLP. However, the environments where ISSA is reused or applied can differ greatly from the mimicked environment by TCLP, for instance, when ISSA is to be reused in construction materials where the matrix is basically alkaline. Overall, as ISSA contains heavy metals, it is necessary to examine the leaching potential by carefully selecting leaching tests to ensure an environmental sound recycling of ISSA.

2.1.3 Recycling of ISSA

The application of waste as a resource is the subject of increasing attention worldwide driven by a combination of factors such as a growing appreciation of the need to develop more sustainable process to utilize Earth's finite resources more efficiently as well as the reduction on waste storage (Hargreaves et al., 2013). There is a substantial amount of research about the reuse and recycling of ISSA which finds applications primarily in the construction industry due to its high contents of SiO_2, Al_2O_3 and CaO (Smol et al., 2015) (as shown in Figure 2-5). Such reuse options can be categorized into (i) as a raw material for cement clinker production or as a cement substitute; (ii) for the fabrication of lightweight aggregate; and (iii) to produce bricks.

1) As a raw material for manufacturing cement clinker or as a cement substitute

The feasibility of reusing ISSA for clinker production is mainly attributed to its relatively rich SiO_2, CaO, Al_2O_3 and Fe_2O_3 contents (Lin et al., 2005). After firing under appropriate conditions, these components can be transferred into calcium aluminates and calcium silicates (e.g., tricalcium silicate (C3S), dicalcium silicate (C2S) and tricalcium aluminate (C3A)) which are the main components of cement (Lin et al., 2005). CaO in ISSA also contributes to reduced CO_2 emissions to some degree due to a lower input amount of limestone which endows the end product the name 'eco-clinker' (Lynn et al., 2015). ISSA incorporated in the feed materials at

2%, 4% and 6% produced eco-clinkers with higher P_2O_5 conents (0.58~1.58% vs 0.17%) and significantly lower amounts of effective C3S (19.3%~38.9% vs 50%) compared to those in OPC (Hoi et al., 2010). The suppressed formation of C3S was associated with high contents of P_2O_5 and SO_3 in the ISSA. In another study, adding 4.5% ISSA in the raw mixture leads to the production of an eco-clinker with phase compositions comparable to OPC, nevertheless, notably lower contents of C3S (31.74 % vs 51.01%) and C2S (23.21% vs 42.47%) were found in the end clinker when the ISSA incorporation amount reached 9% (Lin et al., 2005). The lower C2S content in the clinker synthesized from the addition of 9% ISSA compared to OPC had the setting time of the end paste delayed and the corresponding compressive strength reduced. The use of ISSA as a raw material substiute for clinker production can result in a high heavy metal content in the end clinker, while most of these studies showed end clinkers with leaching of heavy metals in compliance with the regulatory limits based on TCLP (Lin et al., 2005). Considering the side effects on the produced clinker with the use of a high amount of ISSA arising from its rich P_2O_5 contents, P extraction from ISSA before such use can be a better choice (Lynn et al., 2015).

ISSA has also been directly reutilized as a cement replacement in mortar or concrete due to its amorphous SiO_2 and Al_2O_3 contents, which give it some pozzolanic activity that is generally assessed based on the strength activity index (SAI) tests and measuring fixed $Ca(OH)_2$ quantity (Lynn et al., 2015). ISSA's pozzolanic activity can be significantly influenced by the SS combustion temperature. The combustion temperature for most SS incineration plants is around 850 ^oC, and the pozzolanic activity of the resulting ISSA samples have been reported to be low or moderate (Garcés et al., 2008). ISSA is an inferior pozzolan compared to some common pozzolans like fly ash (Donatello and Cheeseman, 2013). An increasing amount of ISSA in cement mortar generally decreases the compressive strength, while milling of ISSA is conducive for mortar's strength development (Pan et al., 2003). ISSA can also reduce the

workability of the mortar due to its irregular morphology (Vouk et al., 2017). When 20% of cement was replaced by ISSA, the average mixture workability decreased by 20%. Nevertheless, it was also reported that the use of less than 20% of ISSA had negligible influence on the compressive strength of the final products (Chen and Poon, 2017; Vouk et al., 2017). At the same cement replacement level up to 20%, the compressive strength and flexural strength of mortars containing pulverized fly ash, ISSA and ball milled ISSA were comparable (Chen and Poon, 2017). Controversial results were obtained regarding the setting time of cement mortar with the incorporation of ISSA due to variations in ISSA components (Vouk et al., 2017). Overall, to maximize the recycling of ISSA as a cement substitute, a proper pre-treatment of ISSA and a careful selection of incorporation amount are critical.

2) Lightweight aggregate (LWA)

Some studies however indicate that ISSA is inappropriate to be reused as a cement substitute due to its low pozzolanic activity and poor mixture workability (Chiou et al., 2006). Given the comparable chemical compositions between ISSA (SiO_2: 33.8±12.7%, Al_2O_3: 14.4±6.6% and CaO: 13.6±8.6%) (Lynn et al., 2015) and the expansive clay (SiO_2: 48~70%, Al_2O_3: 8~25% and flux: 4.5~31%) (Chiou et al., 2006), ISSA has been used alone or in combination with other additives to make LWA. With the use of a little amount of clay (1~16%) to facilitate pellet formation, sintering ISSA at 1060°C produced LWA with comparable properties (density: 1.35 g/cm^3, water absorption: 8% and crushing strengths) to a commercial LWA (Cheeseman and Virdi, 2005). The sintering process generally reduces the leaching of heavy metals as a result of the incorporation of toxic heavy metals into the newly formed crystalline phases and the formation of heavy metal-bearing minerals with low leachability (W. Ma et al., 2020). The leaching of Mn (33.5% vs 16.4%) and Zn (5.2% vs 2.1%) from ISSA sintered at 1050°C was significantly lower compared to the raw ISSA when leached by DI water with a pH value of

3.0 (Cheeseman et al., 2003). While leaching of heavy metals under alkaline conditions is more desirable when the ISSA aggregate is to be used in concrete.

To reduce the energy consumption, ISSA was mixed with an appropriate amount of SS which also produced LWA with satisfactory properties (Chiou et al., 2006). Moreover, a recent study showed that with the addition of a high content of binder, ISSA together with crushed waste wood could be recycled to produce cold bonded LWA with good engineering properties (bulk densities: 0.836~1.011 g/cm^3, water absorption 14%~22%, pellet strength 5.2~8.1 MPa) under the optimal conditions (Tang et al., 2020).

3) Brick

The comparable chemical (SiO_2 and Al_2O_3) and mineral (quartz, hematite, feldspar and mica) compositions of ISSA to the traditional brick-making materials such as clays render it compatible to be reused in manufacturing bricks (Anderson and Skerratt, 2003; Smol et al., 2015). Components such like Fe_2O_3, CaO, P_2O_5 in ISSA can serve as fluxing agents thus lowering the sintering temperature. To produce high quality bricks with the inclusion of ISSA, the ISSA proportion and firing temperatures should be carefully optimized. An ISSA mass fraction in the brick within 20~40%, a moisture content of the raw mixture within 13~15% and a firing temperature of around 1000^{o}C were recommended to produce bricks with high qualities (Lin and Weng, 2001). While some soluble salts (0.15~1.52%) present in the ISSA can adversely affect the durability of the produced bricks (Lynn et al., 2016), and information regarding this issue is still in its infancy.

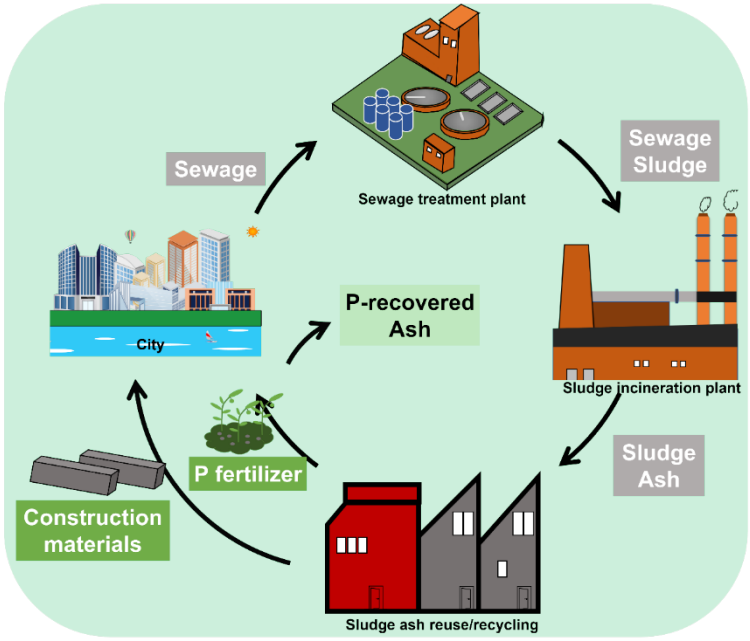

Figure 2-5 Generation of ISSA and its potential recycling.

2.1.4 P recovery from ISSA

The bulk utilization of ISSA through recycling in construction materials is efficient in large-scale applications but represents a loss of valuable elements particularly P (Donatello and Cheeseman, 2013) which is an essential element for all living organisms without substitutes. P-fertilizers are being consumed in huge quantities annually mainly by the agricultural sector to ensure food safety. The global consumption of P fertilizers (as P_2O_5) has increased notably from 32.81 million metric tons in 2000 to 46.34 million metric tons in 2019 (Statista, 2022). The global consumption of P_2O_5 in fertilizer products has increased by 7% from 2020 to 2021 (USGS, 2022). These have put pressure on economical P rock reserves that are the major sources for manufacturing P-fertilizers. P recovery from secondary P resources has thus become more and more important. As shown in Table 2-1, ISSA contains a high amount of P_2O_5 (7.0~25.7%) making it an attractive secondary P resource. However, the low bioavailability of P and the co-existence of heavy metals with contents exceeding the regulatory

limits in the ash impede its direct application as a P-fertilizer in agricultural activities. ISSA is therefore extensively explored for P recovery by methods such as wet extraction, thermochemical and electrodialysis processes (Li et al., 2018).

1) Wet extraction method

The wet extraction method using acids as the extractants can generally achieve a good P extraction efficiency from ISSA via protonation under optimized conditions. Various organic and inorganic acids have been examined to extract P from ISSA, which include HCl, HNO_3, H_2SO_4, citric acid, and oxalic acid. In general, the acid type and concentration, liquid-to-solid ratio and reaction time all can influence the P extraction performance. The leached amount of P from ISSA increases with the acid concentration, liquid-to-solid ratio, or leaching time until the optimal is obtained when the other conditions are all fixed (Fang et al., 2018). An effective P extraction can be obtained when the equilibrium solution pH value is lower than 1.5 irrespective of the ash type (Schaum et al., 2007). While the major drawback of this method is the simultaneous release of harmful heavy metals during the washing process which makes purification of the P-containing extract obligatory (Fang et al., 2020b).

The separation of P from the heavy metal enriched extraction can be achieved via (i) sequential precipitation, (ii) ion exchange, and (iii) selective adsorption. A sequential precipitation method, by raising the pH value of the P-containing extract solution to 3~4, resulted in the precipitation of amorphous aluminium phosphate without the contamination of heavy metals. By dissolving this amorphous aluminium phosphate under an alkaline environment, a clean P-extract was obtained (Schaum et al., 2007). Based on this, the SEPHOS Process-Sequential Precipitation of Phosphorus had been developed and practiced. The addition of a strong acid cation exchange resin (Purolite C-100 × 10) into the P-extract notably reduced the concentration of metals (~100 magnitude reduction in Ca, ~500 magnitude reduction in Fe and

Zn, ~2000 magnitude reduction in Al) with little loss of P (~6%) under the optimized conditions (Donatello et al., 2010b). Followed by concentrating the purified extract, phosphoric acid (80%) was obtained. An adsorption gel synthesized from the Zr(IV) modified orange waste selectively adsorbed P from the acid extract (Biswas et al., 2009). A NaOH solution is needed to further regenerate the adsorbent to recover P. More recently, a Mg/Ca modified biochar was developed from peanut shell and $MgCl_2$/$CaCl_2$, which also selectively adsorbed P from the acid extract (Fang et al., 2020a). The P-loaded biochar samples were directly used as a fertilizer and promoted the growth of choy sum and ryegrass (Fang et al., 2022).

Extraction of P from ISSA by alkalis such ash NaOH, on the contrary, avoids the leaching of heavy metals because (i) amphoteric aluminum phosphate compounds present in ISSA can be dissolved in alkalis and (ii) most heavy metals are not dissolved under alkaline conditions (Petzet et al., 2012). Extraction of P by alkalis can release a higher amount of P for the ash with a low calcium content (Schaum et al., 2007), while the poor P-extraction efficiency for most of the ISSA samples limits its practical application.

2) Thermochemical method

Since many metal chlorides evaporate at a temperature range within 800~1000^{o}C that is far below the melting point of the ash, with the presence of Cl additives, the thermochemical method can be adopted to remove toxic heavy metals from ISSA (Adam et al., 2009; Ottosen et al., 2016). The influencing factors of this method include temperature, type of Cl additive, Cl concentration and reaction time. The Cl additives including NaCl, KCl, $MgCl_2$, $CaCl_2$, polyvinylchloride (PVC), and gaseous hydrochloric acid can all effectively remove heavy metals in ISSA under appropriate conditions (Adam et al., 2009; Vogel et al., 2013; Vogel and Adam, 2011). PVC with a high heating value is a favorable Cl additive and the use of which also contributes the management of solid waste. An increase of heating temperature from 750

to 1000ºC had the Cu and Zn contents dramatically reduced from 1,166 mg/kg and 2,181 mg/kg in the original ash to around 350 and below 100 mg/kg respectively, while the Cr and Ni contents remained similar after the thermal treatment, at a Cl-concentration ($MgCl_2$) of 150 g/kg, a temperature of 1000ºC, and a heating time of 60 min (Adam et al., 2009). The heavy metal removal performance roughly increased with the Cl-additive concentration until 50 and 100 g/kg where the optimal performance was achieved. Even though, contents of most heavy metals in the ISSA can be dramatically reduced by this method, their contents could not always meet the legal requirements for use as fertilizers. Particularly for Cu, a major heavy metal in ISSA, whose removal rates can vary significantly due to differences in its mineral phases in the original ash. Given the high temperature adopted in this method, it is critical to optimize the reaction time, and a retention time of 20 min was sufficient to achieve satisfactory removal of heavy metals in the ISSA to acceptable levels (Adam et al., 2009).

Besides the removal of heavy metals, the bioavailability of P (solubility of P-containing compounds in 2% citric acid) in the raw ash was notably increased from around 30% to over 95%, a value even higher than the commercial single super phosphate (Adam et al., 2009). While the P-water solubility of these thermo-treated ISSA by $MgCl_2$ was negligible (1 < 1%) compared to that of single super phosphate (78%) due to the transformation P-bearing phases such as whitlockite in ISSA to chlorapatite ($Ca_5(PO_4)_3Cl_{1-x}(OH)_x$), farringtonite ($Mg_3(PO_4)_2$) and stanfieldite ($Ca_4Mg_5(PO_4)_6$).The use of $CaCl_2$ as the Cl additive however decreased the P plant-availability compared to the original ISSA (Vogel et al., 2013). Moreover, PVC is needed to be used in combination with MgO to have the treated ISSA having a comparable P plant-bioavailability to the ISSA treated by $MgCl_2$ (Vogel et al., 2013).

Overall, the thermochemical method can achieve a satisfactory removal performance for most heavy metals such as Zn, Cu, Pb, Mn and Sn in ISSA. However, this method suffers from other

disadvantages such as high energy input, ineffectiveness for the removal of non-volatile metals like Cr and Ni, and the equipment lifetime due to the generated corrosive conditions, which significantly impedes its application (Donatello et al., 2010b).

3) Electrodialytic method

The electrodialytic method can achieve P recovery and heavy metal purification simultaneously (Guedes et al., 2014). In a typical three compartment electrodialytic cell, when an electrical direct current of a few mA is applied to the electrodes, pH near the anode and cathode notably decrease and increase due to the electrolytic reactions. The ISSA suspension is acidified as a result of water-splitting reactions at the anion compartment, and proton release from the anode compartment (Ebbers et al., 2015). P and heavy metals are mobilized simultaneously, the negatively charged orthophosphates is transported through a anionic exchange membrane towards the anode, while cationic heavy metals are transported through a cationic exchange membrane towards the cathode by electromigration (Ottosen et al., 2016). The process influencing parameters include type of solution to suspend the ash, liquid-to-solid ratio, stirring speed, current, and reaction time (Ottosen et al., 2014). Acidification of the ISSA suspension is the most critical step to achieve the P release from ISSA, however, a long time from several days to weeks is needed to reduce the pH of the ISSA suspension to sufficiently low that can effectively release P. Even though, the electricity consumption can be reduced by using pulse current during the treatment process (Guedes et al., 2014), this method is generally considered expensive and labor consuming. Moreover, the blockage of membrane is also a problem limiting its application.

Overall, the wet extraction method by acids is the most prevalent method to effectively recover P from ISSA due to its easy operation, low cost, and high efficiency. The acid-washing method has been widely utilized to recover P from ISSA in pilot- to full-scale applications, particularly

in countries with P scarcity like Germany, Switzerland and Japan (Fang et al., 2020b). Recovery of P from ISSA is going to be obligatory in Germany (Schnell et al., 2020). Moreover, a recent study focusing on the sustainability (covering economic, social, and environmental impacts and benefits) of P recovery from SS has revealed that P recovery from ISSA as a P reserve (Scenario 3) was the most sustainable among other scenarios including the baseline scenario i.e., P recovery via land application that is the most extensively adopted method in the US, and Scenario 2 based on P recovery from sludge liquor that is the most commonly practiced P recovery method driven by ease of implementation and potential gains from selling fertilizers (Law and Pagilla, 2021). We can foresee there will be a huge increase in P recovery from ISSA by the acid washing method in large-scale applications.

2.2 Characteristics of the P-recovered ISSA and potential recycling

The acid washing method however unavoidably generates an acid insoluble residual ash i.e., P-recovered ISSA. The exact amount of the P-recovered ISSA residue depends on the chemical compositions of ISSA and the acid used. Based on Table 2-1, the average contents of P_2O_5, CaO, Al_2O_3 and Fe_2O_3 in ISSA are 12.3%, 16.4%, 8.9% and 10.3%. During the acid extraction process, CaO and P_2O_5 in the ISSA are the major acid consumers, while Al_2O_3 and Fe_2O_3 consume only a certain proportion of the acid (Franz, 2008). Based on our experiences, the P-recovered ISSA can exceed 80% by mass of the original ISSA if H_2SO_4 is adopted to extract P from ISSA due to the formation of gypsum. It was also found that when the electrolytic method was adopted, the remaining ash accounted for 60% to the original ISSA (Guedes et al., 2016). Moreover, the mobility and leachability of toxic heavy metals in the P-recovered ISSA after the acid washing process were reported to be higher than the original ISSA (Li et al., 2018). Recycling methods should be developed to gain value from the P-recovered ISSA to achieve resource efficiency and make the whole P-recovery process complete and sustainable.

As with the original ISSA, possible reuse options for the P-recovered ISSA should be investigated to prevent its disposal in landfills, but research on this area is scanty. This part summarizes properties of the P-recovered ISSA residue after P recovery and its potential recycling opportunities.

2.2.1 Characteristics of P-recovered ISSA

The acid washing process changes the physical and chemical properties (e.g., pH, density, surface area, elemental compositions, mineralogy, toxicity and so on) of ISSA (J. shan Li et al., 2018) that significantly affects the potential recycling. Two types of P-recovered ISSA being processed by the acid washing method representative of those produced onsite and in the laboratory respectively are compared. As shown in Figure 2-6, the P-recovered ISSA is reddish brown. The optical images of the ash show the presence of transparent silica grains which can be covered by a layer of red or brown precipitates.

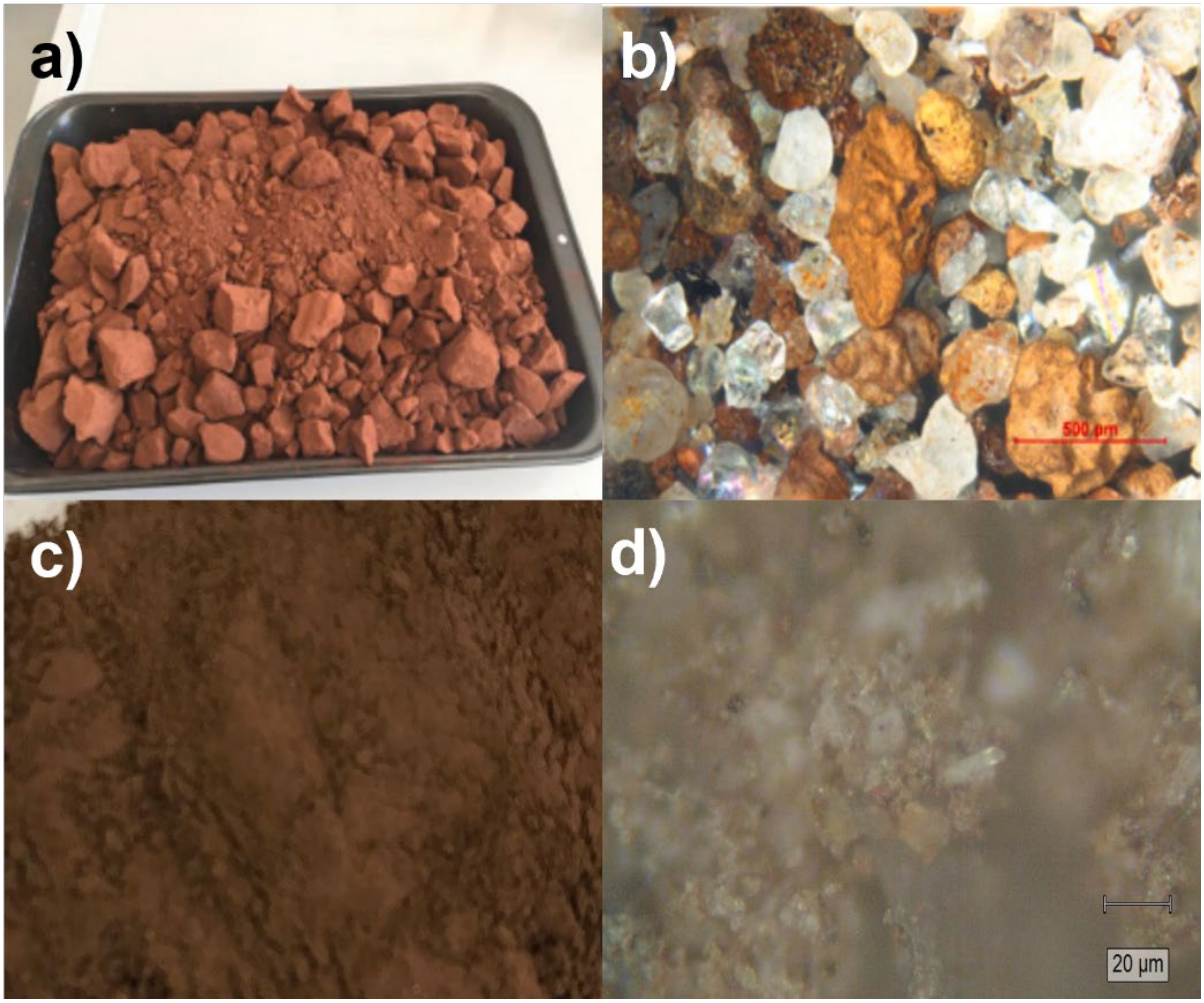

Figure 2-6 P-recovered ISSA (a) and under an optical microscope (b) after HCl washing from Denmark (onsite); P-recovered ISSA (c) and under an optical microscope (d) after H_2SO_4 washing from Hong Kong (laboratory). a, b adapted from ref. (Ottosen et al., 2022).

Properties of the ISSA before and after P-recovery are summarized in Table 2-2. The P-recovered ISSA has a pH of around 5.9, even after neutralizing the residual ash after the acid washing process (Ottosen et al., 2022), which is notably lower than that of ISSA (over 8.0). The density of the P-recovered ISSA is slightly higher than the original ISSA. The LOI of both the original ISSA and the P-recovered ISSA is low (less than 3%). The specific surface area of the P-recovered ISSA however is significantly higher than ISSA (20.09 m^2/g vs 1.83 m^2/g) due

to the removal of soluble compounds such as alkali metal chlorides to the bulk solution (Li et al., 2018).

Table 2-2 Selected properties of ISSA before and after P-recovery by acid washing.

Item	ISSA	P-recovered ISSA	ISSA	P-recovered ISSA
Source	Copenhagen, Demark		Hong Kong	
Treatment	Ash2Phos process		Acid wash in the lab	
pH	9.9	5.9	8.45	4.09
Density (g/cm3)		2.65	2.49	2.75
Loss on ignition (%)		2.3	0.36	0.66
Specific surface area (m^2/g)			1.83	20.09
Cd (mg/kg)		1.5		
Cu (mg/kg)	690	133	621	370
Pb (mg/kg)	140	62	70	43
Zn (mg/kg)	1930	442	2198	1295
Reference	(Ottosen et al., 2022)		This study	

The chemical compositions of the P-recovered ISSA are demonstrated in Table 2-3, which are quite different from ISSA. The content of P_2O_5 in ISSA is reduced by over 80% after the optimized acid washing process (HCl, H_2SO_4, HNO_3 and $C_6H_8O_7$), while content of SiO_2 increased by 30~182% after washing by inorganic acids except when H_2SO_4 is the extractant. The CaO content decreased dramatically except when H_2SO_4 and $C_6H_8O_7$ were used due to the formation of gypsum and calcium oxalate precipitates. For Al_2O_3, its content in the acid treated ISSA was slightly lower than that of the original ISSA. The leaching of iron by the acid washing process is greatly affected by its mineral forms (Gorazda et al., 2016). It was reported that when

the leaching of P from ISSA reached a plateau, i.e., the highest P recovery rate, the pH value of the solution became less than 1.8. Nevertheless, at this pH value, the leaching rates of iron from different ISSA samples were around 20% (Franz, 2008). A further reduction in pH to around 0.75 increased the leaching of iron, but a severe dissolution of heavy metals occurred simultaneously that should be avoided. Iron in most ISSA samples predominantly exists as hematite (even though other iron oxides and iron phosphates had been reported) that is quite stable (Donatello et al., 2010b; Gorazda et al., 2016; Lynn et al., 2015). A complete dissolution of hematite occurs at a pH value less than 1.0 and a temperature as high as 70^{o}C (Pepper et al., 2016). Therefore, despite the P-extraction efficiency reached optimal, the reaction conditions are still too weak to effectively release iron from ISSA (Guedes et al., 2016; Petzet et al., 2012). Consequently, higher content levels of Fe_2O_3 in the treated ISSA (as shown in Table 2-3) compared to the original ISSA have been widely documented since hematite is the main iron-bearing mineral in most ISSA samples (Li et al., 2018). Similarly, the electrodialytic process generated a residual ash with the Fe_2O_3 content almost doubled compared to the original ISSA (from 15.7% to 27.3%) when the optimal P extraction rate (over 80%) was reached (Ottosen et al., 2020). The mineral phases found in the P-recovered ISSA mainly include quartz, anorthite, and hematite (Wang et al., 2021a).

Table 2-3 Chemical compositions (wt.%) of P-recovered ISSA by different extractants.

Ash	Extractant	Na_2O	MgO	Al_2O_3	SiO_2	P_2O_5	SO_3	Cl	K_2O	CaO	TiO_2	Cr_2O_3	MnO	Fe_2O_3	CuO	ZnO	Reference
ISSA	-	2.42	1.66	11.88	31.15	9.27	4.08	0.24	3.53	9.73	0.61	0.07	0.14	23.95	0.24	0.89	
Treated ISSA	H_2SO_4	0.34	1.98	4.9	26.6	1.35	25.96	0.02	2.55	9.34	0.62	0.09	0.11	25.07	0.17	0.76	(J. shan Li et al., 2018)
	HNO_3	1.75	1.13	8.91	41.02	1.83	1.15	0.05	3.8	1.78	0.89	0.09	0.13	36.02	0.2	1.05	
	$C_6H_8O_7$	0.57	0.63	7.88	42.54	1.53	0.59	0.03	3.55	15.48	0.96	0.07	0.07	25.11	0.12	0.58	
	$C_2H_2O_4$	0.81	1.29	8.68	43.29	5.29	0.32	0.06	3.76	5.46	0.75	0.07	0.13	29.09	0.17	0.64	
	EDTA	0.98	1.14	12.22	31.16	18.04	0.64	0.05	3.31	5.61	0.65	0.08	0.1	24.94	0.21	0.71	
	EDTMP	1.69	1.24	12.14	36.26	8.22	0.48	0.05	3.89	7.32	0.65	0.08	0.14	26.69	0.22	0.78	
ISSA	-	1.2	2.3	5.1	17.1	20.2	2.0	<0.1	1.6	23.8				15.7			(Ottosen et al., 2022)
Treated ISSA	HCl		1.4	7.2	48.3	3.0	0.3	<0.1	2.9	1.5				22.9			

The total heavy metal contents in the ISSA before and after P-recovery are summarized in Tables 2-2 & 2-3. As shown from these tables, the total heavy metal contents in the P-recovered ISSA are lower compared to those in ISSA. Even though, the P-recovered ISSA can still contain a considerable amount of heavy metals such as Zn (1295 mg/kg) and Cu (370 mg/kg) (the Hong Kong case). The SEP results as shown in Figure 2-7 indicate that around 32% and 29% of Zn and Cu are in the exchangeable fraction, while the respective residue fractions are 64% and 67%. The exchangeable fraction can be further reduced by washing using deionized (DI) water. As shown in Section 3.2.1, after DI washing of the P-recovered ISSA residue, contents of Cu, Pb and Zn were further reduced from 370 mg/kg, 43 mg/kg and 1295 mg/kg to 264 mg/kg, 32 mg/kg and 882 mg/kg respectively. The P-recovered ISSA can therefore be considered as an environmentally safer material compared to ISSA with a simple treatment.

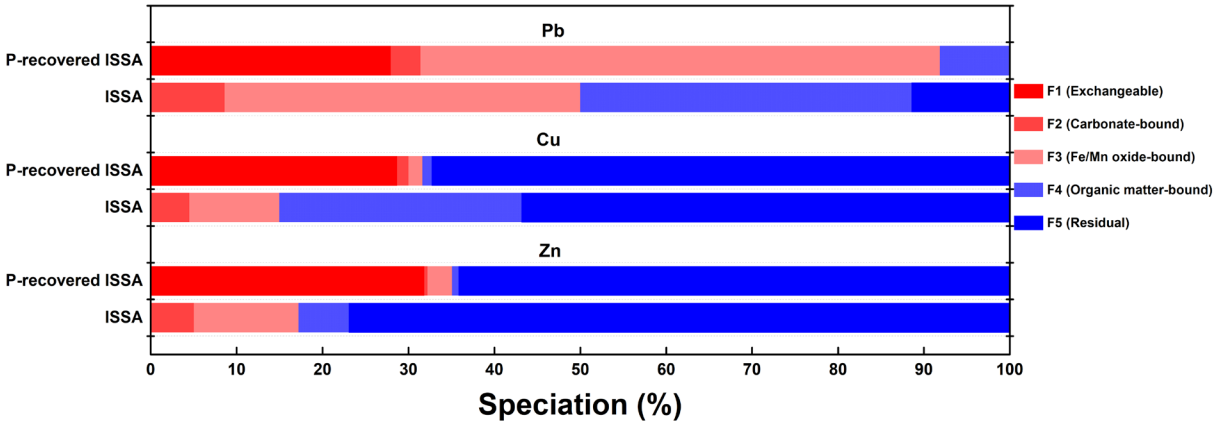

Figure 2-7 Heavy metal speciation of ISSA and P-recovered ISSA after washing by H_2SO_4 (data from ref. (Li et al., 2017)).

2.2.2 Application of P-recovered ISSA

The chemical compositions of the P-recovered ISSA after the acid washing method mainly include SiO_2, Fe_2O_3, Al_2O_3, and/or CaO and SO_3 that are present in the forms of quartz,

hematite/magnetite, and/or gypsum if H_2SO_4 is used to extract P from ISSA. The P-recovered ISSA has also been examined to be used as a cement replacement due to its rich Al and Si contents. Nevertheless, a high amount of oxides including SiO_2, Fe_2O_3 and Al_2O_3 in the ash does not necessarily indicate a good pozzolanic activity due to heterogeneity of the residual ash. The acid insoluble residues after extracting P from ISSA by HCl or H_2SO_4 were reported to have little or no pozzolanic activity even after processed by milling, which was conducive to increase the pozzolanic activity of the ash (Donatello et al., 2010a; Ottosen et al., 2022). When replacing 10% of cement by the P-recovered ISSA, the produced mortar showed a similar 28-day and a higher 42-day compressive strength compared to the plain cement mortar. The rich iron in the P-recovered ISSA residue gave the mortar a clear reddish color making it visually attractive (Ottosen et al., 2022). While some others indicated that the P-recovered ISSA (ball milled at 450 rpm for 6 h) showed a good pozzolanic activity. When used as a partial replacement at 15% by mass for cement in mortars, the P-recovered ISSA incorporated mortars showed compressive strength and flexural strength comparable or even higher than the control mortar prepared from cement and standard sand. The authors concluded that the P-recovered ISSA could be regarded as a potential pozzolanic material in blended cements (Liang et al., 2021). Controversial conclusions have been given by different researchers due to differences in properties of the P-recovered ISSA samples and uncertainties from the testing methods. Since the SAI test could be affected by a range of factors that can lead to uncertainties in the determination of the pozzolanic activity of the acid washed ISSA (Donatello et al., 2010a), test results based on Frattini test were more reliable. Based on Frattini test results, the P-recovered ISSA exhibits a poor or no pozzolanic activity making it inferior to be reused as a cement replacement.

Besides being examined as a pozzolanic material, the P-recovered ISSA was also reused as a clay substitute to manufacture bricks. Similarly to ISSA, Ottosen et al. (2020) showed that the

P-recovered ISSA residue, as a partial clay substitute (10~50%), produced bricks with acceptable properties that allowed them to be used in the building industry. While the firing temperature must be carefully optimized when a high substitution rate was selected because the high hematite content in the ash strikingly affected properties of the produced bricks. In Gifu Japan, heavy metal containing residues after P recovery from ISSA by an alkali extraction method is subjected to a weak acid washing process. The obtained residues are brown with no sewage odor which were reported to meet the environmental criteria for soil contamination prevention and could be reused as roadbed materials or substitutes for stone powder in asphalt filler. But at present, they are mainly sold as a soil improver to materials companies (Nakagawa and Ohta, 2019). In summary, information available for the disposal and management of the P-recovered ISSA residue is limited.

2.3 Reuse P-recovered ISSA in applications for remediation of heavy metal contaminated waters and sediments

2.3.1 Heavy metal pollution in waters and sediments

1) Heavy metal polluted waters

Heavy metals are naturally occurring dense metals with densities of over 5 g/cm^3. They are also called trace elements owing to their low concentrations (from ppb level to 10 ppm) in various environmental matrices (Andreas Luch, 2012). These elements include As, Cd, Cu, Cr, Co, Pb, Sr, Ni, Hg, etc. Some of these such as Cu, Cr and Zn are essential trace elements to the human body. Cu is important in making blood cells and supporting the immune system of the human body. It also functions as a catalyst in enzyme systems. It plays an important role in oxidation-reduction reactions in the energy metabolism. Cr is associated with the carbohydrate metabolism. However, over exposure to these heavy metals can be harmful to human health.

For example, excessive exposure to Cu is related to cellular damage that can lead to Wilson disease (Andreas Luch, 2012).

Some other heavy metal(loid)s like As and Pb are not essential for most living organisms. These heavy metal(loid)s can cause multiple damages to human organs even at low concentrations (Andreas Luch, 2012). As can damage the human body via arsenic metabolism (Chen and Costa, 2021). Exposure to high levels of As due to injection of inorganic As contaminated water are extensively reported to be associated with several cancers including bladder, lung, skin, kidney and prostate cancers as demonstrated in a number of epidemiological studies (Shen et al., 2013). Pb's toxicity became widely known in the late 19th century, the nervous, circulatory, immune, etc. systems can be damaged with an excessive intake of Pb. Moreover, serious disorders and even death can occur with an over intake of Pb (Zhang et al., 2019).

Heavy metals on the other hand have numerous applications in everyday life of human beings. As is used to produce chromated copper arsenate for the preservation of lumber, it is also an important source material to produce GaAs, indium-arsenide, and InGaAs semiconductors for uses in biomedical, communications, and electronics applications. Cr is an element of critical and strategic importance in many nations and plays an important role in the production of stainless steel and nonferrous alloys. Cu is widely used in electronics, architecture materials, insecticides, animal feed and so on. As for Pb, it has extensive applications in construction, plumbing, batteries, paints, gasoline and radiation shielding. Around 92% of the total Pb consumption in America in 2021 was associated with the lead-acid battery industry (USGS, 2022). In 2021, the world's total production of As, Cr, Cu and Pb were around 59 thousand metric tons, 41 million metric tons, 47 million metric tons and 4.3 million metric tons respectively (USGS, 2022).

Table 2-4 Drinking water quality guidelines (unit: μg/L).

Elements	WHO (WHO, 2017)	America (US EPA, 2022)	Japan (MHLW, 2015)	Australia (NHMRC, 2022)	Hong Kong (DWSAC, 2021)	European Union (EC, 2018)	China (SA, 2022)
As	10	10	10	10	10	10	10
Cr	50	100[a]	50[2]	50[b]	50	25	50[b]
Cu	2,000	1,300	1,000	2,000	2,000	2,000	1,000
Pb	10	15	10	10	10	5	10

Note: a. regulated as total chromium; b. regulated as Cr(VI); c. Not of health concern at levels causing acceptability problems in drinking-water.

The enormous consumption of these heavy metals in agricultural, industrial, commercial sectors and so on have resulted in their wide distributions in the environment at levels that can harm the environment and living organisms. As, Cr, Zn, Co, Cd, and Pb are widely found in industrial wastewaters at high concentration levels (Khan et al., 2021). Acidic effluents from ferrous smelting industry often contain As(V) at a high concentration range i.e., 0.5~30 mg/L (Y. Li et al., 2020). As deteriorated water, serving as the dominant source of inorganic As in the diet of humans has affected up to 220 million people globally which is of great concern (Hu et al., 2015; Podgorski and Berg, 2020; Zeng, 2003). Cr is also ubiquitously present in wastewaters from the tannery and electroplating industries (Han, 2020; Prasad et al., 2021; Xia et al., 2019). In China, the total discharge amounts of As, Pb, Cr(VI) and total Cr in all effluents were around 43,297, 52,321, 24,844 and 76,414 kg in 2017 (NBSC, 2020).

Table 2-5 Effluent standards (unit: mg/L).

Elements	Japan (MOE, 2015)		Hong Kong (HK EPD, 1991)	
	Protection of human health	**Protection of the living environment**	**Discharged into sewers leading to government sewage treatment plants[b]**	**Discharged into Group A inland Water[b]**
As	0.1	-		0.05
Cr	0.5[a]	2	0.1-2	0.05
Cu	-	3	1~4	0.1/0.2
Pb	0.1	-		0.1

Note: a. Regulated for Cr(VI); b. allowable limits varies depending on flow rate.

The high toxicity of heavy metals has led the US EPA to add As, Cr, Cu and Pb into the priority pollutant list (EPA, 2014). Nearly all countries have sets of rules to prevent heavy metal pollution in water. Table 2-4 and Table 2-5 show the allowable limits of As, Cr, Cu and Pb in drinking water and effluents in different regions around the world. It is of great significance to remove these heavy metals from water bodies.

2) Heavy metal polluted sediments

In the oceanic environment, sediments are sinks for most heavy metals discharged into the sea. Sediments in coastal areas are sensitive to land-sea interactions, both natural processes (e.g., aeolian and alluvial processes, atmospheric precipitation, surface runoff) and anthropogenic activities (e.g., transportation, aquaculture, leisure activities, industrial wastewater discharge

etc.) can result in the accumulation of heavy metal(loid)s in marine sediments (Gao and Chen, 2012; Zhao et al., 2018a). Table 2-6 shows the heavy metal(loid) contents in sediments in different regions around the world.

Table 2-6 Total heavy metal(loid) contents in sediments on a dry weight basis (mg/kg) in different regions.

Location	As	Cr	Cu	Pb	Reference
Hong Kong	2.8-23.0	8-120	3-830	15-110	(E. P. D. EPD, 2021)
Jiangsu, China			18.90-30.90	12.10-23.90	(Zhao et al., 2018b)
Tangtze Estuary, China	3.5-19.3	42.89-301	6.51-79.9	13.5-48.2	(Zhang et al., 2020a)
Pearl River Estuary, China	1.93-39.49	2-222	5-437.10	15-78	(Zhang et al., 2020b)
Tasmania, Australia[a]	228		591	1880	(Farias et al., 2018)
Western port, Melbourne, Australia			99.67	75.33	(Odell et al., 2021)
Japan		59-200	13-120	11-200	(HOD, 2022)

Note: a. only the maximum concentration is present.

Numerous investigations have shown that anthropogenic activities is the main cause that results in the total heavy metal contents in sediments exceeding the corresponding natural background levels or the local quality guidelines as shown in Table 2-7 (Zhao et al., 2018b). Sediments in

regions with a high level of industrialization and an active maritime economy are therefore especially prone to have higher heavy metal contents than their natural background levels (Khan et al., 2021).

Meanwhile, dredging of marine sediment is world-wide practiced in coastal cities to ensure sufficient depth for navigation purposes and harbor maintenance (Wang et al., 2019a). The dredged marine sediments can be contaminated with Cd, Cu, Pb, Zn, As and Cr (Rahman and Singh, 2019; Y. Yang et al., 2021; Zhang et al., 2018). The management of hazardous marine sediments is widely concerned because of their huge amounts, toxicity, and indispensable disposal costs (J. Li et al., 2020; Zhang et al., 2021). In Hong Kong, the confined disposal fee of contaminated dredged sediments is 50 times higher than the clean ones (92 vs 1.92 Hong Kong dollar/cubic meter sediment in 2019) (CEDD, n.d.). With increasing awareness of the circular economy, the beneficial reuse of excavated sediments has been widely recommended. It is imperative to find technically feasible and economically viable disposal methods for contaminated sediments that can simultaneously achieve the immobilization of pollutants and the recycling of sediments into useful materials.

Table 2-7 Sediment quality guidelines (unit: mg/kg).

	Hong Kong (Bureau, 2002)		**China (AQSIQ, 2002)[a]**			**Australia & New Zealand (ANZG, 2018)**		**Canada (CCME, 2001)**	
Elements	**Lower Chemical Exceed**	**Higher Chemical Exceed**	**Grade I (mg/kg)**	**Grade II (mg/kg)**	**Grade III (mg/kg)**	**Default guideline value**	**Guideline value-High**	**Threshold effect level**	**Probable effect level**

	ance Level	ance Level							
As	12	42	20	65	93	20	70	7.24	41.6
Cr	80	160	80	150	270	80	370	52.3	160
Cu	65	110	35	100	200	65	270	18.7	108
Pb	75	110	60	130	250	50	220	30.2	112

Note: a. Grade I for purposes including marine fisheries, marine natural reserves, protected reserves for rare and endangered species, mariculture, seaside resort and leisure activities; Grade II for general industry and coastal tourism; Grade III for harbors.

2.3.2 Adsorption of heavy metals from polluted waters

Heavy metal removal from contaminated water bodies has been highly explored over past decades. The stringent standards for both industrial effluent and drinking water have promoted the development and adoption of various remediation methods for the abatement of heavy metal pollution in waters. These methods include coagulation/flocculation, (reduction) precipitation, ion-exchange, membrane filtration, electrodialysis, photocatalysis, and adsorption. Albeit treatment technologies for heavy metal removal from wastewaters advance, water pollution is still a critical issue all around the world. Some 2.2 billion people suffer from the lack of safely managed drinking water with the COVID-19 exacerbating the situation (DESA UN, n.d.). Attention to and action on sustainable water and sanitation have been explicitly called for on the 2030 Agenda for Sustainable Development (DESA UN, 2015).

Adsorption, a mass transfer process, is regarded as a promising one among these methods due to its high efficiency, simple operation, low costs, and low space requirement (Bilal et al., 2013). The adsorption process includes (i) transportation of the adsorbate from the liquid phase to the

sorbent's surface, (ii) adsorption of the adsorbate onto the sorbent's surface, and (iii) adsorbate transports within the sorbent. The successful implementation of this method depends largely on the selection of an adsorbent. Activated carbon (AC), a kind of physically or chemically activated carbon produced from various carbonaceous materials such as bamboo, lignite, coal coconut husk etc., is the most widely used adsorbent in wastewater treatment due to its high surface area, excellent pore structure, and a high degree of surface reactivity. While the prevailing shortcoming of AC is the high production costs. Over the past decades, a variety of adsorbents including nanosized metal oxides, graphene, metal organic frameworks, biochar, and cost-efficient adsorbents derived from industrial by-products have been developed for the removal of heavy metals from aqueous solutions (Chai et al., 2021; Costa et al., 2010). Since the main areas (75%) susceptible to heavy metal contamination such as Cr(VI) are many developing countries in South Asia, it is therefore of crucial importance to develop low cost adsorbents to tackle this problem (Rahman and Singh, 2019). Both biochar produced from the pyrolysis of waste biomass and adsorbents derived from industrial by-products have attracted increasing attention to be used as cost-effective adsorbents due to the potential multiple benefits including heavy metal removal ability, environmental friendliness, abundance of raw materials, and contribution to waste management (Hao et al., 2018).

1) Adsorbents from industrial waste

Various industrial by-products and solid waste such as fly ash, iron ore and red mud have been used directly or modified for the removal As(III), As(V), Cd(II), Cr(VI), Cu(II), Ni(II), Pb(II), and Zn(II) from aqueous solutions (Ahmaruzzaman, 2011; Bouabidi et al., 2018; Lee et al., 2017). As a by-product in the stainless-steel manufacturing industry, the steel slag collected from Outokumpu in Avesta, Sweden was ground and sieved to get the 0.25~0.9 mm fraction that removed almost 100% of Cd(II) and Pb(II) within 30 min at an initial metal concentration

of 10 mg/L and an initial solution pH of 3.5 (Huy et al., 2020). The Pb(II) adsorption capacity by a red mud from the Bayer process reached 30 mg/g at an Pb(II) concentration of 250 mg/L, pH of 6.0 and time of 1h (Lyu et al., 2021). Fly ash generated from the wood pellet thermal power plants performed well to remove Cd(II) from aqueous solutions in a wide pH range from 2~6, and showed a maximum Cd(II) adsorption capacity at 142.9 mg/g primarily due to the formation of Cd_2SiO_4 complexes and precipitation as $Cd(OH)_2$ (Park et al., 2020). ISSA exhibited a maximum adsorption capacity for Pb(II) at around 58.28 mg/g when the initial solution pH was around 4.0 (Wang et al., 2019). Solid waste is attractive to be recycled as adsorbents that can be obtained almost without any costs. However, the direct application of low-cost solid waste for the decontamination of heavy metals from aqueous solutions suffers from limitations including the relatively low pollutant adsorption capacity, as well as the presence of impurities (e.g., toxic heavy metals) which can be released during the wastewater treatment process. Therefore, proper pretreatments and modifications are often necessary to make these industrial by products value-added adsorbents for the decontamination of heavy metal contaminated wastewaters without causing secondary pollution. For example, Li et al. (2009) adopted a combined acid dissolution and precipitation process that rearranged the inherent iron in the fly ash into amorphous FeOOH loaded on the surface of the fly ash. The modified fly ash could adsorb 19.46 mg As(V)/g ash from wastewaters. In addition, the resulting material could also serve as an efficient photo-Fenton catalyst, which achieved an almost 100% discolorization of 50 mg/L methyl orange within 80 min at an initial solution pH of around 9.0 (Li and Zhang, 2010). Fly ash modified by lime had increased adsorption capacities for As(V), Pb(II) and Zn(II) respectively at 29.71, 26.06 and 33.13 mg/g (Karanac et al., 2018). Via a combined alkali fusion and dissolution process, red mud could be used to produce magnetic 4A-zeolite that exhibited maximum adsorption capacities towards Cd(II), Cu(II), Ni(II), Pb(II) and Zn(II) respectively at 131.96, 136.33, 119.70, 116.81 and 331.46 mg/g

(Xie et al., 2018). Developing efficient adsorbents from solid waste can be a promising alternative to expensive commercial adsorbent such as AC and ion-exchange resins, which in turn contributes to a sustainable waste management (Ahmaruzzaman, 2011).

2) Biochar

Biochar, the solid residue produced from the pyrolysis of biomass, has attracted tremendous attention to be used as a low-cost adsorbent for wastewater treatment. As shown in Table 2-8, biochar synthesized from various feedstocks such as agricultural and forest residues (pinewood, rich husk, switch grass etc.), industrial by-products (SS, animal waste etc.) and so on have been examined for the removal of heavy metals including Cd(II), Cr(VI), Cu(II), Hg(II), Ni(II), Pb(II), and Zn(II) (Inyang et al., 2016).

Table 2-8 Production of (modified) biochar and their heavy metal adsorption capacities.

Feedstock	Modification	Pyrolysis temperature (°C), time (h)	Dosage (g/L)	pH[1]	Equilibrium time (h)	Heavy metals	Adsorption capacity (mg/g)	Reference
Cotton wood	Feedstock immersed in a ferric salt solution	600, 1	2	-	24	As(V)	3.15	(Zhang et al., 2013)
Bamboo	Feedstock immersed in a ferric salt solution	900, 2	0.2	9.0	4	As(III)	129.24	(Xu et al., 2022)
				6.0		As(V)	127.15	
Digested dairy waste residue	No	600, 2	2	5.0	24	Pb(II)	41.4	(Inyang et al., 2012)

Hickory chips	Biochar impregnated with a ferric salt solution	600, 2	1	5.8	24	As(V)	2.16	(Hu et al., 2015)
Wheat straw	No	800, 2	1	5.0	24	Pb(II)	138.91	(Y. Zhao et al., 2019)
	Hematite mixed with feedstock solution						196.91	
Sewage sludge	No	700, 1	2	-	1	Pb(II)	7.56	(J. Zhang et al., 2019)
Waste activated sludge	No	600, 1.5	2	6.0	6	Pb(II)	53.96	(Ho et al., 2017)
Pine bark	Feedstock immersed in ferric and cobalt salts solution	950, 2		5.0	3	Cd(II)	17.79	(Harikishore Kumar Reddy and Lee, 2014)
						Pb(II)	29.70	

Scots Pine/Silver birch	No	700, 0.75		7.5		Cu(II)	0.13	(Komkiene and Baltrenaite, 2016)
						Pb(II)	0.004	
Sesame straw	No	700, 4	2	7.0	24	Cd(II)	86	(Park et al., 2016)
						Cr(III)	65	
						Cu(II)	55	
						Pb(II)	102	
						Zn(II)	34	
Waste kelp	Feedstock immersed in a ferric salt solution	500, 2	16.7		24	Cd(II)	23.16	(Son et al., 2018)
						Cu(II)	55.86	
						Zn(II)	22.22	

Note: *the pH shown with and without bracket with bracket mean the final and initial pH

While most pristine biochar can suffer from limitations in respect to the removal of heavy metals from wastewaters such as (i) a low heavy metal adsorption capacity due to its low surface area, low porosity, negatively charged surface, and limited surface functional groups, and (ii) difficulty in separation when applied in the powdery form (Li Wang et al., 2019). Surface modification has therefore been introduced in the manufacturing process of biochar to increase the pollutant removal efficiency (Li Wang et al., 2019) and endow the modified biochar other useful properties. Common methods used to modulate properties of the pristine biochar can be divided into chemical (acid/base modification, oxidizing agent modification, metal salts/oxides modification and carbonaceous materials modification) and physical methods (steam and gas purging) (Li Wang et al., 2019). Particularly, the iron salts/oxides modification method has attracted tremendous attention because this method can not only effectively enhance the removal performance towards heavy metals but also endow the modified biochar magnetisms, thus benefiting its separation after adsorption. Furthermore, the wide availability and abundance of iron salts/oxides and their relatively low costs making this modification method attractive and promising. As shown in Table 2-8, iron-biochar composites synthesized from various feedstocks normally outcompete the corresponding pristine biochar regarding the removal of an array of heavy metal(loid)s such as Pb(II), As(V), Cr(VI) and so on. And mechanisms including electrostatic interactions, surface complexation, (co)precipitation, and chemical reduction reactions were reported to be responsible for the removal of heavy metals by iron-biochar composites (Amen et al., 2020; H. Li et al., 2017; Wu et al., 2021; Zhao et al., 2020; Zhou et al., 2014).

Conventional methods to produce iron-biochar composites include loading iron minerals on pristine biochar via wet chemical reduction/precipitation, or pyrolysis of iron-impregnated biomass (Wang et al., 2019). These methods either consume huge amounts of chemicals (e.g., reducing agents, iron salts) or cause potential secondary pollution that limits their applications

(Zhang et al., 2022). Compared to traditionally used iron sources such as ferric/ferrous sulfates or chlorides for the fabrication of iron-biochar composites, a further cost reduction can be obtained by using iron-rich solid waste which is of crucial importance for large-scale applications (Yi et al., 2019). It is also an economic and practical way as biowaste and iron sources coming from agricultural and industrial activities such as various forest/crop residues and iron rich waste (e.g., red mud, steel crap, and iron-ore) are potential feedstock materials of relevance to fabricate iron-biochar composites. For instance, red mud was co-pyrolyzed with rice straw (Chuan Wu et al., 2017) and orange peel (Yoon et al., 2020) which produced iron-biochar composites with satisfactory arsenic removal performance due to improved surface properties and the introduction of active iron minerals. An iron ore tailing was reacted with coke or palm kernel under a high temperature that generated a micro-scale ZVI loaded fly ash-bentonite composite having an excellent adsorption capacity towards crystal violet and methylene blue at 89.9 and 42.8 mg/g respectively (Wang et al., 2017). Similarly, fly ash, iron ore coke and *Enteromorpha prolifera* were first pelletized and sintered in an atmospheric furnace at 900ºC that produced a ZVI-containing composite and showed a maximum adsorption capacity towards Pb(II) and Cr(VI) at around 78.13 and 15.70 mg/g respectively (Liu et al., 2017). A natural iron ore and low-cost biomass were co-pyrolyzed and generated magnetic iron ore-biochar composites exhibiting increased pore width and functional groups compared to pristine biochar. The iron ore-biochar composite could effectively remove norfloxacin from aqueous solutions via excellent adsorption and free radicals actions (Yang et al., 2019).

The brief overview presented above indicates that there is a growing interest in co-valorization of iron-containing waste with bio-waste, by which separable magnetic materials with versatile applications like adsorptive and catalytic abilities for various contaminants can be obtained (Wang et al., 2020). Under the background of circular economy, one-step pyrolysis of a low-

cost iron source with biomass to make iron-biochar composites for the removal of heavy metals from wastewaters is therefore appealing which also contributes to the up-cycling of solid waste (Lawrinenko et al., 2017; Chuan Wu et al., 2017; Yao et al., 2014).

Since the P-recovered ISSA residue is also enriched with iron because of (i) the use of iron salts for sedimentation purposes in wastewater treatment works (Donatello and Cheeseman, 2013; Gorazda et al., 2012) and (ii) its poor leaching during the acid washing process that is mainly optimized for effective P extraction from ISSA as discussed before. It is therefore of interest to explore the possibility of reusing the P-recovered ISSA residue as a low-cost supplementary iron source (a greener secondary iron source compared with other sources that might be contaminated with heavy metals since the acid washing process generally removed most of the toxic heavy metals during P extraction from ISSA), which was then co-pyrolyzed with biomass to produce iron-biochar composites for the removal of toxic heavy metals from aqueous solutions.

The feasibility of producing iron-biochar composites with the P-recovered ISSA residue serving as a supplementary iron source and a model biomass material, lignin, is examined and tested for the removal of Cr(VI) in Chapter 4. Moreover, the P-recovered ISSA residue, similar to other iron-rich waste, typically has complex compositions, and there is a lack of information relevant to how the composition of a low-cost iron source affects the quality of the resulting iron-biochar composite for remediation purposes. Particularly, silica has a widespread existence in the ISSA and other low-cost iron sources (Cho et al., 2019; Yang et al., 2019), its effect on heavy metal removal by the resulting iron-biochar composites deserves attention. This question is thoroughly discussed in Chapter 5 with As(III) and As(V) as the pollutants. Although the ISSA residue contains little toxic heavy metals with negligible leaching potential, and the assessment of the potential leaching of these heavy metals is a still a necessity as the

co-pyrolysis process might change the chemical states of these heavy metals, thus likely causing potential secondary pollution during its application. Therefore, the leaching of heavy metals from the iron-biochar composites should be monitored.

3) Problems in adsorption technology

Present in the form of powder, floc or gel, various adsorbents having large surface areas and super high adsorption capacities towards heavy metals have been synthesized (Chai et al., 2021). While technical problems including head loss, filter blockage, and mass loss could limit their easy use in packed bed filters (Dou et al., 2013). Structuring or shaping of powdery adsorbent into macro-scale bodies is conducive for practical application (Chen et al., 2012). For example, Qi et al. (2015) fabricated a granular adsorbent composed. i.e., Fe-Mn binary oxide impregnated chitosan bead, which was effective in removing As(III) (39.1 mg/g) and As(V) (54.2 mg/g) from wastewaters. In addition, reusability is very important particularly for those adsorbents with high production costs (Lata et al., 2015), which could be offset by the regeneration of the adsorptive media. However, the regeneration process can involve the use of corrosive chemicals (Hering et al., 2017), and produce heavy metal bearing washing liquids with their safe disposal or reuse often ignored. Moreover, the adsorbent gradually losses its adsorption capacity and exhausts at the end of its life cycle. The spent adsorbents can be assessed by TCLP with the non-hazardous ones in compliance to be sent to landfills (Yadav et al., 2022) and the hazardous ones requiring stabilization (Devi et al., 2020). They can also be applied in other processes (reused as fertilizer or catalyst) to expand the application horizon (Fang et al., 2022; Karanac et al., 2018; Pan et al., 2021), which is preferred and should be given more attention as landfilling of waste is no longer a step towards sustainable waste management.

Interestingly, one of the feasible reuse and recycling method for ISSA is to produce LWA with loose bulk densities less than 1200 kg/m^3 that is often present in the form of macro-scale bodies (BS EN, 2016). LWA have an array of applications such as in lightweight aggregate concrete which have reduced structural dead loads and better sound and heat insulation properties compared to the traditional concrete (Hassanpour et al., 2012). More importantly, LWA can be used as sorptive media in wastewater treatment owing to their porous structure and hydraulic conductivity (Kalhori et al., 2013). Manufacturing LWA from ISSA have been previously reported with focus on optimizing properties (e.g., water absorption, density and mechanical strength) of the end aggregates for structural applications by changing sintering temperature or adding auxiliary materials (Cheeseman and Virdi, 2005; Lin et al., 2006). Fewer work has been done on controlling or endowing sorptive properties for the end aggregates for applications in wastewater treatment simultaneously. On the other hand, the reported studies on the production of millimeter-sized sorptive ceramiste from ISSA (Nie et al., 2021; Xu et al., 2008), nevertheless, often focused on producing end products with good removal abilities towards a single or limited heavy metals without finding an end use of the spent material.

Based on these, it is interesting and significant if we can make LWA solely from solid waste like ISSA which can then be adopted for wastewater treatment. More importantly, the pollutant-loaded LWA can be environmentally sound upcycled in construction materials. Since mixture of ISSA and biowaste has poor self-binding property and can hardly produce strong LWA, waste bentonite was therefore introduced to ensure mouldability and produce strong LWA. Detailed investigation about the production of sorptive LWA from the P-recovered ISSA residue and the subsequent upcycling and stabilization in cement mortars is present in Chapter 6.

2.3.3 Remediation of heavy metal contaminated dredged marine sediments

Various biological, electrochemical, physical-chemical processes can achieve acceptable immobilization of heavy metal(loid) contaminated marine sediments (Peng et al., 2018). Since the focus of the study is dredged sediments, only ex-situ treatment methods have been demonstrated as shown in Table 2-9. Conventional treatment methods including landfill disposal and dumping at sea have been widely employed, which however are not considered sustainable due to limited land space and problems associated with its long-term stability (Akcil et al., 2015). Electrokinetic and thermal processes are generally associated with high treatment cost and operational requirements. The bioremediation method is environmentally friendly but time-consuming to achieve satisfactory immobilization efficacy.

Table 2-9 Ex-situ remediation methods for heavy metal contaminated dredged marine sediments. Adapted from ref. (Mulligan et al., 2001).

Method	Process description	Advantages	Disadvantages
Containment	Contaminated sediments are disposed in confined disposal facilities	Lower cost than landfill, able to handle large volumes of sediments, facilities can be used for storage, dewatering and pretreatment for other processes	Potential contaminant release
Landfill disposal	Dispose contaminated sediments in landfills.	Simple and efficient	Small treatment volume, pretreatment including dewatering needed
Chemical washing	Addition of washing solution to contaminated sediments resulting in the transfer of pollutants from sediments to the washing liquids	Efficient for coarser sediments	Post treatment of the metal bearing washing liquid is needed, not suitable for fine grain sediments
Thermal method	Evaporating mercury, arsenic and cadmium	Mainly used for mercury, simultaneously remove organic contaminants,	Some heavy metals are hard to remove, high energy

			consumption, high carbon footprint
Bioleaching	Desorb heavy metals via the use of living organism such as *Thiobacillus sp.* bacteria	Simple and cheap, environmentally friendly	Time consuming, relatively low efficiency
Electrokinetic remediation	Employ direct electric current to remove heavy metals from contaminated sediments	High efficiency	High operation requirement, high cost
Solidification/stabilization	Employ an agent to solidify contaminated sediments with heavy metals immobilized.	High efficiency, low-cost, potential application of end products	Reduction needed to stabilize Cr(VI)

The stabilization/solidification (S/S) process, particularly based on the use of cement, is the most widely acknowledged method, via which low-permeable and low surface area solidified materials with acceptable mechanical strength and reduced mobility of contaminants can be recycled as construction materials (Akhter et al., 1997; Malviya and Chaudhary, 2006; Sörengård et al., 2019). This method is particularly well-known for immobilizing cationic heavy metals such as Cd(II), Cr(III), Cu(II), and Pb(II) in solid matrices via physical encapsulation and chemical fixation, and makes the 'beneficial reuse' of sediments, widely encouraged by different nations (Akcil et al., 2015; US EPA, n.d.), highly possible, which falls into the scope of sustainable waste management.

Nevertheless, S/S process using cement alone suffers from drawbacks including intensive energy consumption and high carbon footprint associated with cement production, as wll as poor stabilization efficiency towards oxyanionic As and Cr in solid matrices (Dixit et al., 2019). Cement is thus often blended with low-cost or functional materials to tackle these issues. Various industrial by-products including fly ash, blast slag, red mud, and ISSA had been blended with cement in S/S treatment for contaminated solid matrices including dredged marine sediments to reduce energy consumption and greenhouse gas emissions (Glasser, 1997; Li and Poon, 2017; Wang et al., 2022). Moreover, the addition of iron-bearing solid waste like red mud also demonstrated enhanced immobilization efficacy for As and Cr in the contaminated solid matrices due to the presence of iron (hydr)oxides favoring the sorptive retention of these oxyanions (Izquierdo and Querol, 2012; J. S. Li et al., 2018; Mandal, 2002; Lei Wang et al., 2019b).

Biochar has also been added in S/S process to increase stabilization efficiency toward toxic trace elements in contaminated sediments (Wan et al., 2020; Yang et al., 2021). The addition of *Acacia confuse* and *Celtis sinensis* derived biochar in sediment-based construction products was effective for immobilizing cationic heavy metals including Zn, Cu and Pb, but less effective for oxyanionic

As and Cr (Wang et al., 2019a). This could be largely caused by the negatively charged surfaces of most pristine biochars (Bakshi et al., 2018). Moreover, a higher substitution rate (5%) of cement by biochar for S/S treatment of marine sediments decreased the mechanical strength of the S/S treated products (Wang et al., 2019a). Incorporating iron-biochar composites in S/S process was proposed to achieve this trade-off, which could enhance immobilization efficiency towards oxyanionic As and Cr without notable mechanical strength loss of the S/S products. This is because modification of biochar by iron minerals (e.g. amorphous ferric oxide, ferrihydrite, goethite etc.) is a cheap and effective strategy to enhance its retention of oxyanionic As and Cr compared to its counterpart pristine biochar as discussed before. Particularly, some Fe-bearing solid waste derived iron-biochar composites also demonstrated excellent removal abilities for oxyanionic Cr and As from aqueous solutions (Cho et al., 2019; Wang et al., 2021a; Yang et al., 2019). These iron-biochar composites fabricated from Fe-bearing solid waste rather than iron chemicals with biowaste are more appealing and practicable to be incorporated in S/S treatment for hazardous sediments in huge quantities from the perspective of reducing treatment costs.

Co-valorization of biowaste and the P-recovered ISSA to produce environmentally sound iron-biochar composites as green additives in cement-based S/S treatment of contaminated marine sediments provides an interesting and sustainable management option for upcycling these concerning solid matrices into valuable construction materials in line with the circular economy. This PhD study therefore further evaluates the feasibility of reusing the P-recovered ISSA derived iron-biochar composites as additives in cement-based S/S process for the stabilization of As-, Cr- and Cu-contaminated marine sediments. As pH is crucial and determines the leaching of As, Cr and Cu, knowledge of the corresponding pH-dependent leaching behavior of the S/S product is conducive to elucidating the mobility of them and determine the potential applications of the S/S

products (Komonweeraket et al., 2015b). In addition, the complex compositions of the P-recovered ISSA compared to pure iron chemicals may impact the cement-based S/S performance, which is addressed in Chapter 7.

2.4 Summary

This chapter reviews the generation, characteristics, and application of ISSA and points out P-recovery from ISSA by the cost-effective and highly efficient acid washing method as a critical step to achieve resource efficient recovery of ISSA. This process however is incomplete as a residual ash, i.e, P-recovered ISSA, accounting for over 80% by mass of the original ISSA (H_2SO_4 as the extractant) is generated simultaneously. As landfilling of waste is no longer regarded a step towards sustainable waste management. This PhD study focuses on reuse and recycling of the P-recovered ISSA as value-add products. The brief review of properties and recycling options for the P-recovered ISSA are restricted by a scanty of available information, most of which, however, focus primarily on using it as a cement replacement by taking advantage of its rich Si and Al contents.

Besides Si and Al, an abundant amount of iron is also present in the P-recovered ISSA due to the use of iron salts in the municipal wastewater treatment process and its insufficient leaching from ISSA by the acid washing method aiming at an optimal P recovery efficiency. Given a serious heavy metal pollution status of waters and dredged sediments that calls for both technologically and economically feasible remediation methods, value-add application opportunities for the P-recovered ISSA are further directed to reuse it as a low-cost supplementary iron source which is modified to make cost-effective functional materials for remediation of heavy metal polluted waters and marine sediments.

Then the promising adsorption method for heavy metal removal from wastewaters is reviewed with a focus on low-cost adsorbents i.e., iron-biochar composites, derived from waste biomass and industrial by-products, which can also be used as additives in cement-based S/S technology for

upcycling contaminated sediments as useful construction materials with enhanced heavy metal immobilization efficiency. Conventional methods for manufacturing iron-biochar composites are summarized with opportunities identified to reuse P-recovered ISSA as a supplementary iron source to make iron-biochar composites. While the complex compositions of P-recovered ISSA give rise to the question of how other co-existing components in the P-recovered ISSA (particularly silica due to its dominant presence) affect properties of the end iron-biochar composites in removing heavy metals from aqueous solutions. Moreover, some technical problems associated with the adsorption technology including solid-liquid separation and disposal of spent adsorbents can be encountered when powdery adsorbents are going to be deployed.

Finally, a review of methods for the immobilization of heavy metals in dredged marine sediments is also presented and shows the necessity for 'beneficial reuse', in harmony with the concept of sustainable waste management, which can be achieved by using cement-based S/S technology. While the plain cement-based S/S technology suffers from poor immobilization efficiency towards oxyanions like As(V) and Cr(VI) and long-term stability. Due to high affinity of iron-biochar composites towards these oxyanions, reusing them as additives in cement-based S/S of marine sediments is favorable to improve the immobilization efficacy.

CHAPTER 3 MATERIALS AND METHODS

3.1 Introduction

The previous chapter presents a review regarding the recycling status of ISSA and identifies the significance to reuse and recycle the P-recovered ISSA. Characteristics of P-recovered ISSA are then summarized, based on which potential recycling methods are proposed. This chapter provides information regarding the raw materials and chemicals used in the research. The experimental programs and analytical methods used to achieve the research objectives are thoroughly described as well.

3.2 Materials

3.2.1 Raw materials

1) ISSA and P-recovered ISSA

ISSA samples used in this study were collected from the sewage sludge incineration facility (T·Park) in Hong Kong, where the dewatered municipal sewage sludge generated in the city were combusted via the fluidized bed incineration technology. Currently, the generated ISSA is mainly landfilled (H. K. EPD, 2021).The as-received ISSA was dried at 105ºC for 24 h. The dried ISSA was washed by 0.2 mol/L H_2SO_4 with a liquid-to-solid ratio of 20 mL/g for 2 h followed by DI water washing, aiming to remove toxic heavy metals such as Zn and Cu and achieve the optimal P recovery from ISSA (Wang et al., 2021a). The residual ash was then dried (105ºC, 24 h), pulverized and sieved (75 μm) to get the P-recovered ISSA. The chemical composition of the P-recovered ISSA is shown in Table 3-1, which shows the dominant presence of SiO_2 and Fe_2O_3. Minerals found in the ash include quartz, hematite/magnetite, and microcline (as shown in Figure

4-1). In addition, the heavy metal contents in the washed P-recovered ISSA residue (Cu: 264 mg/kg, Pb: 32 mg/kg, Zn: 882 mg/kg) were notably lower than the raw ISSA (Cu: 621 mg/kg, Pb: 70 mg/kg, Zn: 2198 mg/kg).

2) Cement

An ASTM Type I Portland Cement (OPC) with a density of 3.10 g/cm^3 was used as the binder and its chemical composition is shown in Table 3-1.

3) Bentonite

The as-received waste bentonite was obtained from a clay supplier in Guangdong, China. Its chemical composition can be found in Table 3-1. Minerals including montmorillonite, quartz and calcite (as shown in Figure 6-6a) were found in the waste bentonite.

4) Peanut shell

Peanut shell was collected from mainland China. The collected peanut shell was thoroughly washed by DI water and dried at 105°C for over 72 h. The dried peanut shell was further pulverized by an electric grinder, sieved (150 μm) and stored in plastic zip lock bags. Before used in experiments, the pulverized peanut shell was dried at 105°C for 24 h.

5) Dredged marine sediments

The marine sediments were collected from the Victoria Harbour, Hong Kong in September 2019, which was first wet sieved to pass a 2 mm sieve, followed by air drying. The collected sediments had a pH of 8.34 ± 0.39 and a total organic matter content of 1.97 ± 0.11%. The chemical compositions of the sediments are shown in Table 3-1 with SiO_2 and Al_2O_3 as the dominant compositions. Minerals found in the sediments included quartz, albite, anorthoclase, calcite and

halite (Figure 7-7). The dredged sediments showed a Cu content of 69.9 ± 8.1 mg/kg exceeding the Lower Chemical Exceedance Level (LCEL) (the LCEL for Cu is 65 mg/kg), requiring proper management according to the local regulation (ETWB, 2002). Additional, other heavy metal(loid)s including As and Cr were found to be present in sediments elsewhere in Hong Kong with contents even higher than the Upper Chemical Exceedance Level (UCEL) (the UCEL value for As and Cr are 42 and 160 mg/kg respectively) according to the local annual marine water quality report (EPD, 2019). For experimental purposes, the collected sediments were spiked by As(V) and Cr(VI) to over the corresponding UCEL value at 68.9 ± 6.6 mg/kg and 233 ± 16.1 mg/kg respectively, and aged for over 2 months before subsequent S/S treatments.

6) River sand

River sand with a density of 2.64 g/cm^3 and a fineness modulus of 3.1 (particle size distribution: 4.75~2.36 mm (15%), 2.36~1.18 mm (20%), 1.18~0.6 mm (25%), 0.6~0.3 mm (25%), 0.3~0.15 mm (10%), and 0.075~0.15 mm (5%)) were used as the fine aggregates.

Table 3-1 Chemical compositions of raw materials used in this study.

Oxides (wt.%)	**Na_2O**	**MgO**	**Al_2O_3**	**SiO_2**	**P_2O_5**	**SO_3**	**Cl**	**K_2O**	**CaO**	**TiO_2**	**Fe_2O_3**	**Others**
P-recovered ISSA	-	1.47	9.7	61.9	2.01	1.54	-	1.49	0.94	0.57	20.3	0.1
Bentonite	4.16	2.35	19.6	54.7	0.12	0.26	-	1.27	8.61	0.9	7.75	0.28
Cement	-	0.96	5.79	19.1	0.15	3.71	-	0.74	65.7	0.31	3.31	0.23
Sediment	2.45	0.88	17.1	66	0.13	1.3	2.26	4.57	3.17	0.20	1.6	0.34

3.2.2 Chemicals, reagents, and standard materials

All chemicals used in this study were of analytical grade. Stock solutions (1000 mg/L) containing As(III), As(V), Cr(VI), Cu(II) or Pb(II) were prepared by dissolving desired amounts $NaAsO_2$ (AJAX-CHEMICALS), $Na_2HAsO_4 \cdot 7H_2O$ (ACCUCHEM), $K_2Cr_2O_4$ (Riedel-de Haën), $Cu(NO_3)_2$ (DH Anala®), and $Pb(NO_3)_2$ (DH Anala®) in DI water (nitrogen purged for the preparation of As(III)-containing stock solution). Working metal containing solutions were prepared by diluting appropriate amounts of stock solutions with DI water. Solutions of HCl and NaOH at 0.1 or 0.5 mol/L were prepared from concentrated HCl (DUKASAN) and sodium hydroxide (Honeywell) for pH adjustment. Concentrated HNO_3 (BDH CHEMICALS) and $HClO_4$ (BDH CHEMICALS) were used in the digestion process for solid samples. Alkali lignin (ALDRICH), silica sand (MACKLIN®) and iron oxide (SIGMA-ALDRICH) were used in the sample preparation process. A Standard Reference Material (Inorganics in Marine Sediments, SRM-2702) from the National Institute of Standards and Technology (NIST, USA) was purchased and used to ensure the quality of measurement for heavy metal(loid) contents in marine sediments. An instrument calibration standard solution containing 100 µg/ml each of Ag, Al, As, Ba, Be, Ca, Cd, Co, Cr, Cu, Fe, K, Mg, Mn, Mo, Na, Ni, Pb, Sb, Se, Sn, Sr, Ti, Tl, V and Zn in 5% HNO_3 was purchased from CPA CHEM and used for calibration purposes in ICP-OES analysis.

3.3 Experimental grogram

3.3.1 Sample preparation

1) Co-pyrolysis of the P-recovered ISSA with lignin for reductive/sorptive removal of Cr(VI) from aqueous solutions (Chapter 4)

The P-recovered ISSA and lignin with a fixed mass ratio of 2:1 (determined by preliminary experiments) were completely mixed by grinding. The mixture was then heated at 650, 850 and 1050ºC (ramp: 10ºC/min) for 1 h in a tube furnace (OTF-1200X) under a nitrogen atmosphere. The obtained sample was denoted as LR-T (T=650, 850 and 1050).

2) Role of silica in P-recovered ISSA on properties of the resulting iron-biochar composite relevant for As(III) and As(V) removal (Chapter 5)

Different amounts of peanut shell and the P-recovered ISSA were completely mixed by grinding (mass ratio: 1:2, 1:1, 2:1, 3:1 and 5:1) and pyrolyzed at 450~1050ºC (ramp: 10ºC /min) for 1 h in a tube furnace under a nitrogen atmosphere. As shown in Figure 3-1, co-pyrolysis of these two types of solid waste at 850ºC generated an iron-biochar composite with significantly increased As(V) removal rates (>70%) compared to the heated peanut shell or P-recovered ISSA residue alone. At a 1:1 mass ratio of peanut shell to the P-recovered ISSA residue, an almost complete removal of As(V) was achieved. Iron-biochar composites made from 450ºC and 650ºC were notably less effective for As(V) removal (<20%). Considering the arsenic removal performance, energy consumption and recycling rate of the P-recovered ISSA, the optimal production condition for the iron-biochar composite used in Chapter 5 was fixed at a mass ratio of the P-recovered ISSA residue to peanut shell at 1:1, pyrolysis temperature at 850ºC, and a residence time of 1 h. The fabricated P-recovered ISSA residue biochar composite was denoted as RBC.

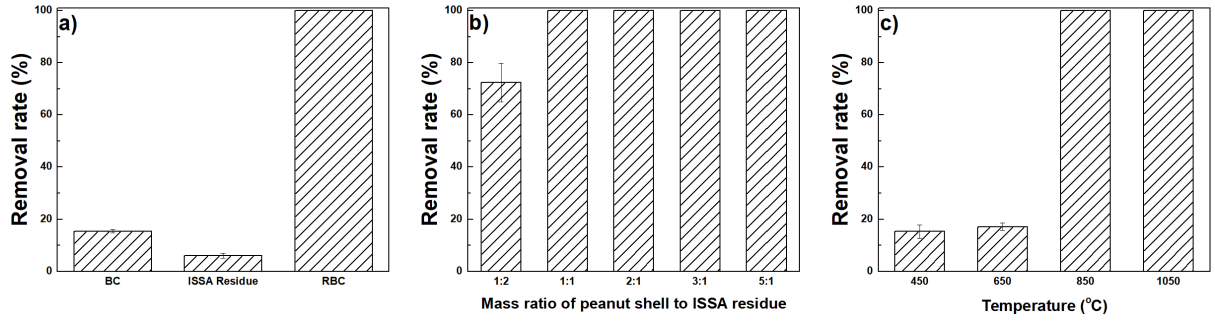

Figure 3-1 Effects of a) raw materials (temperature fixed at 850°C, RBC made from a mixture of peanut shell and P-recovered ISSA residue with a mass ratio of 1:1), b) mass ratio of peanut shell to the P-recovered ISSA residue (temperature fixed at 850°C) and c) heating temperature (fixed mass ratio of peanut shell to the P-recovered ISSA residue at 1:1) on As(V) removal rate by the end iron-biochar composites from aqueous solutions (pH = 3.08, As(V) = 20 mg/L).

Since SiO_2 accounted for over 75% of the remaining mass of the P-recovered ISSA residue besides Fe_2O_3 (Table 3-1), the residue was simplified as a mixture of SiO_2 and Fe_2O_3 with a mass ratio of 4:1. This mixture was pyrolyzed with peanut shell at the same condition with that of RBC, and the produced sample was named as FSBC. For comparison purposes, Fe_2O_3/peanut shell mixture with a mass ratio of 1:5, and SiO_2/peanut shell mixture with a mass ratio of 4:5 were also pyrolyzed under the same condition with that of RBC produced an iron-biochar composite (FBC) from pure Fe_2O_3 and a silica-biochar composite (SBC) for comparison purposes. Pristine biochar (BC) was made from the pyrolysis of plain peanut shell.

3) Production of sorptive granules from the P-recovered ISSA, peanut shell and bentonite, and upcycling the spent granules in cement mortar

The P-recovered ISSA residue and peanut shell mixture with a mass ratio of 1:1 (based on Chapter 5) was thoroughly mixed by a mixer. Varying amounts of waste bentonite was blended with the

mixture followed by adding a suitable amount of water to obtain consistent and moldable pastes for the successful formation of extrudable granules (the green body, with a diameter of around 3~5 mm and a length of around 3~6 mm). The green bodies were dried at 105ºC overnight, and then preheated at 350ºC (ramp 10ºC/min) for 30 min followed by heating at a target temperature (650~1050ºC) for 30 min under a nitrogen atmosphere. After natural cooling to room temperature, the resulting sintered granules were obtained and referred to by a sample ID in the form of IPBG-A(B), where A means the bentonite ratio in the raw mixture, B in the bracket stands for the sintering temperature, and a sample ID without a bracket means the sintering temperature was 1050ºC. The preparation conditions of these granules are summarized in Table 3-2.

Table 3-2 Preparation conditions of granules.

Sample ID	Mix proportion (wt.%)			Heating procedure
	ISSA residue	Peanut shell	Bentonite	
IPBG-10	45	45	10	350ºC, 30 min; 1050ºC, 30 min
IPBG-20(650)	40	40	20	350ºC, 30 min; 650ºC, 30 min
IPBG-20(750)	40	40	20	350ºC, 30 min; 750ºC, 30 min
IPBG-20(850)	40	40	20	350ºC, 30 min; 850ºC, 30 min
IPBG-20(950)	40	40	20	350ºC, 30 min; 950ºC, 30 min
IPBG-20	40	40	20	350ºC, 30 min; 1050ºC, 30 min
IPBG-30	35	35	30	350ºC, 30 min; 1050ºC, 30 min
IPBG-50	25	25	50	350ºC, 30 min; 1050ºC, 30 min
IPBG-80	10	10	80	350ºC, 30 min; 1050ºC, 30 min
IPBG-100	0	0	100	350ºC, 30 min; 1050ºC, 30 min

3.3.2 Batch adsorption experiments (Chapter 4, Chapter 5 and Chapter 6)

The removal performance towards As(III), As(V), Cr(VI), Cu(II), and Pb(II) by the produced samples derived from the P-recovered ISSA was assessed via batch adsorption experiments as shown in Figure 3-2. An appropriate amount of the solid sample was added into As(III)-, As(V)-, Cr(VI)-, Cu(II)-, and/or Pb(II)-containing solution in a centrifuge tube or a polypropylene bottle, which was subjected to shaking in an orbital shaker (HZ-9211KB, HLDKQ) at 200 rpm under ambient temperature. Upon the desired reaction time, the suspensions were centrifuged (4000 rpm, 5 min) and filtered by a 0.45 μm membrane filter, the collected filtrates were measured for pH and digested before the detection of heavy metals.

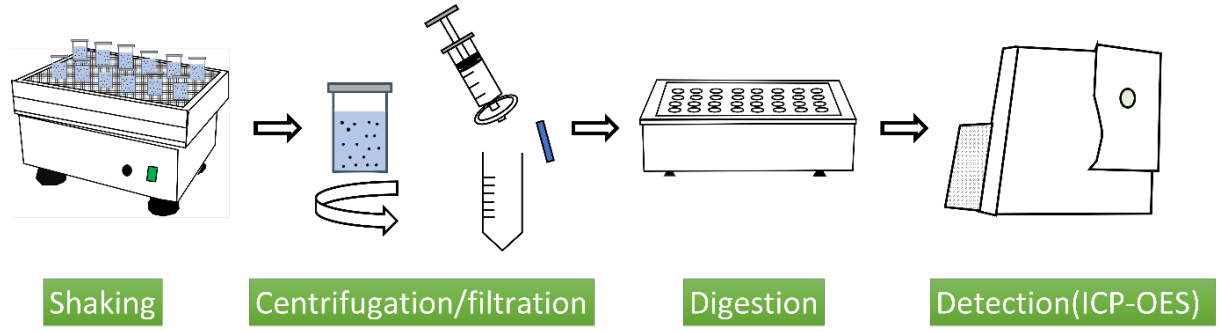

Figure 3-2 Scheme for conducting batch adsorption experiments.

1) Effect of pH

The effect of pH on the removal of a heavy metal was investigated by adding samples into heavy metal(loid)-containing solutions with different initial pH values adjusted by using 0.1 or 0.5 mol/L HCl/NaOH solution

2) Effect of time and adsorption kinetic models

A fixed amount of sample (powder: 1 g/L, granules: 5g/L) was added into a heavy metal(loid)-containing solution with a fixed initial pH. Aliquots of samples were withdrawn at 5, 10, 15, 30, 60, 120, 240, 600, and 1440 min. The experimental data were fitted by three adsorption kinetic models as shown below.

The non-linear and linear forms of the pseudo-first-order (PFO) kinetic model are shown below

$$Q_t = Q_e \times (1 - e^{-k_1 t})$$

$$\ln(Q_e - Q_t) = -k_1 t + \ln Q_e$$

where Q_e and Q_t (mg/g) are the adsorption amount of the adsorbate at equilibrium and time t (min), k_1 (1/min) is the rate constant of the PFO kinetic model.

The non-linear and linear forms of the pseudo-second-order (PSO) kinetic model are shown below

$$Q_t = \frac{Q_e^2 k_2 t}{1 + Q_e k_2 t}$$

$$\frac{t}{Q_t} = \frac{t}{Q_e} + \frac{1}{k_2 Q_e^2}$$

where k_2 (1/min) is the rate constant of the PSO kinetic model.

And the intraparticle diffusion model is shown below

$$Q_t = k_{int} t^{1/2}$$

where k_{int} ($mg \cdot g^{-1} \cdot min^{-0.5}$) is the intraparticle diffusion rate constant. If the intraparticle diffusion is the rate-limiting step, the plot of Q_t against $t^{1/2}$ should be a straight line passing the origin.

3) Effect of initial heavy metal(loid) concentration and adsorption isotherm models

To understand the effect of initial heavy metal(loid) concentration on the adsorption performance of a sample, a fixed amount of sample (powder: 1 g /L, granules: 5 g/L) was added into a heavy metal(loid)-containing solution with concentrations ranging from 1 to 200 mg/L at a fixed initial pH for 24 h. The experimental data were further fitted by two adsorption isotherm models.

The Freundlich isotherm model is shown below.

$$Q_e = K_F C_e^{\frac{1}{n}}$$

where K_F ((mg/g)/(mg/L)^n) is the Freundlich constant, and n (dimensionless) is the Freundlich intensity parameter.

The Langmuir isotherm model is shown below.

$$Q_e = \frac{Q_m K_L C_e}{1 + K_L C_e}$$

where Q_m (mg/g) is the maximum adsorption capacity of the adsobent, K_L (L/mg) is a constant related to the affinity between an adsorbent and the adsorbate.

3.3.3 Preparation of cement-based construction materials (Chapter 6 and Chapter 7)

1) Environmentally safe upcycling of spent IPBG in cement mortar (Chapter 6)

Based on the maximum heavy metal adsorption capacity determined by Chapter 6, IPBG were used for the following experiments at an initial solution pH of 3.0 for 24 h: (i) 20 g/L with a 200 mg/L Cr(VI)-containing solution, (ii) 30 g/L with 300 mg/L As(V)-, 300 mg/L Cu(II)- and 500

mg/L Pb(II)-containing solutions. After the solid liquid separation, the spent IPBG were collected and stored in a desiccator for subsequent uses.

Mortars with plain river sand as the aggregates were used to prepare the control group (CK), where the water to binder ratio and binder to river sand ratio were both 1:2. IPBG with a water absorption capacity of 38.5% (Table 6-2) were prewetted in tap water for 24 h and surface dried before its final use in mortars. The spent IPGB were reused to replace the 2.35~4.76 mm fraction of river sand, aiming to minimize the effect of particle size on properties of the resulting mortar, at volume fractions of 50% and 100% (equal to 7.5% and 15% replacement of the total river sand), and the corresponding group was denoted as IPBG-7.5 and IPBG-15 respectively. The fresh mortars were casted into 40 mm cubic moulds in triplicates and wrapped by plastic films. All specimens were demolded after 24 h and cured in a saturated hydrated lime solution for 28 d to facilitate strength development.

2) Immobilization and recycling of contaminated marine sediment by cement-based S/S incorporating iron-biochar composites (Chapter 7)

Based on the previous findings, a higher heating temperature produced a composite material with a better removal performance towards As(V) and Cr(VI). Therefore, P-recovered ISSA was completely mixed with peanut shell at mass ratio of 1:1 and heated at 1050°C (ramp: 10°C /min) for 1 h in the tube furnace under a nitrogen atmosphere. The composite material produced was denoted as RBC in Chapter 7. To understand the role of silica in the P-recovered ISSA on the immobilization efficiency of the resultant iron-biochar composites in the cement-based S/S process for contaminated sediment, the P-recovered ISSA was simulated by a mixture of Fe_2O_3/SiO_2 with

a mass ratio of 1:4. Then, Fe_2O_3, SiO_2 and their mixture were completely mixed with peanut shell at weight ratios of 1:5, 4:5 and 1:1 and subjected to the same heating process as above to obtain mineral biochar composites, and referred to as FBC, SBC and FSBC. The different mass ratios were selected to ensure the same input weights of iron and biomass. In addition, a plain peanut shell sample which was subjected to the same pyrolysis procedure was named as BC. The produced composite materials were then used as additives and mixed with OPC at a weight ratio of 1:4 to obtain the final binders for S/S treatment of the marine sediment.

In general, cement with a content varying from 5~20% is used in the S/S process for contaminated solid matrices (Malviya and Chaudhary, 2006). In this study, a binder to sediment ratio of 10% was selected. The detailed mixture design for the S/S of sediments is shown in Table 3-3. The sediment with a water content of around 20% was completely mixed with the binder by a mechanical mixer for 2 min. The slurry was transferred into 40 mm cubic moulds and vibrated to remove air bubbles. The blocks were protected by plastic films and cured for 28 days at ambient temperature (ca. 23ºC) and humidity (ca. 80%).

Table 3-3 Mixture design for S/S of contaminated sediment.

Group	Binder to sediment ratio (%)	Binder proportion
CK	10	OPC
FBC		OPC: FBC = 4:1
SBC		OPC: SBC = 4:1
FSBC		OPC: FSBC = 4:1
RBC		OPC: RBC = 4:1
BC		OPC:BC = 4:1

Note: CK represents the control group prepared by contaminated sediments and OPC at a binder to sediment ratio of 10%, FBC, SBC, FSBC, RBC and BC are groups prepared by contaminated sediments and OPC which were substituted by 20% of the corresponding mineral biochar samples.

3.4 Analytical methods

3.4.1 Physicochemical properties

1) pH

The solid sample was mixed with DI water at a liquid-to-solid ratio of 5 mL/g. The mixture was shaken for 4 h and filtrated by 0.45 μm filter before measuring the pH by a pH meter (PHS-3E, LEICI).

2) $\mathbf{pH}_{PZC}$

The pH of the point of zero charge (pH_{PZC}) of the sample was determined by the method "trial of the 11 points" (Regalbuto and Robles, 2004).

3) Moisture content

The moisture content of a sample was determined by drying the sample in an oven at 105ºC to a constant weight. The moisture content was calculated based on the weight difference between the sample before and after drying.

4) Specific surface area

The specific surface area of the sample was determined by a Micromeritics ASAP 2020 Accelerated Surface Area and Porosimetry System (ASAP, 2020 Plus, Micromeritics) using the Brunauer, Emmet and Teller (BET) method.

5) Mercury Intrusion Porosity (MIP)

The pore size distribution of the S/S products was determined by the mercury intrusion porosimetry (MIP, AUTOPORE IV 9500).

6) Total organic carbon (TOC)

The total carbon (TC) and inorganic carbon (IC) contents in a sample were determined via a TOC analyzer (TOC, SSM-5000A, SHIMADZU). TOC was calculated from the difference between TC and IC.

7) X-ray fluorescence (XRF)

Dried (105^{o}C, 24 h) and finely ground (<75 μm) samples were pressed into pellets at 30 MPa with the assistance of a compression machine. The chemical compositions of the sample were determined by X-ray fluorescence (XRF, Rigaku Supermini 200).

8) Heavy metal(loid) content

Heavy metal(loid) contents in liquid and solid samples were processed based on the following procedures before the metal detection by the Inductively Coupled Plasma Optical Emission Spectroscopy (ICP-OES, FMX36, SPECTROBLUE).

Heavy metal(loid) concentrations in liquid samples: all liquid samples together with a reagent blank were digested by concentrated HNO_3 with a sample to acid volumetric ratio of 5:2 in a

digestion block before ICP-OES measurement for targeted element's concentration to reduce interference from organic matters in the sample.

Heavy metal(loid) contents in solid samples: solid samples were digested by concentrated HNO_3 and $HClO_4$. Quality of measured contents of heavy metal(loid)s in marine sediments was controlled by SRM-2702. And the recovery rates for As, Cr and Cu were in the range of 75 to 92%.

A set of standard solutions (Blank, 0.05, 0.1, 0.2, 0.5, 1.0, 2.0 and 5.0 mg/L) were prepared by diluting the instrument calibration solution in 5% HNO_3 prepared by diluting concentrated HNO_3 in Milli-Q water. The regression coefficients (R^2) of all the calibration curves for ICP-OES measurement were over 0.999. A quality control sample containing 2 mg/L of mixed metal sample (deviation within ±10%) was measured after every 20 unknown samples. 2 or 3 measurements were conducted for each sample depending on its volume, and the measurement error was rarely over 5%. Differences among triplicate samples were rarely over 5% and 10% for liquid and solid samples respectively.

9) Amorphous iron

1 g solid samples were extracted by 40 mL acidified ammonium oxalate in the dark by an end-to-end rotator for 4 h. The leached amount of iron in the filtrate was measured by ICP-OES. The crystalline iron content was calculated by the difference between the total iron and the amorphous iron contents (Jurković et al., 2021).

3.4.2 Instrumental characterization methods

1) Fourier Transformation Infrared spectroscopy (FTIR)

Selected powdery samples mixed with KBr were pressed into discs and subjected to Fourier transformation infrared spectroscopy (FTIR, PerkinElmer, Spectrum Two) test for the identification of surface functional groups.

2) High Performance Ion Chromatography (HPIC)

A high performance ion chromatography (DIONEX INTEGRION HPIC, Thermo Scientific) was used to determine concentrations of anions such as Cl^- and SO_4^{2-}.

3) Raman spectroscopy

Raman spectra of selected samples were collected from Raman spectrometer (Renishaw, UK) with 532 nm laser excitation.

4) Scanning Electron Microscopy (SEM)

Scanning electron microscope (SEM, Tescan VEGA3) was used to check the morphologies of the samples, and the equipped energy dispersive X-ray spectroscopy (EDX) detector was employed for determination of surface elemental compositions.

5) Ultraviolet-Visible (UV-Vis) Spectroscopy

A spectrophotometer (UV-11, MRC) was used to measure concentrations of Cr(VI) and Fe(II) by using the 1,5-diphenylcarbazid and o-phenanthroline method respectively. Differences between Cr(VI) and total Cr, and Fe(II) between total Fe were used to calculate concentrations of Cr(III) and Fe(III). Reactive silica in an aqueous solution was tested as per APHA Method 4500-SI D (Kopp and McKee, 1983).

6) X-ray Diffraction Spectroscopy (XRD)

Mineral phases of the milled samples were detected by an X-ray diffraction spectroscopy (XRD, Rigaku SmartLab) with CuKα radiation at a 0.02° stepwise scanning from 5 to 85°.

7) X-ray photoelectron spectroscopy (XPS)

The surface compositions and chemical states of the solid samples were analyzed by using the Nexsa X-ray photoelectron spectroscopy system (XPS, Thermo Scientific, America). The spectra were analyzed by PEAKXPS.

3.4.3 Macroscopic testing

1) Compressive strength

A universal testing machine was used to determine the mechanical strength of selected samples deploying different testing conditions. A loading speed of 1 mm/min was applied to determine the compressive strength of the granular IPBG. The 28-day compressive strength of mortar specimens was determined in accordance with ASTM C109/C109M-02 (2020). The compressive strength of the S/S products was determined at a loading rate of 0.3 mm/min (Li et al., 2017).

2) Thermal gravimetric analysis (TGA)

Thermal gravimetric analysis (TGA, Rigaku, Thermo Plus EVO2) was employed with the mass loss of a grinded sample recorded during the thermal decomposition process. A sample of around 10 mg was weighed and placed in an Al_2O_3 crucible, which was then heated from 50 to 1000ºC (ramp: 10ºC/min) under an argon atmosphere.

3.4.4 Hazardous waste assessment

1) Toxicity characteristic leaching procedure (TCLP) (US EPA, 1992)

Briefly, dried samples were mixed with 0.1 M glacial acetic acid (pH 2.88 ± 0.05 or 4.93 ± 0.05) at a liquid-to-solid ratio of 20 mL/g and rotated at 30 rpm for 18 h by an end-to-end rotator.

2) pH dependent leaching

Samples were mixed with DI water with aliquots of 2 mol/L HNO_3 or 1 mol/L NaOH to achieve a constant liquid-to-solid ratio of 10 mL/g and desired end pH values. Solid samples subjected to DI leaching without acid/base addition represented samples' natural pH. All samples were rotated at an end-to-end rotator at 30 rpm for 48 h at ambient temperature.

3) Sequential extraction procedure (SEP)

The extraction was carried out in 50 mL polyethylene centrifuged tubes using 1 g solid samples according to literatures with minor modifications (Li et al., 1995; Wang et al., 2020). The fractions determined were: the exchangeable fraction (F1) (8 mL 1 M $MgCl_2$ at pH 7.0 for 1 h), carbonates or acid soluble fraction (F2) (8 mL 1 M NaOAc at pH 5 for 5 h), the reducible or Fe-Mn oxide bounded fraction (F3) (20 mL 0.04 M $NH_2OH{\cdot}HCl$ in 25% (V/V) HOAc at 96 ± 3ºC for 6 h), the oxidizable fraction (F4) (3 mL 0.02 M HNO_3 + 5 mL 30% H_2O_2 at pH 2 and 85 ± 2ºC for 2 h, add 3 mL 30% H_2O_2 for 3 h, cool down, add 5 mL 3.2 M NH_4OAc in 20% (v/v) HNO_3 for 0.5 h), and the residual fraction (F5) (use $HClO_4$ mL and HNO_3 4 mL for total digestion).

CHAPTER 4 RECYCLING P-RECOVERED ISSA BY CO-PYROLYSIS WITH LIGNIN FOR CR(VI) REMOVAL FROM AQUEOUS SOLUTIONS

4.1 Introduction

In this chapter, the feasibility of reusing the P-recovered ISSA residue as a supplementary iron source to make iron-biochar composites for the removal of Cr(VI) from aqueous solutions was investigated. A model biomass material, i.e., lignin was selected because (i) it was reported to have the highest possibility for the carbothermal reduction of Fe_2O_3 to its lower valent counterpart minerals compared to cellulose and hemicellulose that are main components in biomass (R. Wei et al., 2020), and (ii) lignin waste are generated in huge quantities globally but with a less than 10% recycle rate (Patil et al., 2018). Briefly, the mixture of lignin and the P-recovered ISSA residue with a mass ratio of 1:2 (determined by preliminary experiments to maximize the reuse amount of the P recovered and to achieve optimal Cr(VI) removal from aqueous solutions) was co-pyrolyzed at 650^{o}C, 850^{o}C and 1050^{o}C for 1 h (ramp: 10^{o}C/min) under a nitrogen atmosphere, which produced LR-650, LR-850 and LR-1050. For comparison purposes, the P-recovered ISSA residue or lignin alone was heated under the same condition which produced L-1050 and Residue-1050. Theses samples were then characterized and compared for the removal of Cr(VI) from wastewaters. The specific targets of this chapter include (i) characterizing the produced composite samples; (ii) evaluating the Cr(VI) removal performance, potential leaching of heavy metals originating from the P-recovered ISSA residue and testing the applicability for Cr(VI) removal from a synthetic tannery wastewater, and (iii) exploring the Cr(VI) removal mechanisms.

4.2 Results and discussion

4.2.1 Characterization of samples

Surface properties including the surface area, pore structure and the active chemical species of the samples can greatly influence the Cr(VI) removal performance. The LR-1050 had a 15 times higher specific surface area compared to L-1050 (i.e. 60.7 vs 3.9 m^2/g), and larger total pore volume (i.e., 0.037 vs 0.02 cm^3/g). The porous structure of LR-1050 could be associated with the enhanced degradation of organic carbon in lignin with the iron oxides present in the ISSA residue (Cho et al., 2019).

XRD analysis was conducted to investigate the evolution of mineral phases with an emphasis on iron species on selected samples. As demonstrated in Figure 4-1, the major crystalline species identified in the ISSA residue included quartz, anorthite, which were quite resistant to heat due to the presence of the characteristic peaks up to 1050°C. Both hematite and magnetite were identified in the ISSA residue. After co-pyrolyzing with lignin at 650°C, peaks of hematite disappeared due to the transformation to magnetite. Under a relative low temperature (<800°C), lignin can be pyrolyzed to generate reducing gases like H_2 and CO arising from the cracking of carbonyl (C-O-C) and carboxyl (C=O) groups, and the process could be promoted with the presence of iron rich solids like red mud and iron ore (Cho et al., 2019; Wei et al., 2017; Yang et al., 2007). The direct reduction of Fe_2O_3 by carbon, and the indirect reduction of Fe_3O_4 by CO were not thermodynamically feasible at temperature below 700°C (Liang et al., 2019), but the reduction of Fe_2O_3 to Fe_3O_4 by reducing gases like CO and H_2 could be initiated at 570°C (Neeli and Ramsurn, 2018). Therefore, at 650°C, Fe_2O_3 in the residue was mainly reduced to Fe_3O_4 by the reducing gases generated from the pyrolysis of lignin. With the increase of temperature to around 850°C,

the generation of CO is significantly increased which could be attributed to (i) the reduction of iron oxide, (ii) the catalytic effect of iron containing solid for the pyrolysis of lignin which contributed to the increase of gas yield, and (ii) Boudouard reaction ($C(s) + CO_2(g) \rightarrow 2CO(g)$) (Wei et al., 2017). At this temperature, direct reduction of iron oxides by carbon and indirect reduction by reducing gasses occurred simultaneously, which resulted in the further reduction of Fe_3O_4 to FeO and ZVI. Meanwhile, silica in the P-recovered ISSA reacted with FeO to form fayalite at 850ºC, which hinders its transformation to ZVI. This reaction is undesirable since fayalite is not magnetic (Nayak et al., 2019) which could make the separation of the sample from waters difficult after the pollutant purification process. However, metallic iron was identified as the dominant iron phase in LR-1050, indicating the most effective reduction of iron oxides in the P-recovered ISSA residue by lignin occurred. In addition, weak XRD peaks of iron sulfide and iron carbide also appeared in LR-1050. The appearance of FeS could be related to the reaction between iron with sulfur derived from the residual sulfates in the P-recovered ISSA or sulfur-containing components in the lignin. The generation of iron carbide could be related to the dissolution of carbon atoms and the subsequent incorporation of atoms into metallic iron (Neeli and Ramsurn, 2018). The increased surface area and the successful introduction of ZVI in LR-1050 is considered beneficial for the removal of Cr(VI). In addition, good thermal stability of the residue gave a high yield of LR-1050 that reached 76%.

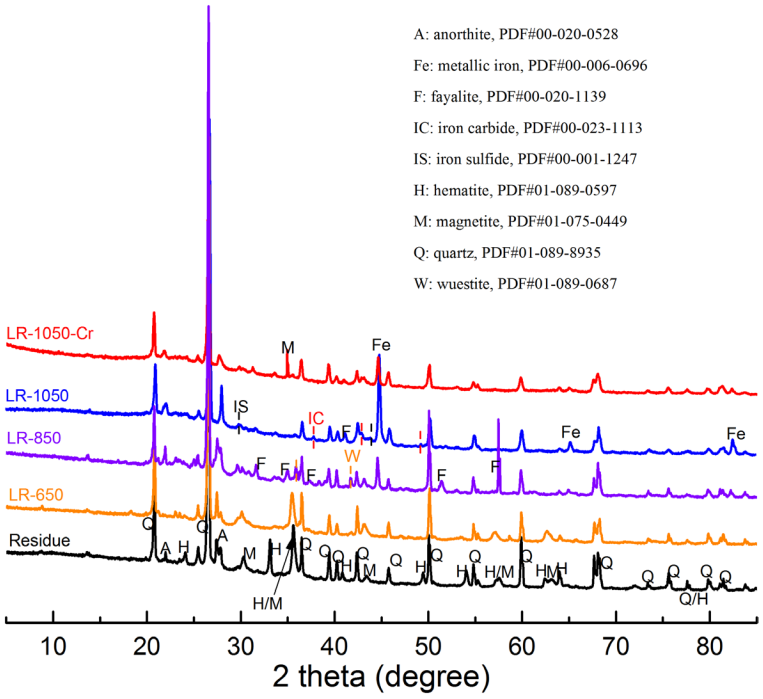

Figure 4-1 X-ray diffraction patterns of selected samples before and after Cr(VI) removal.

The FTIR transmittance spectra of selected samples are also checked as shown in Figure S1. All the samples had a broad peak at 1100~950 cm^{-1} which could be associated with the stretching vibration of T-O-Si (T= Si or Al), and peaks at around 770 cm^{-1} and 690 cm^{-1} were associated with the presence of amorphous silica and quartz respectively (Samantasinghar and Singh, 2018; Tashima et al., 2017). The peak centered at around 520 cm^{-1} in the ISSA residue could be assigned to the Fe-O bond in hematite (Lassoued et al., 2017), and it disappeared after the co-pyrolysis process at 650°C. In addition, there was a weak peak centered at 575 cm^{-1} in the ISSA residue, which could be related to the Fe-O stretching of the tetrahedral and octahedral sites in magnetite (Stoia et al., 2016). This peak became distinct in LR-650, and gradually disappeared with the increase of pyrolysis temperature to 1050°C. These results were consistent with the XRD results,

which showed hematite in the ISSA residue was first reduced to magnetite during the co-pyrolysis process. The above-mentioned Fe-O related peaks disappeared in LR-1050 reflecting an effective reduction of iron oxides to ZVI at 1050ºC.

The surface morphologies of the P-recovered ISSA residue and LR-1050 are shown in Figure S2 and Figure 4-2. As shown in Figure S2, the ISSA residue was mainly composed of irregular particles. EDX analysis showed the bigger irregular particles were dominantly composed of Si and O, which could be associated with the presence of quartz. The smaller debris particles contained high contents of Fe and O, which were associated with the presence of iron oxides. After co-pyrolyzing with lignin at 1050ºC, the produced LR-1050 showed a quite different morphology. As shown in Figure 4-2a, both irregular and spherical particles (partially broken) with carbon as the dominant element merged (shown in Figure S3b) due to the pyrolysis of lignin. Detailed examination of these two types of particles (Figures 4-2b and c) showed a porous structure with many spherical fine particles. The micro-sized spherical particles randomly distributed on the surface of the sample individually or as clusters. The point EDX (Figures S3 a and b) analysis of these micro-sized spherical particles showed the dominant presence of iron with small amounts of carbon, sulfur and oxygen, which could be due to the presence of ZVI (with some oxidation or sulfidation) in LR-1050 as revealed by the XRD analysis. The partly embedment of ZVI in the silica or carbon matrix indicated there might be some mechanical bonding between the produced ZVI with silica or the carbon matrix (Zhang et al., 2013). These results indicated that LR-1050 was successfully loaded by ZVI.

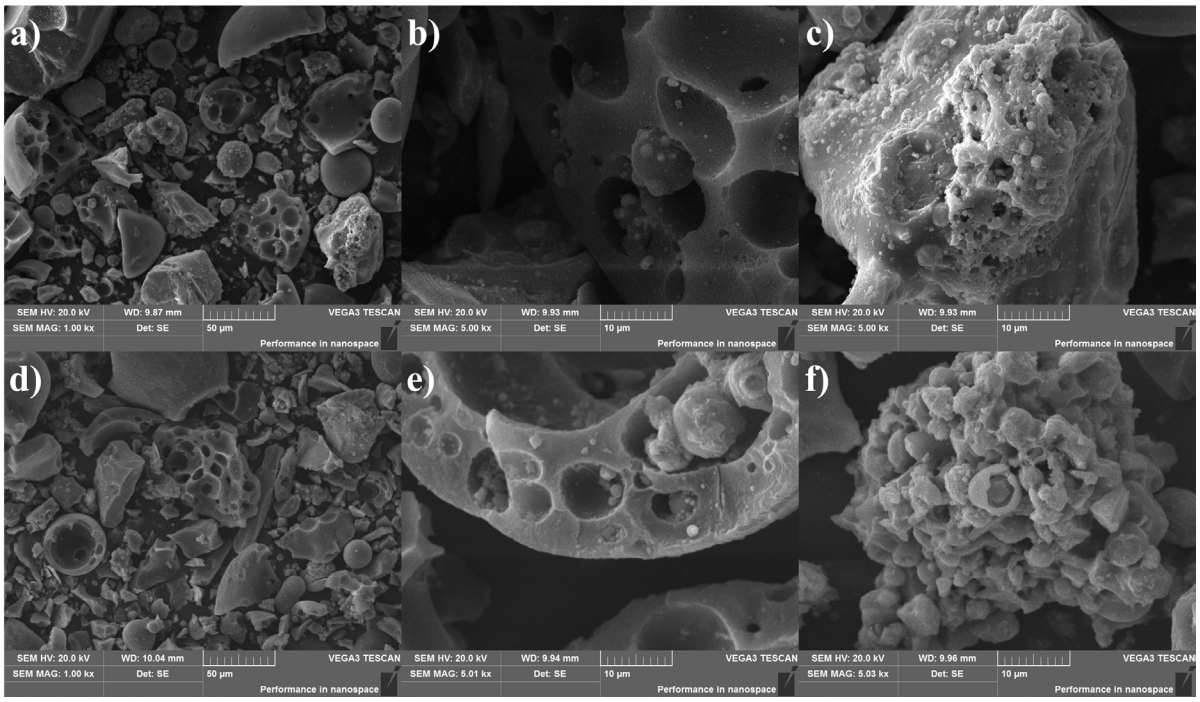

Figure 4-2 SEM images of LR-1050 before (a, b and c) and after (d, e and f) Cr(VI) removal.

XPS analysis was adopted to investigate the surface chemical composition of the solid samples with a focus on the phase transformation of iron after the pyrolysis process. As shown in Figure 4-3a, the survey spectra showed that both the P-recovered ISSA residue and LR-1050 were composed of Si, Al, Fe, and C. The high-resolution Fe spectra of the ISSA residue and LR-1050 were further checked and analyzed (shown in Figure 4-3b). The Fe2p3/2 spectrum of the ISSA residue could be deconvoluted into four peaks that were assigned to Fe(III) in octahedral sites at 710.9 eV, Fe(II) in octahedral sites at 710.6 eV, Fe(III) in tetrahedral sites at 713.9 eV and Fe(III) satellite peak at 718.6 eV (Yamashita and Hayes, 2008; Zhong et al., 2018). This again revealed that iron oxides present in the residue comprised both hematite and magnetite. It should be noted that the iron content of LR-1050 was around 9.20% (as Fe). The high-resolution Fe2p3/2 spectrum

of LR-1050 however only showed signals at a noise level that might be attributed to the formation of ZVI in the pores of the material or the unevenly distribution of ZVI on the surface of LR-1050 that prevented the detection of iron by XPS.

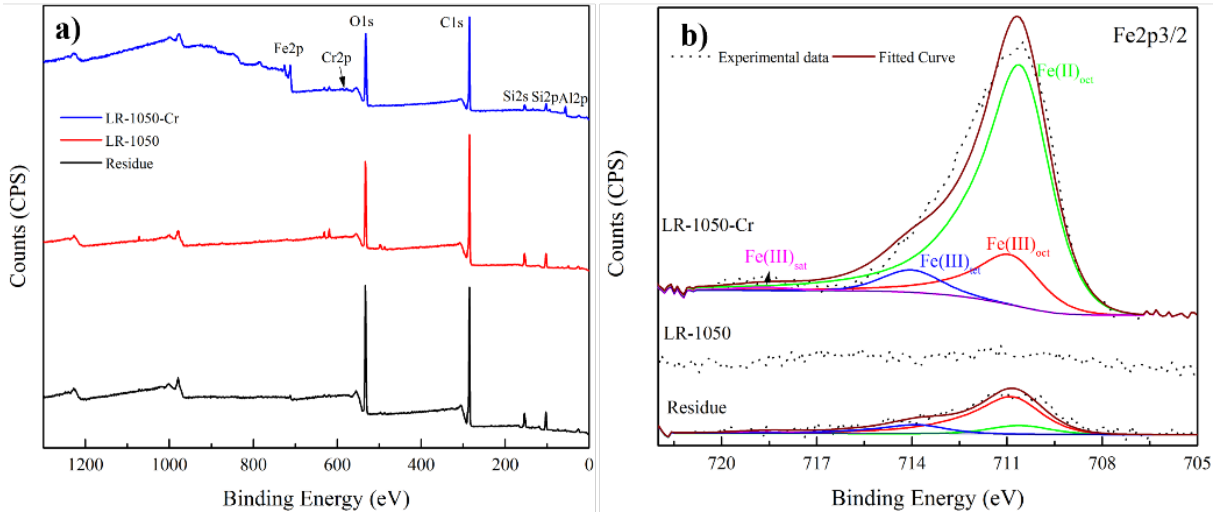

Figure 4-3 XPS analysis of selected solid samples.

4.2.2 Cr(VI) removal from aqueous solutions

1) Batch Cr(VI) removal performance

The Cr(VI) removal (C_0 = 10 mg/L) ability was first compared among all the prepared samples under different conditions (as shown in Figure 4-4a). It can be seen that both the ISSA residue and thermally treated ISSA residue at 1050ºC could only remove less than 3% of Cr(VI) within 4 h demonstrating their poor capabilities for Cr(VI) removal. Lignin alone was also pyrolyzed at 1050ºC and achieved a 55.8 ± 0.6% removal rate of Cr(VI) from the aqueous solution within 4 h. After co-pyrolyzing the P-recovered ISSA residue with lignin under elevated temperatures, the

resulting solid samples showed increased Cr(VI) removal rate compared with the ISSA residue and Residue-1050. LR-650 and LR-850 could remove around 30.0 ± 0.6% and 32.7 ± 2.2% Cr(VI) respectively under the same condition as before, while LR-1050 removed nearly all the Cr(VI) to below the detection limit (0.004 mg/L). This comparison demonstrated that co-pyrolysis of the ISSA residue with lignin under 1050°C produced a composite material with a notably higher Cr(VI) removal efficiency.

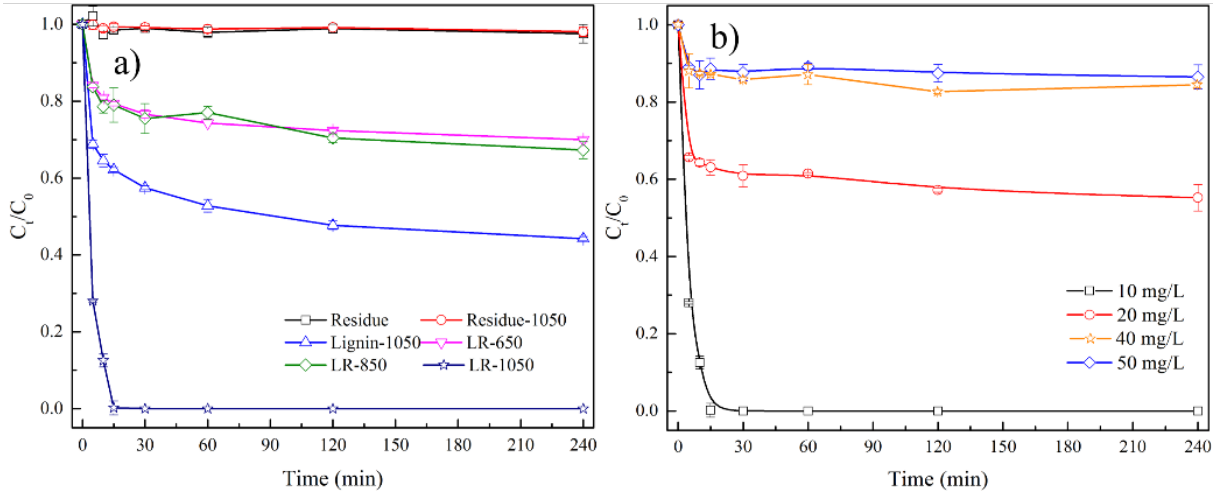

Figure 4-4 Comparison of Cr(VI) reductive/sorptive removal efficiency (a) by different solid materials and (b) effect of Cr(VI) concentration on the removal of Cr(VI) by LR-1050 (dosage: 1 g/L, pH: 2.0).

The Cr(VI) removal performance by LR-1050 under different reaction conditions was further assessed. The effect of initial Cr(VI) concentration on the removal of Cr(VI) is shown in Figure 4-4b and Figure S4. The removal rate of Cr(VI) reached nearly 100% (below the detection limit of 0.004 mg/L) when the initial Cr(VI) concentration was 10 mg/L. With increase in the initial Cr(VI) concentration, the removal rate decreased. The effect of LR-1050 dosage on Cr(VI) removal was

also examined (as shown in Figure S5). The Cr(VI) removal rate increased almost linearly (R^2 = 0.944) with the LR-1050 dosage from 0.05 to 4 g/L, and reached a plateau afterwards. The removal rate of the Cr(VI) was fast within the initial 30 min and gradually reached equilibrium at around 1 h. Similar results have been reported in many other studies adopting carbon-supported ZVI for Cr(VI) removal from aqueous solutions (Dai et al., 2016; Shang et al., 2017). This fast removal rate could be related to the abundance of active sites for the attachment of Cr(VI) on the surface of the material and a higher driving force between the aqueous solution and the material's surface (Wang et al., 2019). The fast removal rate of Cr(VI) within 30 min could also be associated with the rapid dissolution of Fe(II) from LR-1050 (Figure 4-5d) which could reduce Cr(VI) within several minutes (Fendorf and Li, 1996). In addition, a slightly slower removal rate was observed at a higher Cr(VI) concentration. The adsorbed Cr(VI) could be reduced to Cr(III) and form precipitates on the surface of the material which inhibited the electron transfer process between the active sites on the material surface with Cr(VI) resulting in a decreased reaction rates at a higher initial Cr(VI) concentration (Shang et al., 2017). The widely used adsorption kinetic models including the PFO and the PSO kinetic models were adopted to fit the experimental data as shown in Figure S6. The results indicated that the PSO kinetic model could better describe the experimental data due to the higher regression coefficients and the better estimated sorption capacity with the experimental data (shown in Table S1), indicating that the rate-determining step for the removal of Cr(VI) was a chemical process (Fu et al., 2013).

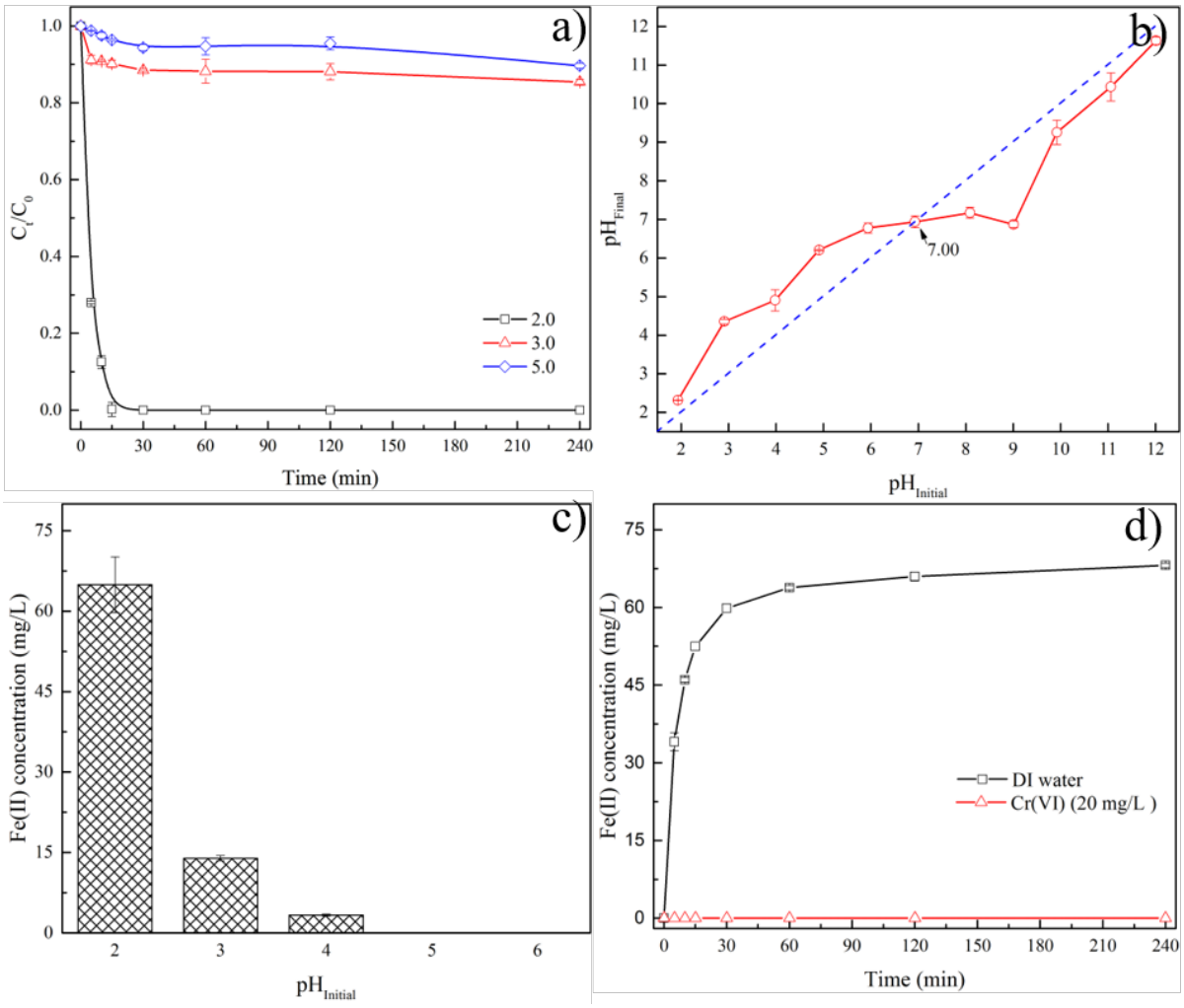

Figure 4-5 pH influence on the removal of Cr(VI), b) pH_{PZC} of the LR-1050; c) leaching of Fe(II) at different pH values (t = 240 min); d) dissolution kinetics of Fe(II) by DI water and Cr(VI) containing solutions at pH 2.

The effect of solution pH on Cr(VI) removal by LR-1050 is demonstrated in Figure 4-5a. An almost complete removal of Cr(VI) (below the detection limit of 0.004 mg/L) was observed within 30 min when the solution pH was around 2.0. With the increase of solution pH to around 3.0 and 5.0, the Cr(VI) removal efficiency dramatically dropped to around 15% and 10% respectively. A

similar optimal Cr(VI) removal pH was reported by a ZVI supported biochar (Shang et al., 2017). The pH-dependent removal of Cr(VI) by LR-1050 could be related to its surface properties and the Cr(VI) chemistry in the aqueous solution (Dai et al., 2016). It is known that the main Cr(VI) species is $HCrO_4^-$ with small amounts of $Cr_2O_7^{2-}$ when the solution pH value is lower than 6.0. As shown in Figure 4-5b, the pH_{PZC} of LR-1050 was around 7.0, and the surface would be positively charged at pH < 7.0. In the solution with pH 2.0, the positively charged LR-1050 surface could favorably attract the negatively charged Cr(VI) via electrostatic attraction (Zhu et al., 2018). It is reported that electron donors such as ZVI can readily reduce Cr(VI) to Cr(III) (Powell et al., 1995). The ZVI on the surface of LR-1050 could thus donate electrons to the adsorbed Cr(VI) and reduce Cr(VI) to Cr(III).

In addition, the dissolution of iron from LR-1050 via corrosion could release Fe(II) into the solution which could be rapidly oxidized by Cr(VI) due to its strong oxidation potential in the acidic environment (Zhong et al., 2018). As shown in Figures 4-5c and d, Fe(II) was continuously leached out from LR-1050 into the aqueous solution and reached a plateau concentration (68 mg/L) at around 120 min when mixed with DI water with a pH value of 2.0. The leached Fe(II) concentration was strikingly reduced to around 14 mg/L and below the detection limit (0.05 mg/L) at pH 3.0 and 5.0 respectively. However, when LR-1050 was mixed with the Cr(VI) containing solution at pH 2.0, Fe(II) was not detected within the reaction time. The total amount of iron and sulfur however continuously increased with time and reached 68 and 63 mg/L after 4 h (as shown in Figure S7). The leached Fe(II) could therefore be largely associated with the dissolution of ZVI or iron sulfide. The dissolved Fe(II) could rapidly reduce Cr(VI) to Cr(III) and be oxidized to Fe(III). The concentration changes of total chromium (TCr), Cr(VI) and Cr(III) are exhibited in Figure S7. As shown from the figure, the removal of TCr was slightly more than 20%. In addition,

after a 4-hour Cr(VI) removal by LR-1050, the final solution pH was increased to around 2.6. Since Cr(III) mainly existed as Cr^{3+} and $Cr(OH)^{2+}$ when solution pH is lower than 3.0 (Zhong et al., 2018), the total Cr detected by ICP-OES was originated from the presence of Cr(III). Even though the TCr removal rate was around 20%, the environmental concern is considered to be significantly reduced because nearly all Cr(VI) was converted to Cr(III) which was considered far less toxic (Xia et al., 2019).

In addition, the solution pH value of around 2.0 was within the typical pH range of real Cr(VI)-containing wastewaters (Han et al., 2020). Test results also showed the presence of commonly existed anions including PO_4^{3-}, SO_4^{2-}, NO_3^- and SiO_3^{2-} at concentration levels of 10, 50 and 100 mg/L had negligible influence on the removal of Cr(VI) (10 mg/L) by LR-1050 (1g/L) at pH 2.0 (data not presented because Cr(VI) was not detected by the 1,5-diphenylcarbazid method). The potential leaching of other heavy metals originating from the ISSA residue is also a critical issue to determine the safe use of LR-1050. Here, we checked the detectable heavy metals after Cr(VI) removal by LR-1050 in the solution with a pH value of 2.0 and compared to a local wastewater discharge standard (EPD, 1991). As shown in Table S2, the detected heavy metals include Cu (0.36 mg/L), Ni (0.014 mg/L) and Zn (0.16 mg/L) that were below the legal discharge limits, and Cd (0.056 mg/L) and Sr (0.29 mg/L) which were also less than the legal limit when the effluent flow rate is less than 400 and 2000 m^3/day, respectively. Particularly, LR-1050 could be safely used in the subsequent fixed-bed column experiments, where other regulated metals including total Fe and Cr could be reduced to below the legal limit level.

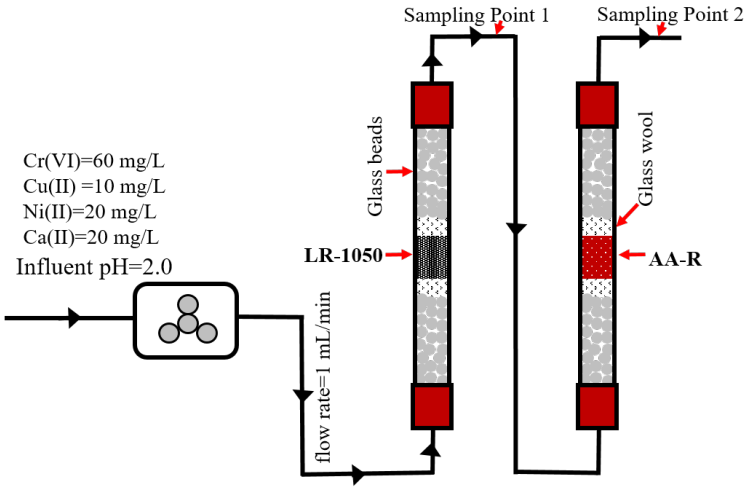

Figure 4-6 Configuration of the fixed-bed column experiment for Cr(VI) removal from a synthetic wastewater.

2) Fixed-bed column experiments for Cr(VI) removal from synthetic tannery wastewaters

The chemical reduction plus precipitation method is widely adopted to remove Cr(VI) from wastewaters in practice (Rosales-Landeros et al., 2013). Here the P-recovered ISSA residue derived materials including LR-1050 (reduction removal of Cr(VI)) and AA-R (AA-R: a product obtained by curing a mixture of P-recovered ISSA residue with water glass at a fixed Na_2O to SiO_2 molar ratio of 1.5:1 at 65ºC for 24 h for enhanced removal towards TCr) (Wang et al., 2021b), serving as alternative cost-effective agents, were evaluated for the removal of Cr(VI) from a synthetic tannery wastewater via the fixed bed column experiments. The configuration of the fixed-bed column (diameter: 1.6 cm, length: 16 cm) experiment is shown in Figure 4-6. Briefly, LR-1050 and AA-R (mass: 2 g, height: 2 cm) were packed in the middle of two columns. The solid samples were protected by two layers of glass wool from leakage, followed by glass beads (diameter: 5~6 cm) at both ends. The synthetic Cr(VI)-containing aqueous solution was

continuously pumped into the columns loaded by LR-1050 and AA-R sequentially in an up-flow mood at a constant flow rate of 1 mL/min by a peristaltic pump (LongerPump®, BT100-1L). Samples were collected after passing through each of the columns (i.e., sampling point 1 and 2 as shown in the figure) at predetermined time intervals and analyzed for concentrations of the targeted elements. The breakthrough points for Cr(VI) and TCr were set in accompliance with the legal limits in China (i.e., 0.5 mg/L for Cr(VI) and 1.5 mg/L for TCr). As shown in Figure 4-7, the breakthrough point of Cr(VI) for LR-1050 (sampling point 1) occurred after 1260 min, which was slightly increased to after 1500 min with the addition of AA-R (sampling point 2). The breakthrough point of TCr for LR-1050 was only after 60 min, whereas the time was significantly extended to after 600 min with the combined use of AA-R. In addition, this column exepriments showed that LR-1050 effectively removed Cu(II) and Ni(II). All these results demonstrated that P-recovered ISSA residue could be modified and produce low-cost alternative h agents including LR-1050 and AA-R for the removal of Cr(VI) from wastewaters.

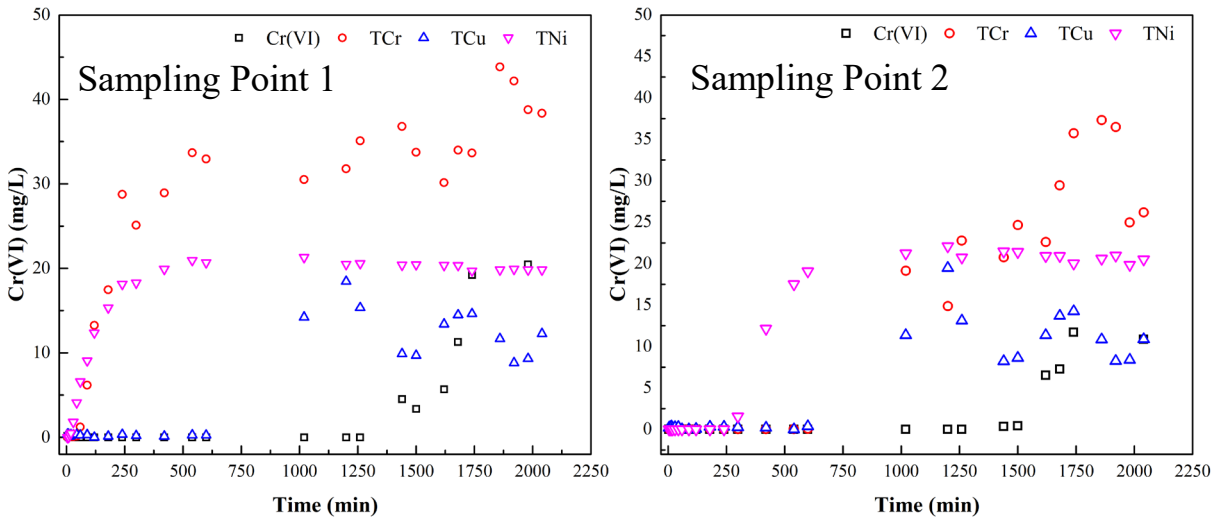

Figure 4-7 Breakthrough curves of Cr(VI) removal from simulated tannery wastewater.

4.2.3 Mechanism study

To further investigate the Cr(VI) removal mechanisms, LR-1050 after Cr(VI) removal was characterized. As shown in Figures 4-2d, e & f, the morphology of LR-1050 after Cr(VI) removal was similar with that of LR-1050. The EDX analysis results confirmed the successful uptake of chromium (Figures S3c, d, e, & f). Particularly, point EDX analysis of the micro-sized spherical particles showed the presence of a higher content of chromium than other locations, which reflected the affinity of metallic iron towards Cr (Wu et al., 2018; Zhao et al., 2020). The speciation of Cr was further identified by deconvoluting the Cr2p3/2 spectrum of LR-1050 after Cr(VI) removal (shown in Figure 4-8). The Cr2p3/2 peak could be fitted by two compositional peaks that corresponded to Cr(III) and Cr(VI) with a binding energy centered at 576.7 eV and 578.5 eV respectively (Zhong et al., 2018). The deconvolution result also suggested that around 71% of the uploaded Cr on the surface of LR-1050 after Cr(VI) removal was present as Cr(III). This result confirmed the effective reduction removal of Cr(VI) could be achieved by LR-1050. In addition, Fe(II) and Fe(III) peaks could be founded in the Fe2p3/2 spectrum of spent LR-1050 (Figure 4-3) indicating the ZVI in LR-1050 was oxidized after the removal process. After Cr(VI) removal (Figure 4-1), a distinct peak at 2θ around 35° in the XRD pattern of spent LR-1050 emerged, which could be assigned to Fe_3O_4 generated from the redox reactions occurred during the removal process. Overall, chemical reduction played an important role (>80%) in the removal of Cr(VI) under the optimal experimental condition.

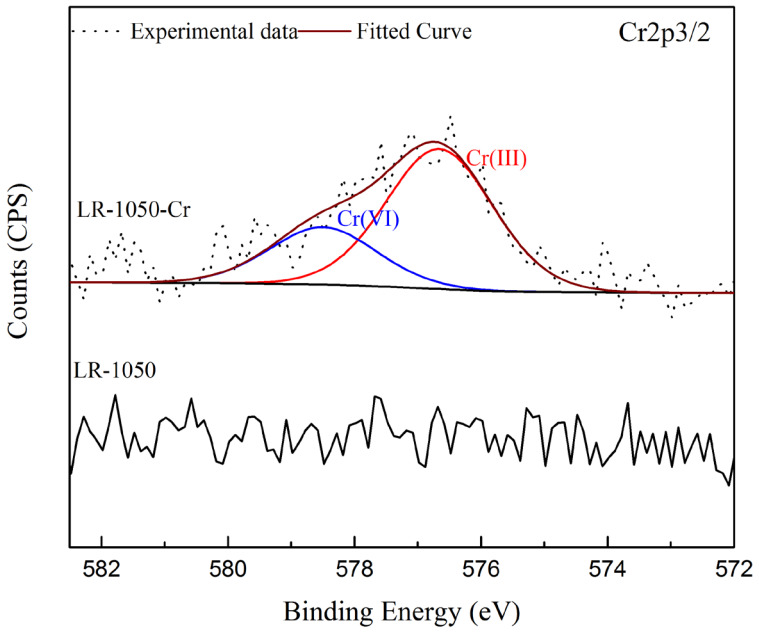

Figure 4-8 XPS analysis of Cr2p3/2 binding states of LR-1050 before and after Cr(VI) removal.

4.3 Summary

In this chapter, a novel recycling route addressing the disposal of iron-rich ISSA after phosphorus recovery was proposed. To be specific, by co-pyrolyzing the P-recovered ISSA residue with lignin at 1050°C under a nitrogen atmosphere, most of the iron oxides in the P-recovered ISSA residue were transformed to ZVI. The resulting sample, with a high BET surface area, could rapidly and effectively remove Cr(VI) from waters under optimized reaction conditions. The fixed-bed column experiments demonstrated its potential to be used in practice as alternative heavy metal removing agents for Cr(VI)-containing industrial wastewaters. Processes including electrostatic attraction and chemical reduction contributed to Cr(VI) removal, but over 80% Cr(VI) removal could be attributed to reduction reactions. Overall, this win-win strategy not only facilitates the sustainable

management of ISSA after P recovery but also provides an alternative cost-effective agents for the remediation of Cr(VI) containing wastewaters.

CHAPTER 5 ROLE OF SILICA IN THE P-RECOVERED ISSA ON ARSENIC REMOVAL BY THE RESULTING IRON-BIOCHAR COMPOSITE

5.1 Introduction

Modification of biochar by low-cost iron sources has gained increasing attention to enhance pollutants removal performance and reduce the production cost compared to conventional chemical modifications. The previous chapter has demonstrated that the P-recovered ISSA can serve as a supplementary iron source to produce iron-biochar composites. To extend the scope of feedstock biomass and expand the application horizon of the end iron-biochar composite to remove other heavy metals, this chapter utilized a real biowaste, i.e. peanut shell, that was co-pyrolyzed with the P-recovered ISSA residue for the removal of inorganic arsenic (As(III) and As(V)).

Nevertheless, as a supplementary iron source, the P-recovered ISSA has a complex composition, and its effect on properties of the iron-biochar composite are not well investigated. This chapter produced an iron-biochar (RBC) composite from co-pyrolyzing the P-recovered ISSA residue and peanut shell, and focused on the role of silica with widespread existence not only in the P-recovered ISSA residue and but also in other low-cost iron sources (Cho et al., 2019; Yang et al., 2019) on properties of the resulting iron-biochar composite relevant to As(III)/As(V) removal. As shown in Section 3.3.1, the P-recovered ISSA residue derived iron-biochar composite (RBC) was synthesized under the following conditions: a mass ratio of ISSA residue to peanut shell at 1:1, pyrolysis temperature at 850^{o}C, and a residence time of 1 h. In addition, the P-recovered ISSA residue was modelled as a mixture of SiO_2 and Fe_2O_3 with a mass ratio of 4:1. This mixture was pyrolyzed with peanut shell at the same condition with that of RBC, and the generated biochar sample was named as FSBC. For comparison purposes, Fe_2O_3/peanut shell mixture with mass ratio

of 1:5, and SiO_2/peanut shell mixture with mass ratio of 4:5 was also pyrolyzed under the same condition which produced an iron-biochar composite (FBC) for pure F_2O_3 and a silica-biochar composite (SBC) for comparison purposes. Pristine biochar (BC) was made from the pyrolysis of plain peanut shell.

This chapter, therefore, aims to investigate the role of silica on the removal of As(III) and As(V) from aqueous solutions by RBC. The specific targets include (i) optimizing the production conditions (e.g., mix proportion of ISSA with peanut shell and pyrolysis temperature); (ii) examining the role of SiO_2 in the P-recovered ISSA on arsenic removal by the produced iron-biochar composite; (iii) illustrating the arsenic removal mechanisms.

5.2 Results and discussion

5.2.1 Characterization of samples

Selected physicochemical properties of the samples are shown in Table 5-1. The yield of BC was 28.8%, which was lower than that of FBC (34.4%), SBC (61.6%), FSBC (61.5%) and RBC (59.7%). The C content was reduced from 81.03% in BC to 50.35% in FBC, and to the range of 18~21% in SBC, FSBC and RBC. These findings indicated that the presence silica with a high thermal degradation resistance contributed to the significantly enhanced yield (Zhao et al., 2019), and reduced C contents in SBC, FSBC and RBC compared to BC due to the dilution effect. The Fe contents in BC and SBC were negligible, which were increased to around 16.86 % in FBC, 8.47% in FSBC and 7.06% in RBC. The lower Fe contents in FSBC and RBC compared to that of FBC (equal initial Fe_2O_3 to peanut shell mixing ratio) was also associated with the presence of silica after initial mixing. The pH of all the samples were relatively high (10.67~11.40) due to the

removal of volatile organic compound and the condensing of basic cations in the mineral components under a high pyrolysis temperature (Amen et al., 2020). The pH_{PZC} of BC and RBC were around 10.47, which were higher than those of FBC (10.19), SBC (9.70) and FSBC (9.75).

Table 5-1 Physicochemical properties of samples.

Item	BC	FBC	SBC	FSBC	RBC
C (%)	81.03	50.35	20.06	18.57	18.08
Fe (%)[a]	0.09±0.008	16.86±0.23	0.037±0.0004	8.47±0.97	7.06±0.24
Yield (%)	28.8	34.4	61.6	61.5	59.7
pH[b]	11.40	11.61	11.20	10.67	11.54
pH_{PZC}	10.47	10.19	9.70	9.75	10.47

Note: a) total digestion by HNO_3 + $HClO_4$ followed by ICP-OES measurement; b) sample mixed with deionized water at 20 mL/g for 4 h.

The textural properties including BET surface area, total pore volume, and average pore diameter of the samples are summarized in Table S3. The surface area of BC was 20.1 m^2/g, which was increased to 189.0 m^2/g for FBC, 50.8 m^2/g for FSBC and 73.0 m^2/g for RBC. BC had a pore volume of 0.014 cm^3/g, which was significantly increased to 0.132 and 0.058 cm^3/g for FBC and RBC. The morphologies and surface elemental compositions of these samples were examined by SEM-EDX. As clearly seen in Figure 5-1a & b, BC showed a porous structure, while rough particles were found on the surface of FBC (Figure 5-1c & d). EDX analysis and elemental mapping of FBC (as shown in Figure S8a) demonstrated that these particles were composed of C, O, Fe, and Si, which indicated the successfully coating of iron on the surface of FBC. Similar structures were also found in FSBC (Figure 5-1f) and RBC (Figure 5-1g). Moreover, irregular

silica grains were easily observed in FSBC (Figure 5-1e) and RBC (Figure 5-1h). The EDX analysis and elemental mapping also showed even distributions of carbon and iron on these silica surface (Figure S8b) due to the formation of Si-C bond during the pyrolysis process (Zhao et al., 2019) or the deposition of carbon on iron oxides covered on the silica surface in the ISSA residue (as shown in Figure S9f) (Ehrensberger et al., 1997). According to our previous studies, iron oxides in the ISSA residue emerged either as discrete phases or attached on the surfaces of silica grains or aluminosilicates (Wang et al., 2021a). Upon mixing the ISSA residue with peanut shell, the discrete iron oxide particles with smaller particle sizes could penetrate into the pores of or be attached on surfaces of peanut shell more easily compared to those covered on larger silica grains, which resulted in the presence of these two main types of particles with distinct morphologies in RBC. Both the biochar and the silica in the ISSA residue provided supporting surfaces for the attachment of the produced iron minerals after pyrolysis.

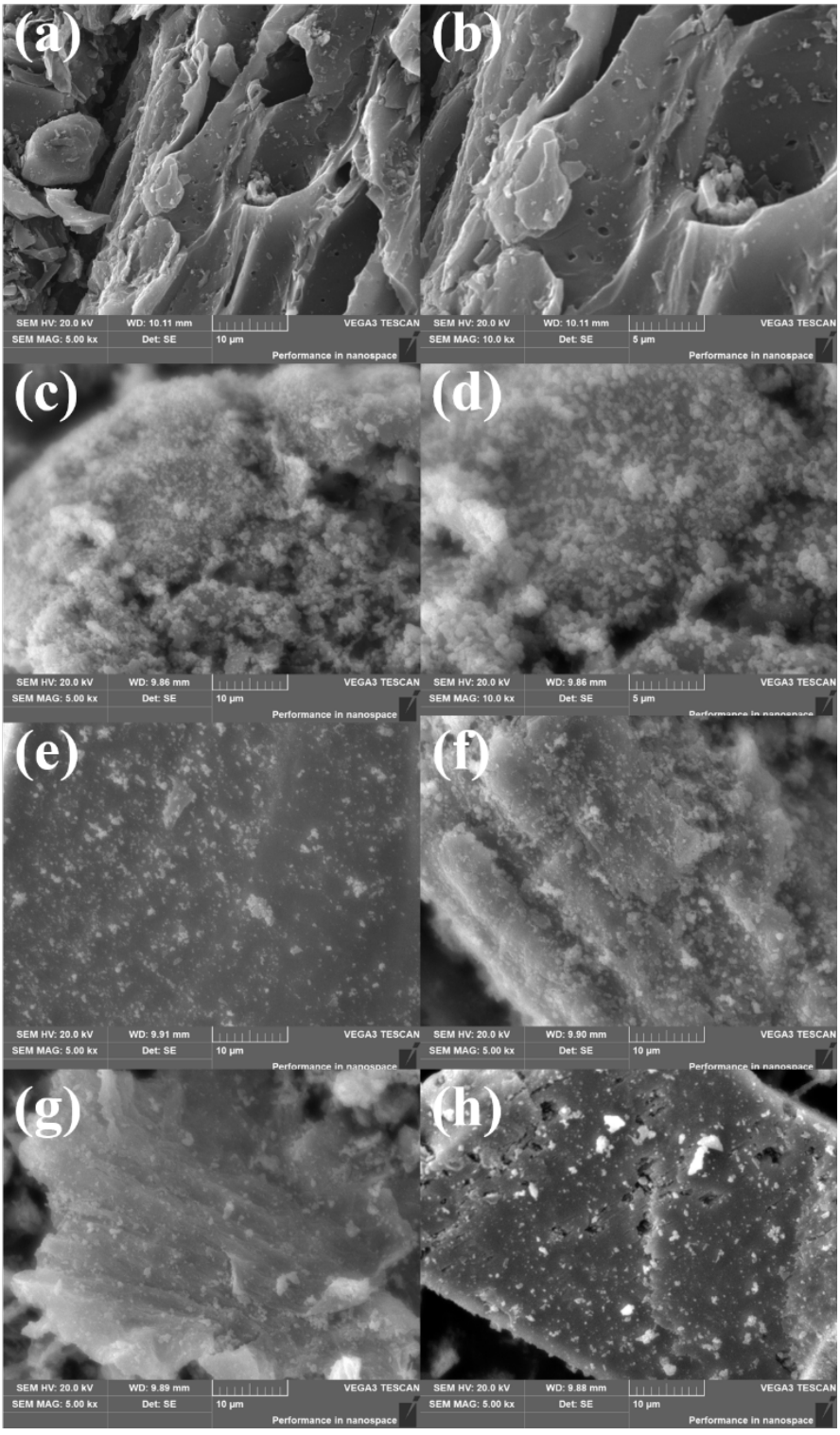

Figure 5-1 SEM images of BC: (a) and (b), FBC: (c) and (d), FSBC: (e) and (f), and RBC: (g) and (h).

The mineral phases, particularly the iron related phases which have great influences on the adsorption performance for removing pollutants (Yoon et al., 2020), in these samples were examined by XRD (Figure 5-2). The XRD pattern of BC showed a 2θ diffraction peak at 26.5° corresponding to the graphite, which was widely detected in an array of pyrolytic carbons produced under a relatively high temperature (Cuong et al., 2021). Relatively strong ZVI peaks were found in FBC, FSBC and RBC, indicating that most of the iron oxides were reduced to ZVI during the co-pyrolysis process. The XRD spectrum of FBC also showed the presence of featured peaks of Fe_3O_4 which was similar to other studies (Zhou et al., 2014). In addition, austenite was found in FBC, FSBC and RBC. Iron silicon whose peaks might overlap with ZVI and austenite was expected to be present in FSBC and RBC. Since the distribution of ZVI on biochar surface affects its adsorption performance, its particle size was further estimated by the Debye-Scherrer equation. As shown in Table S4, the estimated particle size of ZVI in FBC was around 38 nm, which was increase to around 42 nm and 46 nm in FSBC and RBC respectively indicating a slighter poorer dispersion of ZVI in FSBC and RBC compared to FBC. These results indicated that the co-pyrolysis process successfully turned iron oxides in the ISSA residue into nano-sized ZVI, which was beneficial for the removal of arsenic (Bakshi et al., 2018). The presence of silica in ISSA however could react with Fe to form iron silicon at the expense of producing ZVI or Fe_3O_4, thereby leading to a different iron utilization efficiency towards arsenic removal compared to FBC.

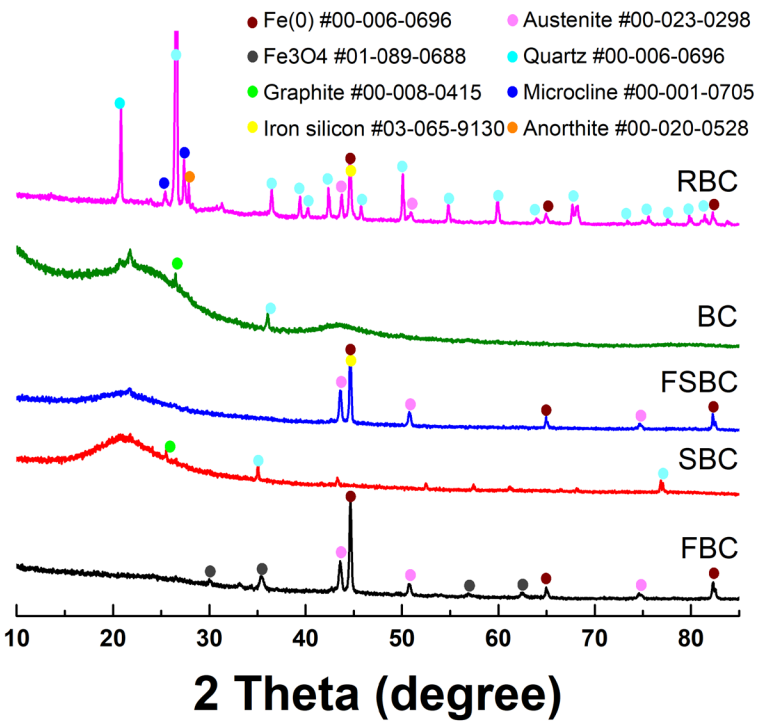

Figure 5-2 XRD spectra of FBC, SBC, FSBC, RBC and BC.

Raman spectroscopy was also adopted to characterize these samples particularly the carbon structure. Optical micrographs of selected samples are collected and shown in Figure S9. As shown in Figure S9f, the ISSA residue contained transparent silica grains which could be covered by a red surface due to the presence of iron oxides. The Raman spectrum of the ISSA residue (Figure 5-3) indicates the presence of hematite (peaks at 220 cm^{-1}, 290 cm^{-1}, 402 cm^{-1}, 493 cm^{-1}, 601 cm^{-1} and 1315 cm^{-1}) and possibly magnetite (peak at 668 cm^{-1}) (Das and Hendry, 2011; Tadic et al., 2019) and quartz (464 cm^{-1}). After pyrolysis, only black carbon surfaces were observed in BC and FBC (Figure S9a & b), and no Fe_2O_3 peaks were detected in the Raman spectrum of FBC. As for SBC, FSBC and RBC, transparent silica surfaces were still observable (Figure S9 c, d, & e), while the majority of these silica surfaces were covered by black carbon. Raman spectra of all these

carbon surfaces in different samples were characterized by two peaks centered at around 1350 cm^{-1} and 1590 cm^{-1} corresponding to the D-band (disorder) and the G-band (graphite) due the presence of disordered graphitic carbon (Ferrari and Robertson, 2000). The intensity ratios of D-band to G-band reflecting the disorder degree of the carbon structure (Chandra et al., 2010) of these samples are summarized in Table S5. This ratio of BC was 0.85, which was higher than SBC but slightly lower than FBC, FSBC and RBC. The presence of SiO_2 improved the graphitization degree of biochar, while the introduction of Fe_2O_3 resulted in the occurrence of more defects (Aziz et al., 2022; Sun et al., 2019). The D-band to G band ratios of FBC and RBC were still around 0.86 which indicated their relatively high degree of graphitization and electron conductivity (Zhao et al., 2020).

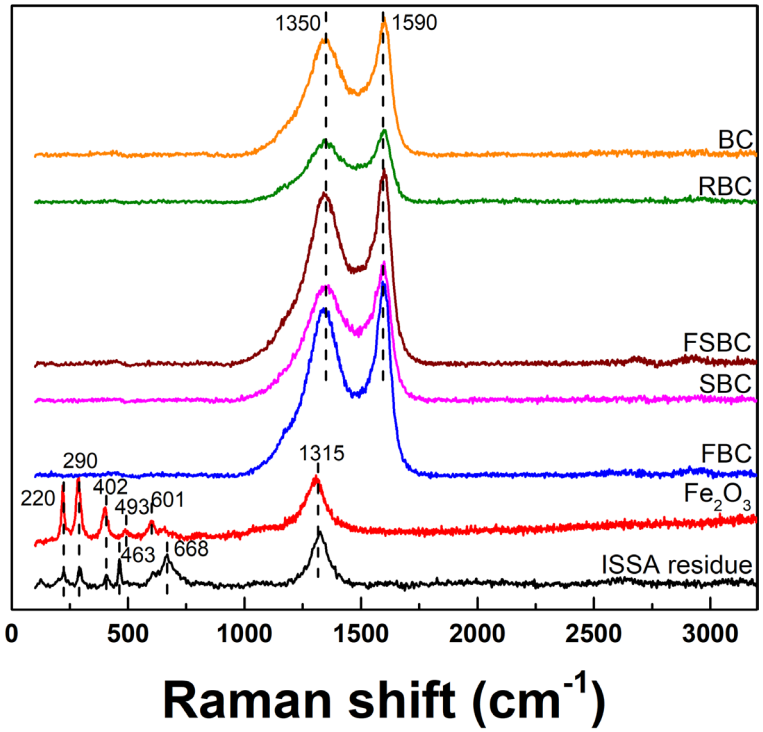

Figure 5-3 Raman spectra of selected samples.

Surface functional groups (hydroxyl, phenolic, carboxyl) are reported to play an important role in the removal of heavy metals by biochars (Amen et al., 2020). As shown in the FTIR spectra in Figure 5-4, the broad peak centered around 3440 cm^{-1} due to the presence of the -OH was observed in all samples. All the samples also exhibited a peak centered at 1629 cm^{-1} due to the stretching vibration of C=C bonds in aromatic carbons (Sun et al., 2019). It was expected that featured vibration peaks of BC produced in this study was not abundant due to the relatively high pyrolysis temperature. While peaks centered at 1100 cm^{-1}, at 800 cm^{-1} and at 473 cm^{-1} attributed to vibration of Si-O-Si were present in FSBC, SBC and RBC due to introduction of silica (Zhao et al., 2019). Oxygen containing surface functional groups particularly quinoid and phenolic groups and graphitic carbon are associated with electron transfers in biochars (Zhao et al., 2020). The lack of quinoid/phenolic groups in FBC and RBC indicated that graphitic carbon could play an important role in mediating the electron transfer process in these samples, thus influencing the removal of As(III) and As(V).

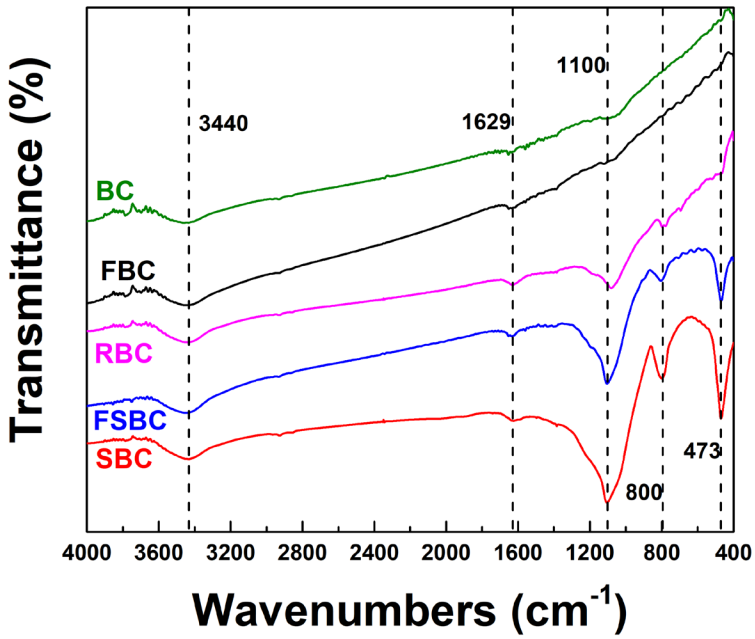

Figure 5-4 FTIR spectra of FBC, SBC, FSBC, RBC and BC.

The XPS survey spectrum of BC (Figure S10) shows the presence of C1s, O1s and Si2p, whereas Fe2p was also found in the survey spectra of FBC and RBC. The high-resolution C1s spectra of FBC and RBC (Figure 5-5) comprised five peaks corresponding to SiC at 283.0 eV (Gupta et al., 2014), sp^2 carbon at 284.5 eV, sp^3 carbon at 285.5 eV, C-O at 286.5 eV, and C=O at 288.5 eV (Lu et al., 2018). The sp^2 carbon dominated in BC (65.6%) indicating its relatively high graphitization degree, which was further increased to 71.8% and 67.1% in FBC and RBC respectively. While the sp^3 carbon accounted for 18.9% of the total carbon in BC, which was reduced to 9.5% and 12.3% in FBC and RBC respectively. This result was consistent with the characterization results from Raman spectroscopy, and the transformation of sp^3 carbon to sp^2 carbon could be attributed to the presence of Fe species in the pyrolysis process occurred under a relatively high temperature (Lesiak et al., 2018; Ma et al., 2020). As sp^2 carbon in carbon materials plays an important role in the electron transfer process (Wang et al., 2019), the lower sp^2 carbon content in RBC indicated its poorer electron transfer capacity compared to FBC. The Si2p spectra of these samples showed the presence of SiO_2, aluminosilicate, and Si-O-C/SiO_x and SiC with the corresponding characteristic peaks centered at 103.5, 102.7, 102.0 eV and 100.0 eV (Zama et al., 2018). The high resolution Fe2p spectra of FBC and RBC (shown in Figure 5-9) are comprised of Fe(0) (peaks at 706.7 eV and 719.8 eV) , Fe(II) (peaks at 709.4 and 723.0 eV), and Fe(III) (peaks at 711.0 eV and 724.6 eV) which indicated the oxidation of ZVI (Cho et al., 2019; Jia et al., 2018; Tang et al., 2017). The Fe(0) contents in FBC and RBC were similar and accounted for around 10% of the total iron. While Fe(III) content was 48% in FBC, which was dropped to around 32% in RBC indicating reduced surface passivation of ZVI in RBC compared to FBC.

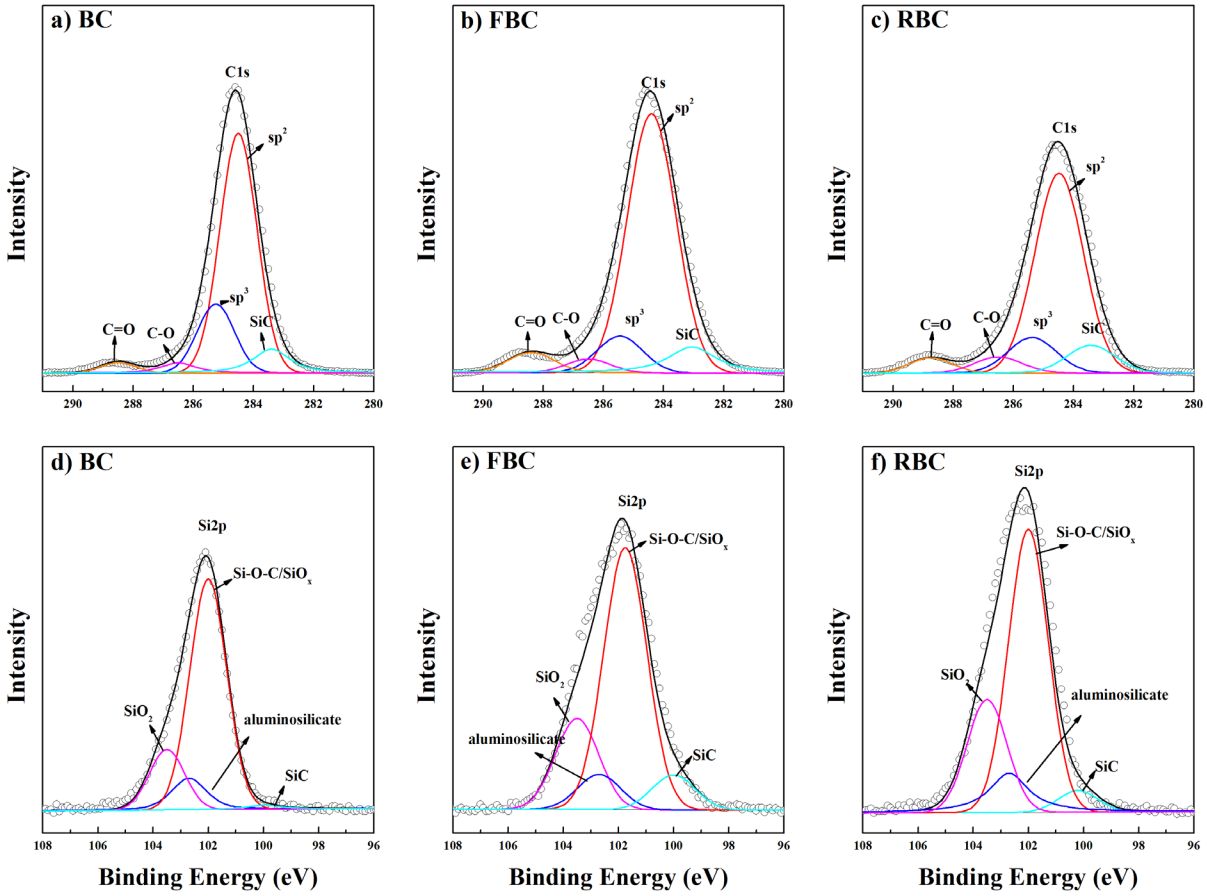

Figure 5-5 XPS C1s spectra of a) BC, b) FBC and c) RBC, and Si2p XPS spectra of d) BC, e) FBC and f) RBC.

5.2.2 Batch As(III)/As(V) adsorption experiments

1) Effect of pH on As(III) and As(V) adsorption

The As(III)/As(V) removal performance by all the samples were compared and the results are shown in Figure 5-6. BC and SBC demonstrated negligible As(III) and As(V) adsorption capacities at pH values of 3.0, 6.0 and 9.0. In comparison, RBC, FBC and FSBC showed significantly higher As(III) and As(V) adsorption capacities. The enhanced adsorption capacities of FBC, FSBC and

RBC were attributed to better textural properties (Table S3) and the introduction of active iron minerals e.g., ZVI. Moreover, FBC, FSBC, and RBC all demonstrated the highest removal capacities towards As(III) and As(V) when the solution pH was around 3.0. An increase in the solution pH reduced the removal of As(III) and As(V) by all these samples. Comparatively, the increase of pH had the most detrimental effect on the removal of arsenic by RBC, which resulted in its As(III) and As(V) adsorption capacities reduced from 15.28 and 19.13 mg/g at pH 3.0 to around 0.22 and 0 mg/g at pH 9.0, respectively. While FBC still showed relatively good adsorption capacities towards As(III) and As(V) at 10.86 and 4.93 mg/g when the initial solution pH was 9.0.

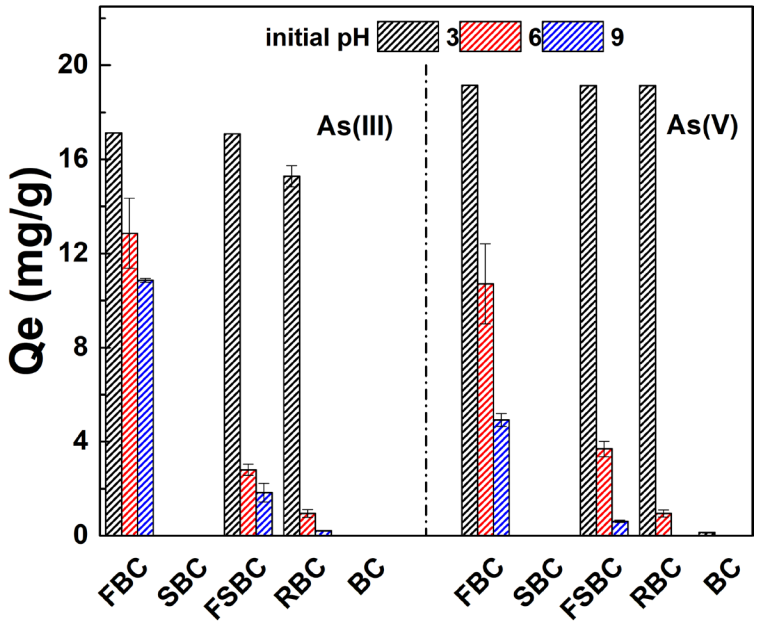

Figure 5-6 Comparison of As(III)/As(V) adsorption performance by different samples (initial concentration: As(III) = 20 mg/L, As(V): 20 mg/L; initial pH: 3, 6 and 9; time: 24 h).

Changes in solution pH can alter both the surface properties (e.g., surface charge) of the sorptive media, as well as the species of As(III) and As(V) in the aqueous solution, thus changing the

adsorption performance (Vithanage et al., 2017). As shown in Figure S11, addition of all materials led to an increase in the solution pH from 3.0 to the range of 3.0~6.0 all below the corresponding pH_{PZC} value (shown in Table 5-1). As shown in Figure S12, As(III) is present predominantly as the neutral H_3AsO_3 ($pK_a = 9.2$) at pH < 9.2, and the $H_2AsO_3^-$ fraction increases with increasing pH and dominates (>80%) at pH > 9.8. While As(V) exists as $H_2AsO_4^-$ and $HAsO_4^{2-}$ within pH range from 4 to 10. The higher As(V) removal rates of by FBC, FSBC and RBC at initial pH 3.0 (final pH around 4.0~6.0) could be associated with the electrostatic attraction. In addition, a low pH solution environment facilities the dissolution of the passivation layer on ZVI surface and accelerates its corrosion which can produce lepidocrocite, magnetite and/or maghemite beneficial to the removal of As(III) and As(V) (Wu et al., 2017).With an increase in solution pH, the surfaces of FBC, FSBC and RBC deprotonated and became negatively charged that generated a repulsion force and hindered the attachment of As(V) onto the adsorbent's surface. Increase in solution pH value also contributed to the precipitation of iron which resulted in the passivation of ZVI surface thus impeding the removal of As(III) and As(V) by these iron-biochar composites containing ZVI (Liu et al., 2021). It is interesting to find that RBC always resulted in a lower equilibrium solution pH compared to that of FBC when the initial solution pH was the same. At pH 9.0, FBC still retained some adsorption ability towards As(III) and As(V), while on the contrary, RBC barely removed As(III) and As(V) which could be attributed to the leaching of reactive silica from RBC and this will be discussed in the following section.

2) Adsorption kinetics

Study of the adsorption rates is important since it determines the suitable design of sorption units in practice (Dou et al., 2013). The effect of time on As(III) and As(V) removal by FBC, FSBC and RBC at different initial solution pH values are shown in Figure 5-7. FBC, FSBC and RBC all

showed obviously faster removal rates of As(III) and As(V) at pH 3.0 than at pH 6.0. For instance, the time needed to reach adsorption equilibrium of As(V) for FBC, FSBC and RBC were all around 30 min at pH 3.0, which were increased to 10 h at pH 6.0. The adsorption kinetic data were then fitted by the PFO and the PSO kinetic models, and the fitted curves and the corresponding parameters are shown in Figure S13 and Table S6 respectively. All the kinetic data could be better described by the PSO kinetic model than PFO kinetic model due to the higher correlation coefficient R^2 (>0.99) and better estimated Q_e values, which were similar to the fitting results from other studies (Bakshi et al., 2018; He et al., 2018).

The intra-particle diffusion model was further applied to understand the adsorption mechanisms and rate-determining step (Tran et al., 2017). The fitted curves and the corresponding parameters are shown in Figure S14 and Table S7, which roughly include 2 regions indicating that the adsorption process was governed by multistep mechanisms. The first region was featured by relatively steeper slopes for all fitted curves which revealed that the external diffusion of As(III)/As(V) was the rate limiting step (Dou et al., 2013; Qi et al., 2015). The second region with a lower slope indicated intraparticle diffusion was rate limiting which was governed by the intraparticle diffusion in mesopores/micropores of the adsorbent (Dou et al., 2013; Qi et al., 2015). Overall, the presence of silica in the ISSA residue showed distinct effects on the removal rates of As(III) and As(V) by RBC. An acidic environment resulted in higher adsorption rates for both FBC and RBC compared to a neutral environment largely due to the enhanced corrosion of ZVI surface. While longer time was needed for RBC in achieving the equilibrium for As(III) removal at pH 3.0 compared to FBC, which could be due to their lower surface area compared to FBC.

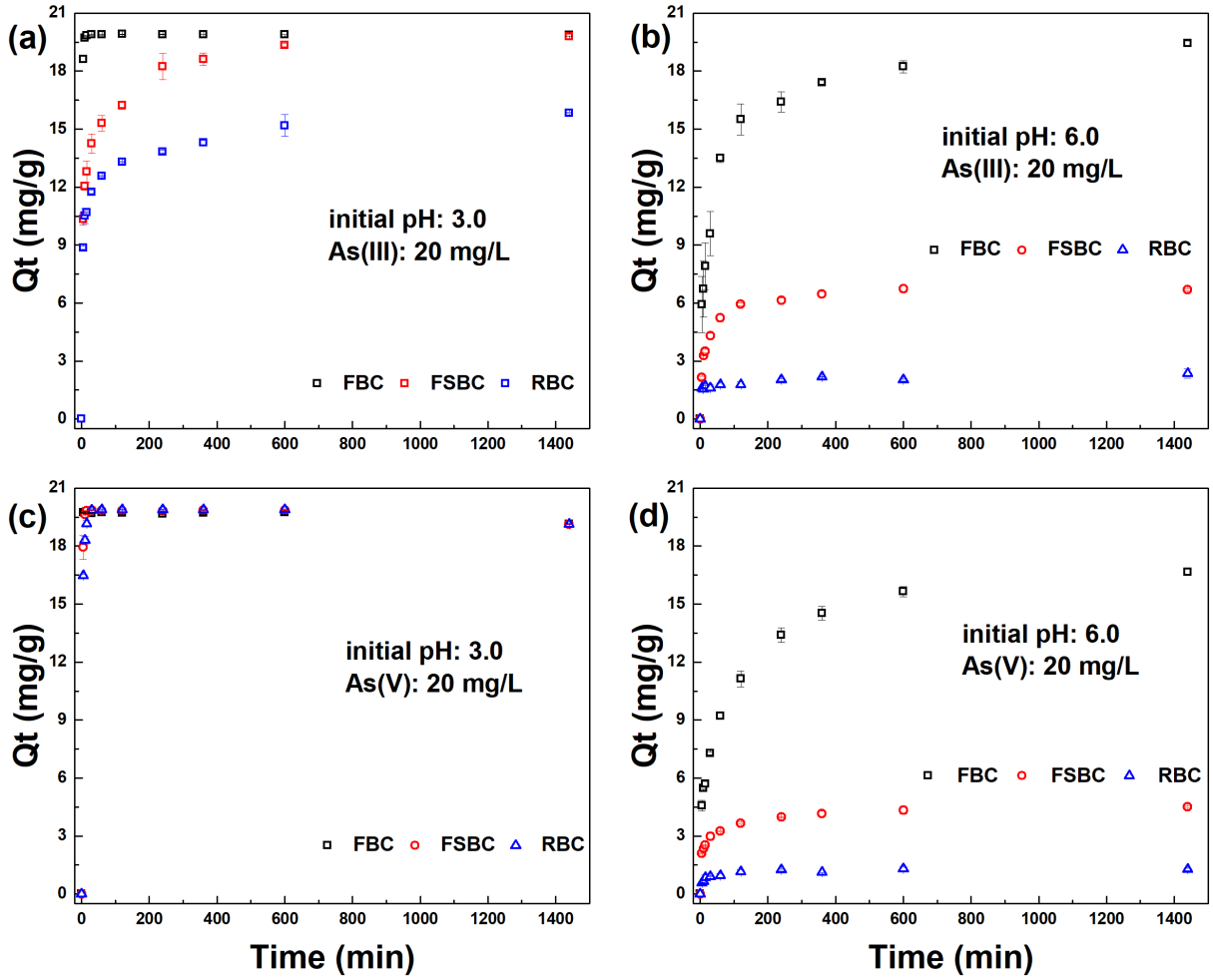

Figure 5-7 Effect of time on As(III)/As(V) removal by FBC, FSBC and RBC (initial As(III)/As(V) concentration: 20 mg/L, initial pH: 3.0/6.0, time: 24 h).

3) Adsorption isotherm

Adsorption isotherm is often used to investigate the interaction between adsorbates and adsorbents and can help in designing the adsorption process (Dou et al., 2013). The experimental data and the fitted curves with the corresponding parameters are shown in Figure 5-8 and Table S8. As indicated by the correlation coefficient R^2 of the fitting, adsorption of As(III) by FBC, FSBC and RBC at

pH 3.0 were better described by the Langmuir model, while their adsorption data towards As(V) were better fitted by the Freundlich model at the same solution pH. The values of n were all greater than 1 suggesting both As(III) and As(V) could be favorably adsorbed by FBC, FSBC and RBC at solution pH 3.0 (Tran et al., 2017). At pH 6.0, the Langmuir model better fitted the experimental data for As(III) and As(V) adsorption by FBC, FSBC and RBC. The maximum As(III) adsorption capacities by FBC, FSBC and RBC were 100.30, 28.79 and 17.44 mg/g when the initial solution pH was 3.0, the corresponding maximum adsorption capacity dropped to 42.40, 14.37 and 10.67 mg/g when the initial solution pH was increased to 6.0. Similarly, higher As(V) adsorption capacities were observed for FBC (264.45 vs 91.22 mg/g), FSBC (89.74 vs 36.76 mg/g) and RBC (57.56 vs 2.88 mg/g) at pH 3.0 than at pH 6.0. Given the negligible As(III) and As(V) adsorption capacities by BC and SBC, the maximum adsorption capacities of FBC and RBC were further normalized to the Fe content and compared to other iron-biochar composites as shown in Table S9. The results showed that the iron utilization efficiencies for the removal of As(III) and As(V) were reduced with the presence of silica and such a negative effect was more obvious at pH 6.0 than at pH 3.0.

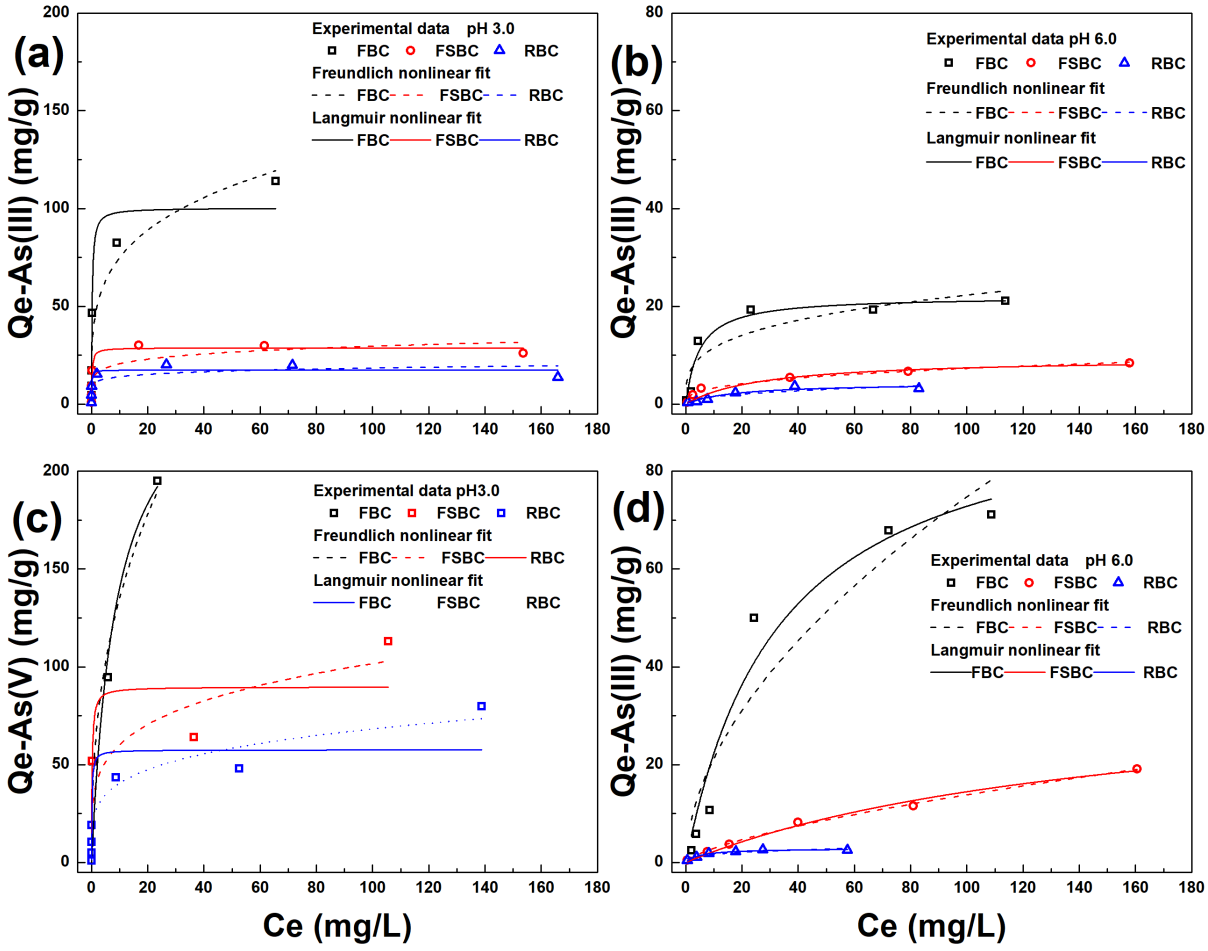

Figure 5-8 Adsorption isotherm for As(III) at pH 3.0 (a) and 6.0 (b), and As(V) at pH 3.0 (c) and 6.0 (d)onto FBC, FSBC and RBC.

5.2.3 Sorption mechanisms

To understand the interactions between As(III)/As(V) with FBC/RBC, SEM-EDX, Raman spectroscopy, XRD, FTIR and XPS were conducted before and after As(III)/As(V) removal. As shown in Figure S15, after As(III) and As(V) removal, small precipitates on the surfaces of FBC and RBC were observed. The EDX analysis confirmed these small precipitates were rich in Fe and O with some As indicating the important role of iron in the removal of As(III) and As(V) by both

FBC and RBC. As further observed in the optical micrographs from Raman spectroscopy, yellowish brown precipitates were found on surfaces of FBC and RBC (Figure S16). The corresponding Raman spectra of these precipitates in FBC after both As(III) and As(V) removal exhibited peaks centered at 250 cm^{-1}, 377 cm^{-1} and 530 cm^{-1} due to the formation of lepidocrocite, while ferrihydrite with broad peaks centered around 720 cm^{-1} and 350 $cm^{-1}$was found in the Raman spectra of RBC after As(III) and As(V) removal (Gunawardana et al., 2018; Li and Hihara, 2015). The XRD pattern of FBC after As(III) removal also showed the presence of lepidocrocite after As(III) removal (as shown in Figure S16). While the lack of featured peaks of ferrihydrite in XRD spectra of RBC after As(III) and As(V) removal indicated its X-ray amorphous nature which might be associated with the dissolved reactive silica (shown in Table S10) from RBC hindering the formation of ferrihydrite (Anderson and Benjamin, 1985). In addition, reactive silica can inhibit the corrosion of ZVI possibly due to the formation of a silica (gel) film on the iron surface. It can also compete with As(V) and As(III) for adsorption sites by forming strong bonds with iron (hydr)oxides, thus decreasing the arsenic removal (Sun et al., 2016; Zhang et al., 2004). As adsorption/co-precipitation with iron oxyhydroxides played an important role for As(III) and As(V) removal via the formation of inner sphere complexes (Zhang et al., 2004). The dissolution of reactive silica from RBC resulted in the reduced iron utilization efficiency for both the removal of As(III) and As(V) compared to FBC.

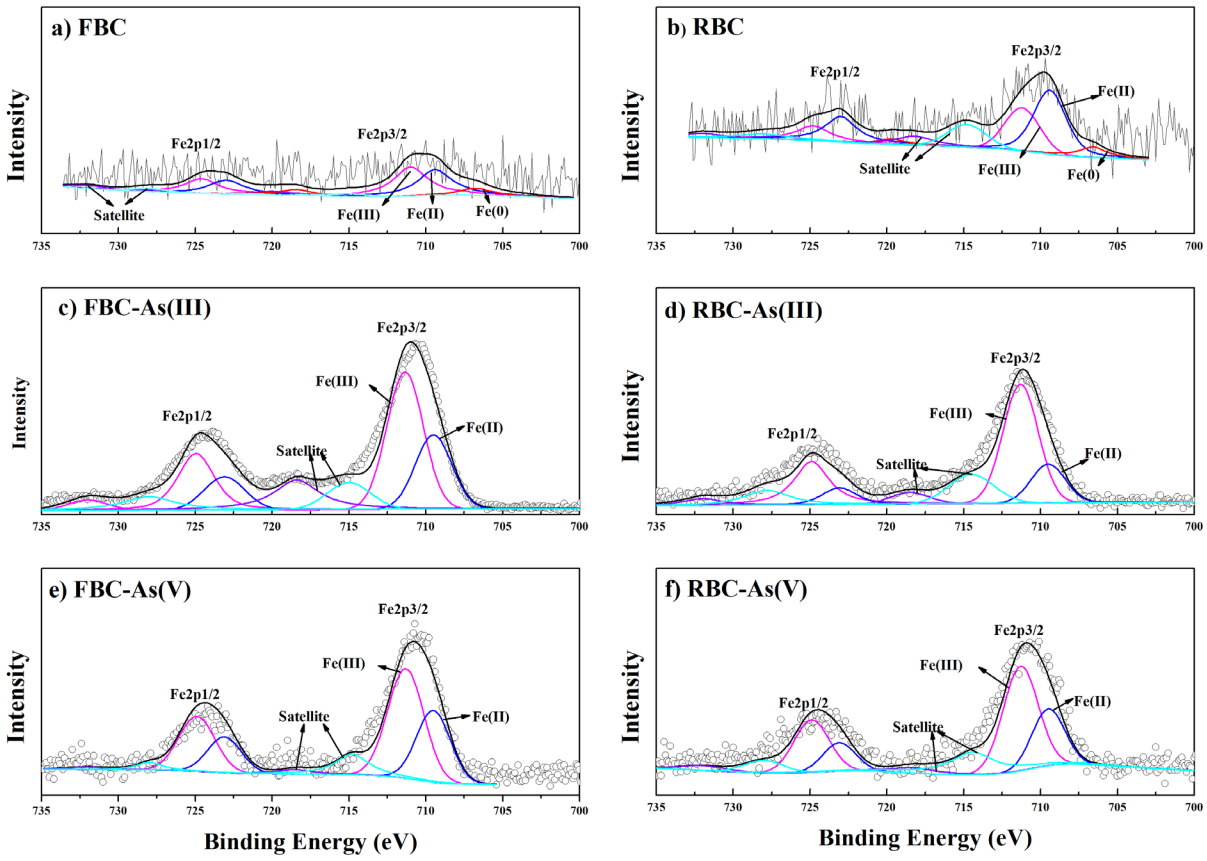

Figure 5-9 XPS Fe2p spectra of FBC and RBC before and after As(III) and As(V) removal.

The high resolution Fe2p spectra of FBC and RBC after As(III) and As(V) removal are shown in Figure 5-9. Only Fe(II) and Fe(III) were observed on surfaces of FBC and RBC, which indicated the oxidation of ZVI after the removal of As(III) and As(V). As shown in Figure 5-10, both As(III) (44.2 eV) and As(V) (45.5 eV) existed on surface of FBC and RBC after removal of As(III) and As(V) due to redox reactions between ZVI and As(III)/As(V) which were widely documented for As removal by iron-biochar composites (Hu et al., 2015). The percentages of As(V) to total As were 62% and 48% after removal of As(III) by FBC and RBC, which changed to 54% and 61% respectively after removal of As(V). This result could be associated with the higher electron

transfer capacity of FBC compared with RBC, thus resulting in higher oxidation and reduction degree during the removal of As(III) and As(V) respectively (Liu et al., 2020).

Overall, both non-normalized and Fe-content normalized adsorption capacities of RBC towards As(III) and As(V) were lower than that of FBC. This could be due to (i) the formation of iron silicon (as shown in Figure 5-2) at the expense of ZVI or magnetite during the co-pyrolysis process which lowered the iron utilization efficiency for arsenic removal, and (ii) the leaching of reactive silica from RBC reduced its removal performance towards As(III) and As(V) particularly at pH 6.0. However, RBC still exhibited relatively good adsorption capacities towards As(III) and As(V) from wastewaters under the optimal reaction conditions compared to other iron-biochar composites (Table S9). Moreover, some silica rich biochars derived from rice husk and sewage sludge were reported to act as alternative Si fertilizers for plant cultivation due to the release of reactive silica (Tao et al., 2022). And the release of reactive silica from a silicon biochar was also beneficial to prevent the uptake of As(III) into spinach contributing to promoted plant growth (Zama et al., 2018). It is therefore expected that RBC could also have the potential to be applied in As-contaminated soil to achieve the remediation of soil and the promotion of plant growth. Overall, it is considered quite appealing to produce iron-biochar composites from the ISSA residue and waste biomass to achieve the upcycling of solid waste into useful materials.

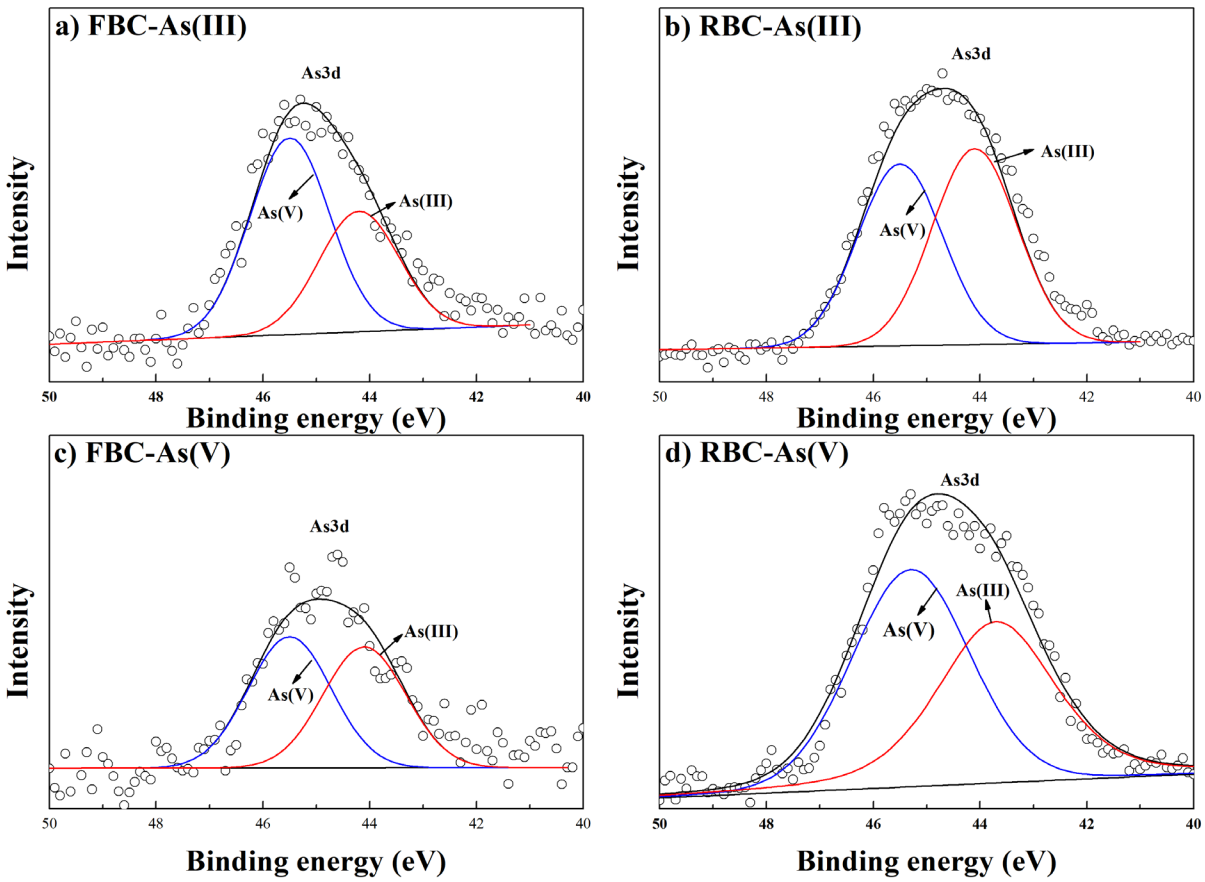

Figure 5-10 XPS As3d spectra of FBC and RBC after As(III) and As(V) removal.

5.3 Summary

In this chapter, RBC containing ZVI was fabricated from co-pyrolysis of the P-recovered ISSA and peanut shell at 850°C. Particularly, the role of silica in the P-recovered ISSA on properties of the produced RBC relevant to As(III) and As(V) removal from aqueous solutions were thoroughly investigated and compared with FBC. The adsorption capacities towards As(III) and As(V) by RBC were all lower than those by FBC, which can be attributed to the presence of silica that reacted with iron and produced iron silicon at the expense of producing ZVI or Fe_3O_4 with a high affinity for As(III) and As(V) during the co-pyrolysis process. Furthermore, the presence of silica

increased the leaching of reactive silica from RBC during the adsorption process, thus hindering the removal of As(III) and As(V) by affecting the ZVI corrosion products and competing with arsenic for active adsorption sites. Irrespective of these side effects, RBC was still considered a promising candidate for the removal of As(III) and As(V) from aqueous solutions because of its high efficacy for arsenic removal under the optimized reaction conditions as well as its contribution to waste recycling.

CHAPTER 6 PRODUCTION OF SORPTIVE GRANULES AND UPCYCLING IN CEMENT MORTAR

6.1 Introduction

Besides enhanced pollutant removal ability, modification of biochar by iron minerals can endow the end iron-biochar magnetism thus facilitating the separation of the powdery medium from aqueous solutions. However, such a favoring property is significantly weakened when P-recovered ISSA is reutilized as a supplementary iron source due to the dominant existence of silica in the P-recovered ISSA. Chapter 5 and Chapter 6 have shown promising As(III), As(V) and Cr(VI) removal from aqueous solutions by iron-biochar composites synthesized with from the P-recovered ISSA residue and biowaste. To further facilitate the practical application, and the sustainable disposal of the spent sorptive media, in this chapter, kilogram-scale production of millimeter-sized granules was obtained via thermal treatment of green bodies made solely from waste i.e., P-recovered ISSA, peanut shell and waste bentonite. Waste bentonite was incorporated to increase the self-binding property of the mixture containing the P-recovered ISSA and peanut shell as optimized in the previous chapter, and to endow strong enough mechanical strength to the end products targeting at ensuring the durability of the granules for applications in construction materials. Moreover, the inclusion of peanut shell can give the end granules a low density, making these granules LWA that can replace natural river sand, an important natural resource, in construction materials. By doing so, a close-loop recycling of ISSA is achievable.

This chapter aims to produce LWA solely from the P-recovered ISSA, peanut shell, and waste bentonite, which can then be adopted for removal of heavy metals from aqueous solutions. More importantly, the spent LWA can be environmental soundly upcycled in construction materials. The

specific targets of this chapter include (i) optimizing the optimal production conditions (e.g. mix proportion of ISSA, biomass and bentonite, heating condition) to endow the end LWA with both good mechanical properties and adsorption capacities for multi kinds of heavy metal(loid)s including As(V), Cr(VI), Cu(II) and Pb(II); (ii) studying the metal adsorption performance and mechanisms; (iii) investigating the suitability to reuse and recycle the spent LWA in making lightweight cement mortar.

6.2 Results and discussion

6.2.1 Optimization of preparation condition for IPBG

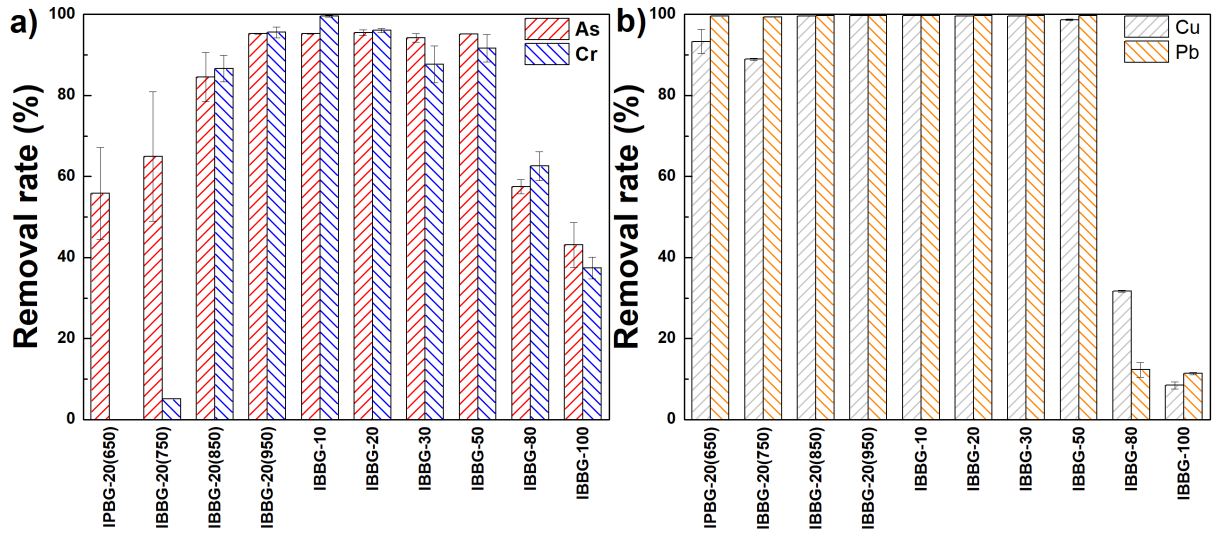

Figure 6-1 Comparison of heavy metal(loid) removal rate in binary-metal systems (a: As and Cr with the same concentration at 10 mg/L, b: Cu(II) and Pb(II) with the same concentration at 10 mg/L; pH 3.0, 24 h) by IPBGs.

IPBGs prepared from different conditions were first compared regarding their As(V), Cr(VI), Cu(II) and Pb(II) removal rates from aqueous solutions. As shown in Figure 6-1a, when the ratio

of waste bentonite to the total materials was fixed at 20% (IPBG-20), an increase in the heating temperature was conducive to the removal of As(V) and Cr(VI). Specifically, increasing the temperature from 650°C to 1050°C had the As(V) removal rate strikingly increased from 55.8% to 95.2%. Negligible Cr(VI) was removed by IPBG-20(650), while around 99.5% of Cr(VI) was removed from the solution by IPBG-20(1050). On the other hand, IPBG-20 heated from 650°C to 1050°C all had excellent removal rates towards Cu(II) and Pb(II) (as shown in Figure 6-1b). When the heating temperature was fixed at 1050°C, the fabricated IPBG derived from raw materials with a bentonite ratio ≤50% all showed similar removal rates for As(V) (>94.2%), Cr(VI) (>84.7), Cu(II) (>98.7%) and Pb(II) (>99.5%). While a further increase in the use of waste bentonite substantially reduced the corresponding removal rate to less than 57.5%, 62.5%, 31.7%, and 12.3%.

Table 6-1 Selected physical and chemical properties of IPBGs.

Sample	IPBG-10	IPBG-20	IPBG-30	IPBG-50	IPBG-80	IPBG-100
Total organic carbon[a] (%)	14.60	12.72	10.29	6.84	1.41	0.02
Total Fe[b] (%)	7.19	6.89	6.54	5.66	4.11	2.46
BET surface area (m^2/g)	63.82	55.46	53.69	29.89	12.65	0.40
Total pore volume (cm^3/g)	0.0586	0.0535	0.0558	0.0346	0.0103	0.0008
Micropore volume	0.0233	0.0191	0.0188	0.0097	0.0047	-
Average pore diameter (nm)	9.02	8.46	9.38	9.94	7.63	12.94
Bulk density	0.60	0.75	0.80	1.21	1.47	2.53
Skeletal density (g/cm^3)	2.70	2.76	2.78	2.73	2.67	

[a]: determined by a total carbon analyzer; [b]: sample digested by HNO_3 + $HClO_4$.

Moreover, both a lower ratio of waste bentonite in the raw mixture and a lower final heating temperature were detrimental for the successful formation of strong enough IPBGs. For IPBG-10, some of the granules were broken after the adsorption equilibrium (shaking at 200 rpm for 24 h), some maintained the shape after the adsorption equilibrium but were easily broken by squeezing. IPBGs with some resistance to breakage (bentonite ratio ≥20%) were further tested for compressive strength and BET surface area. When the bentonite ratio was 10%, the produced IPBG had the highest BET surface area at 63.82 m^2/g but were easily broken. As shown in Figure 6-2, the BET surface area and the compressive strength of the IPBGs decreased and increased almost linearly with the increase in the bentonite ratio. Considering both the removal performance for heavy metal(loid)s and the mechanical strength, the optimal condition to produce IPBG was therefore selected as a 50% waste bentonite ratio, and a heating program as preheating at 350ºC for 30 min followed by heating at 1050ºC for 30 min under a nitrogen atmosphere. And IPBG shown thereafter referred to the ones produced under the optimal conditions.

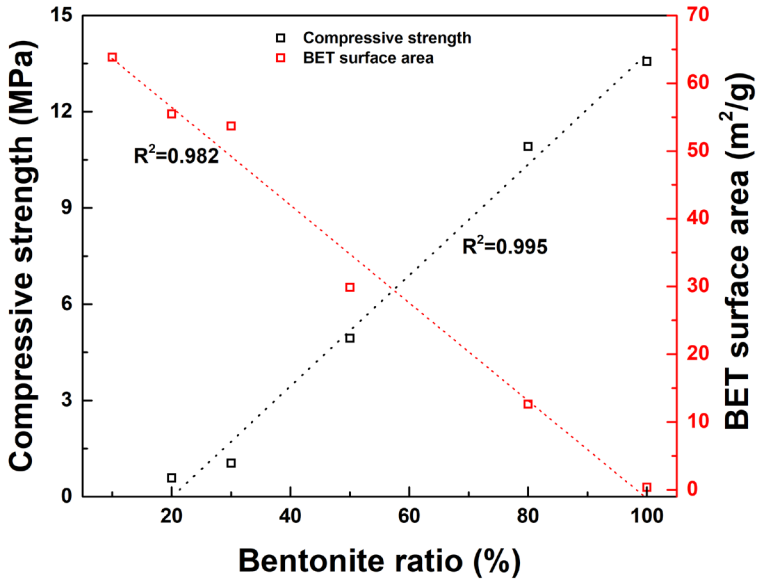

Figure 6-2 Compressive strength and BET surface areas of IPBGs produced at 1050ºC.

6.2.2 Adsorption: performance and mechanisms

1) Adsorption kinetics

Figure 6-3 shows adsorption kinetic curves for the removal of As(V), Cr(VI), Cu(II) and Pb(II) within 24 h by IPBG. IPBG could rapidly remove As(V), Cr(VI) and Cu(II) within the first 1 h, and the corresponding removal percentage was 88%, 60% and 68% respectively. The removal percentage for Pb(II) was only 31% Pb(II) at 1h, which was notably increased to 89% at 2 h. The removal rates towards these heavy metal(loid)s slowed down after 2 h and gradually reached equilibrium at 24 h. All the experimental data were further fitted by the PFO and the PSO kinetic models. The fitted curves and the estimated parameters are shown in Figure 6-3 and Table S11. The adsorption kinetic data of As(V), Cu(II) and Pb(II) by IPBG were better described by the PFO kinetic model due to the higher R^2 and lower χ^2. In addition, the calculated $Q_{e,cal}$ values were in accordance with the experimental $Q_{e,exp}$ values. The adsorption kinetic data of Cr(VI) by IPBG were better fitted by the PSO kinetic model which indicated chemisorption was the rate-determining step for the removal of Cr(VI) by IPBGs (Qiu et al., 2009). These data were further fitted by using intraparticle diffusion model to investigate different steps in the adsorption process (Dou et al., 2013; Qi et al., 2015). The fitted curves and the corresponding parameters are shown in Figure S18 and Table S12 with the fitted curves showing two linear regions. The first region, representing the external diffusion, had a significantly higher rate constant than the second region due to intraparticle pore diffusion (Dou et al., 2013; Qi et al., 2015). As also shown in Figure S19, during the removal of Cu(II) and Pb(II), the leaching concentration of Ca(II) from IPBG was

continuously increased, reflecting the ion exchange process played a role for the removal of these heavy metals (Yuan and Liu, 2013).

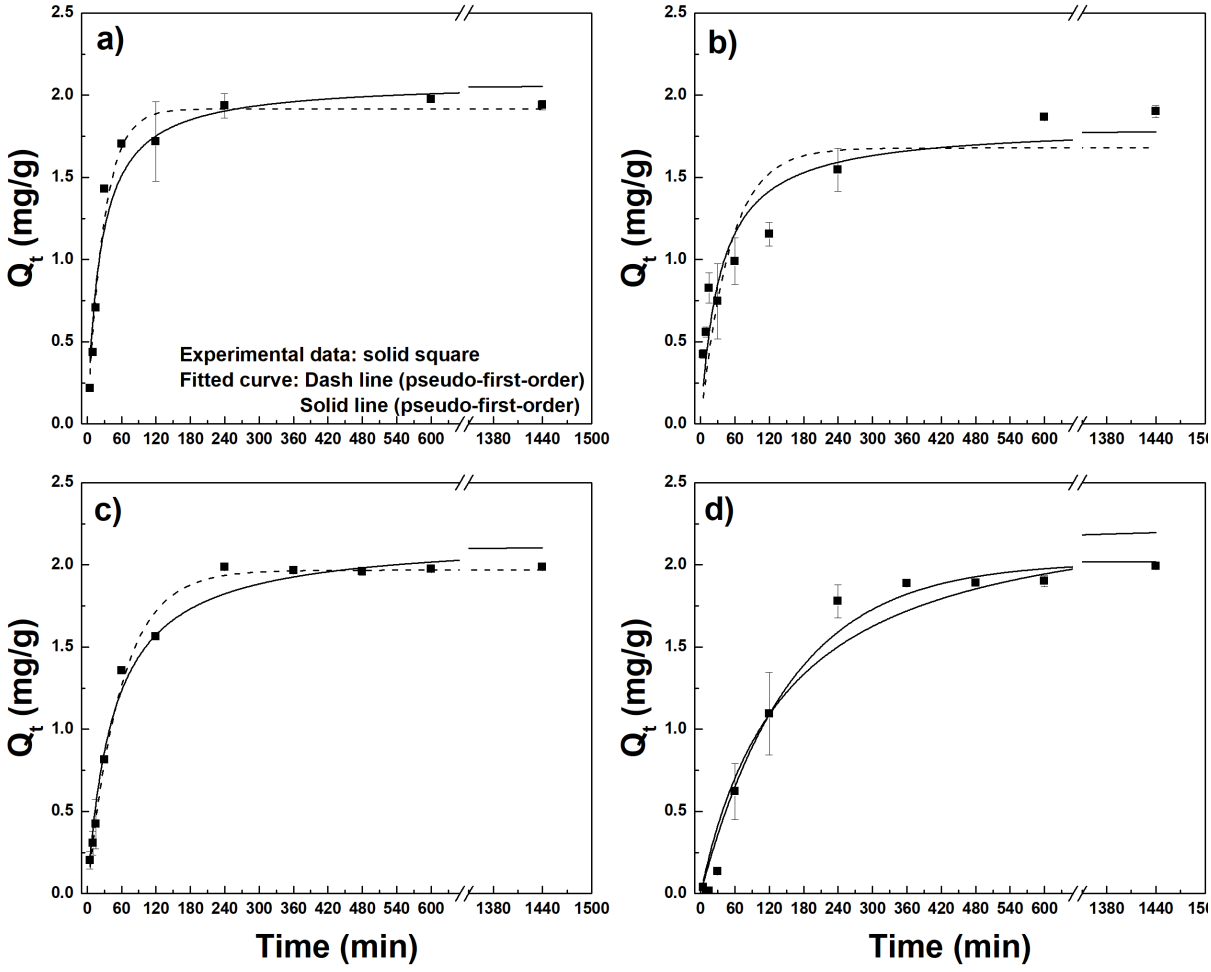

Figure 6-3 Effect of time on a) As(V), b) Cr(VI), c) Cu(II) and d) Pb(II) removal (dosage: 5g/L, initial solution pH 3.0, C_0=10 mg/L).

2) Adsorption isotherm

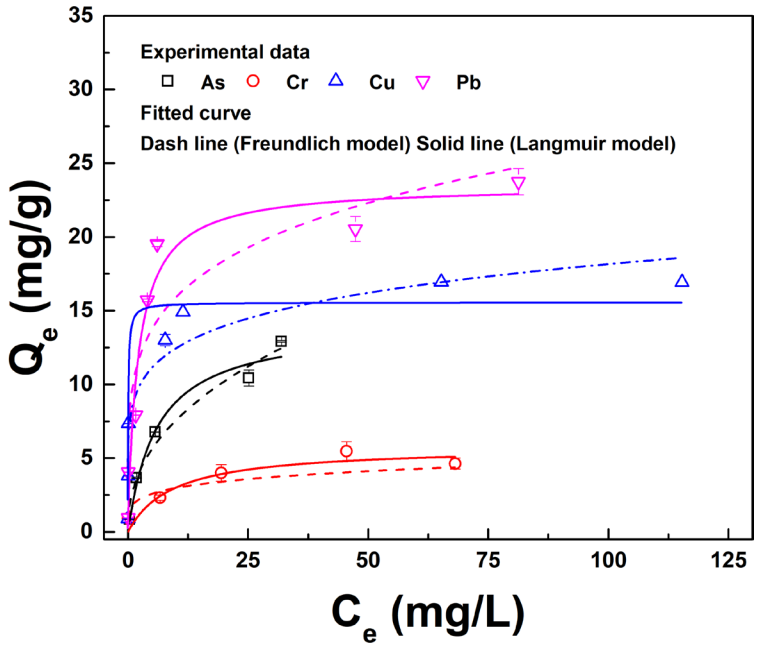

Figure 6-4 Adsorption isotherm curves of As(V), Cr(VI), Cu(II) and Pb(II) by IPBG.

The adsorption isotherm test results for As(V), Cr(VI), Cu(II) and Pb(II) are shown in Figure 6-4, which can be used to compare the conditional adsorption capacities between adsorbents and facilitate the selection of an adsorbent and the design of adsorption process (Dou et al., 2013). The removal capacities of As(V), Cr(VI), Cu(II) and Pb(II) all increased with their corresponding equilibrium concentrations due to the higher concentration gradient for ion transport leading more metal(loid)s to be attached on the surface of IPBG (Cuong et al., 2021). Both Freundlich and Langmuir isotherm models were adopted to fit the experimental data and the results are shown in Figure 6-4 with estimated parameters listed in Table S13. For the adsorption of As(V) and Cu(II), the higher R^2 and lower χ^2 based on fitting results from the Langmuir isotherm model than the Freundlich isotherm model demonstrated that the experimental data were bettered described by the former model. This indicated that the adsorption of As(V) and Cu(II) occurred on a

homogeneous surface (Dou et al., 2013; Qi et al., 2015). On the contrary, Freundlich isotherm model better described the adsorption behavior of Cr(VI) and Pb(II) by the IPBG indicating a multi-layer adsorption process might occur during the adsorption process. In addition, all the constant n values from Freundlich isotherm model were larger than 1, indicating these heavy metal(loid)s could be favorably adsorbed by IPBG. The maximum adsorption capacities for As(V), Cr(VI), Cu(II) and Pb(II) were around 14.11 mg/g, 5.79 mg/g, 14.12 mg/g and 23.52 mg/g respectively. Comparing with other adsorbents in a granular form as shown in Table S14, IPBG could be considered as an attractive adsorbent considering all its source materials coming from solid waste.

3) Heavy metal removal mechanisms

SEM images of IPBG before and after As(V), Cr(VI), Pb(II) and Cu(II) removal are shown in Figure 6-5. The fresh IPBG contained many fine pores even though large pores and irregular gaps were also observed. After the removal of As(V), Cr(V), Cu(II) and Pb(II), the surface of IPBGs were found to be covered by some yellowish brown precipitates. Line scan results also showed that the Fe-Kα intensity is relatively higher at regions near the outer surface.

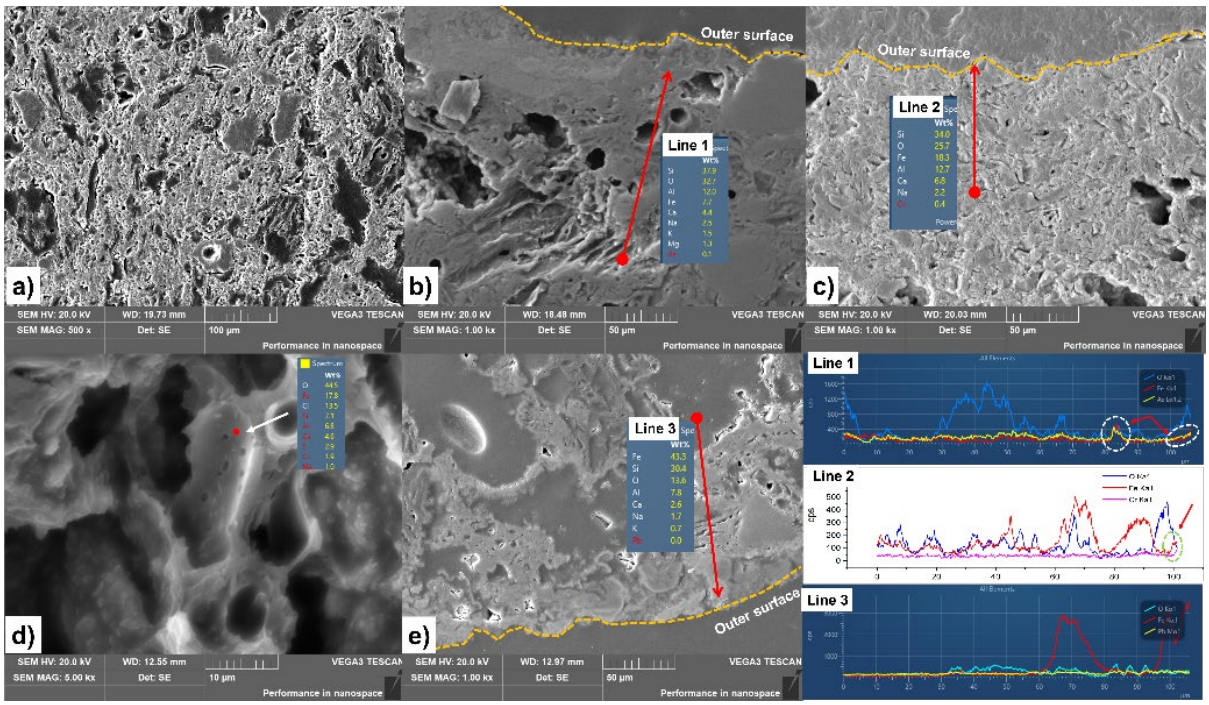

Figure 6-5 Microstructures and line scans of IPBGs before (a) and after As(V) (b), Cr(VI) (c), Cu(II) (d) and Pb(II) (e) removal.

IPBG before and after heavy metal removal were further characterized by XRD, Raman, FTIR and XPS to understand the possible mechanisms. The XRD spectra (Figure 6-6a) showed the presence of montmorillonite, quartz, and calcite in bentonite, and quartz, hematite, magnetite, leucite, and anorthoclase in the P-recovered ISSA residue. Similarly, the Raman spectra (Figure 6-6b) of the P-recovered ISSA residue and bentonite indicate the presence of quartz (Raman shift centered at around 125 cm^{-1}, 206 cm^{-1} and 464 cm^{-1}) and hematite/magnetite (675 cm^{-1}) (Das and Hendry, 2011). Peaks at 1094 cm^{-1} and 785 cm^{-1} assigning to Si-O-Si group in the FTIR spectra (Figure 6-6c) of the P-recovered ISSA residue and bentonite indicate the presence of quartz (Tokarský et al., 2013). Band at 1034 cm^{-1} in bentonite could be assigned to stretching vibrations of M-O (where

M= Si, Al) bands of silicates (Chinoune et al., 2016). Additionally, band at around 464 cm^{-1} could be assigned to the stretching vibration of Fe-O was found in the P-recovered ISSA residue and bentonite.

After heating, featured XRD peaks corresponding to calcite, hematite, magnetite, and montmorillonite disappeared in IPBG, while characteristic peaks of ZVI and albite were observed. Featured FTIR peaks at 1643 cm^{-1} and 1430 cm^{-1} corresponding stretching vibrations of water and carbonates in bentonite disappeared after thermal treatment due to decomposition of carbonates. The Fe-O band also disappeared in the FTIR spectrum of the fresh IPBG. Moreover, only black surface could be found in IPBG which was characterized by two Raman peaks centered around 1350 $cm^{-1}$and 1590 cm^{-1} indicating the generation of disordered graphitic carbon due to the carbonation of peanut shell (Ferrari and Robertson, 2000). These results indicated the reduction of iron oxides to ZVI during the thermal treatment process.

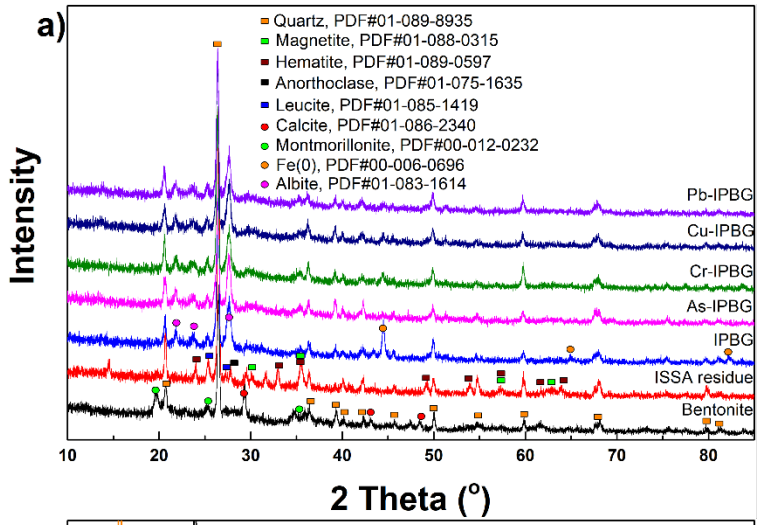
a)
Quartz, PDF#01-089-8935
Magnetite, PDF#01-088-0315
Hematite, PDF#01-089-0597
Anorthoclase, PDF#01-075-1635
Leucite, PDF#01-085-1419
Calcite, PDF#01-086-2340
Montmorillonite, PDF#00-012-0232
Fe(0), PDF#00-006-0696
Albite, PDF#01-083-1614
Pb-IPBG
Cu-IPBG
Cr-IPBG
As-IPBG
IPBG
ISSA residue
Bentonite
Intensity
10
20
30
40
50
60
70
80
2 Theta (°)

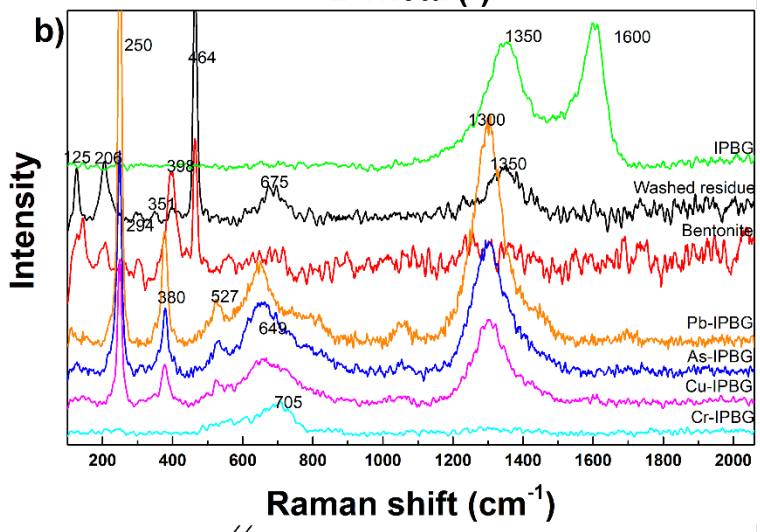
b)
250
464
1350
1600
1300
IPBG
125
206
398
675
1350
Washed residue
351
294
Bentonite
380
527
649
Pb-IPBG
As-IPBG
Cu-IPBG
705
Cr-IPBG
Intensity
200
400
600
800
1000
1200
1400
1600
1800
2000
Raman shift (cm-1)

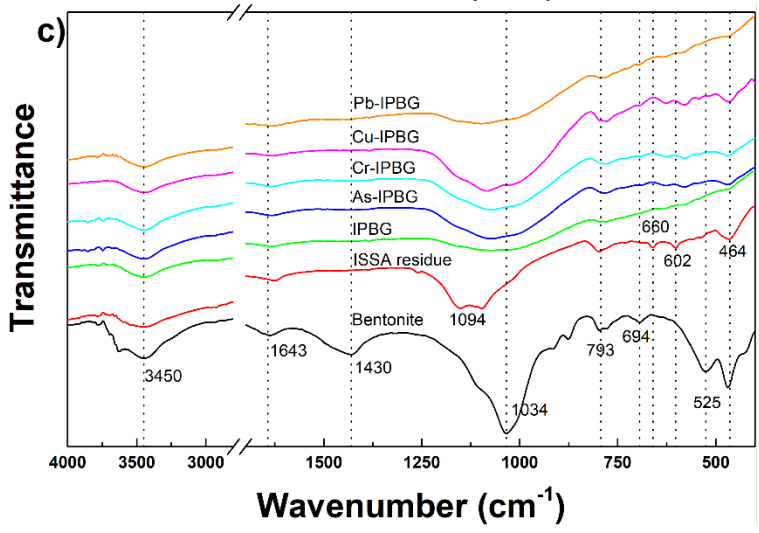
c)
Pb-IPBG
Cu-IPBG
Cr-IPBG
As-IPBG
IPBG
660
602
464
ISSA residue
Bentonite
1094
694
793
1643
1430
3450
1034
525
Transmittance
4000
3500
3000
1500
1250
1000
750
500
Wavenumber (cm-1)

Figure 6-6 XRD patterns (a), Raman (b) and FTIR (c) spectra of bentonite, ISSA residue, and IPBG before and after heavy metal removal.

After the removal of As(V), Cr(VI), Cu(II) and Pb(II), the characteristic XRD peaks corresponding to ZVI significantly reduced or even disappeared with no secondary iron (hydro)oxides or heavy metal-bearing precipitates identified probably due to their amorphous nature for all samples under a testing condition of 50 mg/L As(V), Cr(VI), Cu(II) and Pb(II) respectively. The broadening of featured peaks of a mineral might occur in the Raman spectrum once it is poorly crystallized, while the band positions are still unique (Das and Hendry, 2011). The newly formed yellowish brown precipitates after the removal of As(V), Cu(II) and Pb(II) were characterized by bands centered at around 250 cm^{-1}, 380 cm^{-1}, 527 cm^{-1}, 649 cm^{-1} and 1300 cm^{-1} which were in good agreement with previously published data associated with lepidocrocite (Das and Hendry, 2011; Hanesch, 2009). Only a broad band centered around 705 cm^{-1} associating with the presence of ferrihydrite (Das and Hendry, 2011; Hanesch, 2009) was observed in the Raman spectrum of IPBG after Cr(VI) removal. This could also be reflected from the reappearance of Fe-O in the FTIR spectra of IPBG after As(V), Cr(VI), Cu(II) and Pb(II) removal.

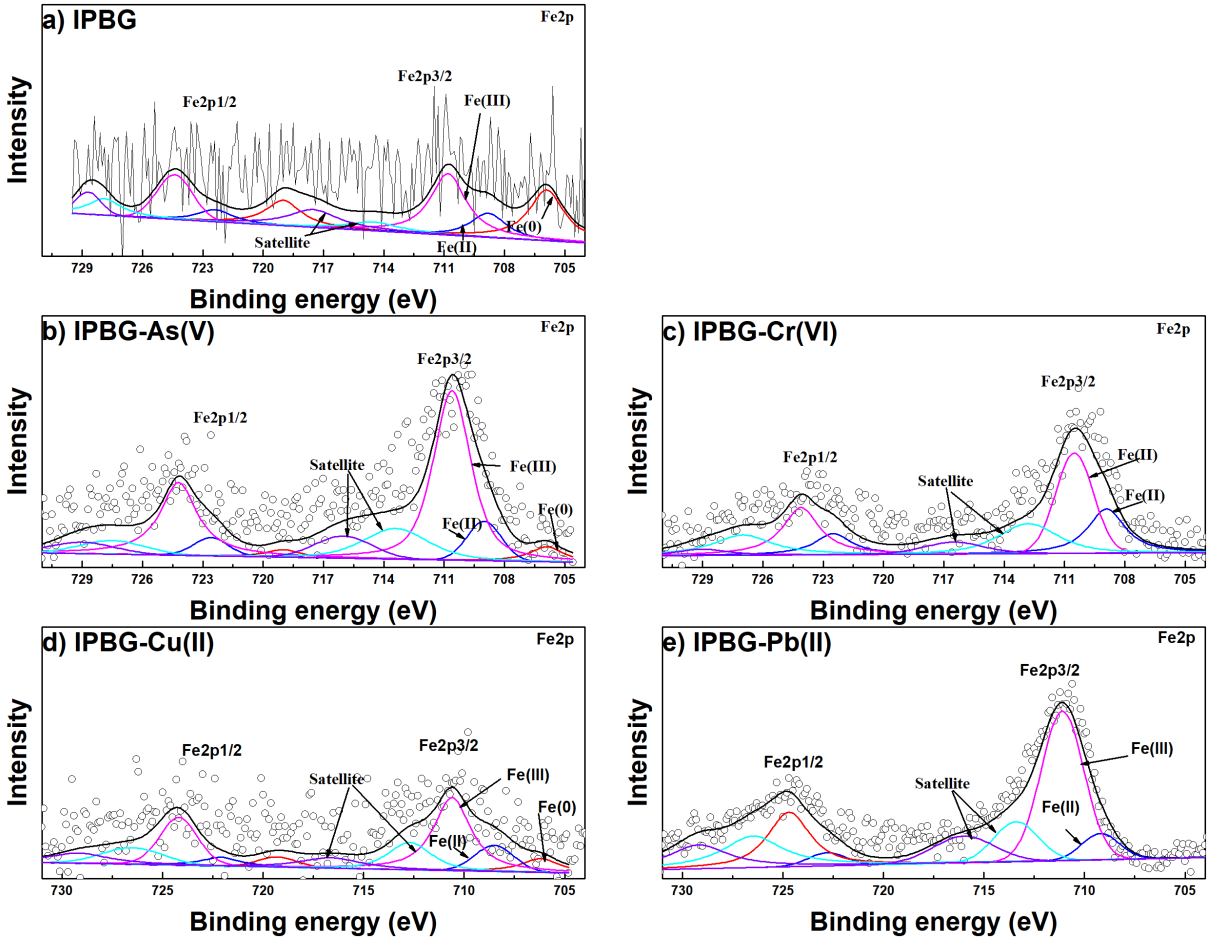

Figure 6-7 Fe2p XPS spectra of a) IPBG, and IPBG after b) As(V), c) Cr(VI), d) Cu(II) and e) Pb(II) removal.

Moreover, as shown in Figure 6-7, the Fe2p spectrum of IPBG indicates the presence of Fe(0) (peaks at around 705.9 eV, 719 eV), Fe(II) (peaks at around 708.8 eV, 722.4 eV) and Fe(III) (peaks at around 710.8 eV, 724.4 eV) (Hu et al., 2015; Zhu et al., 2017), which accounted for around 38%, 17% and 45% to the total iron respectively. The removal of As(V), Cr(VI), Cu(II) and Pb(II) had Fe(0) content significantly dropped to 7%, 14%, 0 and 0, while had Fe(III) notably increased to 79%, 68%, 62% and 87% respectively. Meanwhile, as shown in Figure 6-8, the As3d spectrum of

IPBG after As(V) removal shows the presence of 40% As(III) (peak at around 43.8 eV) and 60% As(V) (peak at around 45.3 eV) (Hu et al., 2015), Cr2p3/2 spectrum of IPBG after Cr(VI) removal indicates the presence of 68% Cr(III) (peak at around 576.5 eV) and 32% Cr(VI) (peak at around 578.4 eV) (Zhong et al., 2018), the Cu2p3/2 spectrum of IPBG after Cu(II) removal indicates the presence of 81% Cu(I) (peak at around 931.7 eV) and 19% Cu(II) (peak at around 934.5 eV) (Zhang et al., 2022), the Pb4f spectrum of IPBG after Pb(II) indicates the presence of 12% $Pb^{2+} - O$ (peaks at around 137.7 eV and 142.6 eV) and 88% $Pb(OH)_2$ (peaks at around 138.8 eV and 143.7 eV) (X. Yang et al., 2021).

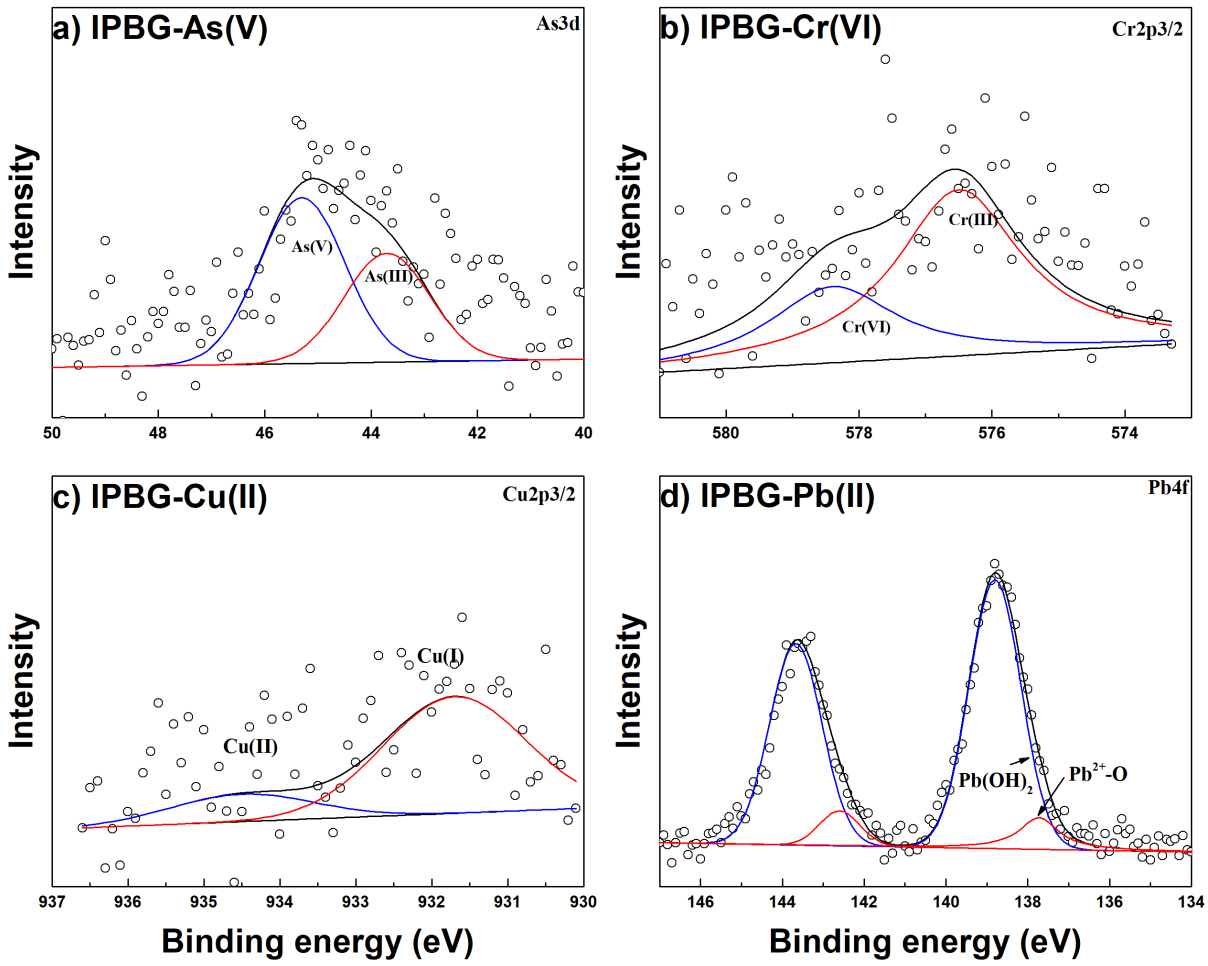

Figure 6-8 As3d, Cr2p3/2, Cu2p3/2 and Pb4f XPS spectra IPBG after a) As(V), b) Cr(VI), c) Cu(II) and d) Pb(II) removal.

Overall, a low solution pH favored the corrosion of ZVI, which generated reactive surfaces for reactions between ZVI and pollutants. During the removal process, redox reactions occurred resulting in the reduction of As(V) to As(III), or Cr(VI) to Cr(III), and the oxidation of ZVI to Fe(II) and Fe(III). The increase in the solution pH due to the corrosion of ZVI and the leaching of Ca2+ from IPBG led to the formation of iron (hydr)oxides or the co-precipitation of the heavy metals with Fe(III) (e.g., the formation of Cr(III)-Fe(III)-hydroxides) (Zhao et al., 2016). In addition, the presence of carbon matrix with good electron transfer ability could be beneficial for

the electron transfer process thus speeding up the above redox reactions, and the concurrent or subsequent precipitation reactions (L. Zhou et al., 2022). Moreover, the newly formed iron (hydr)oxides could further retain these pollutants like As and Cr via surface adsorption (Das and Hendry, 2011; Noubactep, 2015). This is also reflected from the line scan results as shown in Figure 6-5, showing that the Fe-Kα intensity is closely related to the As-Kα or Cr-Kα intensity at the outer surface of the IPBG. On the contrary, Pb(II) was removed predominantly due to precipitation because 88% of Pb was in the form of $Pb(OH)_2$ after removal. In addition, the role of ion exchange should not be ignored for the removal of both Cu(II) and Pb(II) (Figure S19).

6.2.3 Environmentally safe upcycling of spent IPBG in cement mortar

Table 6-2 shows selected properties of IPBG which is characterized by its low bulk density and therefore had the potential to be reused as LWA. Given made solely from solid waste, IPBG had the potential to be used as a one-time throw-away media in the adsorption process. When operated on a throw-away basis, the exhausted IPBG will be the principal waste produced after the adsorption process. Here, we upcycled the spent IPBG as LWA to partially replace river sand in cement mortar.

Table 6-2 Selected properties of IPBG.

Physical properties	IPBG
Water absorption (%)	38.5
Bulk density (g/cm^3)	1.21
Saturated surface dry density (g/cm^3)	1.70

Skeletal density (g/cm^3)/specific gravity	2.73
Compressive strength (MPa)	4.90

1) Mechanical properties

The effect of incorporation rate of spent IPBG on 28-day compressive strength of the prepared cement mortars is shown in Figure 6-9. It is clear from the figure that 7.5% and 15% addition of spent IPBG in cement mortars resulted in respectively a slight (2%) and significant (13%) reduction in the 28-day compressive strength of the mortar compared to the control group. The dry bulk density of mortars reduced from 2.1 g.cm^3 to 2.0 g/cm^3 when 15% of river sand was substituted by the spent IPBG.

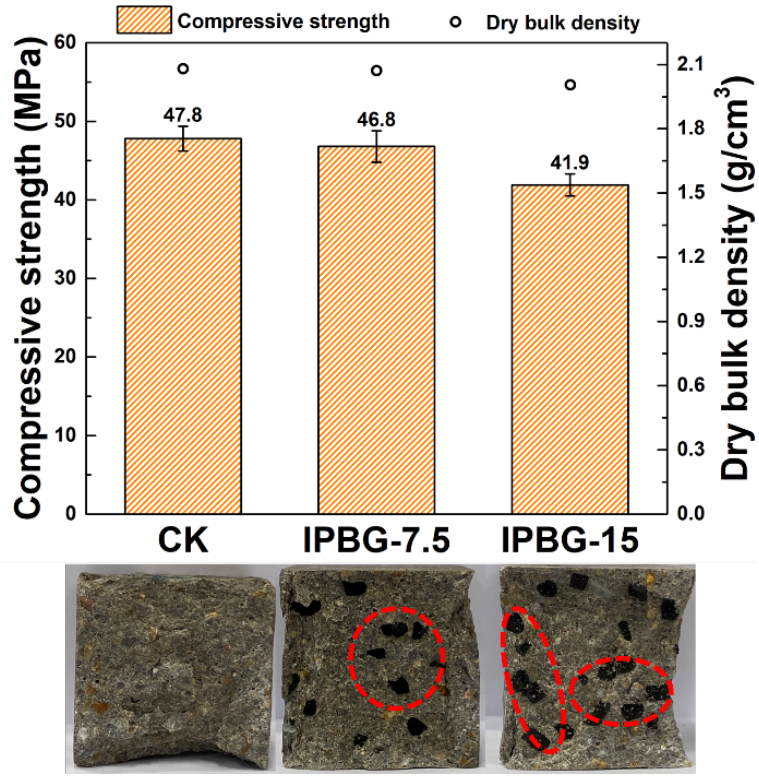

Figure 6-9 The 28-day compressive strength and density of mortar incorporating metal-loaded IPBGs.

2) TCLP

TCLP was further used to study the stabilization efficiency and evaluate the environmental safety of the obtained cement mortar. As shown in Figure 6-10, the amounts of As, Cr, Cu and Pb leached from the spent IPBG based on TCLP were respectively at 0.13, 0.45, 3.78 and 6.33 mg/L with the leaching concentration of Pb exceeding the regulatory limit according to US EPA and the Chinese national TCLP limits (both US EPA and Chinese national regulatory limits for As, Cr and Pb are 5 mg/L, meanwhile Chinese national regulatory limit for Cu is 100 mg/L) (CFR, n.d.; CN-GB, 2007). The spent IPBG were classified as hazardous materials which needed to be safely disposed.

When used as used as partial replacements for river sand at substitution ratios of 7.5% and 15%, the concentrations of these toxic elements leached from mortars were all significantly reduced compared to the spent IPBG and were lower than the TCLP regulatory limits, indicating the environment soundness of such reuse and recycling of spent IPBG in cement mortar.

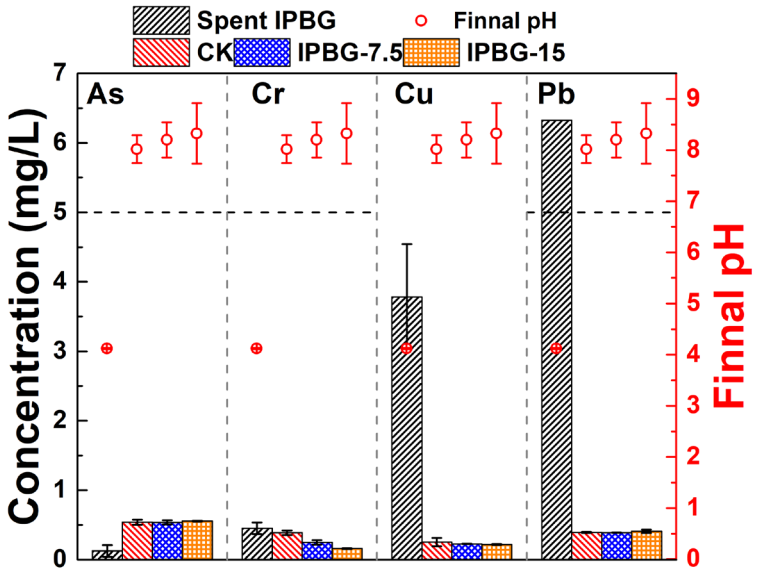

Figure 6-10 Leaching of metals from mortars incorporating metal-loaded IPBGs based on TCLP (black dash line indicates the US EPA regulatory limits).

6.3 Summary

This chapter shows manufacturing of LWA solely from the P-recovered ISSA, waste bentonite and peanut shell with good adsorption capacities towards As(V), Cr(VI), Cu(II) and Pb(II) from aqueous solutions. The production process is optimized making the spent IPBG suitable to be stabilized and upcycled in cement mortar. The exhausted IPBG incorporated mortar at a 15% river sand replacement ratio showed a mechanical strength of 41.9 MPa with negligible leaching of toxic heavy metals based on TCLP demonstrating its environmental safety. Given the non-

biodegradable nature of heavy metals, transferring them from wastewater and stabilizing them in the cement solidified matrices with satisfactory mechanical strength for applications in construction materials helps to progress towards a society with sustainable waste management.

CHAPTER 7 GREEN ADDITIVE IN CEMENT-BASED S/S PROCESS FOR IMMOBILIZATION AND RECYCLING OF CONTAMINATED MARINE SEDIMENTS AS CONSTRUCTION MATERIALS

7.1 Introduction

Promising heavy metal removal results have been obtained by iron-biochar composites fabricated from co-pyrolysis of P-recovered ISSA and biomass as shown in Chapter 4 and Chapter 5. Given difficulties in separation of the powdery adsorbent from aqueous solutions as well as the disposal of the spent adsorbent. In this chapter, the powdery iron-biochar composite was used as a green additive in cement-based S/S process for the immobilization and recycling of contaminated marine sediment into useful construction materials. FBC, FSBC, SBC, RBC and BC in this chapter were produced under the same conditions with those in Chapter 5 except the heating temperature was increased to 1050^{o}C aiming to enhance the immobilization of Cr(VI), As(V) and Cu(II) in the contaminated marine sediments.

The aim of this chapter was therefore to evaluate the feasibility of reusing P-recovered ISSA derived iron-biochar composites as additives in cement-based S/S process for the stabilization of As-, Cr- and Cu-contaminated marine sediments. This was achieved by assessing the mechanical strength and leaching of metal(loid)s of the S/S treated sediments. As pH is crucial and determines the leaching of As, Cr and Cu, knowledge of the corresponding pH-dependent leaching behavior of the S/S product is conducive to elucidating the mobility of them and determine the potential applications of the S/S products (Komonweeraket et al., 2015b).The specific targets of this chapter encompass (i) evaluate the performance of adding iron-biochar composites in cement-based S/S process for the remediation of As-, Cr- and Cu-contaminated sediment; (ii) assess the leaching

behavior of As, Cr and Cu and their corresponding chemical speciations; (iii) assess the mechanical strength of the marine sediment to validate the potential application, and (iv) investigate the leaching behaviors of As, Cr and Cu from the sediments before and after S/S treatment in a wide pH range.

7.2 Results and discussion

7.2.1 Characterization of additives

With the incorporation of additives, the cement-based S/S process varied in its formulation, which could result in variations in physico-chemical characteristics such as elemental compositions, microstructures, and mineralogy of the S/S products, thus altering strength development and the elements leaching behaviors of the S/S products (Glasser, 1997). It is known a high organic carbon content and some minerals such as clay minerals can have disturbing and retarding effects on the curing of S/S products, therefore inferior mechanical properties (Sörengård et al., 2019). As shown in Table 7-1, except from the SBC and BC samples, all the other mineral BC samples showed very low O and H contents due to enhanced degradation of peanut shell at the high pyrolysis temperature and the presence of minerals such as Fe_2O_3 (Ahmad et al., 2014; Liu et al., 2018). In the context of cement-based S/S, more recalcitrant biochar produced at a high temperature is preferred compared to its low temperature counterparts, thus providing a higher long-term stability in the cement-based S/S process (Gupta et al., 2018b). In addition, when applied at the same dosage, the dilution effect due to the presence of other minerals in the mineral biochar samples resulted in a lower concentration of total organic carbon in the S/S products as shown in Table S15.

In the FTIR spectra of these additives (Figure S20), a distinct broad peak centered at 1083 cm^{-1} was found in RBC, FSBC and SBC, but not in BC and FBC, due to the stretching vibration of T-

O-Si (T=Al/Si). These samples also retained a peak centered at 770 cm^{-1} due to the presence of amorphous silica (Wang et al., 2021a). Notable differences were also observed for the spectra present in the range within 400-600 cm^{-1}, all the silica containing mineral biochar samples showed a clear peak centered around 468 cm^{-1} due to Si-O-Si. The presence of active mineral components such as SiO_2 and Al_2O_3 in SBC, FSBC and RBC that could be activated by cement to produce additional cementitious materials, was conducive for strength development of the S/S products compared to BC and FBC (Mahedi et al., 2019).

Table 7-1 Properties of different additives.

Item	FBC	SBC	FSBC	RBC	BC
Fe (%)	13.9 ± 2.1	0.05 ± 0.01	4.8 ± 0.8	7.3 ± 0.4	0.05 ± 0.01
Yield (%)	31.1	59.4	56.3	57.2	40.8
Ash content (%)	42.1 ± 0.4	69.4 ± 6.2	85.6 ± 0.2	83.1 ± 1.6	1.9
C	59.7	21.5	19.0	18.5	88.0
H	0.3	0.1			
N	0.1				0.8
O		8.9			9.3
BET surface area (m^2/g)	76.7	2.7	25.5	35.4	3.6
Total pore volume (cm^3/g)	0.075	0.003	0.025	0.031	0.005
Average pore diameter (nm)	5.26	16.04	5.62	7.03	12.13

As for the immobilization of contaminants, the inclusion of iron-biochar composites in the cement-based S/S process was targeted to enhance the retention of oxyanionic As and Cr, and Cu, which

could be affected by the sample's surface properties such as active mineral species, surface functional groups, and surface area. The Fe contents in FSBC, RBC and FBC were around 4.8%, 7.3% and 13.9%, while BC and SBC contained negligible Fe. The lower Fe contents in FSBC and RBC compared with FBC were associated with the dilution effect due to higher input amount of inert minerals in raw materials. Since Fe species demonstrate varied capabilities towards the removal of oxyanionic species, these biochar samples were subjected to XRD analysis (Figure S21). ZVI was detected in FSBC, RBC and FBC, while no peaks related to Fe oxides were observed in these samples indicating their amorphous nature (Sun et al., 2019). In addition, quartz, microcline and leucite were found in RBC arising from the P-recovered ISSA residue. FTIR spectra of all these additives showed a broad peak centered around 3447 cm^{-1} arising from –OH group, and peaks centered around 2924, 2854 and 1398 cm^{-1} due to the presence of stretching vibration of $–CH_2$ (Ahmad et al., 2012; Sun et al., 2019). Peaks centered around 1632 cm^{-1} due to the presence of carbonyl C=O groups or aromatic C=C groups were also found in all these samples (Chen et al., 2015). The peak centered at 1263 cm^{-1} due to the presence of aromatic C-H was only observed in BC sample (Ahmad et al., 2012). For iron containing mineral biochar samples, a weak characteristic peak of Fe-O in hematite centered at 521 cm^{-1} was found (Wang et al., 2021a). Moreover, the BET surface area of BC was only 3.6 m^2/g, which increased to 25.5, 35.4 and 76.7 m^2/g in FSBC, RBC and FBC (Table 7-1). The low surface area of BC was due to the high pyrolysis temperature adopted in this study (Amen et al., 2020). The modification process with iron minerals significantly increased the BET surface area and pore volume, which could be due to the presence of iron mineral promoting the catalytic degradation of peanut shell to produce more porous structures compared with BC, thus benefiting for the retention of As and Cr (as shown in Figure 7-1) by providing more active sites (Vithanage et al., 2017). These results suggested that

co-pyrolysis of peanut shell with either pure Fe_2O_3 or Fe-bearing ISSA residue could successfully generate ZVI containing biochar samples with increased surface areas compared with pristine biochar, thus FBC, FSBC and RBC could exhibit enhanced removal of oxyanionic As and Cr compared with BC and SBC (Wang et al., 2021a). In addition, as shown in Figure S22, BC and FBC had lower thermal stabilities while SBC, FSBC and RBC demonstrated higher thermal stabilities than cement.

7.2.2 S/S efficiency

1) TCLP

TCLP was adopted to assess the immobilization efficiency of heavy metal(loid)s by different treatment groups. It was also used to assess the suitability of S/S products for landfilling, remediation, or on-site reuse (Zhou et al., 2022). As shown in Figure 7-1, all the treatment groups increased the TCLP leachate pH from 4.04 ± 0.09 to the range of 6.45~7.42 due to the presence of large amounts of CaO and MgO originating from cement (Table S16). All these S/S treatment groups reduced the leaching of As, Cr and Cu from the contaminated sediments. The concentration of As in the TCLP leachate of different S/S groups was similar (within the range of 0.11~0.13 mg/L) and significantly lower than the raw sediment (0.38 ± 0.08 mg/L). All treatment groups notably reduced the Cu concentration in the TCLP leachate from 1.32 ± 0.05 mg/L to a similar level within 0.03~0.07 mg/L. Leaching of Cr as assessed by TCLP however was different even though all the S/S groups notably reduced the Cr concentration in TCLP leachates compared to the raw sediment (6.81 ± 0.50 mg/L). CK, SBC and BC reduced the leaching of Cr to the range of 3.21~3.72 mg/L, higher than the allowable value for on-site reuse of treated soil in Hong Kong (Total Cr: 0.6 mg/L) (Epd, 2011). FBC, FSBC and RBC all reduced the Cr concentration to lower

than the local regulatory standard. These results demonstrated that all the treatment groups were comparable regarding the immobilization of As and Cu, while the immobilization efficiency towards Cr followed the trend of CK ≈ SBC ≈ BC < RBC < FSBC ≈ FBC. The use of FBC, FSBC and RBC reduced the leaching of As, Cr and Cu (As: 5 mg/L, Total Cr: 0.6 mg/L, Cu: reduced by at least 90%) to meeting the heavy metal leaching requirements for on-site reuse of cement S/S treated soil in Hong Kong (Epd, 2011).

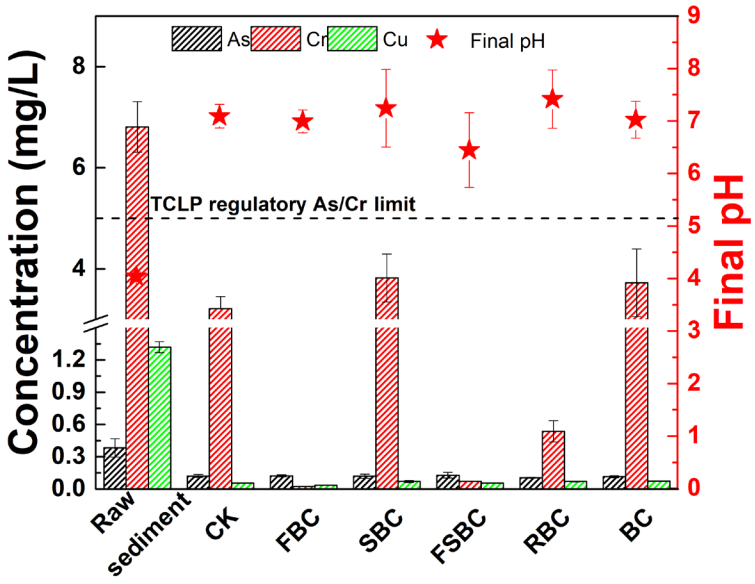

Figure 7-1 Leaching of As, Cr and Cu from the raw sediment before and after S/S treatment with/without mineral biochars based on TCLP.

2) Metal(loid)s speciation

SEP was further used to examine the speciation of As, Cr and Cu before and after S/S treatment. It is widely acknowledged that the exchangeable (F1) and residual (F5) fraction is the most mobile and stable species respectively. While the carbonates (F2) and Fe/Mn oxide bounded (F3) fractions

are susceptible to the surrounding environment such as the pH and redox potentials. As shown in Figure 7-2, the amounts of different As species in the raw sediment followed the order of F3 (36.6%) > F5 (31.3%) > F2 (16.3%) > F4 (7.7%) > F1 (8.1%). This demonstrates the sediment had quite a strong leaching potential of As because the F1 to F3 fractions accounted for around 61% of the total As. After the S/S treatment, all the treatment groups had the F1 fraction reduced from 8.1% to the range of 3.1~4.7%, and the F5 fraction increased from 31.3% to the range of 34.8~39.6%. The amount of F1 to F3 fractions in different treatment groups followed the order of FBC (46.6%) < CK (49.0%) < BC (53.2%) < SBC (55.2%) ≈ RBC (55.3%) ≈ FSBC (55.7%). The sediment however showed a very high leaching potential of Cr, as the F1 fraction was 56.9%, while F5 was only 7.0%. CK, SBC and BC had slightly reduced the F1 fraction to respectively 33.5%, 42.4% and 44.5%. While FBC, FSBC and RBC had strikingly reduced the F1 fraction to 4.8%, 6.9% and 6.3%, and increased the F3 fraction in the contaminated sediments from 19.5% to 46.7%, 61.7% and 71.1%. The F1 to F3 fractions in the contaminated sediments were 88.5%. Those fractions in CK were nearly the same with the contaminated sediments which again indicated cement alone was ineffective in immobilizing mobile Cr. The substitution of cement by other iron-biochar composites i.e. FBC, FSBC and RBC however reduced these fractions to 76.6%, 73.7% and 82.3%.

For Cu, the contaminated sediment had a very low F1 fraction of around 1.2%. The F2 fraction (30.2%) was relatively high. All the S/S treatment groups showed similar F1 fraction in the range of 0.9% to 1.2%. CK achieved the highest reduction in F2 from 30.2% to 11.8%, while increased the F3 fraction from 28.3% in to 52.3%. Other treatment groups also achieved a similar reduction on F2 and increased the F3 fraction.

Overall, the chemical speciation results according to the SEP indicated that all the treatment groups effectively stabilized As and Cu in the contaminated sediments, while using the mineral biochar composites as additives did not achieve a superior As and Cu S/S efficiency compared with CK. However, the iron-biochar composites i.e., FBC, FSBC and RBC demonstrated enhanced immobilization efficiency towards oxyanionic Cr compared to SBC, BC and CK due to the transformation of the mobile Cr species to the more stable forms.

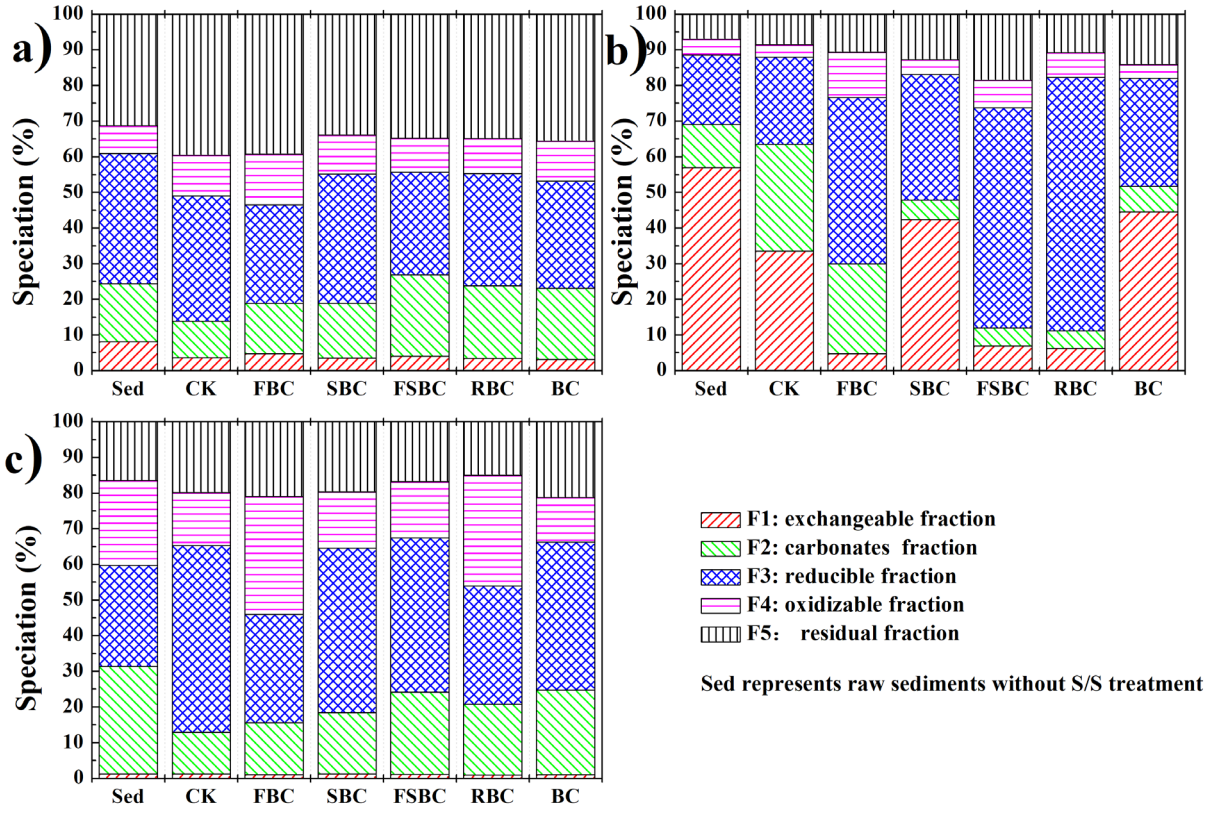

Figure 7-2 Speciation of a) As, b) Cr and c) Cu in raw sediments before and after S/S treatment based on SEP.

3) Amorphous iron

Amorphous iron is known to be active in adsorption of oxyanionic As and Cr in sediments (Lumsdon et al., 2001). As shown in Figure S23, the sediments after S/S treatment showed significantly increased crystalline Fe contents compared with the raw sediment which could be due to the iron present in cement or iron-biochar composites. CK, SBC and BC groups demonstrated comparable amorphous Fe contents compared to the raw sediments, while FBC, FSBC and RBC showed a notably higher amorphous Fe content compared to the raw sediment which could be associated with the oxidation of ZVI present in these iron-biochar composites, thus enhancing the immobilizing performance toward oxyanionic Cr via sorption or co-precipitation (Fan et al., 2020).

7.2.3 Characterization of S/S products

1) Compressive strength

The development of compressive strength of S/S treated sediments is a result of complex physico-chemical reactions comprising cement hydration and hardening, and interactions between sediments, additives and cement (Chen and Wang, 2006). It is also related to the porosity and permeability that affects the leaching of contaminants from the S/S treated sediments, thus determining the potential application (Sörengård et al., 2019). As shown in Figure 7-3, CK group using plain cement as the binder exhibited the highest 28-day compressive strength (7.01 ± 0.30 MPa). 20% substitution of cement by all the other additives notably reduced the compressive strength of the S/S products. BC group had the lowest compressive strength (3.57 ± 0.22 MPa), an almost 49% reduction on mechanical strength compared to CK. The detrimental effect of adding BC could be compensated by using the mineral biochar composites, which had mechanical

strength at levels significantly higher than the BC group. Moreover, compared with the iron-biochar derived from pure iron chemicals (i.e. Fe_2O_3), the presence of SiO_2 irrespective of their origins (i.e. the P-recovered ISSA and pure SiO_2) resulted in notable increases in mechanical strength compared with FBC. Overall, the compressive strength of S/S treated sediments followed the order of CK > SBC > FSBC ≈ RBC > FBC > BC. All the produced S/S products fulfilled the requirement to be recycled as an on-site fill material (mechanical strength > 1 MPa) in Hong Kong (Epd, 2011).

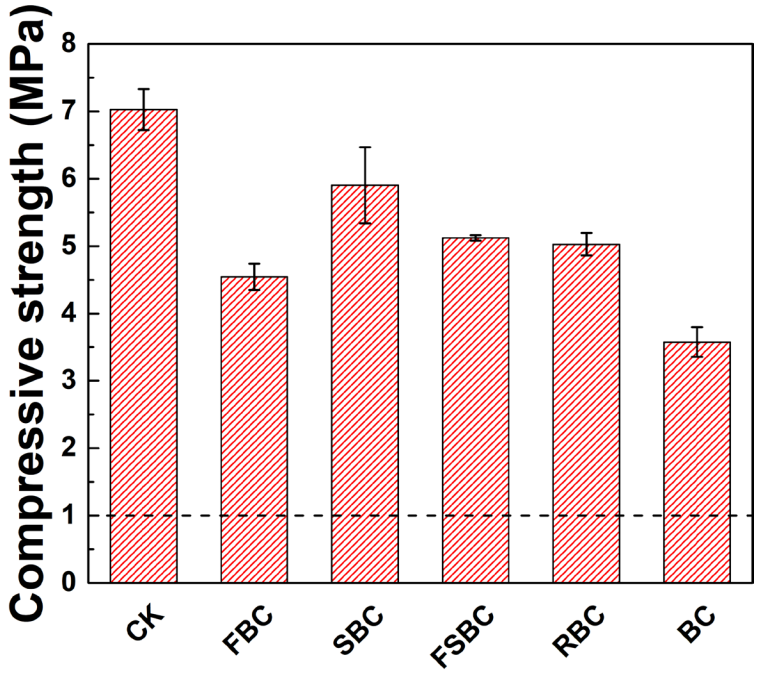

Figure 7-3 Compressive strength of 28-day S/S products of sediments (black dash line at 1 MPa is the minimum strength requirement for on-site fill materials).

2) Microstructure

The strength of the cement composite is dependent on its porosity, pore size distribution and pore shape, which are affected by type and quantity of the constituents forming the pore structure, i.e., cement hydration products and interactions with admixtures (Malviya and Chaudhary, 2006; Pandey and Sharma, 2000). In general, a low porosity means a high mechanical strength due to reasons including higher degree of hydration or better filling of pores with appropriate particle size distribution (Malviya and Chaudhary, 2006). The pore size distribution patterns of the S/S treated sediments are illustrated in Figure 7-4 with corresponding parameters listed in Table S17. The total porosity of S/S products was observed to increase after the addition of mineral biochar samples, and followed the order CK (25.90%) < FBC (27.48%) ≈ FBC (27.53%) ≈ FSBC (27.58%) < RBC (28.23%) < BC (29.06%). Three types of pores including capillary pores (pore diameter < 0.1 μm), mesopores (0.1 μm < pore diameter < 10 μm), and air pores (pore diameter > 10 μm) can be found in cement-based S/S products (Wang et al., 2018). As shown in Figure 7-4a, a broad peak centered at 0.06 μm was present in all the S/S products. A shift toward larger pores was observed with the addition of mineral biochars or BC samples. As a result, these groups demonstrated an average pore diameter larger than CK (56.8 nm) as shown in Table S17. Moreover, a broad peak centered within 1 to 10 μm and a distinct peak within 10 to 100 μm were observed in FBC and BC samples, respectively. The addition of a high amount of BC led to an increase in air voids in cement composites had been reported before (Gupta et al., 2018b, 2018a). In this study, it is interesting to find that the mineral biochar suppressed the formation of air voids compared with prinstine biochar at the same substitution rate of cement, which might be related to its low carbon concent, and better pore filling effect with the presence of other mineral components. Moreover, FBC reduced the air voids but showed an increase in mesopores in the S/S products, which might be the reason for its significantly reduced mechanical strength compared with RBC.

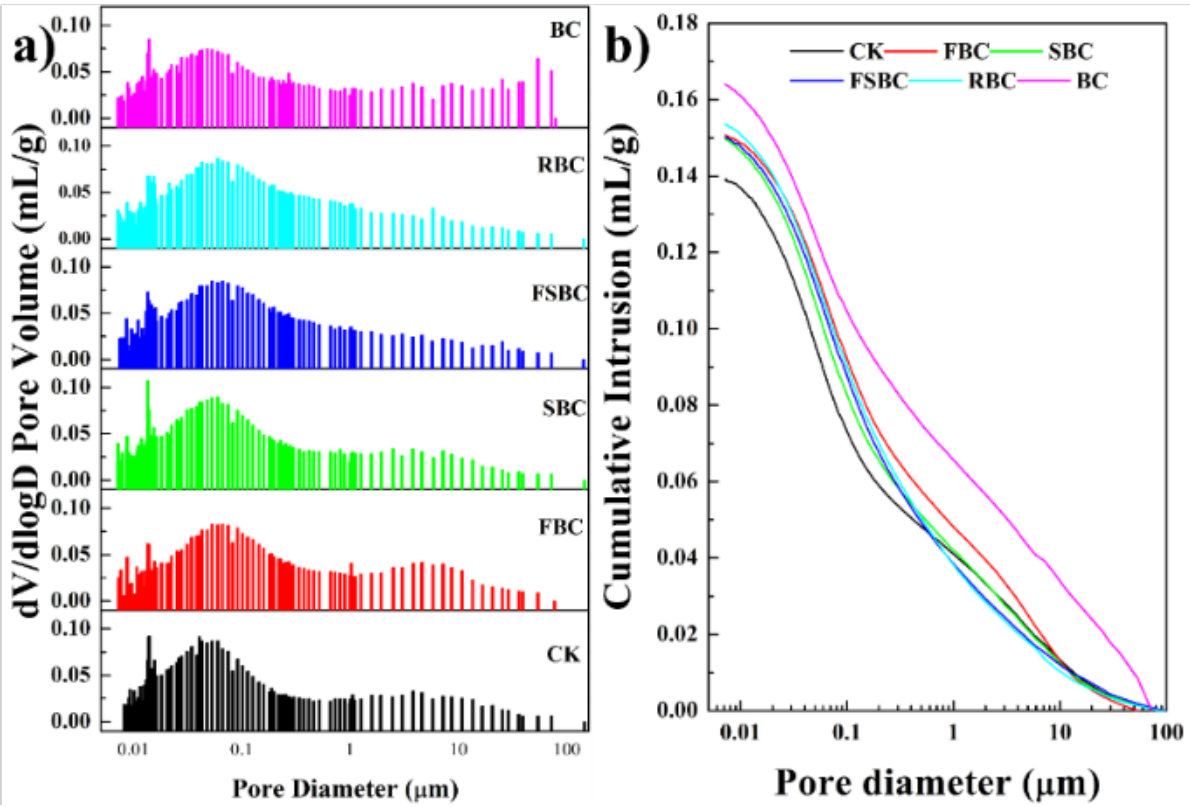

Figure 7-4 Pore size distribution and cumulative mercury intrusion of S/S treated sediments.

The microstructures of the S/S products were further checked by SEM to identify structural differences within different treatment groups. As shown in Figure 7-5, CK group demonstrated a more compact and denser structure compared with other groups, which contributed to its highest mechanical strength. For the samples prepared with the addition of mineral biochars or BC, air void pores, unfilled pores and cracks were more easily observed compared with CK, especially for BC group. Biochar particles were not easily found in this study, which could be due to their small application percentages in the S/S process.

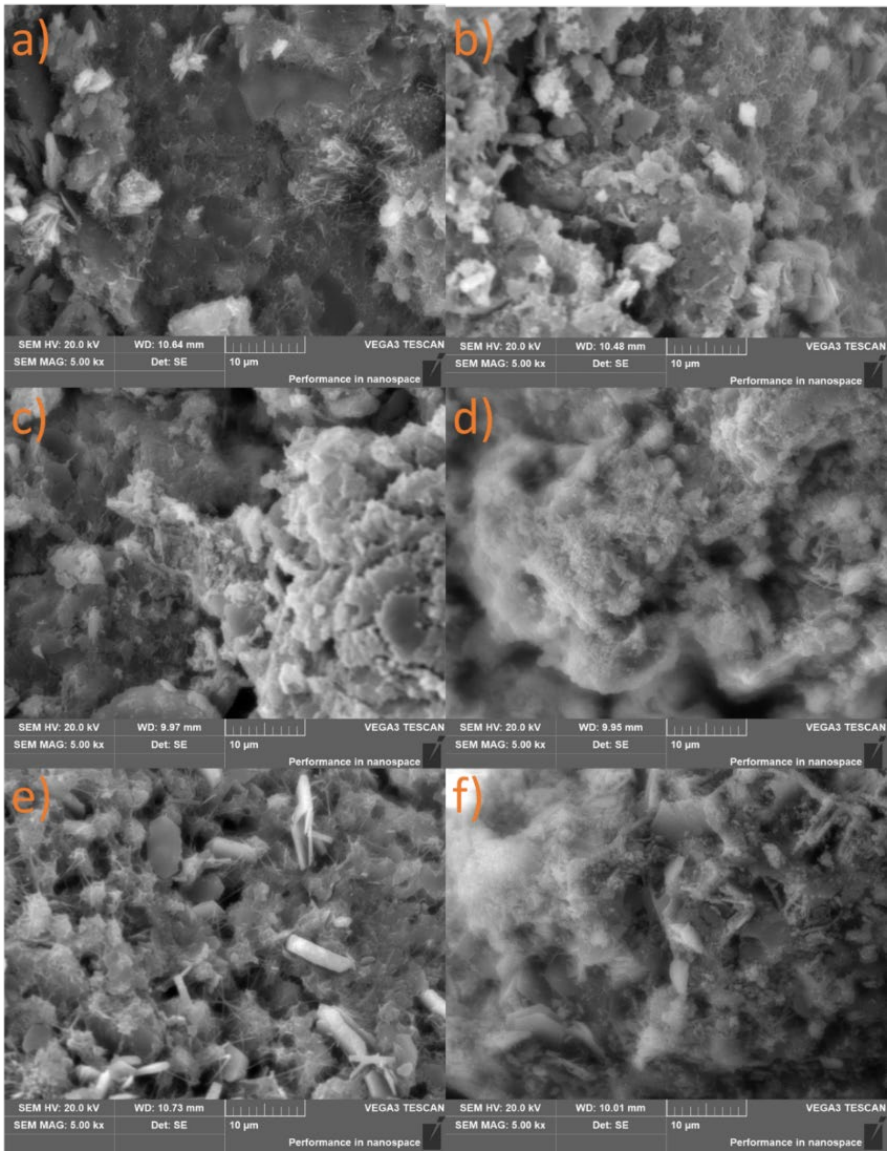

Figure 7-5 SEM images of S/S products: a) CK, b) FBC, c) SBC, d) FSBC, e) RBC, and f) BC.

3) Compositions of S/S products

The S/S products were subjected to TG-DTG and XRD analysis for the examination of hydration products and potential presence of any pollutant-bearing precipitates. As shown in Figure 7-6, three peaks were observed in the DTG curve of the raw sediment. The first decomposition stage

(82~131ºC) with a mass loss of 0.1% was due to the chemically bounded water. The second decomposition peak within 350~550ºC with a mass loss of 1.7% was due to presence of organic matter (Li et al., 2020; Oudghiri et al., 2016). A mass loss of 1% was found within the temperature range of 580~700ºC, which was associated with inorganic carbonates (Oudghiri et al., 2016). After S/S treatment, three distinct decomposition peaks corresponding to physically absorbed water or calcium silicate hydrates gel (C-S-H, 85~158ºC), calcium hydroxide (CH, 350~450ºC), and calcium carbonate (CC, 560~700ºC) were present in the DTG curves of all the S/S treated sediments (Chen et al., 2020; Li et al., 2020). Since the mass losses of mineral biochar composites and cement (Figure S22) within 350 to 430ºC were negligible (< 0.5%) and the additional amount of mineral biochar composites was small, this peak in S/S products could be assigned to CH from cement hydration. As shown in Figure 7-6a, SBC, FSBC, RBC, and BC (0.94~1.04%) showed a similar CH amount level compared with CK (0.99%), while FBC had 12% more CH. This demonstrated that the addition of FBC had the most pronounced promotion effect on the cement hydration which could be attributed to water retention of mineral BC at the initial stage and the subsequent internal curing effect (Chen et al., 2020).

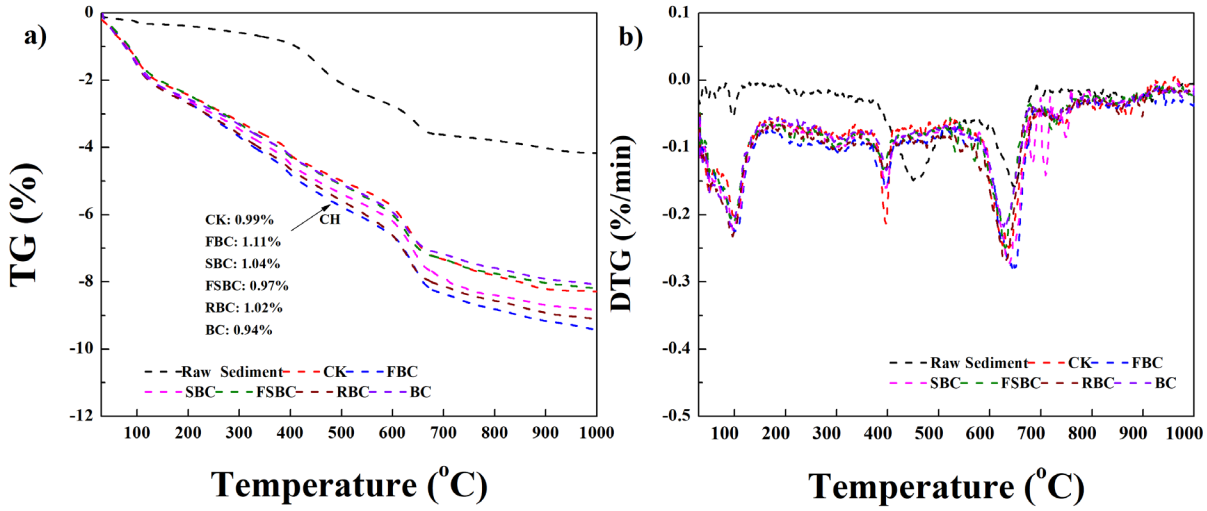

Figure 7-6 TG and DTG of raw sediments before and after S/S treatment (CH content = Mass loss (350ºC -450ºC)).

Figure 7-7 displays X-ray diffractograms of the raw sediments after S/S treatment, which confirmed the presence of cement components like tricalcium silicate(C3S) and dicalcium silicate (C2S), and cement hydration products like CH (Chen et al., 2021). In addition, ZVI was detected in the spectra of FBC, FSBC and RBC, with the FBC demonstrated the strongest peak due to its highest iron content. Under an alkaline environment, ZVI could go through hydrolysis reactions, thus generating secondary iron (hydr)oxides such as magnetite/maghemite and goethite (Gao et al., 2021). When mixed with soil, ZVI was partially transformed to magnetite as a product of ZVI oxidation (Vítková et al., 2017). In this study, it is not easy to find the presence of such iron species which could be due to its amorphous feature. But even after 28 day curing, the presence of ZVI was still detected, which could favorably immobilize metal(loid)s such as As and Cr via chemical reduction and (co)precipitation reactions (Vítková et al., 2017).

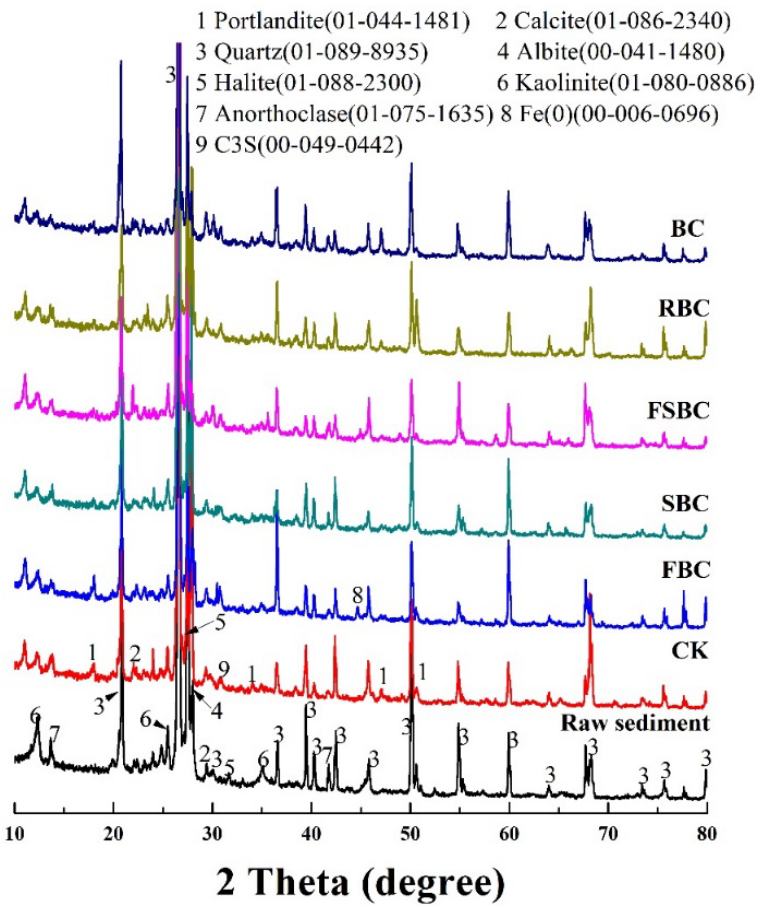

Figure 7-7 XRD patterns of raw sediment before and after S/S treatment.

Various biochar materials have been incorporated into cement composites, and the effect of adding biochar on strength development is quite different, which can be largely affected by the physico-chemical properties of the biochar, particle size and its addition dosages. Around 2% application rate of biochar was reported to be beneficial for strength development of cement-based materials in many cases due to reasons including its water retention capacity and therefore providing internal curing (Chen et al., 2020). Filling effects of the BC particles in the porous structure facilitating the precipitation and growth of hydration products would also enhance the mechanical strength. While a higher BC application rate at 5% resulted in reduced mechanical strength compared with the pure

cement based materials (Chen et al., 2020). In this study, a 20% substitution rate of cement by all the additives demonstrated comparable or increased cement hydration degree possibly due to the preceding reasons but significantly lower mechanical strength compared with CK due to inferior pore structures. Comparatively, the incorporation of mineral biochar composites induced significant increases in mechanical strength of the S/S products compared with the pristine biochar.

7.2.4 pH dependent leaching behaviours

Elemental leaching behaviors from the solid matrices can be significantly affected by the surrounding environmental particularly pH, which could be easily affected by weathering or anthropogenic activities (Vítková et al., 2017). The heavy metal bearing minerals particularly in the forms of oxides, hydroxides, and carbonates are susceptible to pH changes, thus affecting the leaching of elements (Król et al., 2020). In addition, heavy metal(loid)s in solid matrices could be retained on the surfaces of various minerals such as iron (hydr)oxides, aluminum oxides, goethite and so on, or bounded with organic matters via complexation which can be released with pH changes (Król et al., 2020). Understanding the pH-dependent leaching behaviors and mechanisms controlling the leaching of major and trace elements from the S/S products is important for assessing the environment impacts.

1） Acid neutralization capacity (ANC)

The natural pH of the raw sediment was around 8.01 ± 0.39, all the treatment groups resulted in an increase of the sediment pH to around 12.2 (as shown in Figure 7-8a) due to the high content of CaO in cement (Komonweeraket et al., 2015b), as reflected by the significantly increased Ca concentration in the leachate compared with the raw sediment (Figure S25c). The ANC (shown in Figure 7-8) demonstrates the difference between equilibrium pH values as a function of acid

(positive value) or base (negative value) added in terms of meq/g dry solid. It is a crucial parameter for cement based S/S systems, which reflects the durability of the system to acid attack and consequent leachability of heavy metal(loid)s (Zhang et al., 2016). The raw sediment had a small ANC, and 1.0 meq/g acid addition reduced sediment's natural pH from 8.0 to around 4.0. After S/S treatment, all the S/S treatment groups exhibited remarkably increased ANC compared with the raw sediment, and CK had the strongest ANC. The plateau present in the ANC curves represents the presence of solid phases with acid resistance (Zhang et al., 2016). An almost identical plateau within pH 11 to 13 was observed in all ANC curves of the sediments after S/S treatment, which could be attributed to the produced CH and C-S-H gel from cement hydration (Mahedi et al., 2019). The plateau at pH around 8.0 was observed in the ANC curves of CK, SBC and BC due to the presence of silicates and aluminosilicates (Mahedi et al., 2019). Substitution of cement by all the studied mineral biochar composites resulted in a decreased ANC compared with CK.

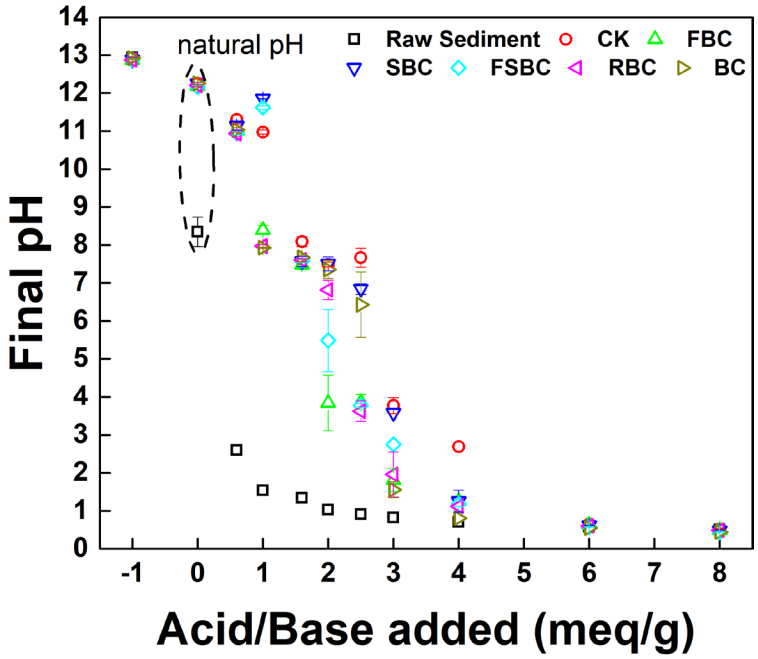

Figure 7-8 Acid neutralization capacity (ANC) of raw sediments before and after S/S treatment.

2） pH dependent leaching of As, Cr and Cu

In general, leaching patterns of elements from solid matrices as a function of pH can be categorized into three types including cationic, oxyanionic and amphoteric (Komonweeraket et al., 2015a, 2015c; Zhang et al., 2016). The leaching patterns of As, Cr and Cu from the raw sediments before and after S/S treatment are shown in Figure 7-9. The leaching of As (Figure 7-9a) from the raw sediment showed an amphoteric leaching pattern. The highest leaching of As occurred at pH < 2, and when pH was increased to around neutral the leaching of As decreased, it increased again under a highly alkaline environment. A similar leaching pattern of As from marine sediments has been documented in the literature (Sanchez et al., 2003; Singh et al., 2020). This is because negatively charged As can be favorably adsorbed on surfaces of iron and aluminum minerals such as goethite, alumina oxides and iron (hydr)oxides in the marine sediments under a neutral pH

environment (Komonweeraket et al., 2015c). An extremely low pH condition results in the protonation of As and promotes the dissolution of these minerals as reflected by the significantly increased leaching of Al, Fe and Ca at pH < 2.0 (Figure S25) or As-bearing precipitates, thus reducing As retention (Komonweeraket et al., 2015c; Singh et al., 2020). At a high pH value, the negatively charged sediment surfaces and enhanced OH^- competition for active sites would lead to an elevated As concentration in the leachate (Komonweeraket et al., 2015c). All the treatment groups demonstrated similar leaching patterns of As and significantly reduced As leaching under neutral to alkaline environments compared to the raw sediment, demonstrating the effectiveness of these S/S treatment for As. The leaching concentration of As from raw sediments after S/S treatment decreased continuously with pH increase to around 11, but increased at pH around 12.8. Similarly, minimal As leaching from a fly ash/soil mixture had been observed at pH 11 and increased with pH increase afterwards (Komonweeraket et al., 2015a). The similar leaching behaviors among sediments after S/S treatment implied the similar As-leaching controlling mechanisms and controlling factors (Komonweeraket et al., 2015c). Under alkaline environment, the surface of iron (hydr)oxides is predominantly negatively charged, therefore unable to adsorb the negatively charged As (predominantly $HAsO_4^{2-}$ at pH within 7-12.5 and as AsO_4^{3-} at pH > 12.5) (Cornelis et al., 2008). So the retention for As was largely related to cement hydration reactions which might result in the inclusion of As in ettringite, calcite or C-S-H gel or precipitated as $CaAsO_4$ (Cornelis et al., 2008; Komonweeraket et al., 2015c).

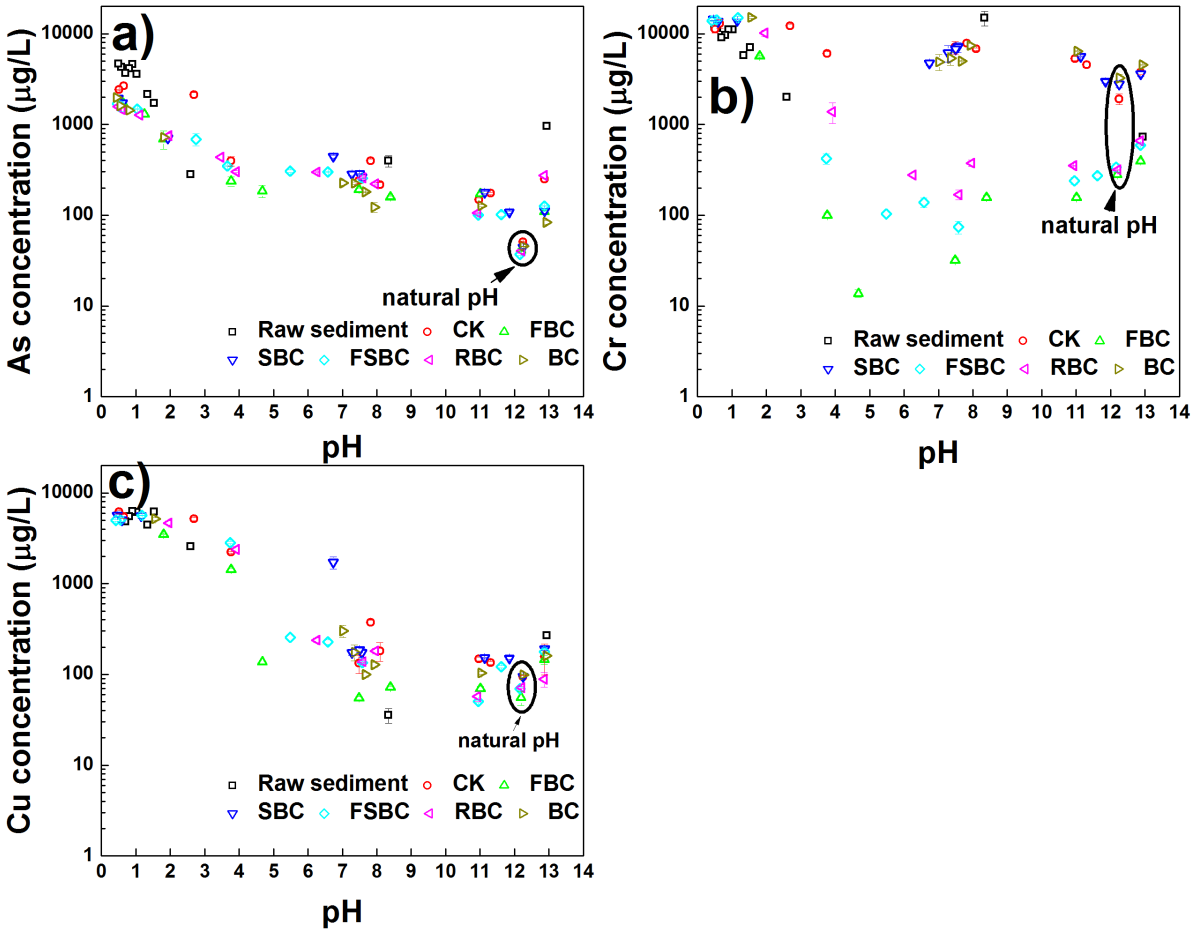

Figure 7-9 pH dependent leaching of As, Cr and Cu from sediments before and after S/S treatment.

As shown in Fig7-9b, all S/S treatment significantly reduced the leaching of Cr compared with the raw sediment. It was reported that oxyanionic Cr could substitute sulfate and be incorporated in cement hydration products like ettringite, resulting in the immobilization of oxyanionic Cr in cement composites (Engelsen et al., 2010). Both a lower and higher pH of natural CK samples resulted in the increase in leachate Cr concentration due to the dissolution of cement hydration products. SBC and BC exhibited a similar pH-dependent leaching pattern to CK, and the leaching concentration of Cr increased immediately at pH lower than the natural pH of S/S product,

demonstrating the retention ability of Cr by cement is very poor and susceptible to pH changes. The addition of SBC and BC had negligible effect on the immobilization of Cr. Nevertheless, incorporating of iron-biochar composites i.e. FBC, FSBC and RBC significantly lowered the leaching of Cr compared to CK (ca. 85% reduction on Cr leaching compared to CK under natural pH), which demonstrated the crucial role of these iron-biochar composites in the retention of Cr. Leaching of oxyanionic Cr could be largely influenced by the adsorption/desorption process by the surfaces of iron (hydr)oxides or dissolution of Cr-bearing solids like Cr-Fe minerals (Król et al., 2020). All the sediments before and after S/S showed the maximum (3 orders magnetite higher than the lowest) leaching of Cr at pH < 2.0 due to the dissolution of iron (hydr)oxides and hydration products (Engelsen et al., 2010) as indicated by the significantly increased leachate concentration of Ca and Fe under the acidic environment (Figure S25). In addition, the solubility of Fe is controlled by Fe hydroxide minerals such as hematite and amorphous $Fe(OH)_3$. A high pH would result in the deprotonation of mineral surfaces and thus enhance the mobilization of oxyanionic Cr via electrostatic repulsion. The addition of FBC, FSBC and RBC also significantly increased the Cr leaching resistance to acid attach as the leaching concentration of Cr remained at a similar level within a broad pH range from 4.5 to 12.

Figure 7-9c exhibits the leaching of Cu from the raw sediments before and after S/S treatment, all followed the amphoteric leaching pattern. The Cu leaching concentration reached its maximum at pH < 2 and decreased with increase of pH to its minimal level within pH 8-12, but increased again with further increase in pH. The amphoteric leaching pattern of Cu sediments before and after S/S treatment demonstrated the leaching process can be largely influenced by the solubility of Cu-oxide and hydroxide minerals (e.g. $Cu(OH)_2$ and amphoteric CuO) (Komonweeraket et al., 2015b; Mahedi et al., 2019). Moreover, dissolved organic carbon (DOC) even in small quantities could

enhance the leaching of Cu from cement composites which was attributed to Cu's known affinity for organic ligands like DOC (Engelsen et al., 2010; Kosson et al., 2017; Z. Sun et al., 2019). As shown in Figure S24, when the pH was higher than the natural pH of the solid samples, the DOC concentration increased significantly, thus contributing to increase Cu leaching at pH around 13.

7.2.5 Stabilization mechanisms

Formation of stable Ca-As precipitates was reported to be the main mechanisms for the stabilization of As(V) in pure cement S/S process, while stabilization of Cr(VI) was associated with formation of Ca-Cr precipitates and CrO4-ettringite by the substitution reaction (Paria and Yuet, 2006). As shown in Figure S26, the As present dominantly as As(V) (82.5%) in the raw sediments with the remaining 17.5% as As(III) according to XPS analysis. After S/S treatment by cement alone, the corresponding As species showed marginal change. However, the incorporation of RBC reduced As(V) to 67.5% and As(III) was increased to 32.5% compared to the raw sediments. As for Cr, it present dominantly as Cr(VI) in both the raw sediment and after S/S treatment by pure cement, while 46.3% Cr(VI) and 53.7% Cr(III) were observed in sediment treated with the addition of RBC. Due to lack of active redox couples in cement (Paria and Yuet, 2006), the increased amounts of As(III) and Cr(III) were related to the addition of RBC. Specifically, ZVI on RBC surface contributed to the chemical reductions of As(V) to As(III), and Cr(VI) to Cr(III). No peaks of iron (hydr)oxides were detected in Figure 7-7, indicating their amorphous nature. Even though As(V) was transformed to its more labile form As(III) with the addition of RBC, the leaching of As based on TCLP however was similar to CK, which could be due to the co-precipitation of As(III) and Fe(III) followed by the redox reactions between As(V) and ZVI (Bakshi et al., 2018), and the formation of Ca-As-O precipitate (Paria and Yuet, 2006). The successful transformation of Cr(VI) to the significantly more insoluble Cr(III) species under

alkaline environment contributed to the effective immobilization of Cr (Glasser, 1997). However, Cr was dominantly present in F3 (Fe-Mn bounded fraction) based on the SEP results (Figure 7-2). Therefore, Cr(VI) was more likely to be firstly reduced by ZVI to Cr(III) followed by co-precipitation with Fe(III) thus enhancing its immobilization performance (Du et al., 2012).

7.3 Summary

This chapter investigated the feasibility of co-valorization of P-recovered ISSA and peanut shell via pyrolysis to produce low-cost iron-biochar composites, which were used to as additives in cement-based S/S process for As, Cr and Cu contaminated marine sediments. To understand the presence of co-existing SiO_2 present in ISSA on the S/S efficiency of the produced iron-biochar composites, pure Fe_2O_3 and SiO_2/Fe_2O_3 mixture were also co-pyrolyzed with peanut shell and produced mineral biochar samples as additives in cement-based S/S treatment process. The leaching mechanisms were investigated by microstructural and spectroscopic techniques and various chemical leaching experiments. The major findings of this chapter are summarized as follows:

(i) 20% substitution of cement by mineral or pristine biochar samples in S/S treatment significantly caused reductions on the mechanical strength of the S/S products. BC had the most detrimental effect on mechanical strength which could be compensated by the use of mineral biochars.

(ii) The leaching of As and Cu were significantly reduced by all S/S groups compared with the raw sediments. Compared with CK (plain cement as binder), treatment by using other mineral biochar composites resulted in similar leaching levels of As and Cu based on TCLP.

However, RBC, FBC and FSBC demonstrated a superior S/S efficiency for oxyanionic Cr compared with CK, SBC and BC.

(iii) For RBC, reduction of Cr(VI) to Cr(III) followed by co-precipitation with Fe(III) contributed to the significantly enhanced immobilization of oxyanionic Cr.

Overall, the use of iron-biochar composites especially derived from ISSA containing other active components such as SiO_2 and Al_2O_3 in cement-based S/S treatment showed enhanced immobilization towards oxyanionic Cr with significantly improved mechanical strength compared with its counterparts derived from pure iron chemicals or pristine biochar samples.

CHAPTER 8 CONCLUSIONS AND RECOMMENDATIONS

8.1 Conclusions

P-recovery from ISSA and reuse and recycling of ISSA in construction materials is a close-loop concept management of sewage sludge. To recover the valuable P resources, direct application of ISSA in construction materials should be avoided. However, the cost-effective method to recover P from ISSA (e.g., acid washing deploying H_2SO_4) leaves the P-recovered ISSA residue accounting for over 80% of the original ash that is difficult to be reused and recycled in construction materials compared to ISSA. Yet there has been little effort to explore opportunities to reuse and recycle the P-recovered ISSA residue so that resource efficient recycling of ISSA is achievable. The primary aim of this study is to investigate the feasibility of utilizing the P-recovered ISSA residue as a supplementary iron source to make iron-biochar composites for remediation of polluted waters and sediments.

The P-recovered ISSA was first co-pyrolyzed with a model biomass material i.e., lignin, and the produced iron-biochar samples were examined for the removal of Cr(VI) as demonstrated in Chapter 4. While hardly as efficient as iron-biochar composites made from pure iron chemicals, this study nevertheless (i) demonstrated the feasibility of producing an iron-biochar by co-pyrolysis of a real waste containing a rich iron content i.e., the P-recovered ISSA residue, with lignin; (ii) revealed the transformation of the iron in the P-recovered ISSA during the carbothermal reduction process, and (iii) showed the capability of the end product for aqueous Cr(VI) removal and the associated mechanisms.

To extend the scope of biomass substrates adopted and expand the application horizon of the end iron-biochar composite to remove more pollutants, a real biowaste i.e., peanut shell was employed

as the carbon source, and As(III) and As(V) were selected as the pollutants in the subsequent study. Moreover, to better understand the role of other components (particularly SiO_2) besides Fe_2O_3 in the P-recovered ISSA residue on properties of the produced iron-biochar composite relevant to pollutant removal, a series of mineral biochar composites were synthesized as shown in Chapter 5. The produced samples were compared for their removal performance towards As(III) and As(V) with various leaching and characterization experiments conducted to understand the underlying mechanisms. This study found that silica in the P-recovered ISSA residue reacted with iron to form iron silicon at the expense of ZVI and Fe_3O_4 and resulted in the leaching of reactive silica during the removal of arsenic from aqueous solutions, both of which caused the end iron-biochar composite inferior to arsenic removal compared to an iron-biochar composite made from pure iron oxide and peanut shell.

Knowledge acquired from the preceding chapters were utilized to progress towards scaling and application (Chapter 6 and Chapter 7). In Chapter 6, a millimeter-sized sorptive media was developed from the P-recovered ISSA residue, peanut shell, and waste bentonite. The end granules demonstrated multi heavy metal (e.g., As(V), Cr(VI), Cu(II) and Pb(II)) removal ability from aqueous solutions. Moreover, the spent granules were lightweight and had a high enough mechanical strength that facilitated their environmentally safe upcycling in lightweight mortar.

In Chapter 7, the powdery iron-biochar was explored as a green additive in the cement-based S/S process for the remediation of As-, Cr-and Cu-contaminated marine sediments. The leaching of As and Cr from S/S products with the inclusion of iron-biochar composites were significantly reduced compared to the control group with cement as the plain binder. Moreover, addition of the P-recovered ISSA residue derived iron-biochar composite had the mechanical strength of the S/S products notably increased compared to the groups with the use of a counterpart iron-biochar

composite derived from pure iron oxide and peanut shell. Given the satisfactory mechanical strength and leaching of heavy metals, the S/S products fulfill the local regulatory requirements as on-site fill materials.

In summary, this study has (i) expanded the limited application horizon of P-recovered ISSA residue i.e., using it as a supplementary iron source to make iron-biochar composites; (ii) investigated not only the optimization process for producing the end products but also revealed the role of the complex composition of the P-recovered ISSA residue on the removal of pollutants; and (iii) explored the up-scaling applications. This PhD thesis contributes to the reuse and recycling of P-recovered ISSA residue, which will shade light on a complete 'zero waste' recycling of ISSA when it is regarded as a valuable secondary P resource.

8.2 Outlook

There is still scope to achieve resource efficient recycling of ISSA. Several areas for future research can be identified from the results reported in this thesis.

First, the co-pyrolysis temperature has been shown to significantly affect pollutant removal efficiency particularly for As(V) and Cr(VI). The high temperature reported in this thesis is conducive to obtaining end products with superior pollutant removal capacity compared to their low-temperature counterparts. Nevertheless, a high material synthesis temperature might be undesirable when it comes to practical applications due to the cost and environmental impact of energy consumption. Therefore, ways to achieve a lower co-pyrolysis temperature to produce comparable end products should be further explored.

Second, besides Fe_2O_3, this thesis simplified the remaining fraction of the P-recovered ISSA residue as SiO_2 due to its dominant presence. However, the role of other co-existing components like Al_2O_3 and CaO should also be identified to better design the process.

Production of lightweight granules in a millimeter size provides an interesting recycling method for the P-recovered ISSA residue. Production of granules in different sizes and examine their heavy metal removal ability from real wastewaters are also important. Even though the leaching of toxic heavy metals from the spent granules incorporated cement mortar were verified to be in compliance with the regulatory limits based on TCLP. The role of the spent granules (with varied diameters) on the microstructure and durability of mortar should also be investigated to facilitate the stabilization and recycling of spent granules as useful materials.

Finally, the role of reusing the powdery end products in cement-based S/S process for the immobilization of heavy metal polluted solid matrices should be further understood, which includes its role in cement hydration, and heavy metal stabilization mechanisms. Moreover, cost benefit analysis and life cycle assessment of the proposed efficient resource recycling of ISSA methods as a package are necessary. Through the implementation of these suggestions, a resource efficient recycling process for ISSA would be gained which not only mitigates the pollution but also contributes to progress our cities towards sustainable waste management.

APPENDIX A SUPPLEMENTARY FIGURES

A.1 Supplementary Figures for Chapter 4

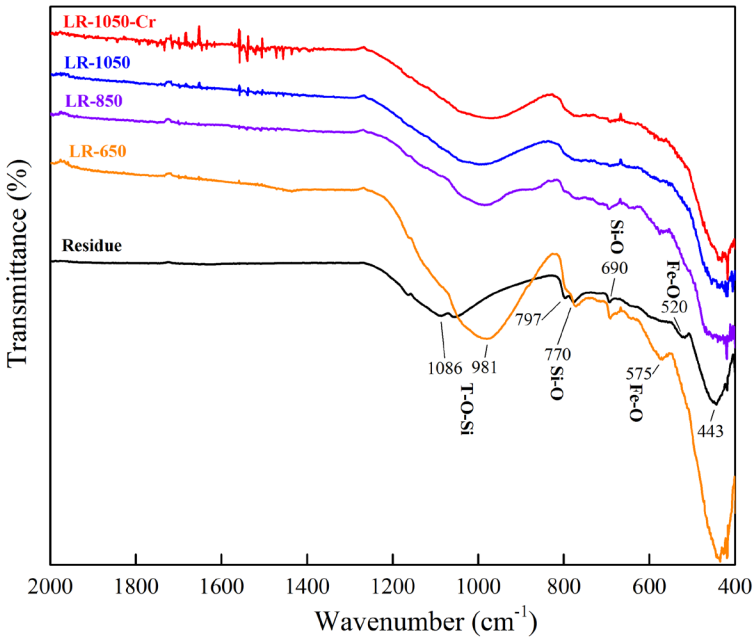

Figure S1 FTIR spectra of selected samples

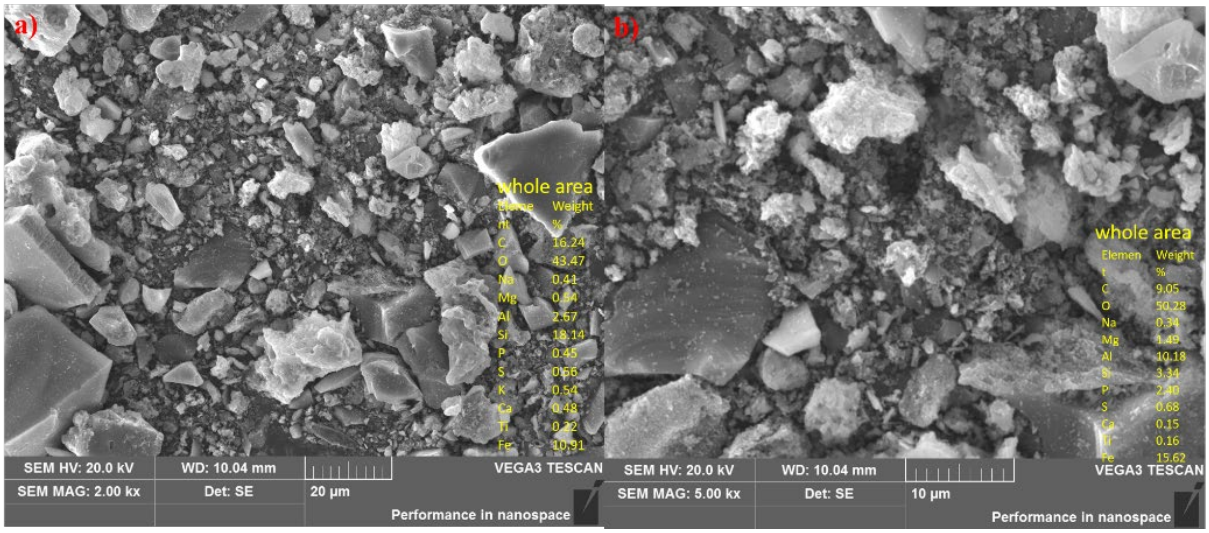

Figure S2 SEM-EDX of the P-recovered ISSA residue.

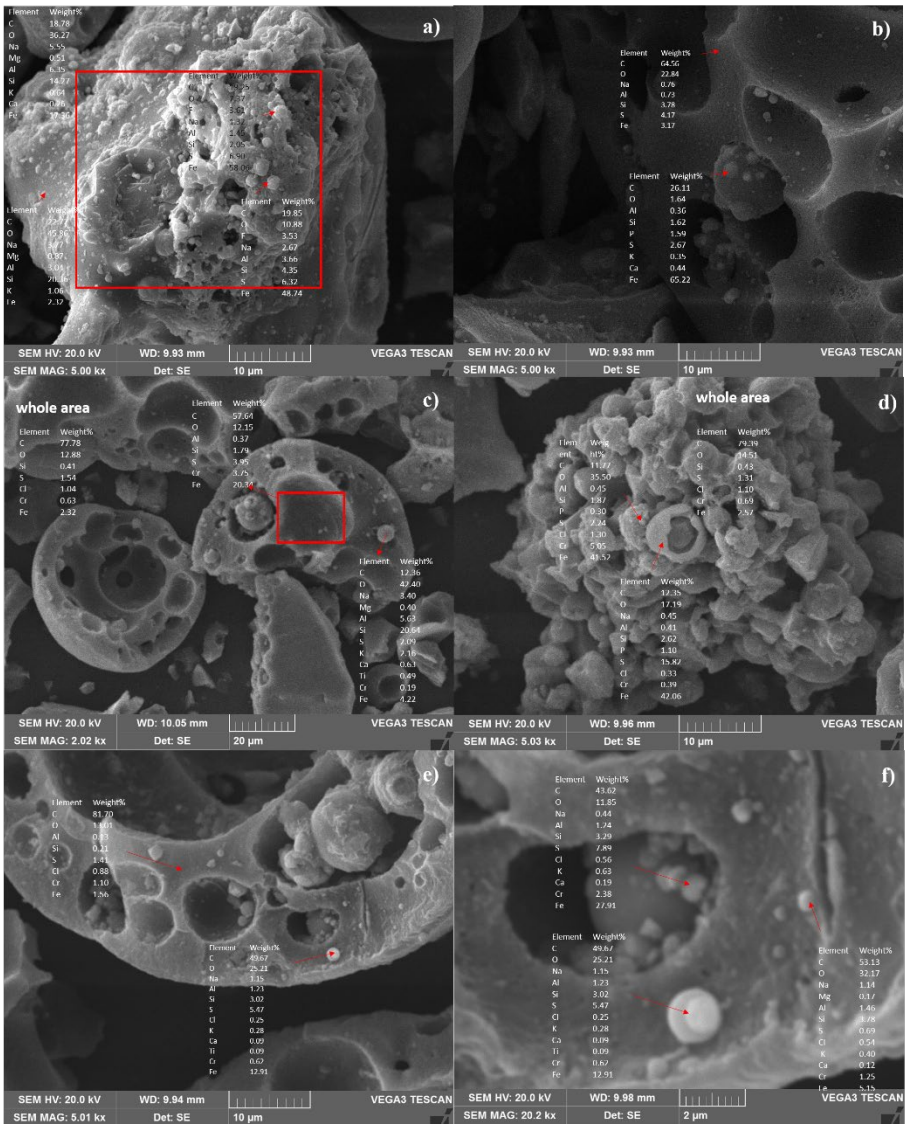

Figure S3 SEM-EDX of LR-1050 before (a and b) and after (c, d, e and f) Cr(VI) removal.

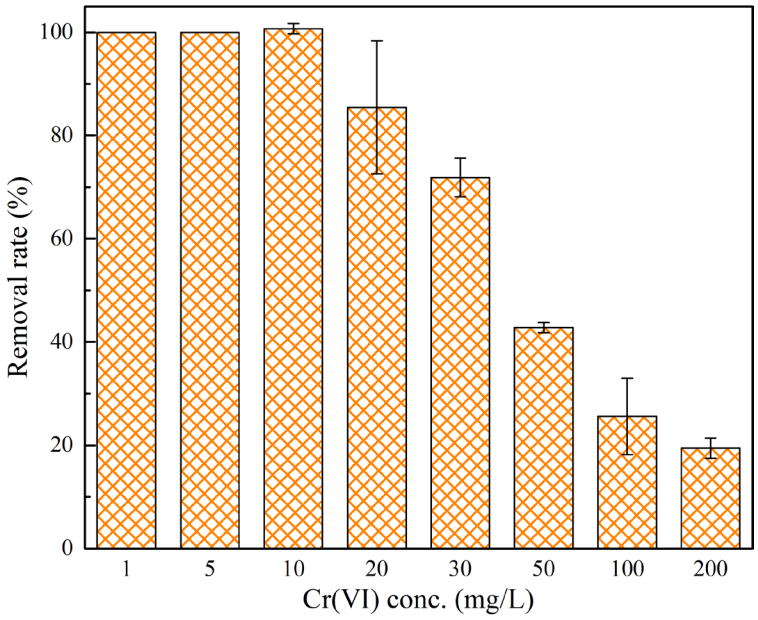

Figure S4 Effect of initial concentration on Cr(VI) removal by LR-1050 (dosage: 1 g/L, pH: 2.0).

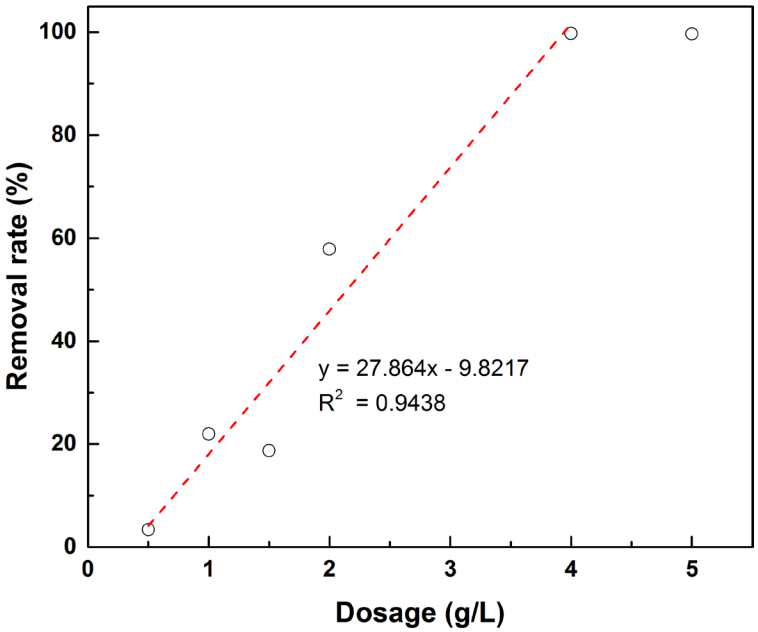

Figure S5 Effect of LR-1050 dosage on Cr(VI) removal rate.

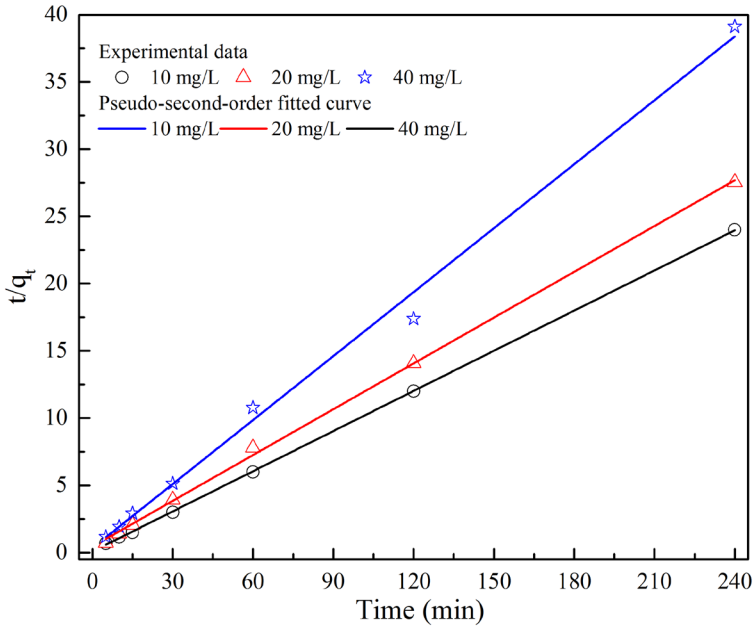

Figure S6 Removal kinetic of LR-1050 towards Cr(VI).

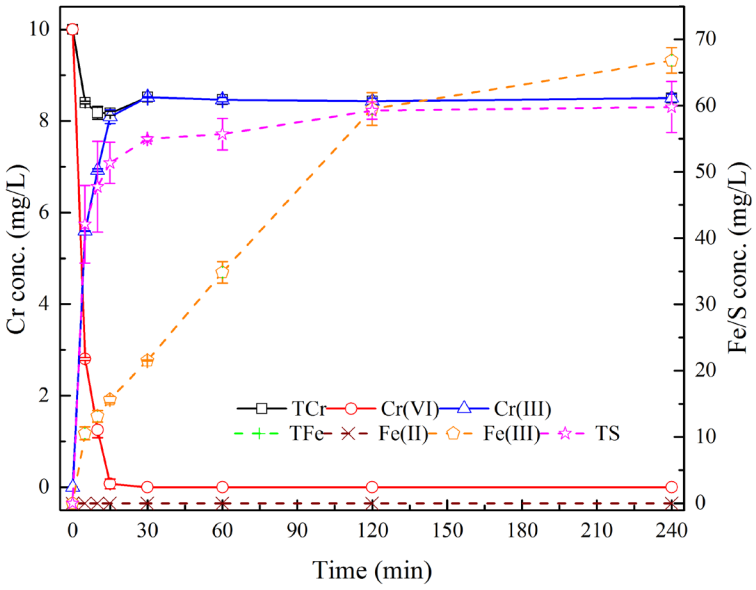

Figure S7 Concentration changes of chromium and iron species and total sulfur (TS) as a function of time (dosage: 1 g/L, pH: 2.0).

A.2 Supplementary Figures for Chapter 5

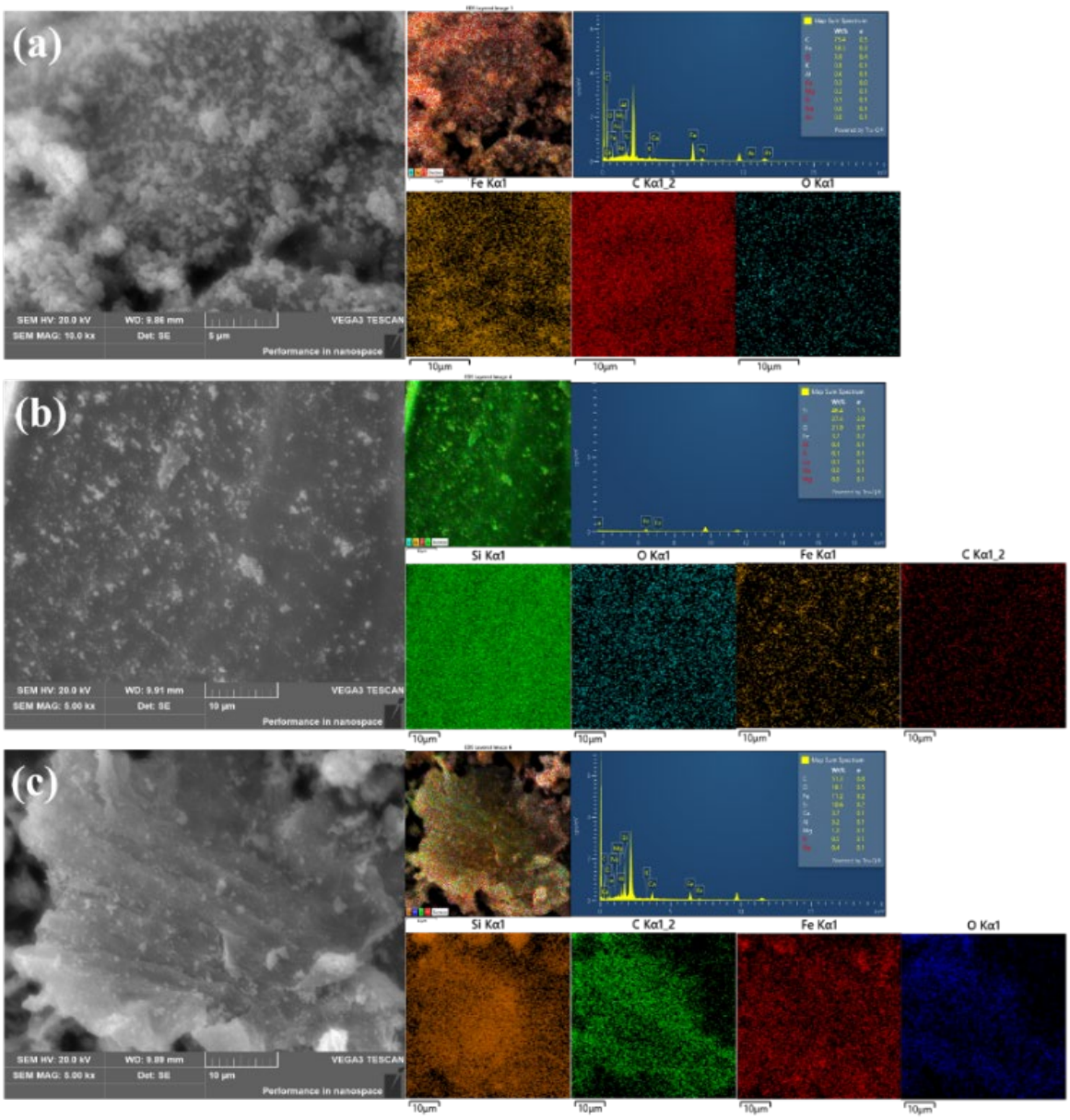

Figure S8 Elemental mapping of FBC: (a), FSBC: (b), and RBC (c).

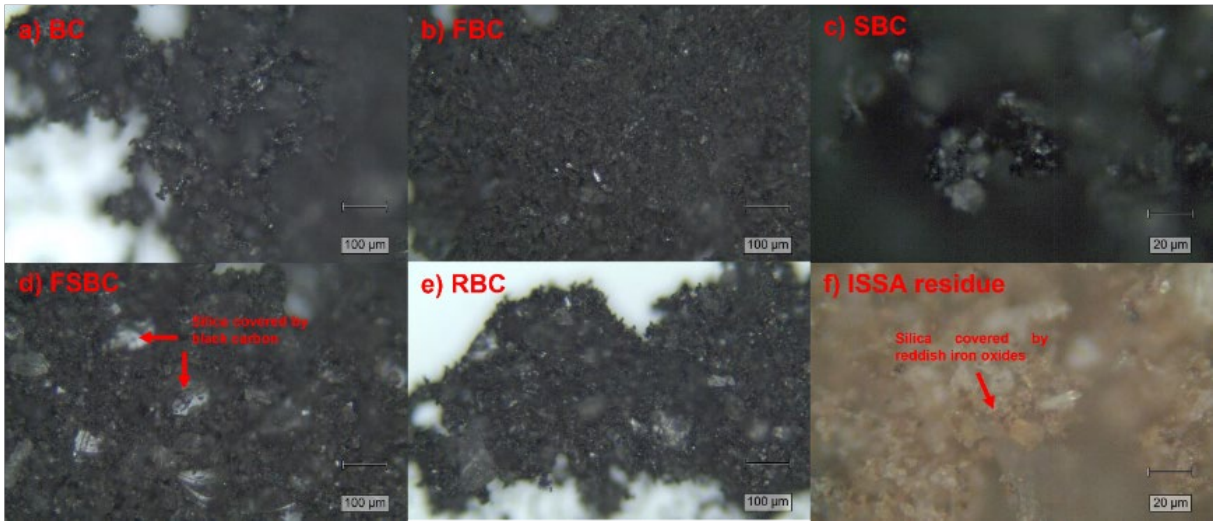

Figure S9 Optical images of BC: (a), FBC: (b), SBC: (c), FSBC: (d), RBC: (e) and the ISSA residue: (f).

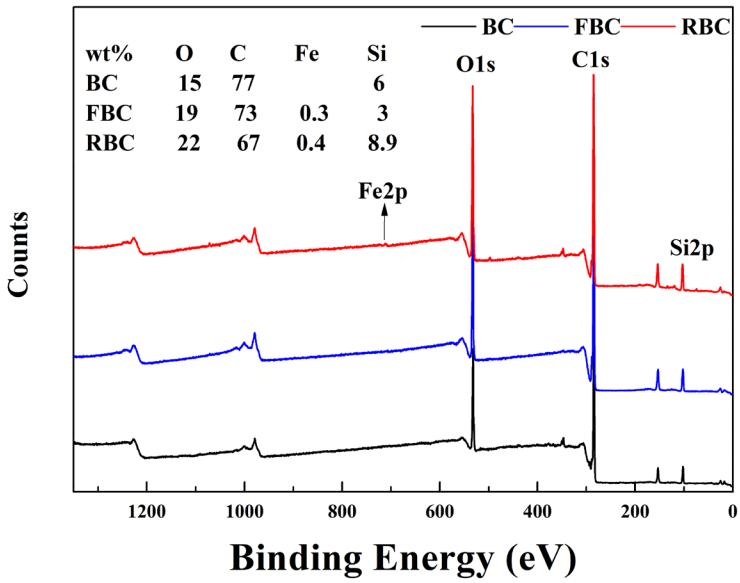

Figure S10 XPS survey spectra of BC, FBC and RBC.

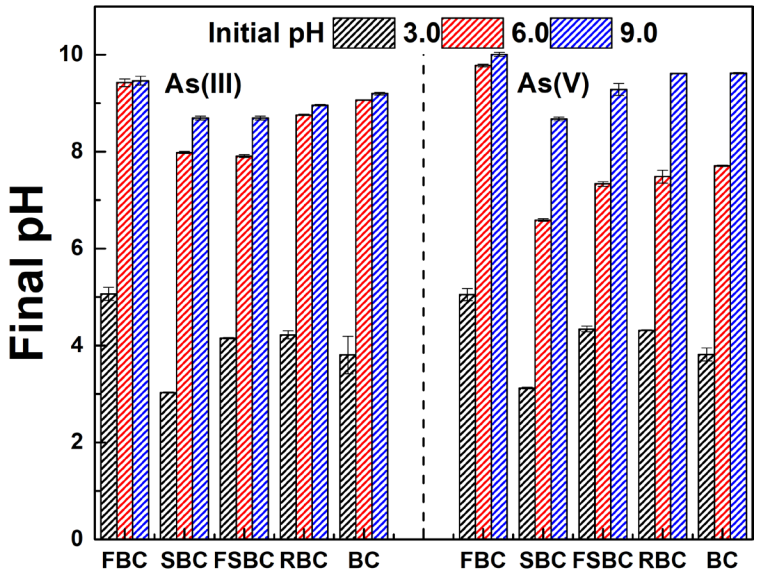

Figure S11 Solution pH change after As(III)/As(V) removal (initial concentration: As(III) = 17.2 mg/L, As(V): 19.2 mg/L; initial pH: 3, 6 and 9; time: 24 h).

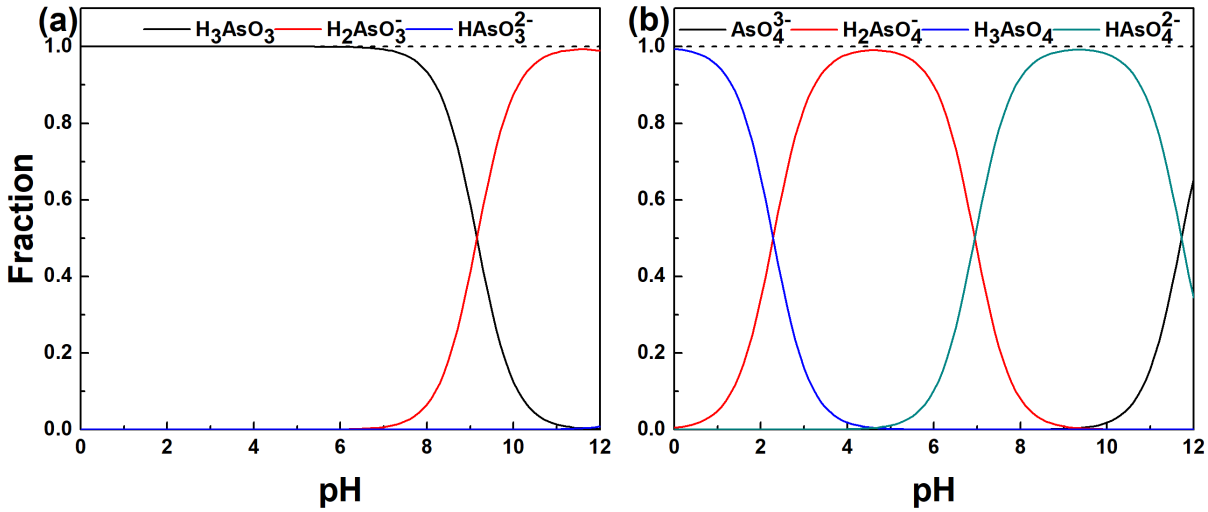

Figure S12 As(III)/As(V) speciation as a function of pH (simulated by MINTEQA).

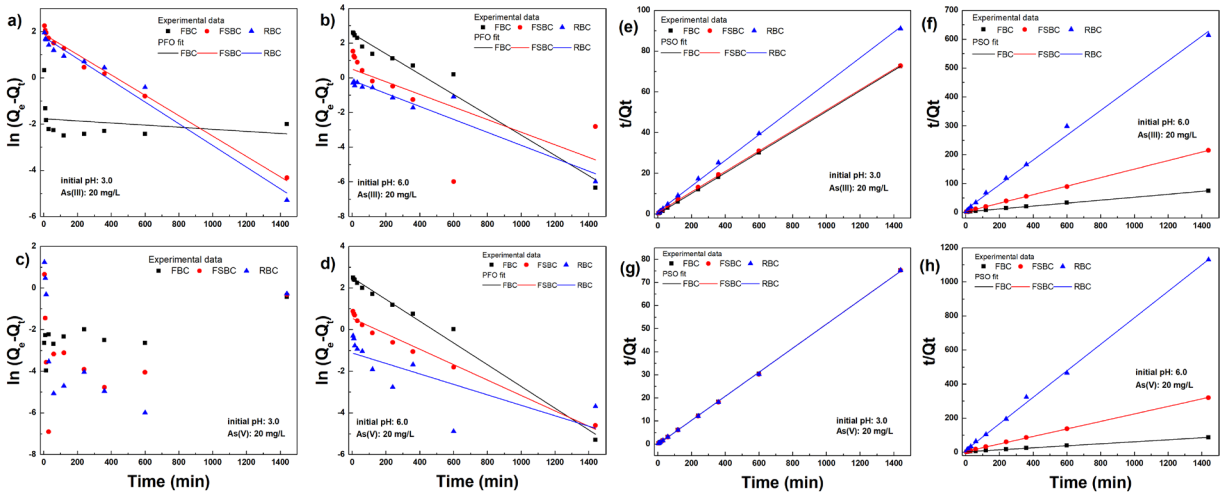

Figure S13 PFO （a, b, c, d）and PSO （e, f, g, h） linear fit of adsorption kinetic data of FBC, FSBC and RBC.

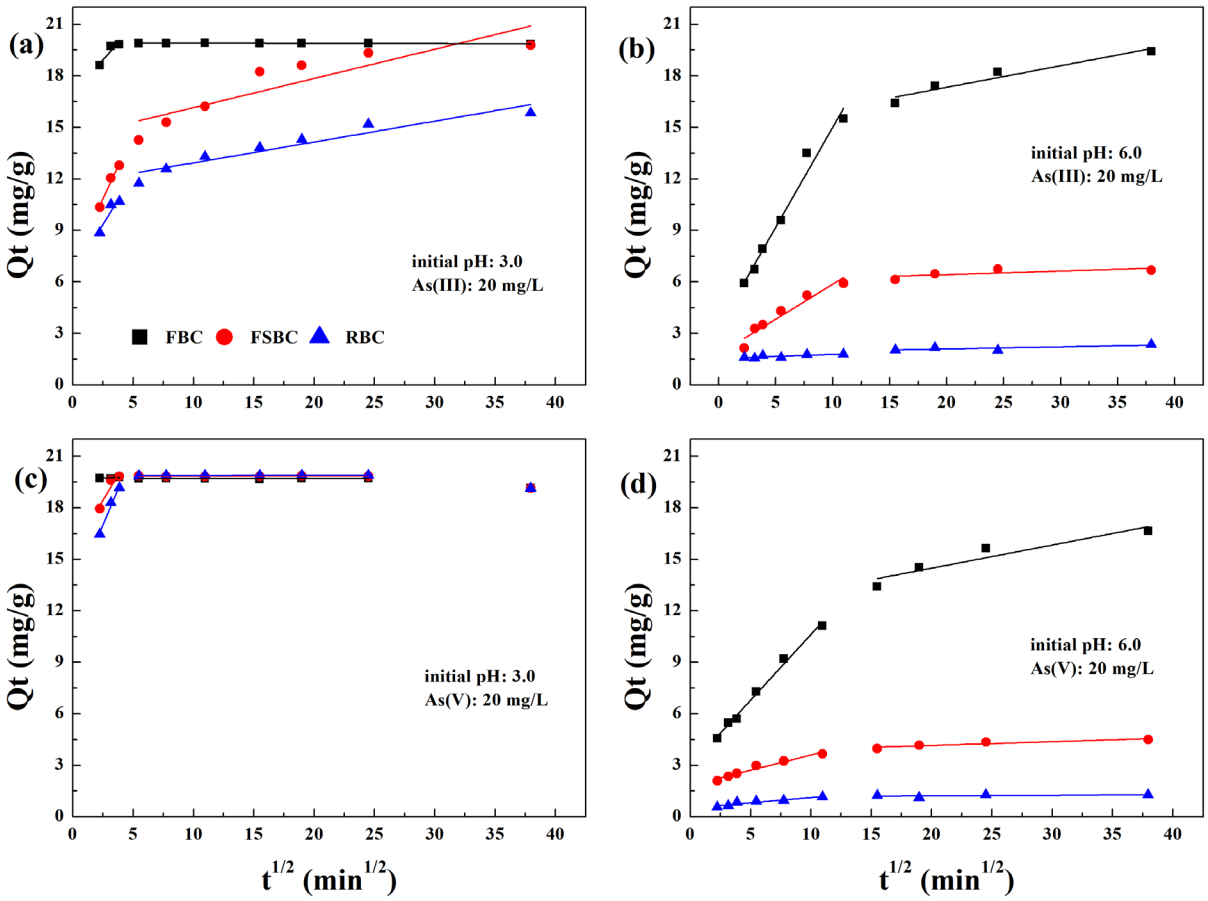

Figure S14 Intraparticle diffusion model fit of adsorption kinetic data of FBC, FSBC and RBC.

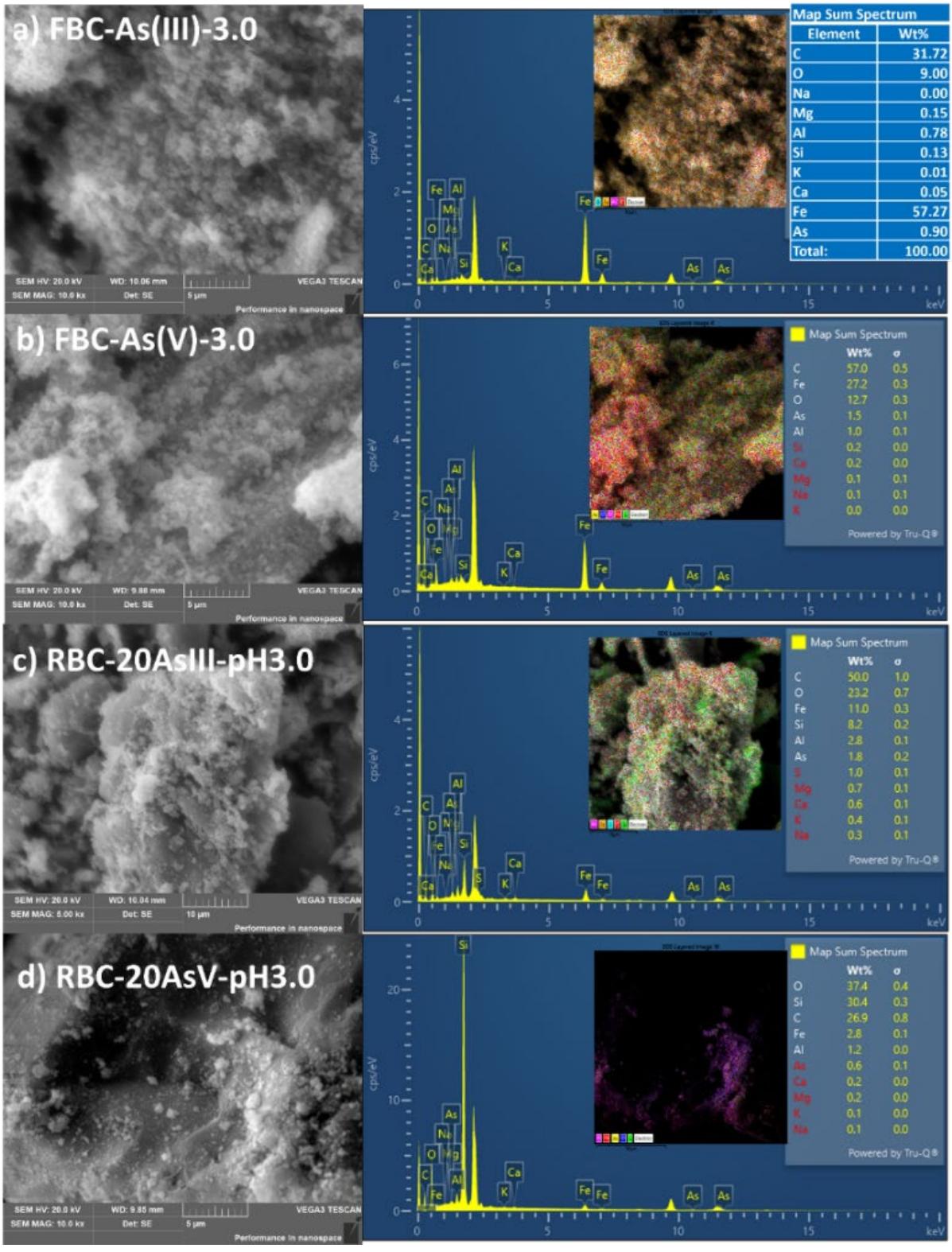
a) FBC-As(III)-3.0
Map Sum Spectrum
Element | Wt%
C | 31.72
O | 9.00
Na | 0.00
Mg | 0.15
Al | 0.78
Si | 0.13
K | 0.01
Ca | 0.05
Fe | 57.27
As | 0.90
Total: | 100.00
b) FBC-As(V)-3.0
Map Sum Spectrum
Wt% σ
C 57.0 0.5
Fe 27.2 0.3
O 12.7 0.3
As 1.5 0.1
Al 1.0 0.1
Si 0.2 0.0
Ca 0.2 0.0
Mg 0.1 0.1
Na 0.1 0.1
K 0.0 0.0
Powered by Tru-Q®
c) RBC-20AsIII-pH3.0
Map Sum Spectrum
Wt% σ
C 50.0 1.0
O 23.2 0.7
Fe 11.0 0.3
Si 8.2 0.2
Al 2.8 0.1
As 1.8 0.2
S 1.0 0.1
Mg 0.7 0.1
Ca 0.6 0.1
K 0.4 0.1
Na 0.3 0.1
Powered by Tru-Q®
d) RBC-20AsV-pH3.0
Map Sum Spectrum
Wt% σ
O 37.4 0.4
Si 30.4 0.3
C 26.9 0.8
Fe 2.8 0.1
Al 1.2 0.0
As 0.6 0.1
Ca 0.2 0.0
Mg 0.2 0.0
K 0.1 0.0
Na 0.1 0.0
Powered by Tru-Q®
cps/eV
keV

Figure S15 SEM-EDX analysis of FBC (a, b) and RBC (c, d) after As(III) and As(V) removal at pH 3.0.

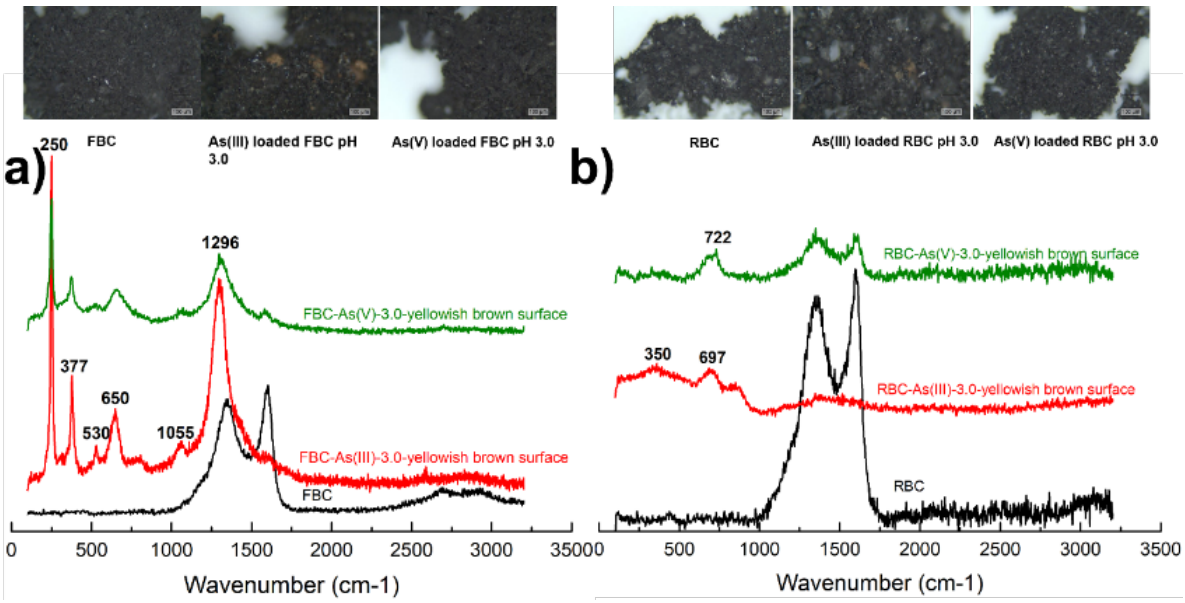

Figure S16 Raman spectra of FBC, FSBC and RBC before and after As(III)/As(V) removal and the corresponding optical microscopic images.

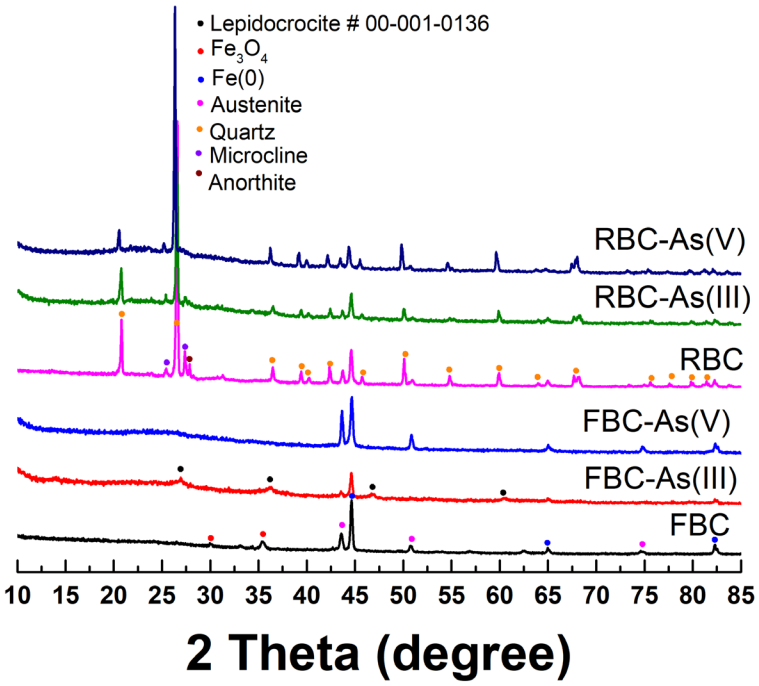

Figure S17 XRD spectra of FBC and RBC before and after As(III) and As(V) removal.

A.3 Supplementary Figures for Chapter 6

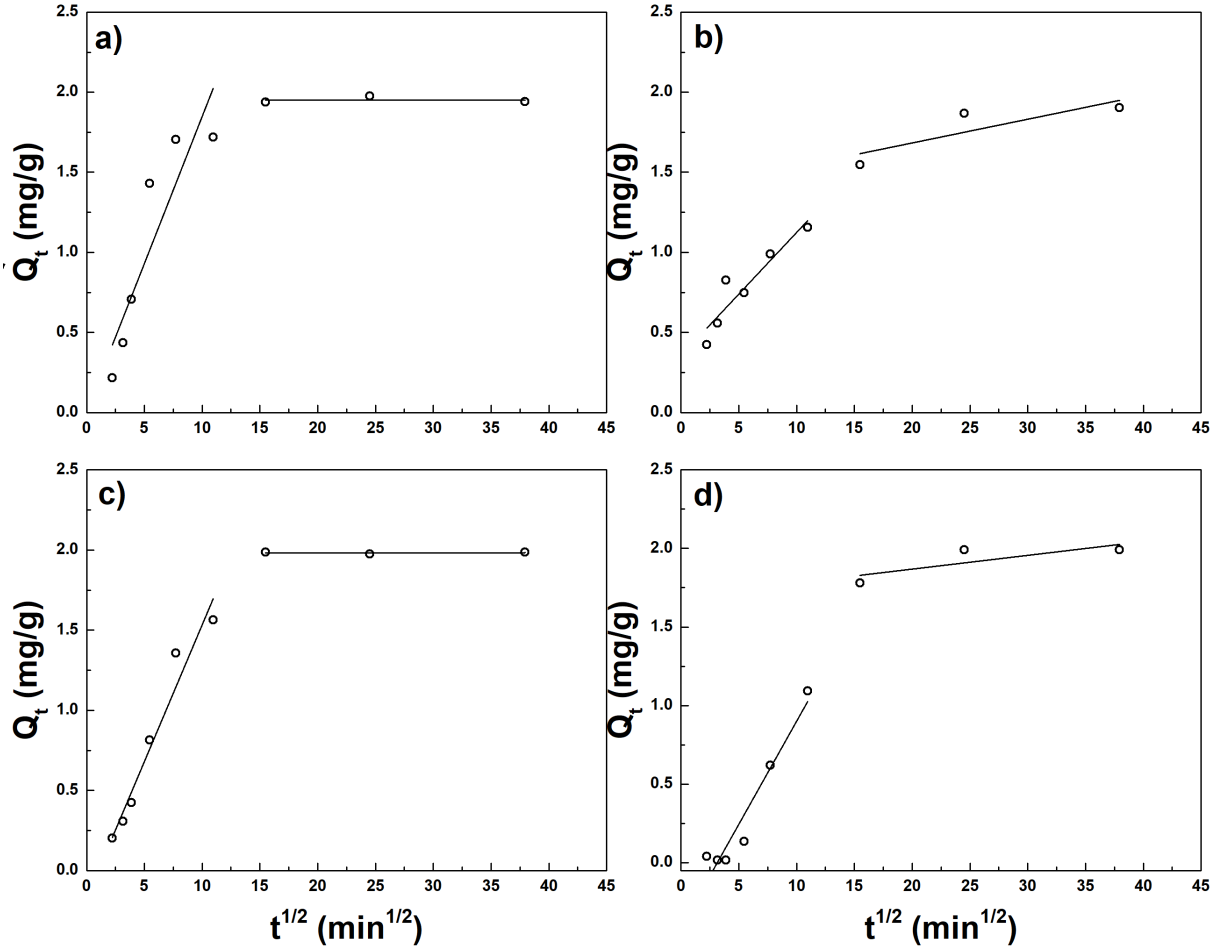

Figure S18 Intraparticle diffusion model fitting of kinetic data a) As(V), b) Cr(VI), c) Cu(II) and d) Pb(II).

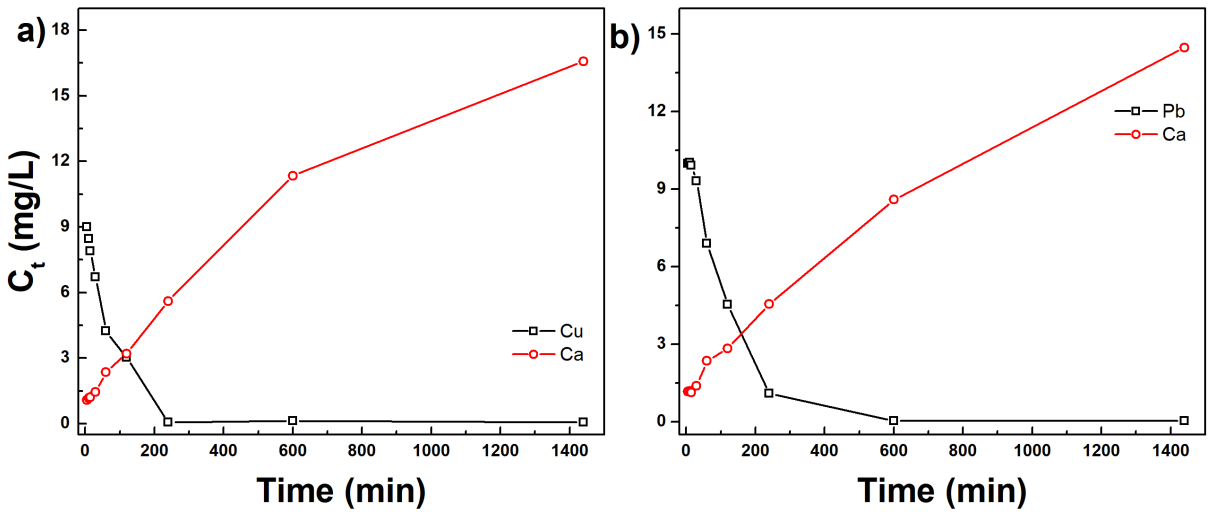

Figure S19 Concentration variations of Pb(II), Cu(II) and Ca(II) as a function of time at pH 3.0 ((a) Pb, C0 = 10 mg/L, (b) Cu, C0 = 10 mg/L).

A.4 Supplementary Figures for Chapter 7

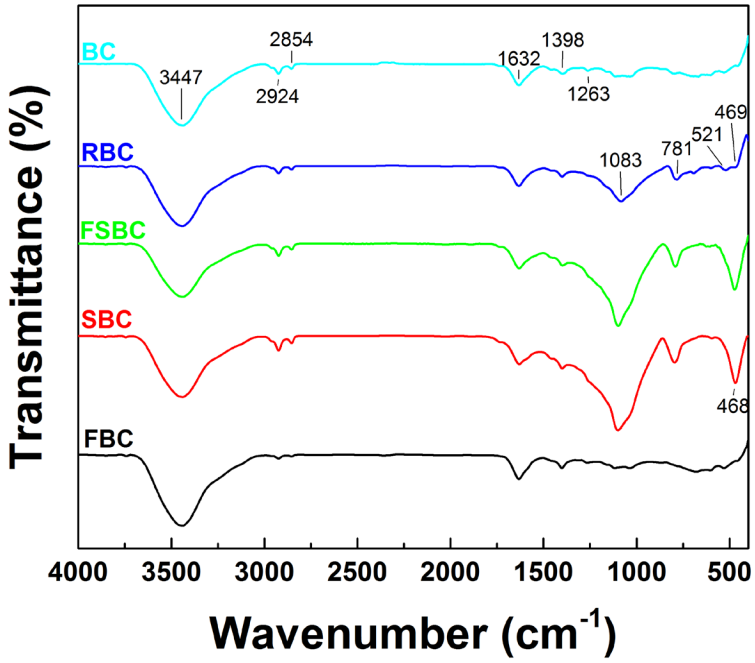

Figure S20 FTIR spectra of mineral BC samples.

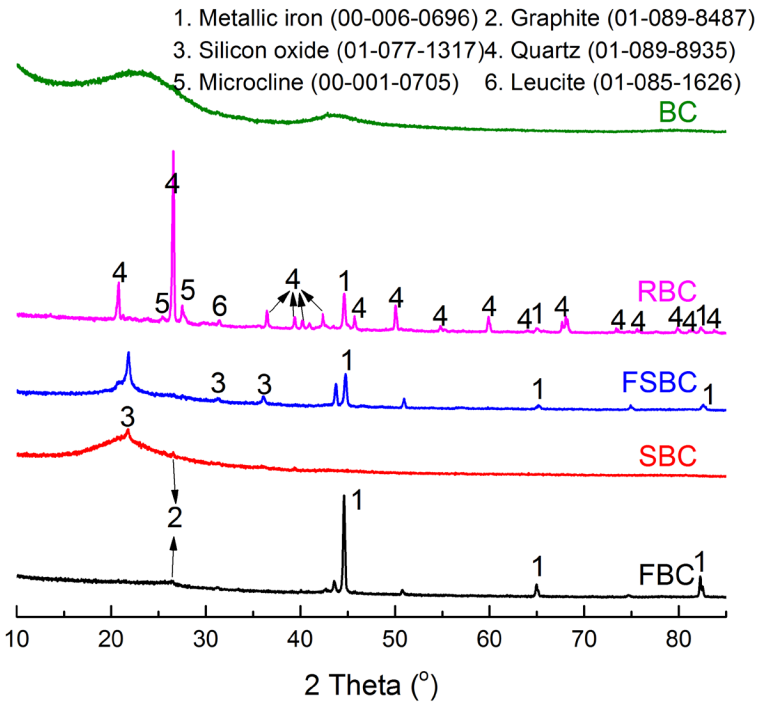

Figure S21 XRD patterns of mineral BC samples.

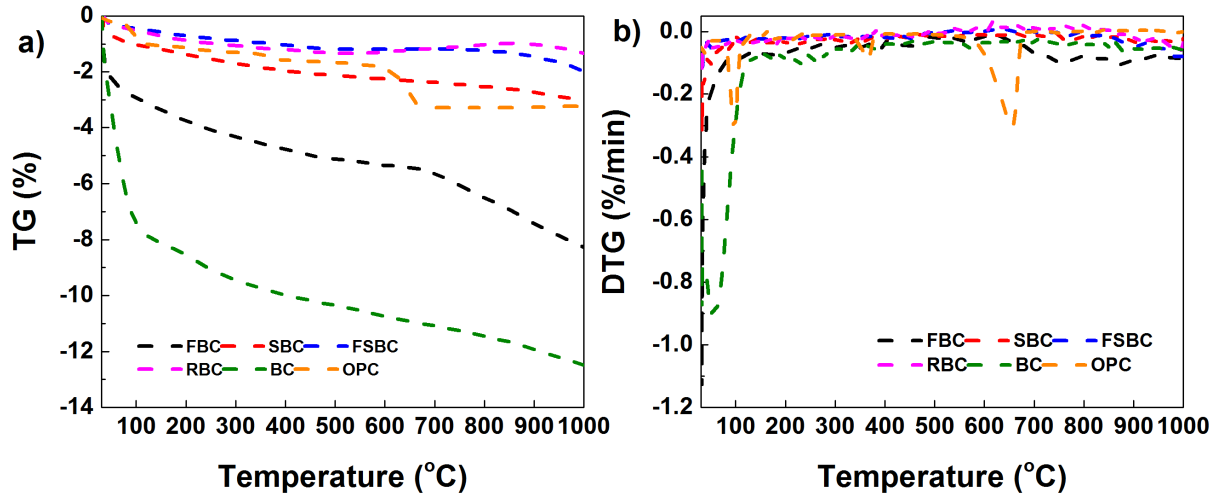

Figure S22 TG and DTG of mineral BC composites.

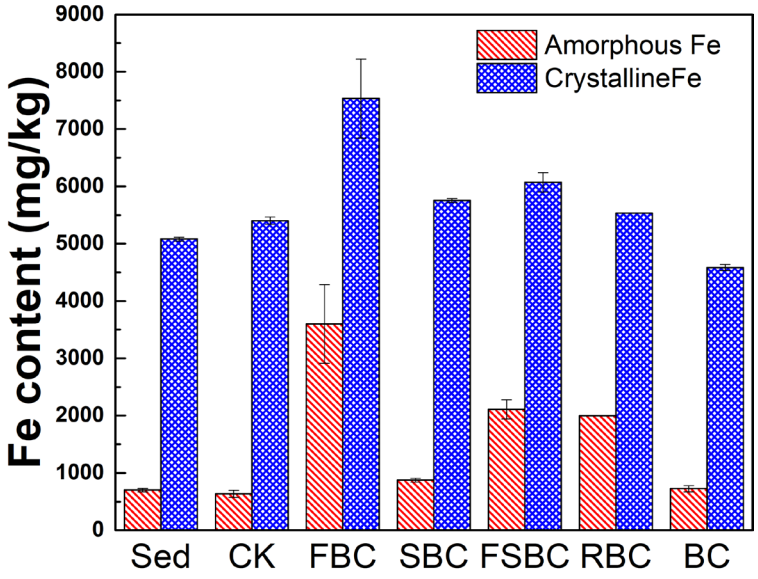

Figure S23 Contents of amorphous Fe and crystalline Fe in raw sediments before and after S/S treatment (Sed represent the raw sediments before S/S treatment).

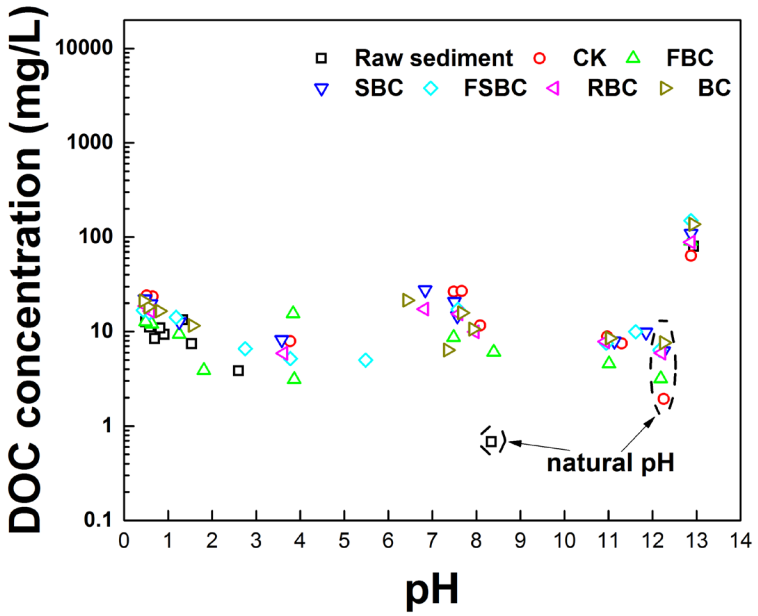

Figure S24 DOC as a function of pH from the raw sediments before and after S/S treatment.

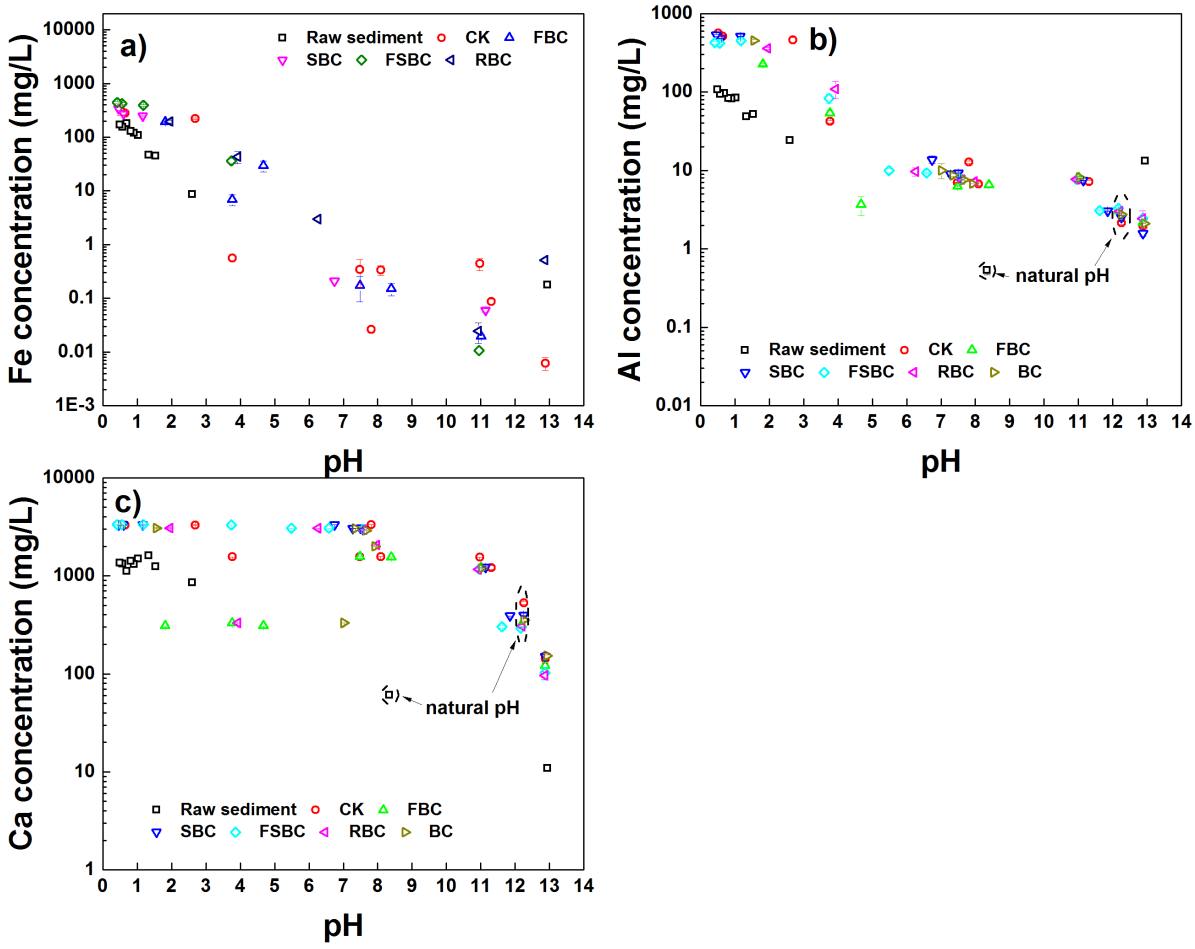

Figure S25 pH dependent leaching behaviours of Fe, Al and Ca from the raw sediments before and after S/S treatment.

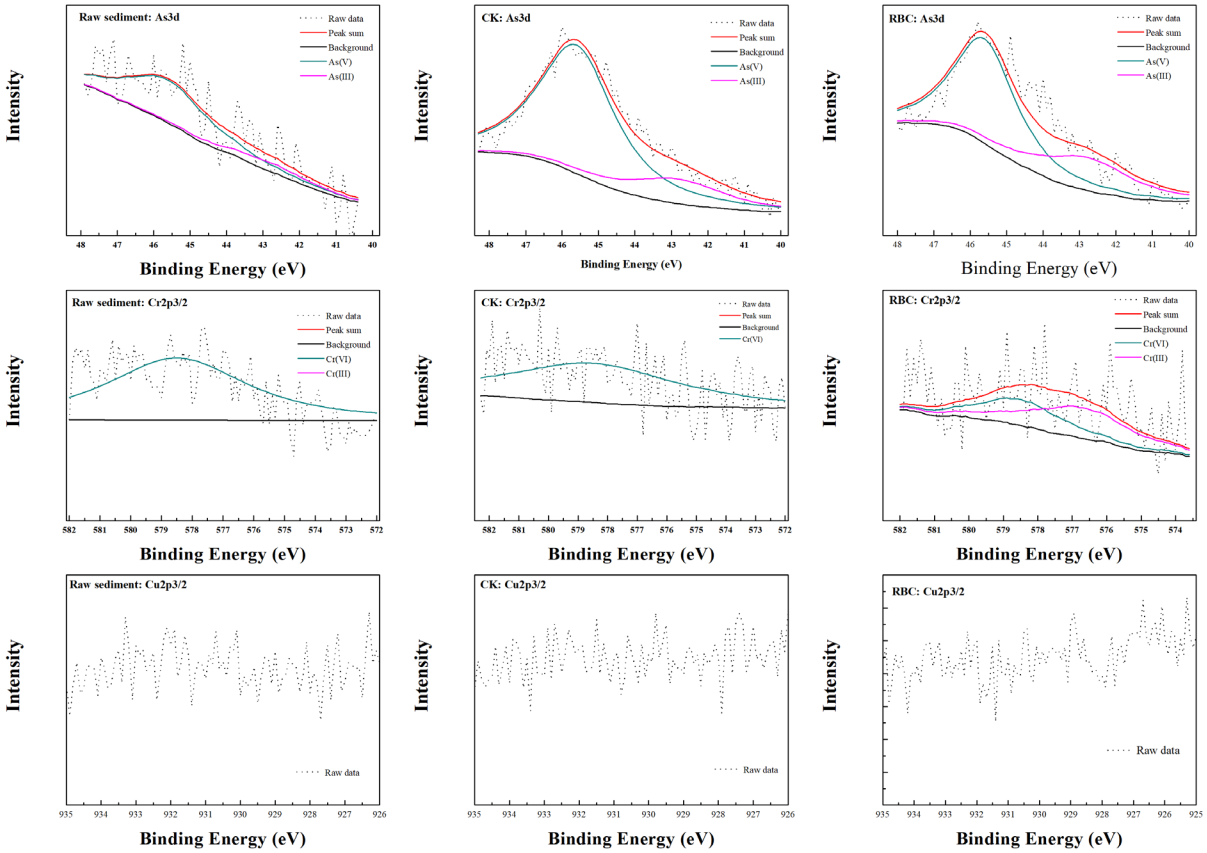

Figure S26 XPS of As3d, Cr2p3/2 and Cu2p3/2 for the raw sediment, CK and RBC groups.

APPENDIX B SUPPLEMENTARY TABLES

B.1 Supplementary Tables for Chapter 4

Table S1 Parameters corresponding to the pseudo-second-order kinetic model.

Concentration (mg/L)	$Q_{e,exp}$ **(mg/g)**	k_2 **(1/min)**	R^2	$Q_{e,cal}$ **((mg/g)**
10	10.1	0.1215	0.9952	10.0
20	8.8	0.0289	0.9992	8.7
50	6.3	0.0738	0.9999	6.9

Table S2 Leaching of toxic metals from LR-1050 (pH = 2.0, Cr(VI) = 10 mg/L, Time = 4 h).

Element	**Ba**	**Cd**	**Cu**	**Ni**	**Zn**	**Sr**
At pH 2.0	N.D.	0.056	0.36	0.014	0.16	0.29
Discharge to sewers leading to government sewage sludge treatment plants	0.4 ~ 8	0.001-0.2	1 ~ 4	0.6-4	0.6-5	N.G.

Note: N.D. not detected; N.G. not regulated. The concentrtaion range is used for effluents with different flow rates.

B.2 Supplementary Tables for Chapter 5

Table S3 Textural properties of biochar samples.

Sample	BET surface area (m^2/g)	Total pore volume (cm^3/g)	BJH aver pore size (nm)
BC	20.1	0.014	6.1
FBC	189.0	0.132	5.3
SBC	1.6	0.002	54.3
FSBC	50.8	0.0419	5.7
RBC	73.0	0.058	8.5

Table S4 Particle size of ZVI on FBC, FSBC and RBC.

Sample	Fe(0) (110) facet		
	2θ	FWHM	D (nm)
FBC	44.65	0.2165	38
FSBC	44.59	0.1968	42
RBC	44.54	0.1771	46

Note: The Fe crystallite sizes on the iron-biochar samples were calculated by the Debye-Scherrer equation: $D = {k \cdot \lambda}/{\beta \cdot \cos\theta}$, where D (nm) is the crystal size, k (0.89) is the crystalline shape factor, λ (0.15406 nm) is the wavelength of X-ray, β is the full width at half the maximum (FWHM) in radians of the X-ray diffraction peak and θ is the Braggs' angle (deg.). Only the main characteristic peaks of Fe(0) were used to calculate the mineral sizes.

Table S5 Intensity ratio of I_D/I_G.

Group	I_D/I_G
FBC	0.86
SBC	0.82
FSBC	0.88
RBC	0.86
BC	0.85

Table S6 Parameters corresponding to PFO and PSO kinetic models.

Group	**As(III)/As(V)**	**Initial pH**	$Q_{e,exp}$ **(mg/g)**	**PFO kinetic model**			PSO kinetic model		
				k_1 **(1/min)**	$\mathbf{R^2}$	$Q_{e,cal}$ **(mg/g)**	k_2 (1/min)	R^2	$Q_{e,cal}$ (mg/g)
FBC	As(III)	3.0	19.99	-	-	-	-	1	19.84
		6.0	19.43	0.0059	0.9644	12.83	0.0017	0.9991	19.65
	As(V)	3.0	19.80	-	-	-	0.0011	0.9998	19.19
		6.0	16.66	0.0052	0.9866	12.12	0.0014	0.9983	16.98
FSBC	As(III)	3.0	19.8	0.0044	0.9871	6.63	0.0033	0.9997	19.92
		6.0	6.75	0.0036	0.4235	1.64	0.0099	0.9998	6.77
	As(V)	3.0	19.86	-	-	-	0.0006	0.9997	19.19
		6.0	4.51	0.0037	0.9775	1.72	0.0111	0.9995	4.38
RBC	As(III)	3.0	15.84	0.0047	0.9756	5.87	0.0036	0.9991	15.87
		6.0	2.35	0.0037	0.9147	-	0.0189	0.9958	2.33
	As(V)	3.0	19.89	-	-	-	0.0002	0.9997	19.19
		6.0	1.30	0.0025	0.4993	3.07	0.0531	0.9988	1.29

Note: $Q_{e,exp}$ and $Q_{e,cal}$ are the equilibrium adsorption capacity calculated by the experimental data and kinetic model respectively. – results for a poor fit between the experimental data and the corresponding model.

Table S7 Parameters estimated from intraparticle diffusion model.

Group	As(III)/As(V)	Initial pH	k_{int-1}	R^2	k_{int-2}	R^2
FBC	As(III)	3.0	0.7673	0.7414	-	-
		6.0	1.1640	0.9707	0.1255	0.9051
	As(V)	3.0	-	-	-	-
		6.0	0.7670	0.9908	0.1347	0.8418
FSBC	As(III)	3.0	1.5092	0.9566	0.1701	0.7596
		6.0	0.4068	0.9157	0.0207	0.3071
	As(V)	3.0	1.1917	0.7678	-	-
		6.0	0.1773	0.9523	0.0218	0.8191
RBC	As(III)	3.0	1.1489	0.7575	0.1216	0.8946
		6.0	0.0237	0.5074	0.0122	0.4196
	As(V)	3.0	1.6675	0.9664	-	-
		6.0	0.0617	0.8634	-	-

Note: the unit of k_{int-1} and k_{int-2} is $mg\ L^{-1}min^{-1/2}$.

Table S8 Parameters corresponding to the Langmuir and Freundlich isotherm models of As(III)/As(V) sorption by the FBC, FSBC and RBC at pH 3.0 and 6.0.

Sample	Arsenic	Initial pH	Langmuir isotherm model			Freundlich isotherm model		
			Q_m (mg/g)	K_L (L/mg)	R^2	$K_F(mg/g)/(mg/g^{1/n})$	n	R^2
FBC	As(III)	3.0	100.32	4.3828	0.9196	42.40	4.0437	0.8975
		6.0	22.03	0.2061	0.9364	5.97	3.4968	0.7789
	As(V)	3.0	264.45	0.1133	0.9169	53.95	2.5089	0.9831
		6.0	97.22	0.0299	0.9509	6.07	1.8336	0.8830
FSBC	As(III)	3.0	28.79	4.9757	0.7965	14.37	6.366	0.6666
		6.0	9.49	0.0359	0.9465	1.49	2.8918	0.9686
	As(V)	3.0	89.74	4.6396	0.8114	35.77	4.4091	0.8289
		6.0	36.76	0.0065	0.9885	0.62	1.4811	0.9950
RBC	As(III)	3.0	17.44	11.6969	0.8831	10.67	8.3890	0.6241
		6.0	4.35	0.0582	0.8910	0.57	2.3337	0.7659
	As(V)	3.0	57.56	6.5663	0.7939	24.11	4.4249	0.9354
		6.0	2.88	0.1931	0.9770	0.85	3.3340	0.8575

Table S9 Comparison of adsorption capacities of different iron-biochar carbon composites for arsenic removal.

Adsorbent	Pyrolysis condition	Iron phase	Initial pH (final pH)	Qm (mg/g)		Fe content (wt. %)	Fe content-normalized Qm (mg/g-Fe)		Reference
				As(III)	As(V)		As(III)	As(V)	
Iron-based chemicals modified biochar									
Biochar supported nZVI	600ºC, 1 h + borohydride reduction	ZVI, maghemite	4.1		124.5	10.5		1185.71	(S. Wang et al., 2017)
Fe-imgregnated biochar	600ºC, 2 h + hydrolysis	geothite	5.8		2.16	3.88		55.67	(Hu et al., 2015)
Fe-imgregnated biochar	Wet impregnation + 600ºC, 1h	maghemite, hematite	7.0		6.80	6.05		112.40	(He et al., 2018)

ZVI biochar	900ºC, 2h	ZVI, wüstite, fayalite			15.58/7.92	-		26.12/14.21	(Bakshi et al., 2018)
Irron oxide decorated biochar fibers	800ºC, 2h + wet impregation	akaganéite	7	6.07	8.13	8.68	69.93	93.66	(Wei et al., 2019)
ZVI biochar	900ºC, 2h	ZVI, magnetite	As(III): 9.0, As(V): 6.0	129.24	127.15	30	430.80	423.83	(Xu et al., 2022)
Iron-biochar	850ºC, 1 h	ZVI, magnetite	6.0(9.5-10.0)	42.40	91.22	16.9	251.48	541.04	This study
Iron containing solid waste modified biochar									
Red mud biochar	600ºC, 6h	hematite, magnetite, geothite	-	0.52	5.92				(Chuan Wu et al., 2017)

Red mud biochar	660°C,	magnetite, ZVI	Unknown(6.5)		33.9				(Yoon et al., 2020)
ISSA residue biochar	850°C, 1h	ZVI, austenite, iron silicon	3.0(4.0) 6.0(8.0-9.0)	17.44 10.67	57.56 2.88	7.06	247.03 151.13	815.30 40.79	This study

Table S10 Leaching of reactive silica from all samples at pH 3.0 and 6.0.

Sample	Reactive silica (mg/L)	
	pH=3.0	**pH=6.0**
BC	3.54	2.99±0.16
FBC	1.77	2.54±0.16
RBC	6.63±0.94	8.29±0.47
Reaction condition: 1g/L, 24 h, ambient temperature		

B.3 Supplementary Tables for Chapter 6

Table S11 Parameters corresponding to PFO and PSO kinetic models.

Metal	$Q_{e,exp}$ (mg/g)	PFO kinetic model				PFO kinetic model			
		k_1 (1/min)	R^2	$Q_{e,cal}$ (mg/g)	χ^2	k_2 (1/min)	R^2	$Q_{e,cal}$ (mg/g)	χ^2
As(V)	1.94	0.035	0.971	1.92	0.014	0.021	0.943	2.08	0.028
Cr(VI)	1.90	0.020	0.733	1.68	0.080	0.016	0.866	1.82	0.040
Cu(II)	1.99	0.017	0.990	1.97	0.004	0.010	0.984	2.17	0.009
Pb(II)	1.99	0.006	0.980	2.02	0.015	0.003	0.957	2.42	0.033

Note: $Q_{e,exp}$ and $Q_{e,cal}$ are the equilibrium adsorption capacity calculated by the experimental data and kinetic model respectively

Table S12 Parameters estimated from intraparticle diffusion model.

Metal	k_{int-1}	R^2	k_{int-2}	R^2
As(V)	0.184	0.772	-	-
Cr(VI)	0.077	0.840	0.015	0.461
Cu(II)	0.171	0.945	-	-
Pb(II)	0.131	0.916	0.008	0.793

Note: the unit of $k_{int-1}$and k_{int-2} is $mg\ L^{-1}min^{-1/2}$.

Table S13 Parameters corresponding to the Langmuir and the Freundlich isotherm models.

Metal	Langmuir isotherm model				Freundlich isotherm model			
	Q_m (mg/g)	K_L (L/mg)	R^2	χ^2	$K_F(mg/g)/(mg/g^{1/n})$	n	R^2	χ^2
As(V)	14.11	0.172	0.969	0.739	2.82	2.33	0.960	0.789
Cr(VI)	5.79	0.108	0.907	0.293	1.71	3.81	0.938	0.195
Cu(II)	15.57	10.214	0.945	2.406	8.54	6.11	0.887	4.834
Pb(II)	23.52	0.460	0.928	5.685	9.78	4.74	0.851	11.735

Table S14 Comparison of maximum adsorption capacity for As(V), Cr(VI), Cu(II) and Pb(II) with other reported granular adsorbents.

Adsorbent	Raw materials for adsorbent synthesis	Size (mm)	Dosage (g/L)	pH	Equilibrium time (h)	Temperature (°C)	Adsorption capacity (mg/g)	Reference
Granular activated carbon	Granular activated carbon	0.6	-	5.5	24	25	Cu(II): 5.85 Pb(II):13.33	(Sulaymon et al., 2009)
Schwertmannite granules	$FeCl_3$	1-2	0.5	7.0	24	25	As(V): 5-34 mg/g	(Dou et al., 2013)
Fe-Mn binary oxide impregnated chitosan bead	$FeSO_4$, $FeCl_3$, $KMnO_4$, chitosan	1.6-1.8	1	7.0	36	25	As(V): 39.1	(Qi et al., 2015)
Granular activated carbon	Granular activated carbon, $FeCl_2$	0.3-0.6	0.1	6	6	25	As(V): 1.01	(Kalaruban et al., 2019)
Iron incorporated granular activated carbon							As(V): 1.43	

Chitosan beads	Iron sludge, chitosan, acetic acid, NH_4OH	1.6-1.8	1	6.5	24	25	As(V): 114.79	(Zeng et al., 2020)
(Modified)Lightweight expanded clay aggregate	Clay, $MgCl_2$, and H_2O_2	0.84-2	6	3.0	-	20	Cr(VI): 198.39-236.24	(Kalhori et al., 2013)

B.4 Supplementary Tables for Chapter 7

Table S15 Total carbon organic and inorganic carbon, total organic matter.

Group	Total organic matter* (%)	Total carbon** (%)	Inorganic carbon** (%)	Total organic carbon** (%)
Raw sed	1.97 ± 0.11	0.82	0.36	0.46
CK	3.28 ± 0.31	1.23	0.64	0.59
FBC	4.86 ± 0.40	3.01	0.53	2.48
SBC	3.78 ± 0.24	1.59	0.51	1.08
FSBC	3.50 ± 0.07	1.52	0.59	0.93
RBC	3.96 ± 0.27	1.43	0.52	0.91
BC	6.05 ± 0.53	3.27	0.12	3.15

*: determined by mass difference after heating dried (105ºC) samples at 550ºC for 4 h; **: determined by TOC analyzer.

Table S16 Elemental composition of S/S products.

Component (wt. %)	Raw sediment	CK	FBC	SBC	FSBC	RBC	BC
Na_2O	2.38			1.88			1.79
MgO	0.74	0.49	0.63	0.56	0.52	0.71	0.39
Al_2O_3	15.4	10.7	11.2	11.1	10.9	10.6	11.1
SiO_2	70.6	66.3	64.5	63.6	66	66.6	65.1
P_2O_5	0.12	0.12	0.14	0.14	0.11	0.16	0.13
SO_3	0.76	1.17	1.22	1.22	1.16	1.21	1.21
Cl	0.95	0.57	0.71	0.68	0.74	0.69	0.74

K_2O	3.97	3.13	3.26	3.22	3.31	3.45	3.36
CaO	3.24	15.3	14.8	15.4	14.2	14	14
TiO_2	0.16	0.14	0.2	0.16	0.23	0.24	0.2
Cr_2O_3	0.08	0.05	0.08	0.06	0.06	0.08	0.08
MnO	0.06	0.06	0.05	0.05	0.07	0.05	0.05
Fe_2O_3	1.45	1.8	3.08	1.84	2.5	2.18	1.73
CuO	0.01	0.02	0.02	0.02	0.02	0.02	0.02
As_2O_3	0.01		0.01	0.01	0.02	0.01	0.01
Others	0.07	0.15	0.1	0.06	0.16	0	0.09

Table S17 Porosity of S/S treated sediments.

Group	**Total intrusion (volume ml/g)**	**Average pore diameter (nm)**	**Total pore area (m2/g)**	**Porosity (%)**
CK	0.1388	56.8	9.774	25.90
FBC	0.1507	69.8	8.631	27.5289
SBC	0.1499	57.4	10.446	27.4796
FSBC	0.1501	63.1	9.510	27.5772
RBC	0.1536	62.3	9.865	28.2295
BC	0.1640	68.1	9.629	29.0566

REFERENCES

Abdel Wahaab, R., Mahmoud, M., van Lier, J.B., 2020. Toward achieving sustainable management of municipal wastewater sludge in Egypt: The current status and future prospective. Renew. Sustain. Energy Rev. 127, 109880. https://doi.org/10.1016/j.rser.2020.109880

Adam, C., Peplinski, B., Michaelis, M., Kley, G., Simon, F.G., 2009. Thermochemical treatment of sewage sludge ashes for phosphorus recovery. Waste Manag. https://doi.org/10.1016/j.wasman.2008.09.011

Ahmad, M., Lee, S.S., Dou, X., Mohan, D., Sung, J.K., Yang, J.E., Ok, Y.S., 2012. Effects of pyrolysis temperature on soybean stover- and peanut shell-derived biochar properties and TCE adsorption in water. Bioresour. Technol. 118, 536–544. https://doi.org/10.1016/j.biortech.2012.05.042

Ahmad, M., Rajapaksha, A.U., Lim, J.E., Zhang, M., Bolan, N., Mohan, D., Vithanage, M., Lee, S.S., Ok, Y.S., 2014. Biochar as a sorbent for contaminant management in soil and water: A review. Chemosphere 99, 19–23. https://doi.org/10.1016/j.chemosphere.2013.10.071

Ahmaruzzaman, M., 2011. Industrial wastes as low-cost potential adsorbents for the treatment of wastewater laden with heavy metals. Adv. Colloid Interface Sci. 166, 36–59. https://doi.org/10.1016/j.cis.2011.04.005

Akcil, A., Erust, C., Ozdemiroglu, S., Fonti, V., Beolchini, F., 2015. A review of approaches and techniques used in aquatic contaminated sediments: Metal removal and stabilization by chemical and biotechnological processes. J. Clean. Prod. 86, 24–26. https://doi.org/10.1016/j.jclepro.2014.08.009

Akhter, H., Cartledge, F.K., Roy, A., Tittlebaum, M.E., 1997. Solidification/stabilization of arsenic salts: Effects of long cure times. J. Hazard. Mater. 52, 247–264. https://doi.org/10.1016/S0304-3894(96)01811-0

Amen, R., Bashir, H., Bibi, I., Shaheen, S.M., Niazi, N.K., Shahid, M., Hussain, M.M., Antoniadis, V., Shakoor, M.B., Al-Solaimani, S.G., Wang, H., Bundschuh, J., Rinklebe, J., 2020. A critical review on arsenic removal from water using biochar-based sorbents: The significance of modification and redox reactions. Chem. Eng. J. 396. https://doi.org/10.1016/j.cej.2020.125195

Anderson, M., Skerratt, R.G., 2003. Variability study of incinerated sewage sludge ash in relation to future use in ceramic brick manufacture. Br. Ceram. Trans. 102, 109–113. https://doi.org/10.1179/096797803225001614

Anderson, P.R., Benjamin, M.M., 1985. Effects of Silicon on the Crystallization and Adsorption Properties of Ferric Oxides. Environ. Sci. Technol. 19, 1048–1053. https://doi.org/10.1021/es00141a004

Andreas Luch, 2012. Molecular, Clinical and Environmental Toxicology, Springer, Experientia Supplementum. Springer Basel, Basel. https://doi.org/10.1007/978-3-7643-8340-4

ANZG, 2018. Australian and New Zealand guidelines for fresh and marine water quality. Aust. New Zeal. Gov. Aust. state Territ. Gov. Canberra ACT, Aust. Available www.waterquality.gov.au/anz-guidelines.

AQSIQ, 2002. Marine sediment quality.

ASTM C109/C109M-02, 2020. Standard Test Method for Compressive Strength of Hydraulic Cement Mortars. Annu. B. ASTM Stand. 04, 9. https://doi.org/10.1520/C0109

AWA, A.W.A., 2020. AUSTRALIAN BIOSOLIDS STATISTICS [WWW Document]. URL https://www.biosolids.com.au/guidelines/australian-biosolids-statistics/ (accessed 6.14.22).

Aziz, M.A., Shah, S.S., Nayem, S.M.A., Shaikh, M.N., Hakeem, A.S., Bakare, I.A., 2022. Peat soil-derived silica doped porous graphitic carbon with high yield for high-performance all-solid-state symmetric supercapacitors. J. Energy Storage 50, 104278. https://doi.org/10.1016/j.est.2022.104278

Bakshi, S., Banik, C., Rathke, S.J., Laird, D.A., 2018. Arsenic sorption on zero-valent iron-biochar complexes. Water Res. 137, 153–163. https://doi.org/10.1016/j.watres.2018.03.021

Benassi, L., Zanoletti, A., Depero, L.E., Bontempi, E., 2019. Sewage sludge ash recovery as valuable raw material for chemical stabilization of leachable heavy metals. J. Environ. Manage. 245, 464–470. https://doi.org/10.1016/j.jenvman.2019.05.104

Bilal, M., Shah, J.A., Ashfaq, T., Gardazi, S.M.H., Tahir, A.A., Pervez, A., Haroon, H., Mahmood, Q., 2013. Waste biomass adsorbents for copper removal from industrial wastewater-A review. J. Hazard. Mater. 263, 322–333. https://doi.org/10.1016/j.jhazmat.2013.07.071

Biswas, B.K., Inoue, K., Harada, H., Ohto, K., Kawakita, H., 2009. Leaching of phosphorus from incinerated sewage sludge ash by means of acid extraction followed by adsorption on orange waste gel. J. Environ. Sci. 21, 1753–1760. https://doi.org/10.1016/S1001-0742(08)62484-5

BOS, B. of S., n.d. Statistics of Sewerage in Tokyo [WWW Document]. URL https://www.gesui.metro.tokyo.lg.jp/english/aboutus/ourprofile/07/index.html (accessed 6.14.22).

Bouabidi, Z.B., El-Naas, M.H., Cortes, D., McKay, G., 2018. Steel-Making dust as a potential adsorbent for the removal of lead (II) from an aqueous solution. Chem. Eng. J. 334, 837–844. https://doi.org/10.1016/j.cej.2017.10.073

BS EN, 2016. 13055: 2016 Lightweight Aggregates.

Bureau, E.T. and W., 2002. Management of Dredged/Excavated Sediment. Environment, Transport and Works Bureau.

CCME, C.C. of M. of the E., 2001. Canadian Sediment Quality Guidelines for the Protection of Aquatic Life.

CEDD, C.E. and D.D., n.d. PUBLIC SERVICES & FORMS [WWW Document]. URL https://www.cedd.gov.hk/eng/public-services-forms/fill-management/marine/sediment-disposal/index.html

CFR, C. of F.R., n.d. Title 40 Code of Federal Regulations (40 CFR), part 261 [WWW Document]. URL https://www.ecfr.gov/current/title-40/chapter-I/subchapter-I/part-261/subpart-C/section-261.24 (accessed 7.11.22).

Chai, W.S., Cheun, J.Y., Kumar, P.S., Mubashir, M., Majeed, Z., Banat, F., Ho, S.H., Show, P.L., 2021. A review on conventional and novel materials towards heavy metal adsorption in wastewater treatment application. J. Clean. Prod. 296, 126589. https://doi.org/10.1016/j.jclepro.2021.126589

Chandra, V., Park, J., Chun, Y., Lee, J.W., Hwang, I., Kim, K.S., 2010. Water-Dispersible Magnetite-Reduced Graphene Oxide Composites for Arsenic Removal. ACS Nano 4, 3979–3986. https://doi.org/10.1021/nn1008897

Chang, Z., Long, G., Zhou, J.L., Ma, C., 2020. Valorization of sewage sludge in the fabrication of construction and building materials: A review. Resour. Conserv. Recycl. 154, 104606. https://doi.org/10.1016/j.resconrec.2019.104606

Cheeseman, C.R., Sollars, C.J., McEntee, S., 2003. Properties, microstructure and leaching of sintered sewage sludge ash. Resour. Conserv. Recycl. 40, 13–25. https://doi.org/10.1016/S0921-3449(03)00022-3

Cheeseman, C.R., Virdi, G.S., 2005. Properties and microstructure of lightweight aggregate produced from sintered sewage sludge ash. Resour. Conserv. Recycl. 45, 18–30. https://doi.org/10.1016/j.resconrec.2004.12.006

Chen, H., Wang, Q., 2006. The behaviour of organic matter in the process of soft soil stabilization using cement. Bull. Eng. Geol. Environ. 65, 445–448. https://doi.org/10.1007/s10064-005-0030-1

Chen, L., Wang, X., Yang, H., Lu, Q., Li, D., Yang, Q., Chen, H., 2015. Study on pyrolysis behaviors of non-woody lignins with TG-FTIR and Py-GC/MS. J. Anal. Appl. Pyrolysis 113, 499–507. https://doi.org/10.1016/j.jaap.2015.03.018

Chen, Q.Y., Costa, M., 2021. Arsenic: A Global Environmental Challenge. Annu. Rev. Pharmacol. Toxicol. 61, 47–63. https://doi.org/10.1146/annurev-pharmtox-030220-013418

Chen, R., Zhang, Z., Lei, Z., Sugiura, N., 2012. Preparation of iron-impregnated tablet ceramic adsorbent for arsenate removal from aqueous solutions. Desalination 286, 56–62. https://doi.org/10.1016/j.desal.2011.11.004

Chen, X., Li, J., Xue, Q., Huang, X., Liu, L., Poon, C.S., 2020. Sludge biochar as a green additive in cement-based composites: Mechanical properties and hydration kinetics. Constr. Build. Mater. 262, 120723. https://doi.org/10.1016/j.conbuildmat.2020.120723

Chen, Z., Poon, C.S., 2017. Comparative studies on the effects of sewage sludge ash and fly ash on cement hydration and properties of cement mortars. Constr. Build. Mater. 154, 791–803. https://doi.org/10.1016/j.conbuildmat.2017.08.003

Chen, Z., Zhang, P., Brown, K.G., Branch, J.L., van der Sloot, H.A., Meeussen, J.C.L., Delapp, R.C., Um, W., Kosson, D.S., 2021. Development of a Geochemical Speciation Model for Use in Evaluating Leaching from a Cementitious Radioactive Waste Form. Environ. Sci. Technol. 55, 8642–8653. https://doi.org/10.1021/acs.est.0c06227

Chinoune, K., Bentaleb, K., Bouberka, Z., Nadim, A., Maschke, U., 2016. Adsorption of reactive dyes from aqueous solution by dirty bentonite. Appl. Clay Sci. 123, 64–75. https://doi.org/10.1016/j.clay.2016.01.006

Chiou, I.J., Wang, K.S., Chen, C.H., Lin, Y.T., 2006. Lightweight aggregate made from sewage sludge and incinerated ash. Waste Manag. 26, 1453–1461. https://doi.org/10.1016/j.wasman.2005.11.024

Cho, D.W., Yoon, K., Ahn, Y., Sun, Y., Tsang, D.C.W., Hou, D., Ok, Y.S., Song, H., 2019. Fabrication and environmental applications of multifunctional mixed metal-biochar composites (MMBC) from red mud and lignin wastes. J. Hazard. Mater. 374, 412–419. https://doi.org/10.1016/j.jhazmat.2019.04.071

CN-GB, 2007. Identification standards for hazardous wastes. Identification for extraction toxicity.

Cornelis, G., Poppe, S., Van Gerven, T., Van den Broeck, E., Ceulemans, M., Vandecasteele, C., 2008. Geochemical modelling of arsenic and selenium leaching in alkaline water treatment sludge from the production of non-ferrous metals. J. Hazard. Mater. 159, 271–279. https://doi.org/10.1016/j.jhazmat.2008.02.016

Costa, R.C.C., Moura, F.C.C., Oliveira, P.E.F., Magalhães, F., Ardisson, J.D., Lago, R.M., 2010. Controlled reduction of red mud waste to produce active systems for environmental applications: Heterogeneous Fenton reaction and reduction of Cr(VI). Chemosphere 78, 1116–1120. https://doi.org/10.1016/j.chemosphere.2009.12.032

Cuong, D.V., Wu, P.C., Chen, L.I., Hou, C.H., 2021. Active MnO2/biochar composite for efficient As(III) removal: Insight into the mechanisms of redox transformation and adsorption. Water Res. 188, 116495. https://doi.org/10.1016/j.watres.2020.116495

Dai, Y., Hu, Y., Jiang, B., Zou, J., Tian, G., Fu, H., 2016. Carbothermal synthesis of ordered mesoporous carbon-supported nano zero-valent iron with enhanced stability and activity for hexavalent chromium reduction. J. Hazard. Mater. 309, 249–258. https://doi.org/10.1016/j.jhazmat.2015.04.013

Das, S., Hendry, M.J., 2011. Application of Raman spectroscopy to identify iron minerals commonly found in mine wastes. Chem. Geol. 290, 101–108. https://doi.org/10.1016/j.chemgeo.2011.09.001

DESA UN, 2015. Transforming our world: The 2030 agenda for sustainable development [WWW Document]. URL https://sdgs.un.org/2030agenda (accessed 6.20.22).

DESA UN, n.d. SUATAINABLE DEVELOPMENT GOALS KNOWLEDGE PLATFORM Water and Sanitation [WWW Document]. URL https://sdgs.un.org/topics/water-and-sanitation (accessed 7.25.22).

Devi, P., Kothari, P., Dalai, A.K., 2020. Stabilization and solidification of arsenic and iron contaminated canola meal biochar using chemically modified phosphate binders. J. Hazard. Mater. 385, 121559. https://doi.org/10.1016/j.jhazmat.2019.121559

Dixit, A., Gupta, S., Pang, S.D., Kua, H.W., 2019. Waste Valorisation using biochar for cement replacement and internal curing in ultra-high performance concrete. J. Clean. Prod. 238, 117876. https://doi.org/10.1016/j.jclepro.2019.117876

Donatello, S., 2009. Characteristics of incinerated sewage sludge ashes: potential for phosphate extraction and re-use as a pozzolanic material in construction products. Imperial College London. https://doi.org/10.13140/RG.2.2.33926.63040

Donatello, S., Cheeseman, C.R., 2013. Recycling and recovery routes for incinerated sewage sludge ash (ISSA): A review. Waste Manag. 33, 2328–2340.

Donatello, S., Freeman-Pask, A., Tyrer, M., Cheeseman, C.R., 2010a. Effect of milling and acid washing on the pozzolanic activity of incinerator sewage sludge ash. Cem. Concr. Compos. 32, 54–61. https://doi.org/10.1016/j.cemconcomp.2009.09.002

Donatello, S., Tong, D., Cheeseman, C.R., 2010b. Production of technical grade phosphoric acid from incinerator sewage sludge ash (ISSA). Waste Manag. 30, 1634–1642. https://doi.org/10.1016/j.wasman.2010.04.009

Dou, X., Mohan, D., Pittman, C.U., 2013. Arsenate adsorption on three types of granular schwertmannite. Water Res. 47, 2938–2948. https://doi.org/10.1016/j.watres.2013.01.035

Du, J., Lu, J., Wu, Q., Jing, C., 2012. Reduction and immobilization of chromate in chromite ore processing residue with nanoscale zero-valent iron. J. Hazard. Mater. 215–216, 152–158. https://doi.org/10.1016/j.jhazmat.2012.02.049

Du Laing, G., 2011. Redox Metal Processes and Controls in Estuaries, in: Treatise on Estuarine and Coastal Science. Elsevier, pp. 115–141. https://doi.org/10.1016/B978-0-12-374711-2.00406-X

Ducoli, S., Zacco, A., Bontempi, E., 2021. Incineration of sewage sludge and recovery of residue ash as building material: A valuable option as a consequence of the COVID-19 pandemic. J. Environ. Manage. 282, 111966. https://doi.org/10.1016/j.jenvman.2021.111966

DWSAC, D.W.S.A.C., 2021. Hong Kong Drinking Water Standards (HKDWS).

Ebbers, B., Ottosen, L.M., Jensen, P.E., 2015. Comparison of two different electrodialytic cells for separation of phosphorus and heavy metals from sewage sludge ash. Chemosphere 125, 122–129. https://doi.org/10.1016/j.chemosphere.2014.12.013

EC, E.C., 2018. DIRECTIVE OF THE EUROPEAN PARLIAMENT AND OF THE COUNCIL on the quality of water intended for human consumption (recast).

Ehrensberger, K., Palumbo, R., Larson, C., Steinfeld, A., 1997. Production of Carbon from Carbon Dioxide with Iron Oxides and High-Temperature Solar Energy. Ind. Eng. Chem. Res. 36, 645–648. https://doi.org/10.1021/ie950780y

Engelsen, C.J., Van Der Sloot, H.A., Wibetoe, G., Justnes, H., Lund, W., Stoltenberg-Hansson, E., 2010. Leaching characterisation and geochemical modelling of minor and trace elements released from recycled concrete aggregates. Cem. Concr. Res. 40, 1639–1649. https://doi.org/10.1016/j.cemconres.2010.08.001

EPA, E.P.A., 2022. Basic Information about Biosolids [WWW Document]. URL https://www.epa.gov/biosolids/basic-information-about-biosolids#uses) (accessed 6.14.22).

EPA, E.P.A., 2014. Priority Pollutant List [WWW Document]. URL https://www.epa.gov/sites/default/files/2015-09/documents/priority-pollutant-list-epa.pdf (accessed 6.16.22).

EPD, E.P.D., 2021. Marine Water Quality in Hong Kong in 2020.

EPD, E.P.D., 2015. Sludge Reception [WWW Document]. URL https://www.epd.gov.hk/epd/english/environmentinhk/waste/prob_solutions/reception.html#:~:text=At present%2C there is about,Drainage Services Department for treatment. (accessed 6.14.22).

Epd, H.K., 2011. Practice guide for investigation and remediation of contaminated land. Environ. Prot. Dep. Hong Kong.

EPD, H.K., 2021. MONITORING OF SOLID WASTE IN HONG KONG-Waste Statistics for 2020.

EPD, P.R., 2010. Contract for sludge treatment facility in Tuen Mun signed [WWW Document]. URL https://www.info.gov.hk/gia/general/201010/27/P201010270116.htm (accessed 6.2.22).

Fan, J., Chen, X., Xu, Z., Xu, X., Zhao, L., Qiu, H., Cao, X., 2020. One-pot synthesis of nZVI-embedded biochar for remediation of two mining arsenic-contaminated soils: Arsenic immobilization associated with iron transformation. J. Hazard. Mater. 398, 122901. https://doi.org/10.1016/j.jhazmat.2020.122901

Fang, L., Li, J. shan, Donatello, S., Cheeseman, C.R., Poon, C.S., Tsang, D.C.W., 2020a. Use of Mg/Ca modified biochars to take up phosphorus from acid-extract of incinerated sewage sludge ash (ISSA) for fertilizer application. J. Clean. Prod. 244, 118853. https://doi.org/10.1016/j.jclepro.2019.118853

Fang, L., Li, J. shan, Guo, M.Z., Cheeseman, C.R., Tsang, D.C.W., Donatello, S., Poon, C.S., 2018. Phosphorus recovery and leaching of trace elements from incinerated sewage sludge ash (ISSA). Chemosphere 193, 278–287. https://doi.org/10.1016/j.chemosphere.2017.11.023

Fang, L., Li, L., Wang, Q., Li, J. shan, Poon, C.S., 2022. Agronomic effectiveness of recovered phosphate fertilizer produced from incinerated sewage sludge ash. Waste Dispos. Sustain. Energy 4, 157–167. https://doi.org/10.1007/s42768-022-00097-0

Fang, L., Wang, Q., Li, J., Poon, C.S., Cheeseman, C.R., Tsang, D.C.W., 2020b. Feasibility of wet-extraction of phosphorus from incinerated sewage sludge ash (ISSA) for phosphate fertilizer production : A critical review. Crit. Rev. Environ. Sci. Technol. 0, 1–33. https://doi.org/10.1080/10643389.2020.1740545

Farias, D.R., Hurd, C.L., Eriksen, R.S., Macleod, C.K., 2018. Macrophytes as bioindicators of heavy metal pollution in estuarine and coastal environments. Mar. Pollut. Bull. 128, 175–184. https://doi.org/10.1016/j.marpolbul.2018.01.023

Fendorf, S.E., Li, G., 1996. Kinetics of chromate reduction by ferrous iron. Environ. Sci. Technol. 30, 1614–1617. https://doi.org/10.1021/es950618m

Ferrari, A.C., Robertson, J., 2000. Interpretation of Raman spectra of disordered and amorphous carbon. Phys. Rev. B 61, 14095–14107. https://doi.org/10.1103/PhysRevB.61.14095

Franz, M., 2008. Phosphate fertilizer from sewage sludge ash (SSA). Waste Manag. 28, 1809–1818. https://doi.org/10.1016/j.wasman.2007.08.011

FSO, F.S.O., 2022. Result 32214-0001 [WWW Document]. URL https://www-genesis.destatis.de/genesis/online?sequenz=tabelleErgebnis&selectionname=32214-0001#abreadcrumb (accessed 6.13.22).

Fu, F., Ma, J., Xie, L., Tang, B., Han, W., Lin, S., 2013. Chromium removal using resin supported nanoscale zero-valent iron. J. Environ. Manage. 128, 822–827. https://doi.org/10.1016/j.jenvman.2013.06.044

Gao, C., Sui, J., Chen, K., Chen, Z., Wu, W., Guo, Z., 2021. Efficient recovery of U(VI) from strongly alkaline solution using nanoscale zero-valent iron. J. Environ. Chem. Eng. 9, 106091. https://doi.org/10.1016/j.jece.2021.106091

Gao, X., Chen, C.T.A., 2012. Heavy metal pollution status in surface sediments of the coastal Bohai Bay. Water Res. 46, 1901–1911. https://doi.org/10.1016/j.watres.2012.01.007

Garcés, P., Pérez Carrión, M., García-Alcocel, E., Payá, J., Monzó, J., Borrachero, M. V., 2008. Mechanical and physical properties of cement blended with sewage sludge ash. Waste Manag. 28, 2495–2502. https://doi.org/10.1016/j.wasman.2008.02.019

Glasser, F.P., 1997. Fundamental aspects of cement solidification and stabilization. J. Hazard. Mater. 52, 1997.

Gorazda, K., Kowalski, Z., Wzorek, Z., 2012. From sewage sludge ash to calcium phosphate fertilizers. Polish J. Chem. Technol. 14, 54–58. https://doi.org/10.2478/v10026-012-0084-3

Gorazda, K., Tarko, B., Wzorek, Z., Nowak, A.K., Kulczycka, J., Henclik, A., 2016. Characteristic of wet method of phosphorus recovery from polish sewage sludge ash with. Open Chem. 14, 37–45. https://doi.org/10.1515/chem-2016-0006

Guedes, P., Couto, N., Ottosen, L.M., Kirkelund, G.M., Mateus, E., Ribeiro, A.B., 2016. Valorisation of ferric sewage sludge ashes: Potential as a phosphorus source. Waste Manag. 52, 193–201. https://doi.org/10.1016/j.wasman.2016.03.040

Guedes, P., Couto, N., Ottosen, L.M., Ribeiro, A.B., 2014. Phosphorus recovery from sewage sludge ash through an electrodialytic process. Waste Manag. https://doi.org/10.1016/j.wasman.2014.02.021

Gunawardana, B., Swedlund, P.J., Singhal, N., Nieuwoudt, M.K., 2018. Pentachlorophenol dechlorination with zero valent iron: a Raman and GCMS study of the complex role of surficial iron oxides. Environ. Sci. Pollut. Res. 25, 17797–17806. https://doi.org/10.1007/s11356-018-2003-5

Gupta, B., Notarianni, M., Mishra, N., Shafiei, M., Iacopi, F., Motta, N., 2014. Evolution of epitaxial graphene layers on 3C SiC/Si (1 1 1) as a function of annealing temperature in UHV. Carbon N. Y. 68, 563–572. https://doi.org/10.1016/j.carbon.2013.11.035

Gupta, S., Kua, H.W., Koh, H.J., 2018a. Application of biochar from food and wood waste as green admixture for cement mortar. Sci. Total Environ. 619–620, 419–435. https://doi.org/10.1016/j.scitotenv.2017.11.044

Gupta, S., Kua, H.W., Pang, S.D., 2018b. Biochar-mortar composite: Manufacturing, evaluation of physical properties and economic viability. Constr. Build. Mater. 167, 874–889. https://doi.org/10.1016/j.conbuildmat.2018.02.104

h2o-china, 2022. Challenges and Opportunities of Wastewater, Rubbish, Sludge Management---Identification of Potential Market Opportunities [WWW Document]. URL https://www.solidwaste.com.cn/news/335404.html (accessed 6.13.22).

Han, T., 2020. Catalytic pyrolysis of lignin to produce fuels and functional carbon materials. KTH Royal Institute of Technology.

Han, T.U., Kim, J., Kim, K., 2020. Freezing-accelerated removal of chromate by biochar synthesized from waste rice husk. Sep. Purif. Technol. 250, 117233. https://doi.org/10.1016/j.seppur.2020.117233

Hanesch, M., 2009. Raman spectroscopy of iron oxides and (oxy)hydroxides at low laser power and possible applications in environmental magnetic studies. Geophys. J. Int. 177, 941–948. https://doi.org/10.1111/j.1365-246X.2009.04122.x

Hao, L., Liu, M., Wang, N., Li, G., 2018. A critical review on arsenic removal from water using iron-based adsorbents. RSC Adv. 8, 39545–39560. https://doi.org/10.1039/c8ra08512a

Hargreaves, J.S.J., Pulford, I.D., Balakrishnan, M., Batra, V.S., 2013. Conversion of large scale wastes into value-added products. Convers. Large Scale Wastes into Value-added Prod. https://doi.org/10.1201/b16233

Harikishore Kumar Reddy, D., Lee, S.M., 2014. Magnetic biochar composite: Facile synthesis, characterization, and application for heavy metal removal. Colloids Surfaces A Physicochem. Eng. Asp. 454, 96–103. https://doi.org/10.1016/j.colsurfa.2014.03.105

Hartman, M., Svoboda, K., Pohořelý, M., Trnka, O., 2005. Combustion of dried sewage sludge in a fluidized-bed reactor. Ind. Eng. Chem. Res. 44, 3432–3441. https://doi.org/10.1021/ie040248n

Hassanpour, M., Shafigh, P., Mahmud, H. Bin, 2012. Lightweight aggregate concrete fiber reinforcement - A review. Constr. Build. Mater. 37, 452–461. https://doi.org/10.1016/j.conbuildmat.2012.07.071

He, R., Peng, Z., Lyu, H., Huang, H., Nan, Q., Tang, J., 2018. Synthesis and characterization of an iron-impregnated biochar for aqueous arsenic removal. Sci. Total Environ. 612, 1177–1186. https://doi.org/10.1016/j.scitotenv.2017.09.016

Hering, J.G., Katsoyiannis, I.A., Theoduloz, G.A., Berg, M., Hug, S.J., 2017. Arsenic Removal from Drinking Water: Experiences with Technologies and Constraints in Practice. J. Environ. Eng. 143, 03117002. https://doi.org/10.1061/(asce)ee.1943-7870.0001225

HK EPD, P., 1991. Technical memorandum: standards for effluents discharged into drainage and sewerage systems, inland and coastal waters. Environmental Protection Department.

Ho, S.H., Chen, Y. di, Yang, Z. kai, Nagarajan, D., Chang, J.S., Ren, N. qi, 2017. High-efficiency removal of lead from wastewater by biochar derived from anaerobic digestion sludge. Bioresour. Technol. 246, 142–149. https://doi.org/10.1016/j.biortech.2017.08.025

HOD, H. and O.D., 2022. REPORT OF MARINE POLLUTION SURVEYS NO.48-Results of Surveys in 2020.

Hoi, C., Lam, K., Barford, J.P., Mckay, G., 2010. Utilization of Incineration Waste Ash Residues in Portland Cement Clinker. Chem. Eng. Trans. 21, 757–762. https://doi.org/10.3303/CET1021127

Hu, X., Ding, Z., Zimmerman, A.R., Wang, S., Gao, B., 2015. Batch and column sorption of arsenic onto iron-impregnated biochar synthesized through hydrolysis. Water Res. 68, 206–216. https://doi.org/10.1016/j.watres.2014.10.009

Huy, D.H., Seelen, E., Liem-Nguyen, V., 2020. Removal mechanisms of cadmium and lead ions in contaminated water by stainless steel slag obtained from scrap metal recycling. J. Water Process Eng. 36, 101369. https://doi.org/10.1016/j.jwpe.2020.101369

Inyang, M., Gao, B., Yao, Y., Xue, Y., Zimmerman, A.R., Pullammanappallil, P., Cao, X., 2012. Removal of heavy metals from aqueous solution by biochars derived from anaerobically digested biomass. Bioresour. Technol. 110, 50–56. https://doi.org/10.1016/j.biortech.2012.01.072

Inyang, M.I., Gao, B., Yao, Y., Xue, Y., Zimmerman, A., Mosa, A., Pullammanappallil, P., Ok, Y.S., Cao, X., 2016. A review of biochar as a low-cost adsorbent for aqueous heavy metal removal. Crit. Rev. Environ. Sci. Technol. 46, 406–433. https://doi.org/10.1080/10643389.2015.1096880

Istuque, D.B., Soriano, L., Akasaki, J.L., Melges, J.L.P., Borrachero, M. V., Monzó, J., Payá, J., Tashima, M.M., 2019. Effect of sewage sludge ash on mechanical and microstructural properties of geopolymers based on metakaolin. Constr. Build. Mater. 203, 95–103. https://doi.org/10.1016/j.conbuildmat.2019.01.093

Izquierdo, M., Querol, X., 2012. Leaching behaviour of elements from coal combustion fly ash: An overview. Int. J. Coal Geol. 94, 54–66. https://doi.org/10.1016/j.coal.2011.10.006

JEMAI, J.E.M.A. for I., 2021. Recycle data book 2021.

Jia, L., Fan, B.G., Yao, Y.X., Han, F., Huo, R.P., Zhao, C.W., Jin, Y., 2018. Study on the Elemental Mercury Adsorption Characteristics and Mechanism of Iron-Based Modified Biochar Materials. Energy and Fuels 32, 12554–12566. https://doi.org/10.1021/acs.energyfuels.8b02890

Jurković, J., Murtić, S., Bašić, F., Gavrić, T., Sijahović, E., Čadro, S., 2021. Relationships between Heavy Metals and Their Connection to Amorphous and Total Iron in a Frequently Subsampled Clay Pit Core Sample. ACS Earth Sp. Chem. 5, 1726–1740. https://doi.org/10.1021/acsearthspacechem.1c00078

Kalaruban, M., Loganathan, P., Nguyen, T.V., Nur, T., Hasan Johir, M.A., Nguyen, T.H., Trinh, M.V., Vigneswaran, S., 2019. Iron-impregnated granular activated carbon for arsenic removal: Application to practical column filters. J. Environ. Manage. 239, 235–243. https://doi.org/10.1016/j.jenvman.2019.03.053

Kalhori, E.M., Yetilmezsoy, K., Uygur, N., Zarrabi, M., Shmeis, R.M.A., 2013. Modeling of adsorption of toxic chromium on natural and surface modified lightweight expanded clay aggregate (LECA). Appl. Surf. Sci. 287, 428–442. https://doi.org/10.1016/j.apsusc.2013.09.175

Karanac, M., Đolić, M., Veljović, Đ., Rajaković-Ognjanović, V., Veličković, Z., Pavićević, V., Marinković, A., 2018. The removal of Zn2+, Pb2+, and As(V) ions by lime activated fly ash and valorization of the exhausted adsorbent. Waste Manag. 78, 366–378. https://doi.org/10.1016/j.wasman.2018.05.052

Kaza, S., Yao, L., Bhada-Tata, P., Van Woerden, F., 2018. What a waste 2.0: a global snapshot of solid waste management to 2050. World Bank Publications.

Khan, S., Naushad, M., Lima, E.C., Zhang, S., Shaheen, S.M., Rinklebe, J., 2021. Global soil pollution by toxic elements: Current status and future perspectives on the risk assessment and remediation strategies – A review. J. Hazard. Mater. 417, 0–2. https://doi.org/10.1016/j.jhazmat.2021.126039

Komkiene, J., Baltrenaite, E., 2016. Biochar as adsorbent for removal of heavy metal ions [Cadmium(II), Copper(II), Lead(II), Zinc(II)] from aqueous phase. Int. J. Environ. Sci. Technol. 13, 471–482. https://doi.org/10.1007/s13762-015-0873-3

Komonweeraket, K., Cetin, B., Aydilek, A., Benson, C.H., Edil, T.B., 2015a. Geochemical Analysis of Leached Elements from Fly Ash Stabilized Soils. J. Geotech. Geoenvironmental Eng. 141, 04015012. https://doi.org/10.1061/(asce)gt.1943-5606.0001288

Komonweeraket, K., Cetin, B., Aydilek, A.H., Benson, C.H., Edil, T.B., 2015b. Effects of pH on the leaching mechanisms of elements from fly ash mixed soils. Fuel 140, 788–802. https://doi.org/10.1016/j.fuel.2014.09.068

Komonweeraket, K., Cetin, B., Benson, C.H., Aydilek, A.H., Edil, T.B., 2015c. Leaching characteristics of toxic constituents from coal fly ash mixed soils under the influence of pH. Waste Manag. 38, 174–184. https://doi.org/10.1016/j.wasman.2014.11.018

Kopp, J.F., McKee, G.D., 1983. Methods for chemical analysis of water and wastes. US Environmental Protection Agency Washington, DC.

Kosson, D.S., Garrabrants, A., Thorneloe, S., Fagnant, D., Helms, G., Connolly, K., Rodgers, M., 2017. Leaching Environmental Assessment Framework (LEAF) How-To Guide. United States Environ. Prot. Agency.

Krejcirikova, B., Ottosen, L.M., Kirkelund, G.M., Rode, C., Peuhkuri, R., 2019. Characterization of sewage sludge ash and its effect on moisture physics of mortar. J. Build. Eng. 21, 396–403. https://doi.org/10.1016/j.jobe.2018.10.021

Król, A., Mizerna, K., Bożym, M., 2020. An assessment of pH-dependent release and mobility of heavy metals from metallurgical slag. J. Hazard. Mater. 384. https://doi.org/10.1016/j.jhazmat.2019.121502

Lassoued, A., Dkhil, B., Gadri, A., Ammar, S., 2017. Control of the shape and size of iron oxide (α-Fe2O3) nanoparticles synthesized through the chemical precipitation method. Results Phys. https://doi.org/10.1016/j.rinp.2017.07.066

Lata, S., Singh, P.K., Samadder, S.R., 2015. Regeneration of adsorbents and recovery of heavy metals: a review. Int. J. Environ. Sci. Technol. 12, 1461–1478. https://doi.org/10.1007/s13762-014-0714-9

Law, K.P., Pagilla, K.R., 2021. A solution to the limited global phosphorus supply: Regionalization of phosphorus recovery from sewage sludge ash. J. Clean. Prod. 290, 125874. https://doi.org/10.1016/j.jclepro.2021.125874

Lawrinenko, M., Laird, D.A., Van Leeuwen, J.H., 2017. Sustainable Pyrolytic Production of Zerovalent Iron. ACS Sustain. Chem. Eng. 5, 767–773. https://doi.org/10.1021/acssuschemeng.6b02105

Lee, Y.R., Soe, J.T., Zhang, S., Ahn, J.W., Park, M.B., Ahn, W.S., 2017. Synthesis of nanoporous materials via recycling coal fly ash and other solid wastes: A mini review. Chem. Eng. J. 317, 821–843. https://doi.org/10.1016/j.cej.2017.02.124

Lesiak, B., Kövér, L., Tóth, J., Zemek, J., Jiricek, P., Kromka, A., Rangam, N., 2018. C sp 2 /sp 3 hybridisations in carbon nanomaterials – XPS and (X)AES study. Appl. Surf. Sci. 452, 223–231. https://doi.org/10.1016/j.apsusc.2018.04.269

Li, H., Dong, X., da Silva, E.B., de Oliveira, L.M., Chen, Y., Ma, L.Q., 2017. Mechanisms of metal sorption by biochars: Biochar characteristics and modifications. Chemosphere 178, 466–478. https://doi.org/10.1016/j.chemosphere.2017.03.072

Li, J., Poon, C.S., 2017. Innovative solidification/stabilization of lead contaminated soil using incineration sewage sludge ash. Chemosphere 173, 143–152. https://doi.org/10.1016/j.chemosphere.2017.01.065

Li, J. shan, Chen, Z., Wang, Q. ming, Fang, L., Xue, Q., Cheeseman, C.R., Donatello, S., Liu, L., Poon, C.S., 2018. Change in re-use value of incinerated sewage sludge ash due to chemical extraction of phosphorus. Waste Manag. 74, 404–412. https://doi.org/10.1016/j.wasman.2018.01.007

Li, J., Zhou, Y., Chen, X., Wang, Q., Xue, Q., Tsang, D.C.W., Poon, C.S., 2020. Engineering and microstructure properties of contaminated marine sediments solidified by high content of incinerated sewage sludge ash. J. Rock Mech. Geotech. Eng. https://doi.org/10.1016/j.jrmge.2020.10.002

Li, J.S., Beiyuan, J., Tsang, D.C.W., Wang, L., Poon, C.S., Li, X.D., Fendorf, S., 2017. Arsenic-containing soil from geogenic source in Hong Kong: Leaching characteristics and stabilization/solidification. Chemosphere 182, 31–39. https://doi.org/10.1016/j.chemosphere.2017.05.019

Li, J.S., Wang, L., Cui, J.L., Poon, C.S., Beiyuan, J., Tsang, D.C.W., Li, X.D., 2018. Effects of low-alkalinity binders on stabilization/solidification of geogenic As-containing soils:

Spectroscopic investigation and leaching tests. Sci. Total Environ. 631–632, 1486–1494. https://doi.org/10.1016/j.scitotenv.2018.02.247

Li, S., Hihara, L.H., 2015. A Micro-Raman Spectroscopic Study of Marine Atmospheric Corrosion of Carbon Steel: The Effect of Akaganeite. J. Electrochem. Soc. 162, C495–C502. https://doi.org/10.1149/2.0881509jes

Li, X., Coles, B.J., Ramsey, M.H., Thornton, I., 1995. Sequential extraction of soils for multielement analysis by ICP-AES. Chem. Geol. 124, 109–123. https://doi.org/10.1016/0009-2541(95)00029-L

Li, Y., Zhang, F.S., 2010. Catalytic oxidation of Methyl Orange by an amorphous FeOOH catalyst developed from a high iron-containing fly ash. Chem. Eng. J. 158, 148–153. https://doi.org/10.1016/j.cej.2009.12.021

Li, Y., Zhang, F.S., Xiu, F.R., 2009. Arsenic (V) removal from aqueous system using adsorbent developed from a high iron-containing fly ash. Sci. Total Environ. 407, 5780–5786. https://doi.org/10.1016/j.scitotenv.2009.07.017

Li, Y., Zhu, X., Qi, X., Shu, B., Zhang, X., Li, K., Wei, Y., Wang, H., 2020. Removal and immobilization of arsenic from copper smelting wastewater using copper slag by in situ encapsulation with silica gel. Chem. Eng. J. 394, 124833. https://doi.org/10.1016/j.cej.2020.124833

Liang, S., Yang, L., Chen, H., Yu, W., Tao, S., Yuan, S., Xiao, K., Hu, J., Hou, H., Liu, B., Yang, J., 2021. Phosphorus recovery from incinerated sewage sludge ash (ISSA) and reutilization of residues for sludge pretreated by different conditioners. Resour. Conserv. Recycl. 169, 105524. https://doi.org/10.1016/j.resconrec.2021.105524

Liang, Z., Yi, L., Huang, Z., Huang, B., Han, H., 2019. A Novel and Green Metallurgical Technique of Highly Efficient Iron Recovery from Refractory Low-Grade Iron Ores. ACS Sustain. Chem. Eng. https://doi.org/10.1021/acssuschemeng.9b05423

Lin, D.-F., Weng, C.-H., 2001. Use of sewage sludge ash as brick material. J. Environ. Eng. 127, 922–927.

Lin, K.L., Chiang, K.Y., Lin, C.Y., 2005. Hydration characteristics of waste sludge ash that is reused in eco-cement clinkers. Cem. Concr. Res. 35, 1074–1081. https://doi.org/10.1016/j.cemconres.2004.11.014

Lin, K.L., Chiang, K.Y., Lin, D.F., 2006. Effect of heating temperature on the sintering characteristics of sewage sludge ash. J. Hazard. Mater. 128, 175–181. https://doi.org/10.1016/j.jhazmat.2005.07.051

Liu, J., Mwamulima, T., Wang, Y., Fang, Y., Song, S., Peng, C., 2017. Removal of Pb(II) and Cr(VI) from aqueous solutions using the fly ash-based adsorbent material-supported zero-valent iron. J. Mol. Liq. 243, 205–211. https://doi.org/10.1016/j.molliq.2017.08.004

Liu, K., Li, F., Cui, J., Yang, S., Fang, L., 2020. Simultaneous removal of Cd(II) and As(III) by graphene-like biochar-supported zero-valent iron from irrigation waters under aerobic conditions: Synergistic effects and mechanisms. J. Hazard. Mater. 395, 122623. https://doi.org/10.1016/j.jhazmat.2020.122623

Liu, K., Li, F., Zhao, X., Wang, G., Fang, L., 2021. The overlooked role of carbonaceous supports in enhancing arsenite oxidation and removal by nZVI: Surface area versus electrochemical property. Chem. Eng. J. 406, 126851. https://doi.org/10.1016/j.cej.2020.126851

Liu, R., Liu, G., Yousaf, B., Abbas, Q., 2018. Operating conditions-induced changes in product yield and characteristics during thermal-conversion of peanut shell to biochar in relation to economic analysis. J. Clean. Prod. 193, 479–490. https://doi.org/10.1016/j.jclepro.2018.05.034

Lu, S.Y., Jin, M., Zhang, Y., Niu, Y.B., Gao, J.C., Li, C.M., 2018. Chemically Exfoliating Biomass into a Graphene-like Porous Active Carbon with Rational Pore Structure, Good Conductivity, and Large Surface Area for High-Performance Supercapacitors. Adv. Energy Mater. 8, 1–9. https://doi.org/10.1002/aenm.201702545

Lumsdon, D.G., Meeussen, J.C.L., Paterson, E., Garden, L.M., Anderson, P., 2001. Use of solid phase characterisation and chemical modelling for assessing the behaviour of arsenic in contaminated soils. Appl. Geochemistry 16, 571–581. https://doi.org/10.1016/S0883-2927(00)00063-9

Lynn, C.J., Dhir, R.K., Ghataora, G.S., 2018. Environmental impacts of sewage sludge ash in construction: Leaching assessment. Resour. Conserv. Recycl. 136, 306–314. https://doi.org/10.1016/j.resconrec.2018.04.029

Lynn, C.J., Dhir, R.K., Ghataora, G.S., 2016. Sewage sludge ash characteristics and potential for use in bricks, tiles and glass ceramics. Water Sci. Technol. 74, 17–29. https://doi.org/10.2166/wst.2016.040

Lynn, C.J., Dhir, R.K., Ghataora, G.S., West, R.P., 2015. Sewage sludge ash characteristics and potential for use in concrete. Constr. Build. Mater. 98, 767–779. https://doi.org/10.1016/j.conbuildmat.2015.08.122

Lyu, F., Niu, S., Wang, L., Liu, R., Sun, W., He, D., 2021. Efficient removal of Pb(II) ions from aqueous solution by modified red mud. J. Hazard. Mater. 406, 124678. https://doi.org/10.1016/j.jhazmat.2020.124678

Ma, L.L., Liu, W.J., Hu, X., Lam, P.K.S., Zeng, J.R., Yu, H.Q., 2020. Ionothermal carbonization of biomass to construct sp2/sp3 carbon interface in N-doped biochar as efficient oxygen reduction electrocatalysts. Chem. Eng. J. 400, 125969. https://doi.org/10.1016/j.cej.2020.125969

Ma, W., Meng, F., Qiu, D., Tang, Y., 2020. Co-stabilization of Pb/Cu/Zn by beneficial utilization of sewage sludge incineration ash: Effects of heavy metal type and content. Resour. Conserv. Recycl. 156. https://doi.org/10.1016/j.resconrec.2019.104671

Mahedi, M., Cetin, B., Dayioglu, A.Y., 2019. Leaching behavior of aluminum, copper, iron and zinc from cement activated fly ash and slag stabilized soils. Waste Manag. 95, 334–355. https://doi.org/10.1016/j.wasman.2019.06.018

Malviya, R., Chaudhary, R., 2006. Factors affecting hazardous waste solidification/stabilization: A review. J. Hazard. Mater. 137, 267–276. https://doi.org/10.1016/j.jhazmat.2006.01.065

Mandal, B., 2002. Arsenic round the world: a review. Talanta 58, 201–235. https://doi.org/10.1016/S0039-9140(02)00268-0

Mejdi, M., Saillio, M., Chaussadent, T., Divet, L., Tagnit-Hamou, A., 2020. Hydration mechanisms of sewage sludge ashes used as cement replacement. Cem. Concr. Res. 135, 106115. https://doi.org/10.1016/j.cemconres.2020.106115

MHLW, M. of H.L. and W., 2015. Drinking Water Quality Standards.

MOE, 2015. National Effluent Standards.

Mulligan, C.N., Yong, R.N., Gibbs, B.F., 2001. An evaluation of technologies for the heavy metal remediation of dredged sediments. J. Hazard. Mater. 85, 145–163. https://doi.org/10.1016/S0304-3894(01)00226-6

Nakagawa, H., Ohta, J., 2019. Phosphorus Recovery from Sewage Sludge Ash: A Case Study in Gifu, Japan, in: Phosphorus Recovery and Recycling. Springer, pp. 149–155.

Nayak, D., Dash, N., Ray, N., Rath, S.S., 2019. Utilization of waste coconut shells in the reduction roasting of overburden from iron ore mines. Powder Technol. 353, 450–458. https://doi.org/10.1016/j.powtec.2019.05.053

NBSC, N.B. of S. of C., 2020. CHINA STATISTICAL YEARBOOK [WWW Document]. URL http://www.stats.gov.cn/tjsj/ndsj/2020/indexch.htm (accessed 6.13.22).

Neeli, S.T., Ramsurn, H., 2018. Synthesis and formation mechanism of iron nanoparticles in graphitized carbon matrix using biochar from biomass model compounds as a support. Carbon N. Y. 134, 480–490. https://doi.org/10.1016/j.carbon.2018.03.079

NHMRC, N.H. and M.R.C. (Australia), 2022. Australian drinking water guidelines 6 2011 : national water quality management strategy.

Nie, J., Wang, Q., Gao, S., Poon, C.S., Zhou, Y., Li, J. shan, 2021. Novel recycling of incinerated sewage sludge ash (ISSA) and waste bentonite as ceramsite for Pb-containing wastewater treatment: Performance and mechanism. J. Environ. Manage. 288, 112382. https://doi.org/10.1016/j.jenvman.2021.112382

Noubactep, C., 2015. Metallic iron for environmental remediation: A review of reviews. Water Res. 85, 114–123. https://doi.org/10.1016/j.watres.2015.08.023

Odell, E., Kathryn, H., Daniel, M., Vincent, P., 2021. A3P Project: Melbourne Water Sediment Quality Assessment Program.

Ottosen, L.M., Bertelsen, I.M.G., Jensen, P.E., Kirkelund, G.M., 2020. Sewage sludge ash as resource for phosphorous and material for clay brick manufacturing. Constr. Build. Mater. 249, 118684. https://doi.org/10.1016/j.conbuildmat.2020.118684

Ottosen, L.M., Jensen, P.E., Kirkelund, G.M., 2016. Phosphorous recovery from sewage sludge ash suspended in water in a two-compartment electrodialytic cell. Waste Manag. 51, 142–148. https://doi.org/10.1016/j.wasman.2016.02.015

Ottosen, L.M., Jensen, P.E., Kirkelund, G.M., 2014. Electrodialytic Separation of Phosphorus and Heavy Metals from Two Types of Sewage Sludge Ash. Sep. Sci. Technol. 49, 1910–1920. https://doi.org/10.1080/01496395.2014.904347

Ottosen, L.M., Thornberg, D., Cohen, Y., Stiernström, S., 2022. Utilization of acid-washed sewage sludge ash as sand or cement replacement in concrete. Resour. Conserv. Recycl. 176. https://doi.org/10.1016/j.resconrec.2021.105943

Oudghiri, F., Allali, N., Quiroga, J.M., Rodríguez-Barroso, M.R., 2016. TG–FTIR analysis on pyrolysis and combustion of marine sediment. Infrared Phys. Technol. 78, 268–274. https://doi.org/10.1016/j.infrared.2016.08.015

Pan, J., Gao, B., Duan, P., Guo, K., Xu, X., Yue, Q., 2021. Recycling exhausted magnetic biochar with adsorbed Cu2+ as a cost-effective permonosulfate activator for norfloxacin degradation: Cu contribution and mechanism. J. Hazard. Mater. 413, 125413. https://doi.org/10.1016/j.jhazmat.2021.125413

Pan, S.C., Tseng, D.H., Lee, C.C., Lee, C., 2003. Influence of the fineness of sewage sludge ash on the mortar properties. Cem. Concr. Res. 33, 1749–1754. https://doi.org/10.1016/S0008-8846(03)00165-0

Pandey, S.P., Sharma, R.L., 2000. Influence of mineral additives on the strength and porosity of OPC mortar. Cem. Concr. Res. 30, 19–23. https://doi.org/10.1016/S0008-8846(99)00180-5

Paria, S., Yuet, P.K., 2006. Solidification-stabilization of organic and inorganic contaminants using portland cement: A literature review. Environ. Rev. 14, 217–255. https://doi.org/10.1139/A06-004

Park, J.H., Eom, J.H., Lee, S.L., Hwang, S.W., Kim, S.H., Kang, S.W., Yun, J.J., Cho, J.S., Lee, Y.H., Seo, D.C., 2020. Exploration of the potential capacity of fly ash and bottom ash derived from wood pellet-based thermal power plant for heavy metal removal. Sci. Total Environ. 740, 140205. https://doi.org/10.1016/j.scitotenv.2020.140205

Park, J.H., Ok, Y.S., Kim, S.H., Cho, J.S., Heo, J.S., Delaune, R.D., Seo, D.C., 2016. Competitive adsorption of heavy metals onto sesame straw biochar in aqueous solutions. Chemosphere 142, 77–83. https://doi.org/10.1016/j.chemosphere.2015.05.093

Patil, V., Adhikari, S., Cross, P., 2018. Co-pyrolysis of lignin and plastics using red clay as catalyst in a micro-pyrolyzer. Bioresour. Technol. 270, 311–319. https://doi.org/10.1016/j.biortech.2018.09.034

Pepper, R.A., Couperthwaite, S.J., Millar, G.J., 2016. Comprehensive examination of acid leaching behaviour of mineral phases from red mud: Recovery of Fe, Al, Ti, and Si. Miner. Eng. 99, 8–18. https://doi.org/10.1016/j.mineng.2016.09.012

Petzet, S., Peplinski, B., Cornel, P., 2012. On wet chemical phosphorus recovery from sewage sludge ash by acidic or alkaline leaching and an optimized combination of both. Water Res. 46, 3769–3780. https://doi.org/10.1016/j.watres.2012.03.068

Podgorski, J., Berg, M., 2020. Global threat of arsenic in groundwater. Science (80-.). 368, 845–850. https://doi.org/10.1126/science.aba1510

Powell, R.M., Puls, R.W., Hightower, S.K., Sabatini, D.A., 1995. Coupled Iron Corrosion and Chromate Reduction: Mechanisms for Subsurface Remediation. Environ. Sci. Technol. 29, 1913–1922. https://doi.org/10.1021/es00008a008

Prasad, S., Kumar, K., Kumar, S., Gupta, N., Marina, M., Cabral-pinto, S., Rezania, S., Radwan, N., Alam, J., 2021. Chromium contamination and effect on environmental health and its remediation : A sustainable approaches. J. Environ. Manage. 285, 112174. https://doi.org/10.1016/j.jenvman.2021.112174

Qi, J., Zhang, G., Li, H., 2015. Efficient removal of arsenic from water using a granular adsorbent: Fe-Mn binary oxide impregnated chitosan bead. Bioresour. Technol. 193, 243–249. https://doi.org/10.1016/j.biortech.2015.06.102

Qiu, H., Lv, L., Pan, B.C., Zhang, Q.J., Zhang, W.M., Zhang, Q.X., 2009. Critical review in adsorption kinetic models. J. Zhejiang Univ. Sci. A 10, 716–724. https://doi.org/10.1631/jzus.A0820524

Rahman, Z., Singh, V.P., 2019. The relative impact of toxic heavy metals (THMs) (arsenic (As), cadmium (Cd), chromium (Cr)(VI), mercury (Hg), and lead (Pb)) on the total environment: an overview. Environ. Monit. Assess. 191. https://doi.org/10.1007/s10661-019-7528-7

Regalbuto, J.R., Robles, J., 2004. The engineering of Pt/carbon catalyst preparation. Univ. Illinois, Chicago.

Rosales-Landeros, C., Barrera-Díaz, C.E., Bilyeu, B., Guerrero, V.V., Núñez, F.U., 2013. A Review on Cr(VI) Adsorption Using Inorganic Materials. Am. J. Anal. Chem. 04, 8–16. https://doi.org/10.4236/ajac.2013.47a002

SA, S.A., 2022. Standards for drinking water quality.

Samantasinghar, S., Singh, S.P., 2018. Effect of synthesis parameters on compressive strength of fly ash-slag blended geopolymer. Constr. Build. Mater. 170, 225–234. https://doi.org/10.1016/j.conbuildmat.2018.03.026

Sanchez, F., Garrabrants, A.C., Vandecasteele, C., Moszkowicz, P., Kosson, D.S., 2003. Environmental assessment of waste matrices contaminated with arsenic. J. Hazard. Mater. 96, 229–257. https://doi.org/10.1016/S0304-3894(02)00215-7

Schaum, C., Cornel, P., Jardin, N., 2007. Phosphorus Recovery from Sewage Sludge Ash – A Wet Chemical Approach. IWA Conf. biosolids, Mov. Forw. Wastewater Biosolids Sustain. Tech. Manag. Public Synerg. 583–590.

Schnell, M., Horst, T., Quicker, P., 2020. Thermal treatment of sewage sludge in Germany: A review. J. Environ. Manage. 263, 110367. https://doi.org/10.1016/j.jenvman.2020.110367

Shang, J., Zong, M., Yu, Y., Kong, X., Du, Q., Liao, Q., 2017. Removal of chromium (VI) from water using nanoscale zerovalent iron particles supported on herb-residue biochar. J. Environ. Manage. 197, 331–337. https://doi.org/10.1016/j.jenvman.2017.03.085

Shen, S., Li, X.F., Cullen, W.R., Weinfeld, M., Le, X.C., 2013. Arsenic binding to proteins. Chem. Rev. 113, 7769–7792. https://doi.org/10.1021/cr300015c

Singh, A., Houlihan, M., Dayioglu, A.Y., Aydilek, A.H., 2020. Batch leaching testing of stabilized dredged bottom-sea sediments. J. Soils Sediments 20, 3793–3806. https://doi.org/10.1007/s11368-020-02646-8

Smol, M., Kulczycka, J., Henclik, A., Gorazda, K., Wzorek, Z., 2015. The possible use of sewage sludge ash (SSA) in the construction industry as a way towards a circular economy. J. Clean. Prod. 95, 45–54. https://doi.org/10.1016/j.jclepro.2015.02.051

Son, E.B., Poo, K.M., Chang, J.S., Chae, K.J., 2018. Heavy metal removal from aqueous solutions using engineered magnetic biochars derived from waste marine macro-algal biomass. Sci. Total Environ. 615, 161–168. https://doi.org/10.1016/j.scitotenv.2017.09.171

Sörengård, M., Kleja, D.B., Ahrens, L., 2019. Stabilization and solidification remediation of soil contaminated with poly- and perfluoroalkyl substances (PFASs). J. Hazard. Mater. 367, 639–646. https://doi.org/10.1016/j.jhazmat.2019.01.005

statista, 2022. Global consumption of agricultural fertilizer from 1965 to 2019, by nutrient [WWW Document]. URL https://www-statista-com.ezproxy.lb.polyu.edu.hk/statistics/438967/fertilizer-consumption-globally-by-nutrient/ (accessed 9.9.22).

Stoia, M., Istratie, R., Păcurariu, C., 2016. Investigation of magnetite nanoparticles stability in air by thermal analysis and FTIR spectroscopy. J. Therm. Anal. Calorim. 125, 1185–1198. https://doi.org/10.1007/s10973-016-5393-y

Sulaymon, A.H., Abid, B.A., Al-Najar, J.A., 2009. Removal of lead copper chromium and cobalt ions onto granular activated carbon in batch and fixed-bed adsorbers. Chem. Eng. J. 155, 647–653. https://doi.org/10.1016/j.cej.2009.08.021

Sun, Y., Li, J., Huang, T., Guan, X., 2016. The influences of iron characteristics, operating conditions and solution chemistry on contaminants removal by zero-valent iron: A review. Water Res. 100, 277–295. https://doi.org/10.1016/j.watres.2016.05.031

Sun, Y., Yu, I.K.M., Tsang, D.C.W., Cao, X., Lin, D., Wang, L., Graham, N.J.D., Alessi, D.S., Komárek, M., Ok, Y.S., Feng, Y., Li, X.D., 2019. Multifunctional iron-biochar composites for the removal of potentially toxic elements, inherent cations, and hetero-chloride from hydraulic fracturing wastewater. Environ. Int. 124, 521–532. https://doi.org/10.1016/j.envint.2019.01.047

Sun, Z., Vollpracht, A., van der Sloot, H.A., 2019. pH dependent leaching characterization of major and trace elements from fly ash and metakaolin geopolymers. Cem. Concr. Res. 125, 105889. https://doi.org/10.1016/j.cemconres.2019.105889

Tadic, M., Panjan, M., Tadic, B.V., Lazovic, J., Damnjanovic, V., Kopani, M., Kopanja, L., 2019. Magnetic properties of hematite (α - Fe2O3) nanoparticles synthesized by sol-gel synthesis method: The influence of particle size and particle size distribution. J. Electr. Eng. https://doi.org/10.2478/jee-2019-0044

Tang, L., Feng, H., Tang, J., Zeng, G., Deng, Y., Wang, J., Liu, Y., Zhou, Y., 2017. Treatment of arsenic in acid wastewater and river sediment by Fe@Fe2O3 nanobunches: The effect of environmental conditions and reaction mechanism. Water Res. 117, 175–186. https://doi.org/10.1016/j.watres.2017.03.059

Tang, P., Xuan, D., Li, J., Cheng, H.W., Poon, C.S., Tsang, D.C.W., 2020. Investigation of cold bonded lightweight aggregates produced with incineration sewage sludge ash (ISSA) and cementitious waste. J. Clean. Prod. 251, 119709. https://doi.org/10.1016/j.jclepro.2019.119709

Tao, S., Liang, S., Wu, X., Hou, H., Yu, W., Xiao, K., Liu, B., Yuan, S., Hu, J., Yang, J., 2022. Enhanced silicon bioavailability of biochar derived from sludge conditioned with Fenton's reagent and lime. Sci. Total Environ. 806, 150941. https://doi.org/10.1016/j.scitotenv.2021.150941

Tashima, M.M., Reig, L., Santini, M.A., B Moraes, J.C., Akasaki, J.L., Payá, J., Borrachero, M. V., Soriano, L., 2017. Compressive Strength and Microstructure of Alkali-Activated Blast Furnace Slag/Sewage Sludge Ash (GGBS/SSA) Blends Cured at Room Temperature. Waste and Biomass Valorization 8, 1441–1451. https://doi.org/10.1007/s12649-016-9659-1

Tokarský, J., Matějka, V., Neuwirthová, L., Vontorová, J., Mamulová Kutláková, K., Kukutschová, J., Čapková, P., 2013. A low-cost photoactive composite quartz sand/TiO2. Chem. Eng. J. 222, 488–497. https://doi.org/10.1016/j.cej.2013.02.056

TPARK, n.d. Process: Waste to Energy [WWW Document]. URL https://www.tpark.hk/en/process/ (accessed 6.14.22).

Tran, H.N., You, S.J., Hosseini-Bandegharaei, A., Chao, H.P., 2017. Mistakes and inconsistencies regarding adsorption of contaminants from aqueous solutions: A critical review. Water Res. 120, 88–116. https://doi.org/10.1016/j.watres.2017.04.014

US EPA, 2022. National Primary Drinking Water Regulations [WWW Document]. URL https://www.epa.gov/ground-water-and-drinking-water/national-primary-drinking-water-regulations#Inorganic (accessed 6.10.22).

US EPA, 1992. Toxicity Characterization Leaching Procedure (TCLP), EPA Method 1311. Washington, U.S.A.

US EPA, n.d. Section 404 of the Clean Water Act Dredging and Sediment Management [WWW Document]. URL https://www.epa.gov/cwa-404/dredging-and-sediment-management (accessed 8.3.22).

USGS, U.S.G.S., 2022. MINERAL COMMODITY SUMMARIES 2022.

Vithanage, M., Herath, I., Joseph, S., Bundschuh, J., Bolan, N., Ok, Y.S., Kirkham, M.B., Rinklebe, J., 2017. Interaction of arsenic with biochar in soil and water: A critical review. Carbon N. Y. 113, 219–230. https://doi.org/10.1016/j.carbon.2016.11.032

Vítková, M., Rákosová, S., Michálková, Z., Komárek, M., 2017. Metal(loid)s behaviour in soils amended with nano zero-valent iron as a function of pH and time. J. Environ. Manage. 186, 268–276. https://doi.org/10.1016/j.jenvman.2016.06.003

Vogel, C., Adam, C., 2011. Heavy Metal Removal from Sewage Sludge Ash by Thermochemical Treatment with Gaseous Hydrochloric acid. Environ. Sci. Technol. 45, 7445–7450. https://doi.org/10.1021/es2007319

Vogel, C., Exner, R.M., Adam, C., 2013. Heavy metal removal from sewage sludge ash by thermochemical treatment with polyvinylchloride. Environ. Sci. Technol. 47, 563–567. https://doi.org/10.1021/es300610e

Vouk, D., Nakic, D., Stirmer, N., Cheeseman, C.R., 2017. Use of sewage sludge ash in cementitious materials. Rev. Adv. Mater. Sci. 49, 158–170.

Wan, X., Li, C., Parikh, S.J., 2020. Simultaneous removal of arsenic, cadmium, and lead from soil by iron-modified magnetic biochar. Environ. Pollut. 261, 114157. https://doi.org/10.1016/j.envpol.2020.114157

Wang, D., Wang, Q., Xue, J., 2020. Reuse of hazardous electrolytic manganese residue: Detailed leaching characterization and novel application as a cementitious material. Resour. Conserv. Recycl. 154, 104645. https://doi.org/10.1016/j.resconrec.2019.104645

Wang, J., Shen, M., Wang, Hailong, Du, Y., Zhou, X., Liao, Z., Wang, Huabin, Chen, Z., 2020. Red mud modified sludge biochar for the activation of peroxymonosulfate: Singlet oxygen dominated mechanism and toxicity prediction. Sci. Total Environ. 740, 140388. https://doi.org/10.1016/j.scitotenv.2020.140388

Wang, Lei, Chen, L., Tsang, D.C.W., Kua, H.W., Yang, J., Ok, Y.S., Ding, S., Hou, D., Poon, C.S., 2019a. The roles of biochar as green admixture for sediment-based construction products. Cem. Concr. Compos. 104, 103348. https://doi.org/10.1016/j.cemconcomp.2019.103348

Wang, L., Chen, L., Tsang, D.C.W., Li, J.S., Baek, K., Hou, D., Ding, S., Poon, C.S., 2018. Recycling dredged sediment into fill materials, partition blocks, and paving blocks: Technical and economic assessment. J. Clean. Prod. 199, 69–76. https://doi.org/10.1016/j.jclepro.2018.07.165

Wang, Lei, Chen, L., Tsang, D.C.W., Zhou, Y., Rinklebe, J., Song, H., Kwon, E.E., Baek, K., Sik Ok, Y., 2019b. Mechanistic insights into red mud, blast furnace slag, or metakaolin-assisted stabilization/solidification of arsenic-contaminated sediment. Environ. Int. 133, 105247. https://doi.org/10.1016/j.envint.2019.105247

Wang, Li, Wang, Y., Ma, F., Tankpa, V., Bai, S., Guo, X., Wang, X., 2019. Mechanisms and reutilization of modified biochar used for removal of heavy metals from wastewater: A review. Sci. Total Environ. 668, 1298–1309. https://doi.org/10.1016/j.scitotenv.2019.03.011

Wang, L., Zhang, Y., Chen, L., Guo, B., Tan, Y., Sasaki, K., Tsang, D.C.W., 2022. Designing novel magnesium oxysulfate cement for stabilization/solidification of municipal solid waste incineration fly ash. J. Hazard. Mater. 423, 127025. https://doi.org/10.1016/j.jhazmat.2021.127025

Wang, Q., Li, J., Poon, C.S., 2019. Using incinerated sewage sludge ash as a high-performance adsorbent for lead removal from aqueous solutions: Performances and mechanisms. Chemosphere 226, 587–596. https://doi.org/10.1016/j.chemosphere.2019.03.193

Wang, Q., Li, J. shan, Poon, C.S., 2021a. Novel recycling of phosphorus-recovered incinerated sewage sludge ash residues by co-pyrolysis with lignin for reductive/sorptive removal of hexavalent chromium from aqueous solutions. Chemosphere 285, 131434. https://doi.org/10.1016/j.chemosphere.2021.131434

Wang, Q., Li, J. shan, Xue, Q., Poon, C.S., 2021b. Alkaline modification of the acid residue of incinerated sewage sludge ash after phosphorus recovery for heavy metal removal from aqueous solutions. Waste Manag. 123, 80–87. https://doi.org/10.1016/j.wasman.2021.01.025

Wang, S., Gao, B., Li, Y., Creamer, A.E., He, F., 2017. Adsorptive removal of arsenate from aqueous solutions by biochar supported zero-valent iron nanocomposite: Batch and continuous flow tests. J. Hazard. Mater. 322, 172–181. https://doi.org/10.1016/j.jhazmat.2016.01.052

Wang, S., Zhao, M., Zhou, M., Li, Y.C., Wang, J., Gao, B., Sato, S., Feng, K., Yin, W., Igalavithana, A.D., Oleszczuk, P., Wang, X., Ok, Y.S., 2019. Biochar-supported nZVI (nZVI/BC) for contaminant removal from soil and water: A critical review. J. Hazard. Mater. 373, 820–834. https://doi.org/10.1016/j.jhazmat.2019.03.080

Wang, Y., López-Valdivieso, A., Zhang, T., Mwamulima, T., Zhang, X., Song, S., Peng, C., 2017. Preparation of microscale zero-valent iron-fly ash-bentonite composite and evaluation of its adsorption performance of crystal violet and methylene blue dyes. Environ. Sci. Pollut. Res. 24, 20050–20062. https://doi.org/10.1007/s11356-017-9426-2

Wei, L., Zhu, F., Li, Q., Xue, C., Xia, X., Yu, H., Zhao, Q., Jiang, J., Bai, S., 2020. Development, current state and future trends of sludge management in China: Based on exploratory data and CO2-equivaient emissions analysis. Environ. Int. 144, 106093. https://doi.org/10.1016/j.envint.2020.106093

Wei, R., Feng, S., Long, H., Li, J., Yuan, Z., Cang, D., Xu, C. (Charles), 2017. Coupled biomass (lignin) gasification and iron ore reduction: A novel approach for biomass conversion and application. Energy 140, 406–414. https://doi.org/10.1016/j.energy.2017.08.080

Wei, R., Xiang, D., Long, H., Xu, C. (Charles), Li, J., 2020. Reduction of iron oxide by lignin: Characteristics, kinetics and superiority. Energy 197, 117203. https://doi.org/10.1016/j.energy.2020.117203

Wei, Y., Wei, S., Liu, C., Chen, T., Tang, Y., Ma, J., Yin, K., Luo, S., 2019. Efficient removal of arsenic from groundwater using iron oxide nanoneedle array-decorated biochar fibers with high Fe utilization and fast adsorption kinetics. Water Res. 167, 115107. https://doi.org/10.1016/j.watres.2019.115107

WHO, W.H.O., 2017. Guidelines for drinking-water quality: fourth edition incorporating the first addendum, 4th ed.

Wu, B., Peng, D., Hou, S., Tang, B., Wang, C., Xu, H., 2018. Dynamic study of Cr(VI) removal performance and mechanism from water using multilayer material coated

nanoscale zerovalent iron. Environ. Pollut. 240, 717–724. https://doi.org/10.1016/j.envpol.2018.04.099

Wu, Chuan, Huang, L., Xue, S.G., Huang, Y.Y., Hartley, W., Cui, M. qian, Wong, M.H., 2017. Arsenic sorption by red mud-modified biochar produced from rice straw. Environ. Sci. Pollut. Res. 24, 18168–18178. https://doi.org/10.1007/s11356-017-9466-7

Wu, Can, Tu, J., Liu, W., Zhang, J., Chu, S., Lu, G., Lin, Z., Dang, Z., 2017. The double influence mechanism of pH on arsenic removal by nano zero valent iron: Electrostatic interactions and the corrosion of Fe0. Environ. Sci. Nano 4, 1544–1552. https://doi.org/10.1039/c7en00240h

Wu, J., Yan, M., Lv, S., Yin, W., Bu, H., Liu, L., Li, P., Deng, H., Zheng, X., 2021. Preparation of highly dispersive and antioxidative nano zero-valent iron for the removal of hexavalent chromium. Chemosphere 262, 127733. https://doi.org/10.1016/j.chemosphere.2020.127733

Xia, S., Song, Z., Jeyakumar, P., Shaheen, S.M., Rinklebe, J., Ok, Y.S., Bolan, N., Wang, H., 2019. A critical review on bioremediation technologies for Cr(VI)-contaminated soils and wastewater. Crit. Rev. Environ. Sci. Technol. 49, 1027–1078. https://doi.org/10.1080/10643389.2018.1564526

Xie, W.M., Zhou, F.P., Bi, X.L., Chen, D.D., Li, J., Sun, S.Y., Liu, J.Y., Chen, X.Q., 2018. Accelerated crystallization of magnetic 4A-zeolite synthesized from red mud for application in removal of mixed heavy metal ions. J. Hazard. Mater. 358, 441–449. https://doi.org/10.1016/j.jhazmat.2018.07.007

Xu, G., Zou, J., Li, G., 2008. Ceramsite made with water and wastewater sludge and its characteristics affected by SiO2 and Al2O3. Environ. Sci. Technol. 42, 7417–7423. https://doi.org/10.1021/es801446h

Xu, L., Shu, Z., Feng, L., Zhou, J., Li, T., Zhao, Z., Wang, W., 2022. Fresh biomass derived biochar with high-load zero-valent iron prepared in one step for efficient arsenic removal. J. Clean. Prod. 352, 131616. https://doi.org/10.1016/j.jclepro.2022.131616

Yadav, M.K., Saidulu, D., Ghosal, P.S., Mukherjee, A., Gupta, A.K., 2022. A review on the management of arsenic-laden spent adsorbent: Insights of global practices, process criticality, and sustainable solutions. Environ. Technol. Innov. 27, 102500. https://doi.org/10.1016/j.eti.2022.102500

Yamashita, T., Hayes, P., 2008. Analysis of XPS spectra of Fe 2+ and Fe 3+ ions in oxide materials. Appl. Surf. Sci. 254, 2441–2449. https://doi.org/10.1016/j.apsusc.2007.09.063

Yang, H., Yan, R., Chen, H., Lee, D.H., Zheng, C., 2007. Characteristics of hemicellulose, cellulose and lignin pyrolysis. Fuel 86, 1781–1788. https://doi.org/10.1016/j.fuel.2006.12.013

Yang, X., Mu, Y., Peng, Y., 2021. Comparing lead and copper activation on pyrite with different degrees of surface oxidation. Miner. Eng. 168, 106926. https://doi.org/10.1016/j.mineng.2021.106926

Yang, X., Zhang, X., Wang, Z., Li, S., Zhao, J., Liang, G., Xie, X., 2019. Mechanistic insights into removal of norfloxacin from water using different natural iron ore – biochar composites: more rich free radicals derived from natural pyrite-biochar composites than hematite-biochar composites. Appl. Catal. B Environ. 255, 117752. https://doi.org/10.1016/j.apcatb.2019.117752

Yang, Y., Ye, S., Zhang, C., Zeng, G., Tan, X., Song, B., Zhang, P., Yang, H., Li, M., Chen, Q., 2021. Application of biochar for the remediation of polluted sediments. J. Hazard. Mater. 404, 124052. https://doi.org/10.1016/j.jhazmat.2020.124052

Yao, Y., Gao, B., Fang, J., Zhang, M., Chen, H., Zhou, Y., Creamer, A.E., Sun, Y., Yang, L., 2014. Characterization and environmental applications of clay-biochar composites. Chem. Eng. J. 242, 136–143. https://doi.org/10.1016/j.cej.2013.12.062

Yi, Y., Huang, Z., Lu, B., Xian, J., Tsang, E.P., Cheng, W., Fang, J., Fang, Z., 2019. Magnetic biochar for environmental remediation: A review. Bioresour. Technol. 298. https://doi.org/10.1016/j.biortech.2019.122468

Yoon, K., Cho, D.W., Bhatnagar, A., Song, H., 2020. Adsorption of As(V) and Ni(II) by Fe-Biochar composite fabricated by co-pyrolysis of orange peel and red mud. Environ. Res. 188, 109809. https://doi.org/10.1016/j.envres.2020.109809

Yuan, L., Liu, Y., 2013. Removal of Pb(II) and Zn(II) from aqueous solution by ceramisite prepared by sintering bentonite, iron powder and activated carbon. Chem. Eng. J. 215–216, 432–439. https://doi.org/10.1016/j.cej.2012.11.016

Zama, E.F., Reid, B.J., Sun, G.X., Yuan, H.Y., Li, X.M., Zhu, Y.G., 2018. Silicon (Si) biochar for the mitigation of arsenic (As) bioaccumulation in spinach (Spinacia oleracean) and improvement in the plant growth. J. Clean. Prod. 189, 386–395. https://doi.org/10.1016/j.jclepro.2018.04.056

Zeng, H., Yu, Y., Wang, F., Zhang, J., Li, D., 2020. Arsenic(V) removal by granular adsorbents made from water treatment residuals materials and chitosan. Colloids Surfaces A Physicochem. Eng. Asp. 585, 124036. https://doi.org/10.1016/j.colsurfa.2019.124036

Zeng, L., 2003. A method for preparing silica-containing iron(III) oxide adsorbents for arsenic removal. Water Res. 37, 4351–4358. https://doi.org/10.1016/S0043-1354(03)00402-0

Zhang, C., Shan, B., Zhu, Y., Tang, W., 2018. Remediation effectiveness of Phyllostachys pubescens biochar in reducing the bioavailability and bioaccumulation of metals in sediments. Environ. Pollut. https://doi.org/10.1016/j.envpol.2018.07.091

Zhang, J., Shao, J., Jin, Q., Li, Z., Zhang, X., Chen, Y., Zhang, S., Chen, H., 2019. Sludge-based biochar activation to enhance Pb(II) adsorption. Fuel 252, 101–108. https://doi.org/10.1016/j.fuel.2019.04.096

Zhang, M., Gao, B., Varnoosfaderani, S., Hebard, A., Yao, Y., Inyang, M., 2013. Preparation and characterization of a novel magnetic biochar for arsenic removal. Bioresour. Technol. 130, 457–462. https://doi.org/10.1016/j.biortech.2012.11.132

Zhang, M., Sun, X., Xu, J., 2020a. Heavy metal pollution in the East China Sea: A review. Mar. Pollut. Bull. 159, 111473. https://doi.org/10.1016/j.marpolbul.2020.111473

Zhang, M., Sun, X., Xu, J., 2020b. Heavy metal pollution in the East China Sea: A review. Mar. Pollut. Bull. 159, 111473. https://doi.org/10.1016/j.marpolbul.2020.111473

Zhang, W., Singh, P., Paling, E., Delides, S., 2004. Arsenic removal from contaminated water by natural iron ores. Miner. Eng. 17, 517–524. https://doi.org/10.1016/j.mineng.2003.11.020

Zhang, X., Gao, Y., Li, Y., Zhou, Y., Ma, H., Shang, J., Cheng, X., 2022. Synthesis of magnetic NiFe2O4/CuS activator for degradation of lomefloxacin via the activation of peroxymonosulfate under simulated sunlight illumination. Sep. Purif. Technol. 288, 120664. https://doi.org/10.1016/j.seppur.2022.120664

Zhang, Y., Cetin, B., Likos, W.J., Edil, T.B., 2016. Impacts of pH on leaching potential of elements from MSW incineration fly ash. Fuel 184, 815–825. https://doi.org/10.1016/j.fuel.2016.07.089

Zhang, Y., Hou, D., O'Connor, D., Shen, Z., Shi, P., Ok, Y.S., Tsang, D.C.W., Wen, Y., Luo, M., 2019. Lead contamination in Chinese surface soils: Source identification, spatial-temporal distribution and associated health risks. Crit. Rev. Environ. Sci. Technol. 49, 1386–1423. https://doi.org/10.1080/10643389.2019.1571354

Zhang, Y., Labianca, C., Chen, L., De Gisi, S., Notarnicola, M., Guo, B., Sun, J., Ding, S., Wang, L., 2021. Sustainable ex-situ remediation of contaminated sediment: A review. Environ. Pollut. 287, 117333. https://doi.org/10.1016/j.envpol.2021.117333

Zhao, M., Zhang, C., Yang, X., Liu, L., Wang, X., Yin, W., Li, Y.C., Wang, S., Fu, W., 2020. Preparation of highly-conductive pyrogenic carbon-supported zero-valent iron for enhanced Cr(VI) reduction. J. Hazard. Mater. 396, 122712. https://doi.org/10.1016/j.jhazmat.2020.122712

Zhao, X., Liu, W., Cai, Z., Han, B., Qian, T., Zhao, D., 2016. An overview of preparation and applications of stabilized zero-valent iron nanoparticles for soil and groundwater remediation. Water Res. 100, 245–266. https://doi.org/10.1016/j.watres.2016.05.019

Zhao, Y., Xu, M., Liu, Q., Wang, Z., Zhao, L., Chen, Y., 2018a. Study of heavy metal pollution, ecological risk and source apportionment in the surface water and sediments of the Jiangsu coastal region, China: A case study of the Sheyang Estuary. Mar. Pollut. Bull. 137, 601–609. https://doi.org/10.1016/j.marpolbul.2018.10.044

Zhao, Y., Xu, M., Liu, Q., Wang, Z., Zhao, L., Chen, Y., 2018b. Study of heavy metal pollution, ecological risk and source apportionment in the surface water and sediments

of the Jiangsu coastal region, China: A case study of the Sheyang Estuary. Mar. Pollut. Bull. 137, 601–609. https://doi.org/10.1016/j.marpolbul.2018.10.044

Zhao, Y., Zhang, R., Liu, H., Li, M., Chen, T., Chen, D., Zou, X., Frost, R.L., 2019. Green preparation of magnetic biochar for the effective accumulation of Pb(II): Performance and mechanism. Chem. Eng. J. 375, 122011. https://doi.org/10.1016/j.cej.2019.122011

Zhao, Z., Nie, T., Zhou, W., 2019. Enhanced biochar stabilities and adsorption properties for tetracycline by synthesizing silica-composited biochar. Environ. Pollut. 254, 113015. https://doi.org/10.1016/j.envpol.2019.113015

Zhong, D., Zhang, Y., Wang, L., Chen, J., Jiang, Y., Tsang, D.C.W., Zhao, Z., Ren, S., Liu, Z., Crittenden, J.C., 2018. Mechanistic insights into adsorption and reduction of hexavalent chromium from water using magnetic biochar composite: Key roles of Fe3O4 and persistent free radicals. Environ. Pollut. 243, 1302–1309. https://doi.org/10.1016/j.envpol.2018.08.093

Zhou, L., Chi, T., Zhou, Y., Lv, J., Chen, H., Sun, S., Zhu, X., Wu, H., Hu, X., 2022. Efficient removal of hexavalent chromium through adsorption-reduction-adsorption pathway by iron-clay biochar composite prepared from Populus nigra. Sep. Purif. Technol. 285. https://doi.org/10.1016/j.seppur.2021.120386

Zhou, Y., Cai, G., Cheeseman, C., Li, J., Poon, C.S., 2022. Sewage sludge ash-incorporated stabilisation/solidification for recycling and remediation of marine sediments. J. Environ. Manage. 301, 113877. https://doi.org/10.1016/j.jenvman.2021.113877

Zhou, Y., Gao, B., Zimmerman, A.R., Chen, H., Zhang, M., Cao, X., 2014. Biochar-supported zerovalent iron for removal of various contaminants from aqueous solutions. Bioresour. Technol. 152, 538–542. https://doi.org/10.1016/j.biortech.2013.11.021

Zhou, Y., Li, J., Lu, J., Cheeseman, C., Sun, C., 2019. Recycling incinerated sewage sludge ash (ISSA) as a cementitious binder by lime activation. J. Clean. Prod. 118856. https://doi.org/10.1016/j.jclepro.2019.118856

Zhu, S., Ho, S.H., Huang, X., Wang, D., Yang, F., Wang, L., Wang, C., Cao, X., Ma, F., 2017. Magnetic Nanoscale Zerovalent Iron Assisted Biochar: Interfacial Chemical Behaviors and Heavy Metals Remediation Performance. ACS Sustain. Chem. Eng. 5, 9673–9682. https://doi.org/10.1021/acssuschemeng.7b00542

Zhu, S., Huang, X., Wang, D., Wang, L., Ma, F., 2018. Enhanced hexavalent chromium removal performance and stabilization by magnetic iron nanoparticles assisted biochar in aqueous solution: Mechanisms and application potential. Chemosphere 207, 50–59. https://doi.org/10.1016/j.chemosphere.2018.05.046